Linking Microstructure to Irradiation Defects in Advanced Manufacture of Steels



Megan Carter
Lincoln College
University of Oxford

A thesis submitted for the degree of
Doctor of Philosophy
Michaelmas Term 2021

Abstract

Embrittlement of reactor pressure vessel (RPV) steel during neutron irradiation is a well documented phenomenon. Hardening embrittlement in low-Cu RPV steels is known to be associated with the development of solute clusters, primarily containing Mn, Ni and Si. Understanding the microstructural changes, and the corresponding impact on mechanical properties, caused by irradiation is critical in predicting the safe operating lifetime of commercial fission reactors. Multiple factors influence how a steel may respond to neutron bombardment; notably, composition and existing microstructure. Another significant variable involved in dictating the microstructure of steels is the manufacturing process. However, there is limited research on how varying these processes influences the irradiation response of RPV steels.

To investigate the role of manufacturing route on irradiation response, this thesis considers four different SA508 steels, each with a unique manufacturing route: Hot Isostatic Pressing (HIP), conventional large forging (LF), and two trial forgings tempered for distinct durations. HIP is a novel method for the manufacture of structural nuclear components, with the benefits of net-shape casting and microstructural homogeneity. The viability of HIPed components for use in the nuclear industry is dependent on understanding the effect of the microstructure on the irradiation response of the steel. HIPed material also presents an opportunity to deduce the role of different microconstituents within the same specimen.

Atom probe tomography (APT) was chosen as the primary investigative tool as it is a proven method for investigating the development of potentially embrittling microstructural features with high chemical and spatial resolution. APT was employed to analyse the early-stage development of Mn-Ni-Si (MNS) solute clusters of the different steel types, following neutron (HIP and conventional forging) and self-ion (all four steels) irradiation. Specifically, samples produced via the various manufacturing routes were compared with respect to the observable solute segregation behaviours.

Neutron irradiation of the conventional forged (LF) and HIPed samples was conducted using the OPAL reactor at the Australian Nuclear Science and Technology Organisation (ANSTO). Two sets of irradiations were used to produce samples of approximately 0.1 dpa ($\approx 6.7 \times 10^{21}$ n/m^2) and 0.2 dpa ($\approx 1.3 \times 10^{22}$ n/m^2) respectively. APT analysis found that the HIPed ferritic and bainitic samples exhibited similar MNS clustering behaviour under neutron irradiation. After three-months of irradiation, the LF sample hardened to a lesser extent ($\Delta\sigma_y \approx 157 \pm 112$ MPa) compared to the HIPed sample ($\approx 490 \pm 235$ MPa). This slightly increased relative hardening may be a cause for concern when considering HIPed SA508 for nuclear applications.

A set of three Fe^{4+} irradiations enabled analysis of the three forged and the HIPed steels under varying dose and temperature. P atmospheres were found in the HIP and LF alloys after ~0.1 dpa of damage at 300°C. The influence of manufacturing role was explored further, considering grain types, carbides and solute segregation to interfaces and dislocations. MNS clusters were found to grow in size as fluence increased, with additional Mn-rich solute clusters found after the 5 dpa irradiation.

Preface

The work presented in this doctoral thesis has been carried out at the Department of Materials, University of Oxford from October 2017 to December 2021, under the supervision of Prof. Michael Moody, Dr. Paul Bagot, and Dr. James Douglas. All of the research carried out for this thesis is original and where the work of others has been included it has been clearly referenced and acknowledged. No part of this thesis has been submitted for a degree at this, or any other university. Some of this work has been published in peer-reviewed journals and presented at conferences, as detailed below:

Publications

Megan Carter, Claudia Gasparrini, James O. Douglas, Nick Riddle, Lyndon Edwards, Paul A.J. Bagot, Christopher D. Hardie, Mark R. Wenman, Michael P. Moody. *On the influence of microstructure on the neutron irradiation response of HIPed SA508 steel for nuclear applications.* Journal of Nuclear Materials, Volume 559, 2022.

Conference Presentations

Megan Carter, J.O. Douglas, N. Riddle, P.A.J. Bagot, M.P. Moody. *The impact of self-ion irradiation on SA508 RPV steel produced via novel manufacturing methods.* European Atom Probe Tomography Workshop, Rouen, France, November 2019.

Megan Carter, J.O. Douglas, N. Riddle, P.A.J. Bagot, M.P. Moody. *Comparing Hot Isostatic Pressed and conventionally forged steel: An APT study of irradiation effects.* International Group on Radiation Damage Mechanisms, Gifu, Japan. May 2019

Acknowledgements

The completion of this thesis owes much to the contributions of many people, to whom I would like to convey my appreciation and gratitude.

Firstly, I would like thank Professor Michael Moody, Dr Paul Bagot and Dr James Douglas for their supervision during this project. Each of them have been influential in my atom probe journey, from my Part II research as an undergraduate, through to comforting conversations during my write-up. Some things haven't gone entirely smoothly, and I'm sure they too imagined spending a bit more time in the lab over the last two years, but together they provided the support, advice and deep pools of knowledge that enabled this thesis to be completed.

I would like to extend a particular thanks to James for the comfort and company he provided in the form of his wealth of FIB/APT experience, accompanying me on many a (sometimes sadly futile) experimental road trip. I know I was his first research student, and he went above and beyond in his selflessness and dedication, including willingness to educate me on some of this world's finer alcoholic beverages.

Members of the NEUIRR steels research programme have been influential in steering the direction of this project, providing the funding required to enable the study of active materials at the MRF. A special thanks to Dr Claudia Gasparrini for her contributions to this work.

I would like to acknowledge EPSRC for financing this research. I am also grateful for the funding provided by the NNUF, which ultimately was crucial in allowing me to gather the remaining data from the neutron-irradiated ANSTO samples. I am also thankful for the work of staff members at the MRF. I would also like to thank Rolls Royce for the provision of the materials used in this research. Specifically, discussions with Nick Riddle were incredibly insightful and helpful, and I would like to extend my thanks to him for his role in this project.

In particular, I would like to highlight the contribution of Dr Jack Haley, who gave his time to provide excellent TEM images, and Dr Hazel Gardner for some emergency nanoindentation. Also, thanks to Dr Ben Jenkins for providing the cluster analysis R scripts used in this project.

Of course, a lot of the enjoyment I experienced during this project is down to the Oxford Atom Probe Group members. Michael has cultivated a very special collection of scientists; everyone contributes to making a friendly, collaborative atmosphere, and I'm concerned at how quickly some of you can create memes.

I am forever grateful for the love and support I receive from my family and friends. You are all wonderful. Special thanks to Mum, Dad, Emma, Lauren and Sam; you may not have written this thesis, but you're responsible for every page.

Acronyms

ANSTO Australian Nuclear Science and Technology Organisation
APT Atom probe tomography
DCF Dalton Cumbrian Facility
EBSD Electron backscatter diffraction
EDS Energy dispersive spectroscopy
FIB Focused ion beam
HIP Hot isostatic pressing
IVAS Imago Visualisation and Analysis Software
LEAP Local electrode atom probe
LF Large forging
LWR Light water reactor
MD Matrix damage
MNS clusters Mn-Ni-Si clusters
MRF Materials Research Facility
MSM Maximum Separation Method
OPAL Open Pool Australian Lightweight
PWR Pressurised water reactor
RED Radiation enhanced diffusion
RIS Radiation induced segregation
RPV Reactor pressure vessel
SEM Scanning electrode microscopy
SMR Small modular reactor
SRIM Stopping and Range of Ions in Materials
TEM Transmission electron microscopy
TKD Transmission Kikuchi diffraction

Contents

List of Figures **vii**

1 Introduction **1**

2 Literature Review **5**
2.1 Reactor Pressure Vessels . . . 5
2.2 SA508 Grade 3 RPV Steel Metallurgy . . . 7
2.2.1 HIPed SA508 . . . 9
2.3 Interaction of Neutrons with Matter . . . 10
2.3.1 Irradiation Terminology . . . 13
2.3.2 The Neutron Irradiation Embrittlement of RPV Steels . . . 13
2.4 Mn-Ni-Si Rich Precipitates . . . 17
2.5 Modelling Realistic Neutron Flux Effects . . . 19
2.5.1 Materials Test Reactors . . . 20
2.5.2 Impact of irradiation temperature . . . 21
2.5.3 Ion irradiation . . . 22
2.6 Influence of Initial Microstructure on Radiation Response . . . 26
2.7 Role of Composition in Radiation-Induced Precipitation . . . 28
2.8 Atom Probe Tomography of Irradiated RPV Steels . . . 33
2.8.1 APT of Mn-Ni-Si clusters . . . 35
2.8.2 Cluster identification methods in APT . . . 37
2.8.3 Presence of iron in RPV clusters . . . 38
2.9 Scope for Further Work . . . 39

3 Materials and Methods **41**
3.1 Materials: SA508 Grade 3 Class 1 Steel . . . 41
3.1.1 Variation in post-forging heat treatment . . . 43
3.1.2 Hot Isostatic Pressing . . . 44
3.2 ANSTO Neutron Irradiations . . . 46
3.3 Ion Irradiations at Dalton Cumbrian Facility . . . 47
3.3.1 Calculating ion irradiation parameters . . . 48
3.3.2 SRIM profiles . . . 49
3.4 Atom Probe Tomography . . . 49
3.4.1 APT mass spectrum . . . 53
3.4.2 Hitmaps . . . 55
3.4.3 Trajectory aberrations . . . 56

3.5 Isosurfaces and Proxigrams . . . 57
3.6 Cluster Analysis . . . 58
3.7 Focused Ion Beam . . . 62
3.7.1 Site-specific FIB preparation of HIPed samples . . . 64
3.8 Nanoindentation . . . 66

4 Characterisation of As-Received SA508 Steel 69
4.1 HIPed Microstructure . . . 70
4.1.1 Determining ferrite fraction . . . 70
4.1.2 EBSD and EDS mapping . . . 72
4.2 APT Observations in As-received Samples . . . 74
4.2.1 Matrix compositions . . . 74
4.2.2 Solute segregation to dislocations and grain boundaries . . . 79
4.2.3 Carbides and carbide interfaces . . . 83
4.2.4 Silicon inclusions within carbides . . . 87
4.3 TEM . . . 90
4.4 Discussion . . . 94
4.4.1 Characterisation of HIPed SA508 . . . 94
4.4.2 Dislocations, interfaces and carbides . . . 95
4.4.3 Secondary intra-carbide precipitates . . . 96
4.5 Conclusions . . . 97

5 Neutron Irradiation of SA508 Steel 98
5.1 Three-month HIPed SA508 ANSTO Irradiation . . . 99
5.1.1 Nanoindentation . . . 99
5.1.2 Atom probe tomography . . . 101
5.2 Three-month Forged SA508 ANSTO Irradiation . . . 106
5.2.1 Nanoindentation . . . 107
5.2.2 Atom probe tomography . . . 108
5.3 Six-month HIPed SA508 ANSTO Irradiation . . . 112
5.3.1 Nanoindentation . . . 112
5.3.2 Atom probe tomography . . . 114
5.4 Six-month Forged SA508 ANSTO Irradiation . . . 118
5.4.1 Nanoindentation . . . 119
5.4.2 Atom probe tomography . . . 119
5.5 Carbides and Interfaces . . . 123
5.6 Cluster Size Distribution and Fluence . . . 130
5.7 Discussion . . . 134
5.7.1 Observation of early-stage neutron-induced clustering . . . 136
5.7.2 Irradiation hardening . . . 138
5.7.3 Clustering behaviour of HIPed and Forged SA508 . . . 144
5.8 Conclusions . . . 151

6 Ion Irradiation of SA508 Steel **153**
6.1 A: 0.1 dpa Fe^{4+} 300°C . . . 154
6.1.1 Phosphorus segregation . . . 158
6.1.2 Early stage MNS clustering . . . 162
6.1.3 Dislocations . . . 166
6.2 B: 0.6 dpa Fe^{4+} 150°C . . . 167
6.2.1 MNS clustering . . . 168
6.2.2 Case study: influence of depth-damage profile on defects observed in Large Forging . . . 170
6.3 F: 5 dpa Fe^{4+} 300°C . . . 172
6.3.1 MNS clusters . . . 174
6.3.2 Mn-rich solute clustering . . . 183
6.3.3 Dislocations and dislocation loops . . . 185
6.4 Self-Ion Irradiation Induced Segregation to Interfaces . . . 186
6.4.1 Carbide interfaces . . . 186
6.4.2 Grain boundary segregation . . . 189
6.5 Discussion . . . 192
6.5.1 Early-onset P segregation . . . 192
6.5.2 Impact of varying irradiation conditions . . . 194
6.5.3 Role of manganese in irradiation-induced solute clustering . . . 201
6.5.4 Role of manufacturing route on irradiation response . . . 203
6.6 Conclusions . . . 206

7 Discussion of Ion vs. Neutron Irradiation of SA508 Grade 3 Class 1 Steel **209**
7.1 Cluster Development . . . 210
7.2 Role of P . . . 213
7.3 Radiation-induced Solute Segregation . . . 214
7.4 Application to Alloy Comparison Studies . . . 216
7.5 Summary . . . 216

8 Conclusions **218**

9 Future Work **222**

Bibliography **225**

A ANSTO TEM **241**

B Application of Maximum Separation Method to Fe^{4+} Irradiation Features **244**
B.1 Investigation into MSM Parameters for P atmospheres . . . 244
B.2 MSM Order Parameter Changing for Irradiation A Mn-Ni-Si Clusters . . . 245

List of Figures

1.1 Low-carbon energy generation mix in the UK: 1990-2018 2

2.1 Schematic of typical Westinghouse RPV. 6
2.2 Typical SA508 Microstructure. 8
2.3 Schematic demonstrating the formation of a displacement cascade upon neutron impact with an atomic lattice. 11
2.4 Schematic highlighting the DBTT shifts and lowering of upper-shelf energy (USE) observed in irradiated RPVs. 14
2.5 Schematic demonstrating the arrangement of Cu atoms used to define the terms atmosphere, cluster and precipitate. 16
2.6 Plot of neutron damage against DBTT shift predicting the late-onset of embrittlement caused by MNSPs in low-Cu RPVs. 17
2.7 Plot of Frenkel pair (FP) and injected interstitial (II) production rates as a function of distance into a sample surface, as calculated by SRIM. 23
2.8 Indication of the 'safe analysis region' for a Fe-10%Cr steel irradiated with 5 MeV Fe^{+} ions. 24
2.9 Atom map showing clusters of Cu atoms formed in high nickel, high copper RPV welds after irradiation. 29
2.10 Plot demonstrating the change in Cu cluster density (N_{crp}), mean radius ($< R >$) and volume fraction (f_{crp}) with increasing neutron fluence. . . . 30
2.11 APT data set from high copper, high fluence RPV weld alloy. 34
2.12 Plot showing the relationship between cluster volume fraction and DBTT shift in surveillance samples. 36
2.13 Maximum Separation Method Schematic. 39

3.1 Tensile test data for novel trial forgings of SA508 Grade 3 Class 1 Steel at various temperatures. 43
3.2 Forged and HIPed SA508 Optical Micrographs 45
3.3 Comparison of the 0.2% proof test data obtained for Forgings B/C and HIPed SA508. 45
3.4 Image of the front face of the sample holder used for DCF ion-irradiations. 48
3.5 Damage profile into Fe^{4+} irradiated surface for a SA508 HIPed sample with target damage of 0.1 dpa at 500 nm depth. 50
3.6 Schematic of a Local Electrode Atom Probe. 51
3.7 Example SA508 Grade 3 Class 1 ranged mass spectrum 54
3.8 Schematic indicating the $^{58}Fe^{2+}$ and $^{58}Ni^{2+}$ ion peak overlap. 55
3.9 Example APT hitmap for SA508 steel (bcc) with major poles indexed. . . 56

3.10 Outline of the FIB liftout procedure to produce APT samples 63
3.11 Process of producing APT tips with an apex at a chosen surface depth (used for self-ion irradiated samples). 64
3.12 Example of a HIP SA508 steel APT wedge cross-section imaged using TKD. 65
3.13 Ferrite Grain Selection using SEM imaging 65
3.14 Tracking location of microconstituent grains in irradiated HIPed samples. 67
3.15 Example of a 80 nanoindent array 67

4.1 The process of using morphological segmentation in ImageJ to determine approximate ferrite fraction. 71
4.2 An EBSD map from as-received HIPed SA508 indicating the misorientation angles across various grain boundaries. 72
4.3 Frequency distribution of grain boundary misorientations in a) HIP and b) LF SA508 steel. 73
4.4 Process of identifying potential metallic inclusion and extracting EDS information. 75
4.5 Bar plot of the average Si, Ni, Mo and Mn contents in each type of SA508 alloy, acquired using APT 76
4.6 Solute segregation to a carbide and dislocations in as-received HIPed SA508. 78
4.7 APT map indicating solute segregation to a dislocation in as-received HIPed SA508 steel 78
4.8 Band contrast map indicating regions (yellow) where prior-austenite grain boundaries for APT liftout were identified using EBSD. 79
4.9 The isolation of a PAGB in as-received LF SA508 using TKD. 80
4.10 Indication of segregating species to a prior-austenite, ferrite grain boundary in as-received HIPed SA508 steel. 80
4.11 Analysis of solute segregation to grain boundary in as-received HIPed SA508 steel. 82
4.12 APT maps (showing C atoms only) of carbides found in as-received HIPed SA508 steel. 84
4.13 Proxigrams across carbide interfaces in as-received SA508 HIPed APT samples (original carbides shown in Figure 4.12) 87
4.14 APT data indicating the presence of Si-rich secondary precipitates within a carbide in HIPed SA508. 88
4.15 Bright field (BF) TEM images of as-received HIPed SA508 91
4.16 Bright field (BF) TEM images of the LF SA508 alloy. 92
4.17 Bright field (BF) TEM image montage of the forged C SA508 alloy. 93

5.1 EBSD images of nanoindent arrays in as-received and three-month irradiated HIPed SA508 steel 100
5.2 As-received and three-month irradiated HIPed SA508 steel nanohardness data 101
5.3 APT reconstructions of clustering in 0.1 dpa neutron-irradiated HIPed SA508 102
5.4 Plot detailing the volume fraction of clusters vs the total clusterable solute for 0.1dpa HIPed SA508 103

5.5 Plot indicating the relationship between the cluster volume fraction observed in samples and the relative Mn content, with respect to Ni, for the three-month irradiated HIPed ANSTO samples. . . . 104
5.6 Plot showing the composition of clusters (averaged) in each APT dataset of 0.1 dpa HIPed SA508 steel. . . . 105
5.7 Ternary diagrams of average cluster compositions for 0.1 dpa HIPed ferrite and bainite grains. . . . 106
5.8 Variation of measured nanohardness with indent depth for the as-received and 0.1 dpa forged SA508 samples. . . . 107
5.9 APT maps of 0.1 dpa forged SA508 steel. . . . 108
5.10 Plot showing average cluster compositions for each APT dataset obtained for the three-month irradiated forged SA508 sample. . . . 110
5.11 Plot showing volume fraction of clusters vs the total number of solute atoms involved in clustering present for each atom probe dataset of the three-month irradiated forged SA508. . . . 111
5.12 Variation of the measured nanohardness with indentation depth for the 0.2 dpa HIPed SA508 steel. . . . 113
5.13 APT reconstructions of clustering in 0.2 dpa neutron-irradiated HIPed SA508. . . . 114
5.14 Plot detailing the volume fraction of clusters vs the total clusterable solute for 0.2 dpa HIPed SA508. . . . 116
5.15 Plot showing the composition of clusters (averaged) in each APT dataset of 0.2 dpa HIPed SA508 steel. . . . 117
5.16 Plot correlating the tip composition with cluster composition in the 0.2 dpa HIPed sample. . . . 118
5.17 Variation of measured nanohardness with indent depth for the 0.1 dpa and 0.2 dpa forged SA508 samples. . . . 119
5.18 APT maps of 0.2 dpa forged SA508 steel. . . . 120
5.19 Plot detailing the volume fraction of clusters vs the total clusterable solute for 0.2 dpa forged SA508 . . . 121
5.20 Plot showing the composition of clusters (averaged) in each APT dataset of 0.2 dpa forged SA508 steel. . . . 122
5.21 Plot showing volume fraction of clusters vs the total number of solute atoms involved in clustering present for each atom probe dataset of the six-month irradiated forged SA508. . . . 123
5.22 APT maps of carbide found in 0.1 dpa HIPed bainite sample, Run 8834. . 124
5.23 APT maps of carbide and grain boundary found in 0.1 dpa HIPed bainite sample, Run 9753. . . . 126
5.24 Atom map and isosurface proxigram (15at.% C) for the carbide found in Run 10643 (0.2 dpa HIPed SA508) . . . 128
5.25 APT maps of the carbide and grain boundary found in 0.2 dpa forged bainite sample, Run 10649 . . . 129
5.26 Cluster size density histogram for the 0.1 dpa and 0.2 dpa ANSTO SA508 steel samples. . . . 131

5.27 Ternary composition diagrams for a series of cluster size (equal to number of detected solute atoms) divisions across all clusters seen in ANSTO neutron-irradiated steel APT datasets. . . . 133
5.28 Plot of cluster size against solute concentration for the key clustering solute across all clusters seen in the ANSTO neutron-irradiated steel APT datasets. . . . 133
5.29 Plot of the average hardness (at a depth interval of 100-200 nm) of the ANSTO samples, going from the as-received state, through to 0.2 dpa of damage. . . . 138
5.30 Plot of the average $\Delta\sigma_y$ against $\sqrt{V_f}$ for neutron-irradiated samples from the three-month irradiated (0.1 dpa) HIP and LF alloys, and the six-month irradiated (0.2 dpa) LF alloy. . . . 141
5.31 Plot detailing the volume fraction of clusters vs the total clusterable solute for the 0.1 dpa and 0.2 dpa HIPed SA508 steel samples. . . . 144
5.32 Average Mn, Ni, Si content (%) for clusters extracted from APT reconstructions of a) 0.1 dpa and b) 0.2 dpa neutron-irradiated HIPed and forged SA508 steel . . . 146
5.33 Plot of the cluster volume fraction each dataset against the corresponding overall tip composition, for both the three-month (0.1 dpa) and six-month (0.2 dpa) ANSTO irradiations. . . . 148
5.34 Plot of the average cluster compositions of each dataset against the corresponding overall tip composition, for both the three-month (0.1 dpa) and six-month (0.2 dpa) ANSTO irradiations. . . . 149

6.1 Damage profile into Fe^{4+} irradiated surface for a SA508 HIPed sample with target damage of 0.1 dpa at 500 nm depth. . . . 154
6.2 Overview of APT representative atom maps obtained from the Cartridge A Fe^{4+} irradiation of HIP SA508 Steel . . . 155
6.3 Plots illustrating the impact of Mn, Ni, Si and P composition in APT tips on the nature of segregation observed following self-ion Irradiation A. . 157
6.4 APT reconstructions showing only the local P concentration around P atoms present in an array of Cartridge A Fe^{4+} irradiated SA508 samples . 159
6.5 P atmospheres in HIPed and LF Fe^{4+} irradiated samples, at 0.09 dpa, 0.12 dpa and 0.23 dpa, 300°C. . . . 160
6.6 Plot indicating the Ni:Si ratio in each APT tip from the Irradiation A samples. 162
6.7 Ternary diagrams illustrating the relative fractions of Mn, Ni and Si in the clusters extracted from samples subjected to Irradiation A, according to the dose received. . . . 164
6.8 Two methods of matching MNS cluster location to regions of P enrichment. 165
6.9 C, P and Mo decorated dislocations in SA508 samples following Irradiation A. . . . 166
6.10 Damage profile into Fe^{4+} irradiated surface for a SA508 HIPed sample with target damage of 0.6 dpa at 500 nm depth. . . . 167
6.11 Example atom maps from the Irradiation B SA508 steel samples. . . . 168
6.12 Ternary diagram illustrating the relative fractions of Mn, Ni and Si in the clusters extracted from samples subjected to Irradiation B. . . . 170

6.13 Variation of N_d (a) and V_f (b) in LF samples at various dpa (from Irradiation B). . . . 171
6.14 Mn, Ni and Si decorated dislocations in two 1.18 dpa self-ion-irradiated LF SA508 steel. . . . 171
6.15 Concentration profiles indicating Mn, Ni and Si enrichment at dislocation lines in 1.18 dpa LF samples from self-ion Irradiation B. . . . 172
6.16 Damage profile into Fe^{4+} irradiated surface for a SA508 HIPed sample with target damage of 0.5 dpa at 500 nm depth . . . 173
6.17 Overview of APT maps from samples produced by Irradiation F. Only Mn, Ni and Si atoms are shown for clarity (with the exception of the C in forging C, sample 10269). . . . 175
6.18 Application of the standard MSM procedure (previously utilised in this work) to a APT dataset from a SA508 sample produced by Irradiation F. . 176
6.19 Process for the extraction of MNS clusters from Irradiation F APT datasets. 177
6.20 Ternary diagram illustrating the relative fractions of Mn, Ni and Si in the clusters extracted from samples subjected to Irradiation F . . . 179
6.21 Ternary diagram illustrating the relative fractions of Mn, Ni and Si in the clusters extracted from samples subjected to Irradiation F, based on nucleation site . . . 179
6.22 Plot of average cluster compositions in Irradiation F sample, according to classified cluster nucleation site. . . . 180
6.24 Variation of cluster composition with cluster size (as-detected), with data point colour denoting the determined nucleation site of each cluster. . . 182
6.25 Examples of the different forms of Mn-rich solute clustering present in Irradiation F samples. . . . 183
6.26 Atom maps from Irradiation F samples illustrating the correlative segregation of various elements to regions of primarily Mn-enrichment. . . . 184
6.27 Dislocation loops found in Irradiation F samples. . . . 186
6.28 0.09 dpa (Irradiation A) HIPed dataset showing the segregation of certain species to a carbide interface and a grain boundary. . . . 187
6.29 Carbide found in a 0.6 dpa (Irradiation B) forged B APT dataset, with accompanying proxigrams. . . . 187
6.30 Carbides found in Irradiation F samples of a) HIPed SA508 and b) forged B SA508. . . . 188
6.31 Solute segregation to a grain boundary observed in 0.23 dpa alloy C, visualised using an ROI perpendicular to the boundary plane. . . . 191
6.32 Mn, Ni and Si ternary plots illustrating average cluster composition for APT datasets from each self-ion irradiation. . . . 195
6.33 Cluster size distributions for the 0.23 dpa (Irradiation A), 0.6 dpa (Irradiation B) and 5 dpa (Irradiation F) SA508 steel samples. . . . 196
6.34 Plot of cluster size (atoms) vs P content for the clusters found in the 0.23 dpa (Irradiation A) and 5 dpa (Irradiation F) samples, coloured by alloy origin. . . . 205

7.1 Atom maps from LF samples produced by the neutron and self-ion irradiations, including the corresponding average cluster volume fraction and number densities. 211
7.2 Atom maps containing local concentration values and isosurfaces to illustrate the presence of P atmospheres and dislocation segregation in self-ion Irradiation A samples. 213

A.1 STEM-EDX analysis of a bainite grain extracted from neutron irradiated SA508 steel sample. 242

B.1 Comparing the use of isosurfaces and MSM to extract P atmospheres from same APT atom map. 245
B.2 Reduced view of a 8 nm thick slice of atom map (8 nm x 8 nm x 70 nm) from Forging B showing the identification of a cluster using MSM 246

Chapter 1

Introduction

The use of nuclear power as a means of worldwide, large-scale energy production is reaching a critical crossroads. With the Paris Agreement strongly steering nations towards an energy future not reliant on fossil fuels, an energy dense, low carbon method of power generation is required to supplement the use of renewable sources. With commercial nuclear fusion not a short-term solution, the most viable option is to implement a new generation of nuclear fission power plants.

Funding new reactors or full-scale plants requires extremely high investment capital, with the extreme start-up costs and long waits for profitable returns meaning many governments have been reluctant to initialise the construction of new nuclear power plants. In the UK, of the 15 reactors currently in use, 14 are due for decommissioning by 2032 [1]. Given the current low-carbon energy-mix in the UK (see Figure 1.1), this would leave a large deficit in energy generation against demand.

The plausibility of meeting low-carbon targets is thus dependent on either extending lifetimes of existing reactors, or the utilisation of nuclear fission technologies with quicker installation-to-generation times and lower capital costs. The development of small modular reactors (SMRs) is one such advancement, employing existing, proven fission reactor

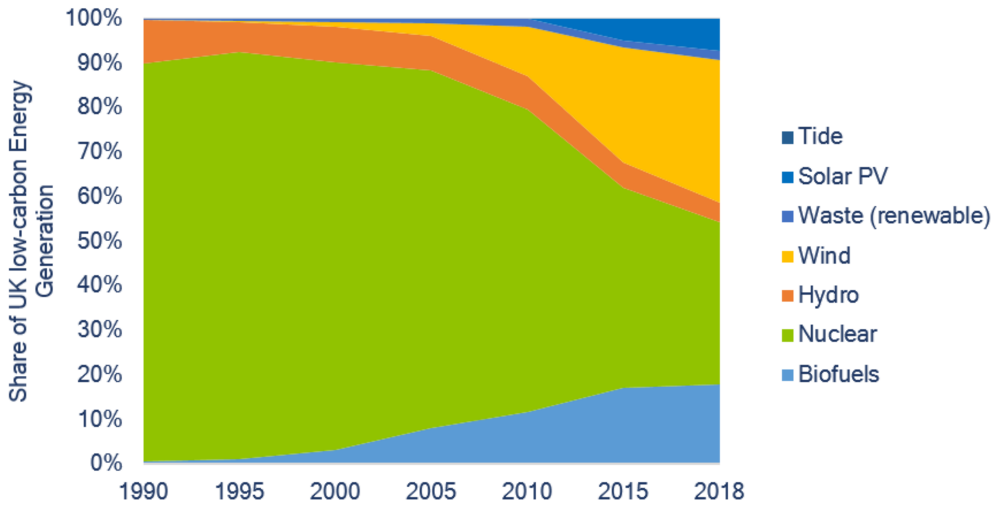

Figure 1.1: Low-carbon energy generation mix in the UK: 1990-2018. Based on IEA data from IEA (2020) World Energy Balances, IEA, www.iea.org/statistics, All rights reserved; as modified by Megan Carter

technology on a much reduced scale compared to existing power plants. This allows the pre-fabrication of components prior to on-site installation and the employment of 'factory-line'-type construction, with the aim of significantly reducing installation time and costs. The development of new reactor designs brings a possibility to utilise manufacturing methods (such as Hot Isostatic Pressing) different to those traditionally employed for nuclear components. If these novel methods were to be used, any influence on component lifetime must be understood.

Extensive research has shown that, for the case of reactor pressure vessel (RPV) steels, the primary lifetime-inhibitor is the onset of hardening and embrittlement introduced by reactor operating conditions. Specifically, a key area of consideration is the role exposure to long-term neutron irradiation plays on steel microstructure and subsequent mechanical properties. Literature has demonstrated that, with the reduction in RPV steel Cu contents, Mn, Ni and Si have dominated in the formation of nanoscale solute clusters known to induce hardening [2]. The nature of these solute clusters has been shown to depend on various

factors; principally, fluence, flux, alloy composition and irradiation temperature. However, investigations tend to utilise steels produced with established methods of manufacture, and thus the impact of changing manufacturing route has not been sufficiently explored.

This thesis presents work detailing the development of Mn, Ni and Si cluster defects in RPV steels of commercially-conventional composition (SA508 Grade 3 Class 1), with varying manufacturing routes. Four alloys are utilised: a conventional forging; a Hot Isostatic Pressing (HIP); and two forged alloys of matching composition but different tempering durations. Neutron and self-ion irradiation is used with the aim of examining the impact of pre-existing alloy microstructure on the onset and development of solute cluster defects induced by exposure to radiation. The primary form of materials characterisation employed throughout this research is atom probe tomography (APT) - chosen due to its capability in visualising atomic-scale volumes, necessary for the identification of irradiation-induced MnNiSi (MNS) solute clusters.

A critical review of the existing literature covering the impact of irradiation on RPV steels and the role of irradiation conditions is presented in Chapter 2. This is followed by a discussion of the materials and experimental methods relevant to this thesis in Chapter 3.

Initial characterisation of the investigated alloys is presented in Chapter 4, focusing on the microstructure of the HIPed steel and the gathering of baseline APT results for all materials analysed.

Neutron irradiation work, described in Chapter 5, concentrates on the potential of HIP as a manufacturing method for RPV or nuclear steel components in fission reactors, based on the irradiation response of steel fabricated using this powder-processing method. In particular, the variance in irradiation response between bainitic and ferritic microconstituent phases are investigated using APT and nanoindentation. The conventional forging sample is subjected to the same irradiations and post-irradiation analysis, with any differences in the irradiation response of two alloy types discussed.

A wider variety of materials and irradiation conditions were investigated using self-ion irradiation, including the two experimental forgings, with findings presented in Chapter 6. Results focus on whether the influence of manufacturing route changes with irradiation dose and temperature, whilst also analysing the development of irradiation-induced damage with fluence.

Chapter 7 gives a brief comparison of the impact of neutron and self-ion irradiation on the steels investigated, focusing on qualitative discussion given the differing nature of the two incident particles.

A summary of the key findings of this work is set forth in Chapter 8, with Chapter 9 outlining the areas of potential further research.

Chapter 2

Literature Review

2.1 Reactor Pressure Vessels

In nuclear fission power plants, the Reactor Pressure Vessel (RPV) is a critical component; it cannot be replaced, and as such is a limit to plant lifetime. RPVs contain coolant water necessary for reactors to operate at acceptable efficiency levels, and thus they must be able to withstand the harsh reactor environment; the water can be at an elevated temperature of approximately 290°C and pressures between 7 MPa and 14 MPa [3]. Furthermore, the RPV is exposed to high neutron fluence of around 10^{23} neutrons/m^2 [3]. With stringent regulations concerning failure probabilities of an RPV in service, material selections determine constraints on RPV dimensions and mechanical properties, subsequently influencing the lifetime of reactors.

Extending the amount of time a light water reactor (LWR) can safely operate by 20 years is worth an estimated £7-9billion per reactor [4]. This, combined with the fact that decommissioning costs are responsible for approximately 9-15% of the capital cost of a nuclear power plant [5], makes it economical to increase reactor lifetimes. However, these extensions can only be authorised if the regulatory agencies involved are provided with

sufficient proof that critical materials employed in the reactors can continue to maintain their integrity throughout prolonged operation [6].

For decades, steel has been the obvious choice for RPV construction. The response of RPV steels to the demanding environment inside a fission reactor substantially affects how long the component can safely be utilised before the risk of failure is sufficiently high to necessitate decommissioning. It is well known that the combination of high

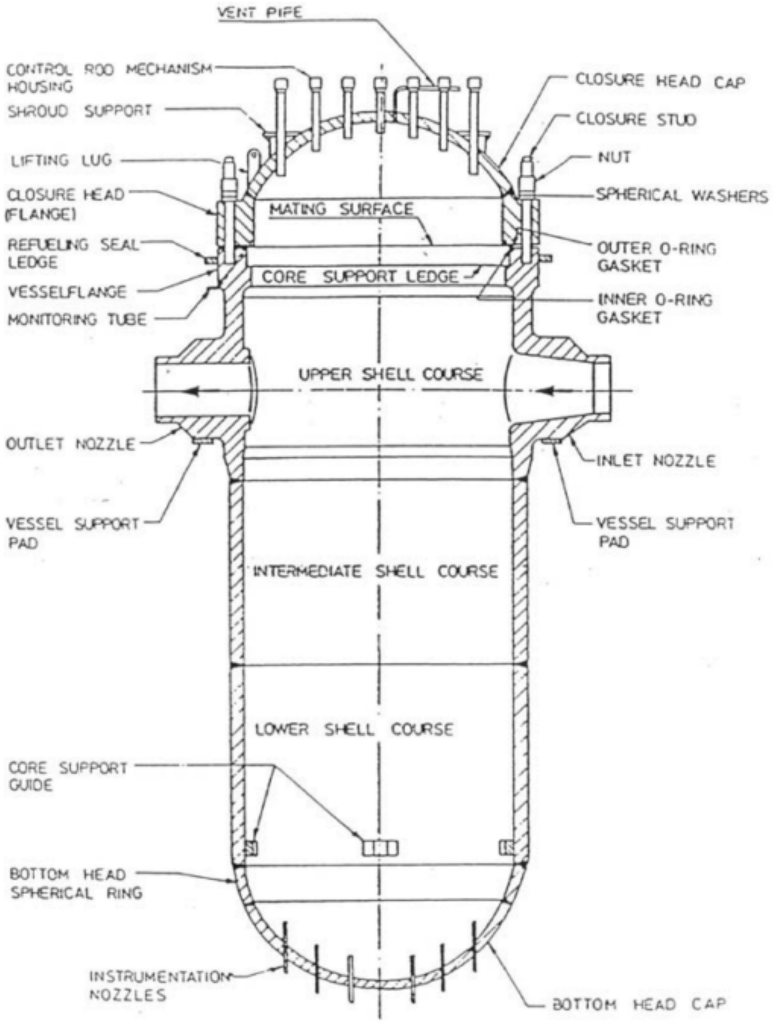

Figure 2.1: Schematic of typical Westinghouse RPV. Nuclear Energy Series No. NP-T-3.11 © IAEA (2009) [7].

temperature and neutron flux incident on the vessel induces embrittlement [8–12]. As a result, the material properties of RPV steel 40 years into operation are inferior to those at installation; understanding the mechanisms behind, and resulting extent of, this degradation in properties is critical for predicting viable reactor lifetimes. However, the known response of an RPV to neutron irradiation may not provide sufficient information to accurately infer its response to greater cumulative neutron fluence [6]. So called *late-blooming phases*, and the role of potential further cluster growth, has been predicted to play a detrimental role as lifetimes surpass 60 years, likely becoming a leading limiting factor in service extensions [6, 13]. A need for further research on this has therefore been identified [14].

With the development of small modular reactors (SMRs), and the move by the UK government to invest up to £56 million in SMR R&D over three-years, the scope for innovative RPV manufacturing has widened [15]. Commissioning SMRs brings the possibility of using methods and materials that are either a developing technology or that previously could not have been realistically scaled for larger components. This diversification and scaling of the UK nuclear programme necessitates both improved understanding of how conventionally manufactured RPVs respond to operation conditions (as they continue to be used for large-scale plants) and investigation of the resilience of RPV components produced by new manufacturing routes.

2.2 SA508 Grade 3 RPV Steel Metallurgy

The materials used for RPVs have commonly been variations on Mn-Ni-Mo steel for over 50 years. Initially, R&D programmes focussed on the creation of a new type of steel that could be forged into relatively thick components, necessary for constructing reactors that can withstand high pressures and temperatures, and possess the radiation resistance necessary [16]. This resulted in the introduction of low-alloy Mn-Ni-Mo steels [14], which,

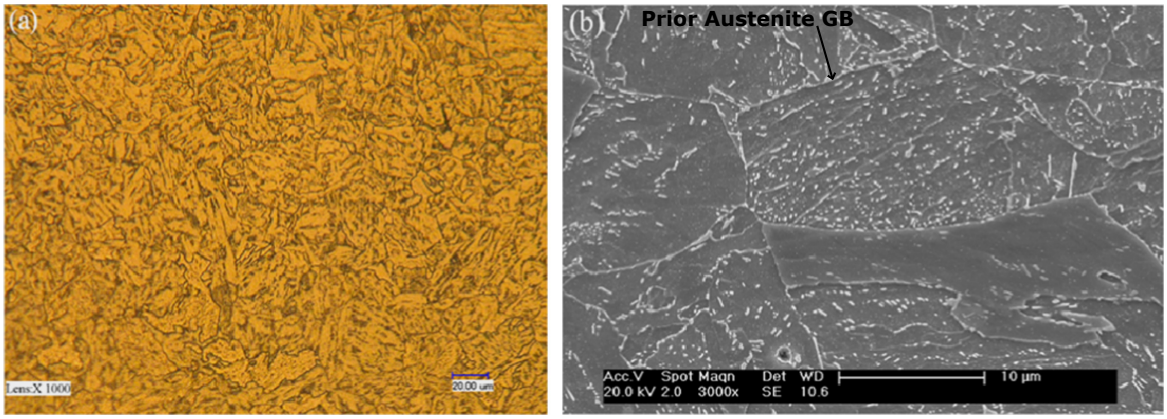

Figure 2.2: Image of as-received SA508 a) Optical Image showing tempered bainite structure b) SEM image highlighting prior-austenite grain boundary. Adapted from [17].

following a specific heat treatment, incorporated a complex microstructure of tempered bainite within prior-austenite grains of approximately 30 µm [7] (see Figure 2.2). Variants of this steel demonstrate good fracture resistance and the required yield stress for use in RPVs.

A typical heat treatment for a forged RPV component would include austenisation, quenching and tempering stages. Austenisation is particularly important as it dictates the grain size; a characteristic linked to the response of an alloy to radiation. The degree of tempering may also have an effect on the resulting microstructure, and hence the initial mechanical properties.

Research has continued to refine the composition by investigating the effect of individual alloying elements on steel's mechanical properties and response to radiation. For example, nickel acts to increase the hardenability of steel whilst decreasing its ductile-to-brittle transition temperature (DBTT) [18]. Mo and Mn suppress the ferrite-pearlite transformation, thus making bainite formation favourable, with Mo also working as a solid solution strengthener and carbide former.

The most notable changes in alloy composition came with the discovery of detrimental Cu-precipitation behaviour. The influence of copper content on post-irradiation mechanical properties will be discussed further in Section 2.3.2. Research in this area prompted the

development of modern RPV alloys high in Mn, Ni and Mo whilst low in Cu.

2.2.1 HIPed SA508

Conventionally, RPVs are produced from steel forgings. Hot Isostatic Pressing (HIP) is a powder-metallurgy manufacturing technique, consisting of the consolidation of metal powders under high temperature and pressure [19], which could provide an alternative route for producing nuclear components. Significant investigation into the radiation response of HIPed steels is required if they are to be implemented into reactor designs. However, very little research has been conducted. Zinkle et al. note that HIP is a potential processing route for SMRs, although they stress the importance of comparing the stability of potential HIPed material microstructures and performance with that of more conventional RPV specimens [6].

The benefits of exploiting this method lie in its production of components that possess a fine, consistent grain size, combined with a reduced need for post-forming machining [20]. Furthermore, large-scale forged samples are known to exhibit macroscopic inhomogeneity (often due to thick cross-sections causing differential cooling rates during quenching) corresponding to location-dependent mechanical properties [21]. By using HIP processing, variation in cooling rate is avoided during manufacture, producing a more consistent microstructure and thus a more dependable knowledge of a component's macro-scale properties [19].

Notably, the microstructure of HIPed SA508 steel incorporates significant volumes of idiomorphic ferrite - a microconstituent phase formed through the intragranular, heterogeneous nucleation of ferrite grains displaying crystallographic faceting [22]. This results in polygonal, or roughly equiaxed, ferrite grains. It has been suggested that this form of ferrite is associated with high transformation temperatures, where the rate of growth

is independent of boundary orientation [23]. Compared to bainite, polygonal ferrite is softer, and associated with nucleation upon existing particles, notably MnS in steels [24, 25]. There is scope for investigating the role of equiaxed, idiomorphic ferrite in dictating the embrittlement experienced by irradiated HIPed specimens.

2.3 Interaction of Neutrons with Matter

To investigate the changes induced within a material by neutron irradiation, the nature of interactions between incident neutrons, produced by the fission process, and the material microstructure must first be identified. The damage mechanisms involved are well understood, with literature detailing the process both qualitatively and utilising computer modelling to aid visualisation. Figure 2.3 is a schematic demonstrating the effects of fast neutron (0.1-10 MeV) bombardment. In fission reactors, fast neutrons are responsible for the majority of radiation damage due to their elastic collisions with the material's atoms causing atomic displacements within the lattice [9]. These displacements are collectively known as a *cascade*, and generally have the following sequence [7, 9, 26, 27]:

1. a lattice-atom, known as the Primary Knock-on Atom (PKA), is hit by an incident neutron (E>1 MeV)
2. the PKA is displaced from its site (if the energy transferred exceeds the threshold displacement energy) and begins to move through the lattice
3. interactions/collisions with other lattice atoms cause the PKA to lose energy
4. atoms impacted by the PKA can be displaced, which can in turn displace further atoms, producing a cascade
5. displacements off lattice sites create vacancies, whilst the knocked-on atoms become self-interstitial atoms (SIAs) after sufficient energy is lost through interactions

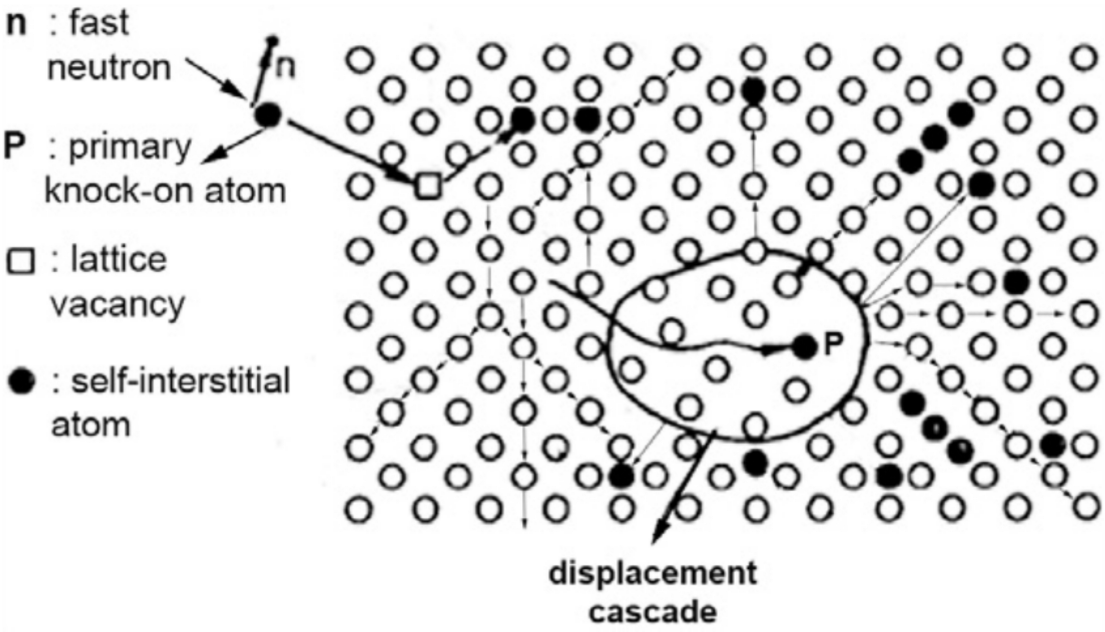

Figure 2.3: Schematic demonstrating the formation of a displacement cascade upon neutron impact with an atomic lattice. Image sourced from [31] © Copyright 1976, reprinted by permission of Informa UK Limited, trading as Taylor & Taylor & Francis Group, http://www.tandfonline.com

The displacement cascades result in the formation of *Frenkel Pairs*, the combination of a vacancy and SIA, corresponding to an elevated concentration of mobile point defects. How the overall microstructure develops depends on the migration and clustering mechanisms of these point defects, along with their interaction with solute atoms [28]. It has been proposed that these defects can go on to interact via three possible paths [29, 30]:

(a) the defects diffuse to sinks, such as dislocations or grain boundaries

(b) defect clusters accumulate point defects (such as vacancies or interstitial solute)

(c) Frenkel pairs annihilate due to recombination of the vacancy and interstitial

Predicting the outcome of the interaction of these defect paths is complicated by the role of thermal ageing, which, although not a direct focus of this review, is discussed in relation to RPV steel environments in Sections 2.3.2 and 2.5.2.

Although the principles of a neutron displacement cascade were known, the mechanisms

behind observed irradiation embrittlement took longer to be concluded. Understanding of this critical issue has rapidly increased in recent decades [32]. It is now comprehensively documented that the primary changes in mechanical properties induced by radiation are a result of dislocation motion being inhibited by defects formed by displacement cascades. A consequence of this is an increase in hardness, which is detrimental for those materials employed as structural components. The features involved in embrittlement are one of two types of defects within the metal microstructure, which act independently of each other and often require the diffusion of solute atoms [33].

The first is *non-hardening*, which refers to solute segregation (primarily by P and Ni) to grain boundaries and corresponds to increased likelihood of brittle intergranular fracture due to lowered boundary cohesions [7, 34]. Radiation-induced segregation (RIS) is a diffusion-driven process caused by the flux of point defects (created as a result of the irradiation process) to specific microstructural features, in this case grain boundaries, which act as point-defect sinks. A comprehensive review of this phenomenon is found in [35]. Each type of solute's respective diffusivity dictates the extent of segregation; if diffusion of a particular species is quickest via vacancies it is depleted adjacent to the sink, whereas if diffusion is quicker via interstitials there is solute enrichment [36].

Hardening defects refer to those that strengthen the metal, such as precipitates and matrix damage (MD), by impeding dislocation motion [37]. Primarily, it is the *hardening* defects that have been researched the most extensively in relation to neutron embrittlement; the effect of *non-hardening* embrittlement is low in comparison [38]. These are discussed in more detail in relation to RPVs in Section 2.3.2.

An important determination to be made with many features formed during irradiation is whether they have formed as a result of radiation-enhanced diffusion (RED), a result of excess mobile point-defects due to neutron-induced atomic displacement, or radiation-induced segregation (RIS). Whilst often used interchangeably, the use of these terms hints

at the underlying nature of the features observed; RIS is used to describe solute segregation during irradiation which would otherwise not occur, whereas RED refers to a diffusion process, often involving the formation of a thermodynamically stable phase, which would be expected to occur but at a much reduced rate compared to that seen under irradiation. The distinction between these processes is often an important argument when deducing the formation and growth mechanics for various aspects of radiation damage.

2.3.1 Irradiation Terminology

When discussing irradiation effects it is important to carefully define the terminology involved, as a range of different parameters can influence the experimental observations.

- **Flux** - the number of neutrons incident on a surface per unit area per unit time.
- **Fluence** - a measure of the number of neutrons incident per unit area of the irradiated surface (generally only considers those of sufficient energy to effect the material) [7].
- **dpa** - *displacements per atom* is a parameter used to quantify matrix damage levels during/post an irradiation and essentially measures the average number of site-ejections each atom experiences. It equates to the number of Frenkel Pairs produced by neutron irradiation within a given volume, divided by the total number of atoms within that volume [7]. It was developed as a parameter for comparison of neutron and self-ion damage as a first approximation [39].

2.3.2 The Neutron Irradiation Embrittlement of RPV Steels

As stated, a RPV is subjected to significant neutron fluxes during its lifetime. However, the damage rates are relatively low ($<10^{-10}$ dpa/s), and thus a typical reactor only experiences around 0.08 dpa of MD by the end of its operation [40].

The fundamental safety criterion of RPVs is to maintain sufficient toughness [3], hence

post-irradiation mechanical testing is essential for developing an understanding of the rate of toughness degradation experienced by RPV steels. Charpy vertical-notch (CVN) tests are the most common tool utilised. An example of the data obtained from a CVN experiment is shown in Figure 2.4. A significant number of studies have determined that the fundamental effect of the hardness increase caused by prolonged neutron fluence on RPV steel was a significant embrittlement, characterised by a marked increase in DBTT, ΔT and lowering of the upper shelf energy (USE), as shown in Figure 2.4 [3, 27]. The shift is often measured at 41 J as a standard for comparison.

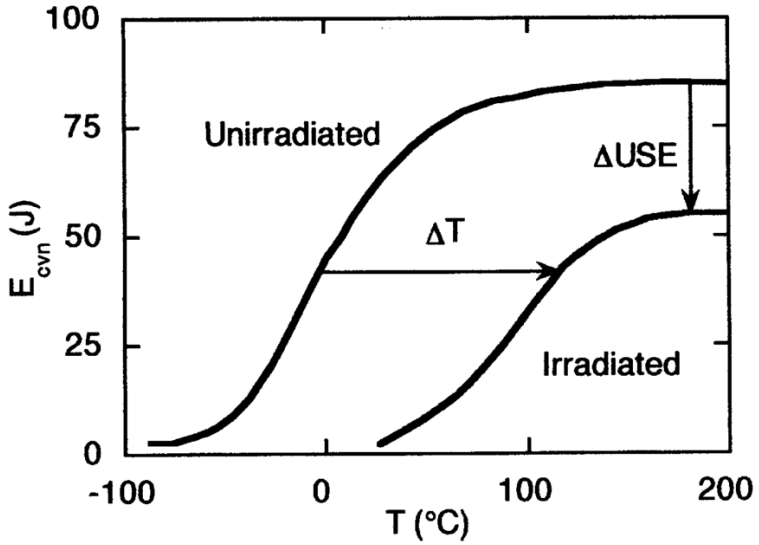

Figure 2.4: Schematic highlighting the DBTT shifts and lowering of upper-shelf energy (USE) observed in irradiated RPVs. Image sourced from [41] © Copyright 1998, reprinted by permission of Informa UK Limited, trading as Taylor & Taylor & Francis Group, http://www.tandfonline.com

Hardness measurements from indentation studies are also an indicator of RPV embrittlement. There exists issues translating small-volume testing into knowledge of macro-scale properties, although some studies have shown that this is possible [42–44]. Rice and Stoller have reported a numerical relationship between nanohardness and macro-scale tensile yield stress results for ferritic steels, shown in Equation 2.1 [42]. Use of this form of conversion is instrumental in opening up the use of micro-mechanical testing of irradiated samples.

$$\Delta\sigma_y[\text{MPa}] = 274\Delta H_N[\text{GPa}] \tag{2.1}$$

As discussed above, the nature of this irradiation-induced deterioration of RPV properties originates from the combined contributions of three distinct microstructural forms, each playing a role in the overall material embrittlement and subsequent DBTT shift [45, 46]. These features are: the direct MD induced by neutron collisions (can be stable, i.e. clusters of interstitials, or unstable, i.e. vacancy aggregates); nanoscale solute precipitates; and solute segregation to grain boundaries. The two latter features are often a result of the constituent defects of MD migrating within the lattice; vacancies and/or interstitials can coalesce to form heterogeneous nucleation sites for solute precipitates, whilst vacancies alone can facilitate rapid diffusion of solute atoms [37].

The unstable types of MD are those that may then be redissolved back into solution upon exposure to elevated temperatures, such as those observed in reactor service conditions [16, 45]. This has the effect of recovering the crystal lattice to a certain extent. A high temperature environment also corresponds to greater diffusion lengths for the residual vacancies and interstitials formed by neutron irradiation [7, 31]. Consequently, the role of thermodynamics is still critical in dictating the end damage resulting from a given irradiation. This factor must be considered when using test reactors or alternative neutron sources that do not expose the investigated material to 60 years in a fission reactor.

Of these features, the decrease in fracture toughness has been most widely attributed to the formation of solute clusters. As previously noted, these clusters are described as *hardening* features and literature has shown that this increase in hardness corresponds to an increase in DBTT [3, 16, 33, 47]. Although embrittling solute clusters are often referred to as *precipitates*, they are perhaps more accurately described as *clusters* or *atmospheres*, given they have yet to be commonly observed with a distinct crystallographic structure

[48]. This work will characterise solute segregations using the terminology described by Miller and Burke in 1992, shown in Figure 2.5 [48].

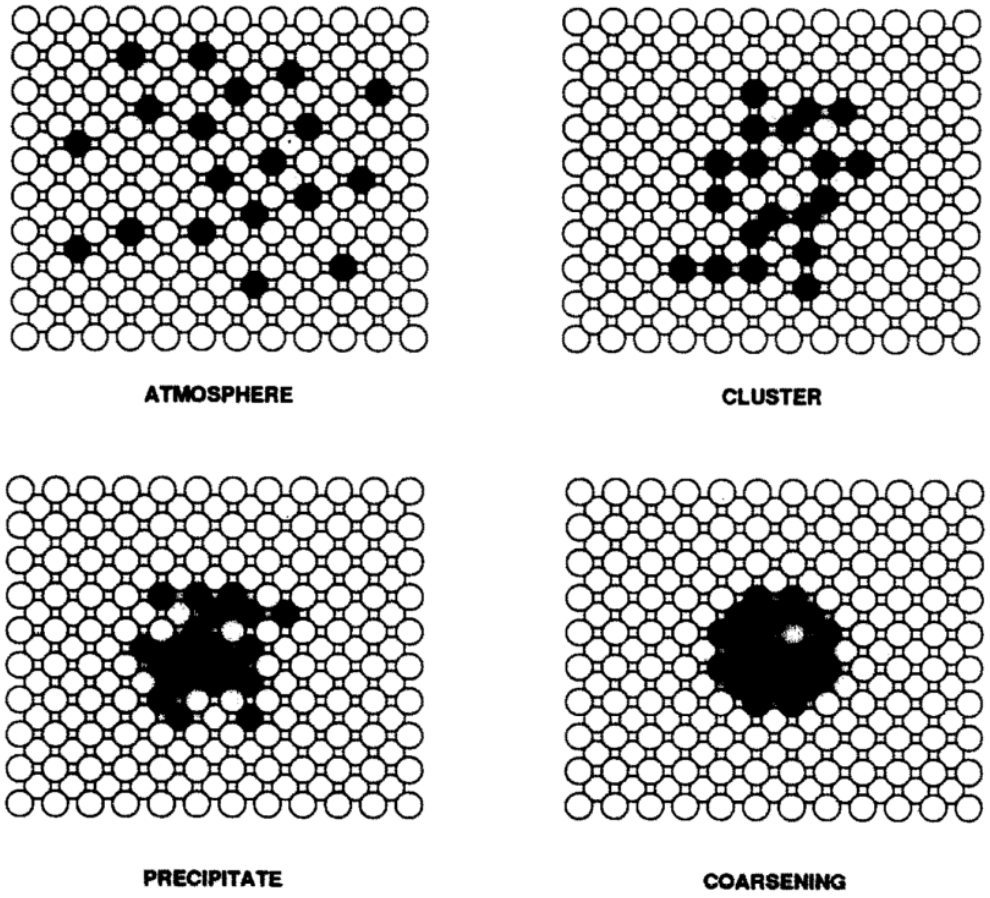

Figure 2.5: Schematic demonstrating the arrangement of Cu atoms used to define the terms atmosphere, cluster and precipitate. Reprinted from [48] © Copyright 1992, with permission from Elsevier.

Early research highlighted the formation of nanoscale Cu solute clusters as the dominating hardening mechanism in RPV steels [11]. However, the focus of studies have recently shifted towards the influence of Mn-Ni-Si clusters (MNSPs) in low-Cu Mn-Ni-Mo alloys (refer to Section 2.4 for more background on MNSPs). The level of hardening induced by inclusions of these types has been shown to vary according to the square-root of their volume fraction within the material [49, 50]. Characterisation techniques have

been extensively utilised to investigate irradiated microstructures, specifically focusing on the clusters, and include: SANS (Small Angle Neutron Scattering) [27, 40, 47, 49, 51]; TEM [31, 52, 53]; FIM (Field Ion Microscopy) [54, 55]; and APT (Atom Probe Tomography) [56–58]. It is the final technique that, arguably, has enabled the most significant insights into cluster formation, development and composition. Accordingly, and also given its prominent role in the focus of this research, its contribution to analysing precipitation hardening in RPV steels is discussed in detail in Section 2.8.

2.4 Mn-Ni-Si Rich Precipitates

Mn-Ni-Si rich precipitates were first observed in low-Cu RPVs exposed to high fluences in the 1990s, leading Odette to coin the term *late-blooming phases* (LBPs) to describe

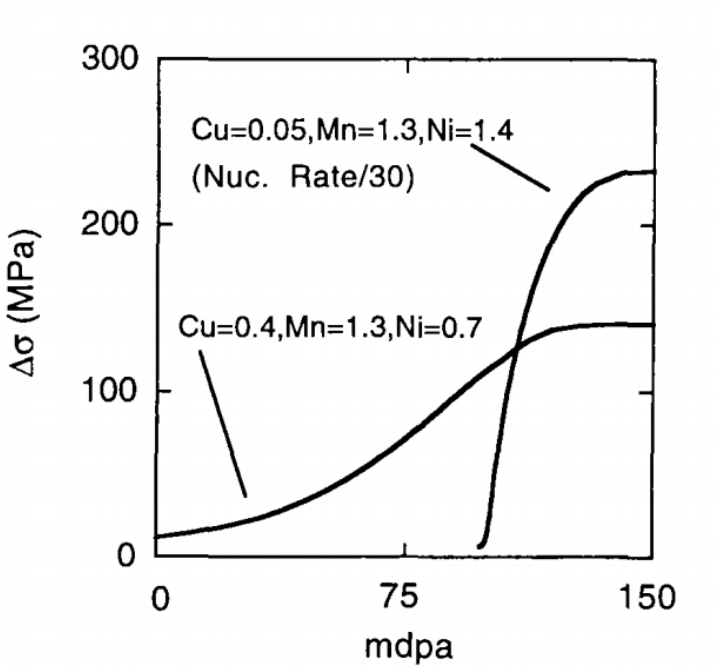

Figure 2.6: Plot of neutron damage against DBTT shift predicting the late-onset of embrittlement caused by MNSPs in low-Cu RPVs. Reprinted from [59] © Copyright 1995, with permission from Elsevier.

them [59]. The development of these phases, at a stage in irradiation where previously it was thought the influence of CRPs plateaued, is a potential source of serious deterioration in RPV fracture toughness far into it's lifetime. Odette predicted this outcome, as shown in Figure 2.6, and SANS data collected by Bergner et al. confirmed delayed hardening acceleration by observing an increase in integrated magnetic scattering with increased dpa [60].

The study of MNSPs has since become a key focus for operation extension, with two main proposed mechanisms for their formation [37].

The first is that they are thermodynamically favourable phases but require a heterogeneous nucleation site in order to form [41]. Studies have shown MNSP stability in post-irradiation anneals of 450°C, thus suggesting they are stable at the lower reactor temperatures [61, 62]. Thermodynamic modelling [40, 63] has resulted in some researchers postulating that the interactions between Mn, Ni and Si reduces their solubility limits within the Fe-Mn-Ni-Si system. These findings, combined with evidence of a crystallographic structure collected in a recent X-ray diffraction study [64], suggest Mn-Ni-Si precipitates are stable, equilibrium features within the microstructure.

The second theory is MNSPs can only be induced by irradiation, and are not thermodynamic phases. Radiation induced segregation (RIS) has been shown to occur for these elements in both experimental [65, 66] and simulation [67–69] studies; specifically their diffusion to solute sinks such as vacancy clusters and dislocations. Furthermore, Monte Carlo calculations have shown that Mn and Ni aggregate earlier than Cu in the matrix, but have a lower growth rate, hence Cu would not be a necessary factor in MNSP formation [67]. This kinetic role in RIS could correspond to differences in formation rate observed in high and low dose irradiations [2].

There are suggestions that MNSP formation may actually be an amalgamation of these mechanisms; essentially a combination of RIS (for cluster nucleation) and RED (giving enhanced cluster growth) [70]. Odette proposed that CRPs and MNSPs would both form

thermally, but are kinetically limited [59], whilst high neutron fluence has been shown to correlate with sufficient formation of copper cluster complexes to enable precipitation, thus radiation enhances MNSP formation [2]. Original nucleation theories assumed the presence of a small Cu core within all MNSPs observed, however, Mn-Ni-Si clusters with low Cu levels present (no core structure observed) have now been consistently observed in surveillance specimens [45]. RIS is likely to play a more important role in highly sub-saturated alloys, given the reduced drive for initial MNSP formation [63, 71, 72]. Hence, it is considered to be stable MD features or solute-vacancy complexes which act as the heterogeneous nucleation sites for MNSPs in low-Cu alloys [2, 70, 73]. It is also becoming clearer that MNSPs exhibit some degree of thermal stability close to typical reactor temperature [69], and thus demonstrate RED dependent growth, given that MNSPs formed via high fluence neutron irradiation have been shown to persist during Post Irradiation Annealing (PIA) [70].

MNSPs remain unaccounted for in current RPV regulatory models (*dose-damage-relationships*) [2]. In order to gain an improved insight into the nature of these clusters, the exact mechanics of their formation and their link to macro-scale mechanical properties, effective atomic-scale detection and compositional analysis is required in correlation with mechanical testing.

2.5 Modelling Realistic Neutron Flux Effects

There is an impracticality in waiting 40-60 years for specimens to be irradiated within a functioning fission reactor. This is especially problematic given the critical importance, for safety considerations, of gaining insights into RPV irradiation response over very extended periods, before the current operational reactors reach those lifetimes. Given this, various techniques are used to allow microstructure and property evaluations at a given dose with reasonable turn-over times. Some samples are surveillance materials taken from fission

plants, though even these are not subjected to the exact same conditions as an RPV due to being located in a different region for ease of extraction [74].

Generally, due to the logistical and safety difficulties involved in obtaining samples from operational commercial reactors, alternative irradiation sources have been commonly utilised by researchers in attempts to simulate the effect of long-term neutron irradiation.

2.5.1 Materials Test Reactors

As a consequence of the difficulty obtaining, and awaiting sufficient reduction in activity of, historical reactor samples, much of the data obtained (and utilised for lifetime prediction) on neutron-irradiated RPV steels is from material test reactors (MTRs). To simulate the neutron fluence induced by long-term reactor operation, high-flux, but short-lasting, irradiations are conducted in these experiments. The extent to which this accurately reproduces the low flux incident on RPVs over their lifetime has been questioned [13]. There is some evidence that the artificially high flux used in MTRs produces radiation damage of a different nature to those seen in PWR specimens; in particular, Cu precipitates in MTR samples have been shown to be smaller and denser, whilst matrix damage exhibits a lower degree of thermal stability and thus contributes less to hardening [75].

Furthermore, it is important to note that neutron fluence alone does not dictate irradiation damage levels, rather other parameters, such as neutron flux, neutron energy spectrum and gamma ray flux, play a role [76]. There appears to be a marked difference in mechanical properties recorded in post-irradiation samples (at 290°C) from power reactors (lower neutron flux) compared to those from test reactors (high neutron flux). However, there exists no simple linear relationship between flux and embrittlement; higher flux can increase or decrease hardening depending on other factors, such as temperature, fluence and alloy composition [14]. Notably, more recent studies by Lindgren et al. conclude that

there is no overall effect of flux on the resulting hardness, rather the effects are balanced out due to high flux conditions giving smaller solute clusters but at a higher number density [66]. This mirrors the findings of Dohi, Wagner and Bergner [77–79].

The difficulties and variables involved in provision of neutron-irradiated samples severely complicates developing prediction models that align experimental data with reality. As a result, alternative processes for analysing irradiation effects have been developed, often substituting the type of irradiation particle used. There is also holistic operational parameter effects with flux, notably composition and temperature [80]. For power reactors or test reactors, there is an interplay between the experimental temperature and the neutron flux applied, potentially as a result of the processes responsible for the primary radiation damage differing, corresponding to variance in point defect cluster population [76]. At operational temperatures nearer the 300°C for a functional PWR, it was generally observed that the amount of embrittlement increased with reduced flux [81]. For lower temperatures (50-150°C), a negligible flux effect was reported [76]. However, this is perhaps an oversimplification of a complex problem; many researchers also reported an influence of composition and fluence, with flux effects less pronounced as fluence increases towards saturation embrittlement levels.

2.5.2 Impact of irradiation temperature

The temperature at which radiation experiments occur plays a significant role in the nature of microstructural damage observed - it has generally been demonstrated that lower temperatures give rise to an increase in matrix damage features (such as dislocation loops and voids) [60, 82]. A sufficient amount of thermal energy available during irradiation (or after in the case of post-irradiation annealing) can allow increased rates of defect annihilation or recombination such to mitigate the levels of MD experienced [29, 83].

Subsequently, any change in microstructure (and, by continuation, mechanical properties) is dictated by the amalgamation of continually occurring damage and annealing processes. The irradiation temperature (T_{irr}), with respect to the melting temperature (T_m) of the target material, dictates the degree of interstitial and vacancy mobility possible [34]. At lower temperatures ($0.06T_m < T_{irr} < 0.3T_m$, where T is in K) only interstitial atoms are free to diffuse, whereas at higher temperatures ($0.3T_m < T_{irr}$) both interstitials and vacancies are mobile, although the thermal energy available is insufficient for complete recombination and the point defect concentration is higher than that expected at thermal equilibrium [34]. In the case of SA508 Grade 3 Class 1 RPV steel ($T_m \sim 1770$ K), LWR operation temperatures are equivalent to approximately $0.32T_m$.

Given the interplay between multiple damage mechanisms and recovery processes during irradiation, which in turn are affected by numerous variables (dose rate, particle type, fluence etc.), isolating the role of temperature on mechanical properties in a given radiation is difficult. Generally, it is expected that increasing irradiation temperature corresponds to reduced irradiation embrittlement, likely as a result of increase point defect recombination [81, 84]. Whilst the typical temperature range fission RPVs are exposed to lies at around 300°C, the temperature chosen for MTR or accelerator irradiations can vary.

2.5.3 Ion irradiation

The most common technique used to replicate the effects of neutron irradiation on RPV steels is ion irradiation, with proposals for its use dating back to the 1960s [85]. The advantages of using a charged-particle source lies in its ability to generate damage 10^4 times faster than with neutrons, whilst introducing negligible (proton) or zero (heavy ion) residual radioactivity into the sample [85, 86]. Accelerators also provide greater control over dose rate, temperature and fluence, which is essential if long-term RPV

irradiation is to be modelled within the lifetime of existing commercial reactors. However, fundamentally the use of ions as a surrogate to neutrons is an "unphysical" process; the particle types are different to such an extent that, even though damage effects may be replicated, any interpretation or extrapolation from such results, with respect to comments on neutron-irradiation, is likely to introduce significant uncertainties. Subsequently, should an experimentalist aim to emulate neutron irradiation using ions, a significant amount of care should be taken over selecting conditions and understanding the influence of utilising the different methods [85, 87]. Given an appropriate amount of caution, many researchers have published work supporting the use of ion-irradiation [50, 86, 88, 89].

For any charged-particle irradiation, there exists a significant divergence in scattering cross-section when compared to neutrons; ions can have a collision cross-section exceeding six orders of magnitude larger that of neutrons, giving a major reduction in the possible mean free paths between collisions [90]. This results in an inhomogeneous damage profile induced by ion bombardment, where damage effects are limited up to a certain depth, in contrast to neutrons, where the damage is uniform [30]. The nature of this damage

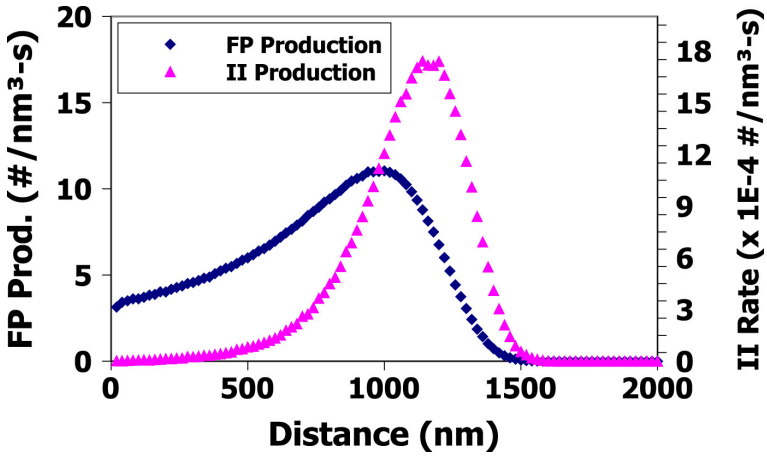

Figure 2.7: Plot of Frenkel pair (FP) and injected interstitial (II) production rates as a function of distance into a sample surface, as calculated by SRIM. Reprinted from [91] © Copyright 2016, with permission from Elsevier.

profile renders the existence of the free, incident surface of significant importance - the amount of damage observed is often a function of the distance away from this surface. Free surfaces act as defect sinks, thus a defect-depleted zone is often observed near the incident surface [30, 87]. There is also a region of injected interstitials at a greater depth, caused by the forward-skewed momentum of ion-atom collisions resulting in a local-enrichment of interstitials beyond the peak in vacancy production, as shown in Figure 2.7 [39, 86, 91, 92].

This variation of dpa with depth gives rise to a very narrow volume from which viable analysis can occur, as shown in Figure 2.8, with Was noting the significance of even a small error (500 nm) in volume isolation on the corresponding dose [86]. Although knowledge

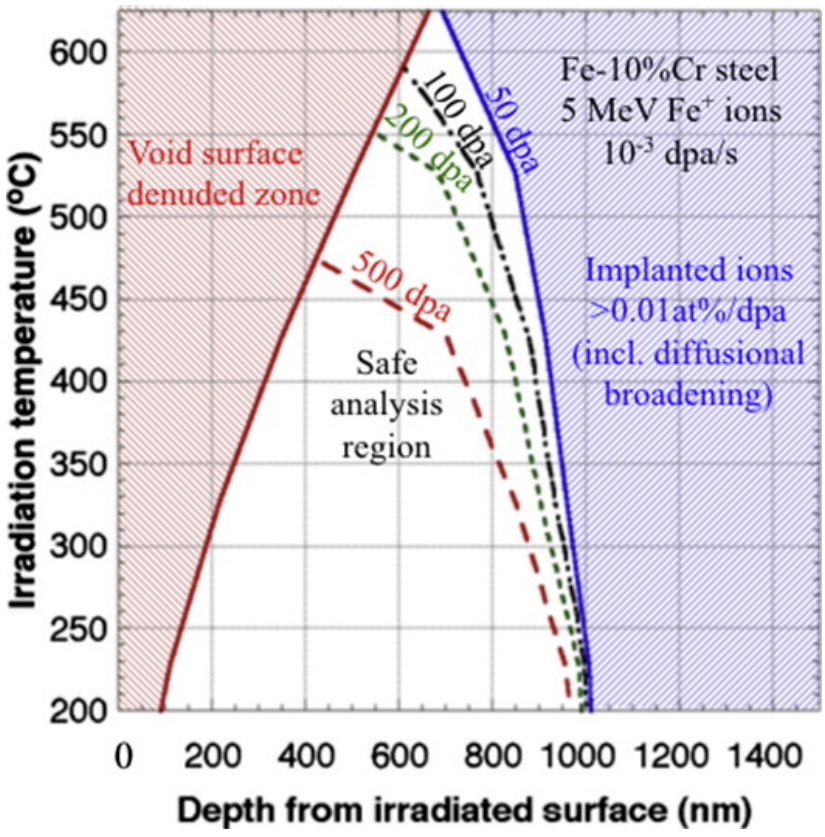

Figure 2.8: Indication of the 'safe analysis region' for a Fe-10%Cr steel irradiated with 5 MeV Fe^+ ions to a damage level of 50-500 dpa at 10^{-3} dpa/s. Diffusional broadening effects have been included, indicating the shrinking of the 'safe' region as temperature and dose increases. Reprinted from [87] © Copyright 2018, with permission from Elsevier.

of the expected profile can be obtained using SRIM models [93], this applies only where defects are immobile; in reality, some degree of diffusion of the implanted interstitials would be expected for ongoing irradiations, especially at raised temperatures, resulting in a broadening of the ion profile [87, 94, 95]. Due to the limited amount of 'safe' volume, specialised, localised mechanical testing techniques, such as nanoindentation, are necessary to determine the embrittling influence of ion-irradiation [44, 96, 97]. However, these techniques are non-standard in the nuclear industry; using them in conjunction with ion irradiation raises the issue of whether materials investigated using this practice will be accepted as evidence in licensing or life-extension feasibility studies [98].

By having a greater spread in the possible PKA energies responsible for collisions, including collisions at lower energies than are possible with neutrons, ion irradiations are associated with a greater rate of primary defect production [87]. It has been suggested irradiation temperature should be higher when using ions at high flux to reproduce neutrons, as it enhances defect diffusion kinetics. This produces similar defect arrival times at solute sinks or vacancy-solute clusters, ensuring the proportion of recombined defects and those that go on to form microstructural faults is more in line with that observed for neutron irradiation [99, 100]. However, quantifying the exact shift in temperature required for each ion irradiation experiment is beyond current understanding, due to the complicating influences of vacancy migration kinetics and temperature [87, 101].

Self-ion irradiation

Self-ion irradiation refers to using the ionised form of the majority bulk element in the target material, for example, iron ions for the irradiation of a steel. Significantly heavier incident particles are used compared to neutrons, subsequently producing dense damage cascades within the material which induce a region far from equilibrium [102].

It has been suggested that using dpa as a parameter to convert neutron damage to that

caused by self-ions is a first-order approximation [39]. This highlights the main issues with using heavy particles to induce damage effects; although atomic displacements still occur, comparisons based only on displacements is simplistic and ignores other influences (such as dose rate and cascade effects) on the genuine damage experienced by the steel. In particular, it is the increased dose rate associated with heavy-ion irradiation which is known to have significant effects on the extent of RED and RIS observed, given the increased level of vacancy-SIA recombination [36, 103]. However, one benefit of this form of charged-particle irradiation is that the large amount of implanted interstitials ascribed to heavy-ion bombardment does not also contribute to a local change in chemistry [30].

Use of self-ion irradiation for the study of irradiation damage effects has been reported in [97, 104–106]. Although generally it is agreed that heavy ions are not an exact surrogate for neutrons, they have been shown to successfully reproduce irradiation effects observed in power reactors [107], including dislocation loops, similar clustering behaviour [103], swelling [91] and creep [108].

2.6 Influence of Initial Microstructure on Radiation Response

Generally, it is the desired initial strength of an alloy that determines the chosen method, or the manufacturing restrictions, for the component being produced. There is a knowledge deficit regarding the influence of processing route on the irradiation behaviour of RPV steels. In past studies, microstructural parameters, such as grain size and morphology, of reactor materials, which can be effected by the heat treatment experienced, have been investigated. This provides a starting point for inferring any potential role processing may have in neutron embrittlement.

The importance of a fine grain size has been explored in the literature [16, 109, 110], but no clear relationship with radiation response has yet been identified. The most definitive hypothesis, presented by Steele, states that the role of grain size is only influential at low temperatures, below those experienced in fission reactors [16]. However, this area needs further investigation.

The phases within microstructure may also influence embrittlement sensitivity. In investigations by Marini et al. bainite appeared less sensitive to non-hardening irradiation embrittlement (based on the extent to which intergranular fracture) compared to martensite [38]. Post-irradiation, the fracture-mode for martensitic grains became more likely to be intergranular, whereas for bainitic microstructures the mode of brittle fracture remains transgranular cleavage. Marini et al. suggests that this is due to interface misorientation. Edmondson et al. found an increase in Cu-enriched clusters in the ferrite region of a low-copper forging and attributed this to local variation in copper concentration depending on phase [111]. This highlights the value of future studies investigating the role of phase fraction in cluster number density. There is thus an opportunity for research focusing on the hardness changes following irradiation of bainitic and ferritic grains, relating hardening to the nature and density of clusters within those grains. This could give an improved insight into the role of phase fractions in resultant embrittlement.

Steele concludes that microstructure, though influential, is always a secondary factor, in relation to embrittlement behaviour, when compared to composition [16]. Although this conclusion seems rational, given the significant role of elemental diffusion on DBTT, there is still scope to further explore the impact manufacture has on location, severity and mechanism of embrittlement.

2.7 Role of Composition in Radiation-Induced Precipitation

Alloy composition dictates the solute atoms available that can potentially exhibit or exacerbate precipitation in RPV steels. However, the effect of radiation-induced behaviour on certain elements must be weighed against their initial contribution to solute strengthening. Decreasing solute levels may reduce the post-irradiation embrittlement, but simultaneously correspond to a weaker starting alloy. There may also be synergistic effects between alloying elements, making the discerning of the exact role of each solute difficult; any progress in this area was most commonly achieved via systematic variation of alloy composition for a particular (model) alloy system.

Copper

Cu was identified as a problem element in RPV steel composition late in the 1960s; the addition of copper to a steel increases its sensitivity to radiation [112]. The presence of relatively high impurity levels of copper in RPVs was attributed to the use of copper-coated welding rods [3, 37, 113].

An increased level of embrittlement was linked to the formation of copper-rich clusters and Cu-vacancy complexes, in addition to the agglomerated point-defects produced via neutron cascade [114]. Clustered Cu solute are described as 'copper-rich precipitates' (CRPs) - produced as a result of irradiation-enhanced diffusion mechanisms [11, 115, 116]. These features (shown in Figure 2.9) are the dominant cause of RPV embrittlement in steels with Cu content >0.1 wt.%, where there is sufficient supersaturation driving their nucleation [41, 81].

Studies have shown the growth mechanisms of CRPs are non-linear; their average radii increase rapidly at low fluence, but the growth-rate decreases over time [14]. Subsequently,

if only CRPs were being considered, a saturation in irradiation hardening would be observed [65]. Figure 2.10 presents the nucleation (N), growth (G) and coarsening (C) stages of cluster growth, as predicted by thermodynamic and kinetic theory [59].

Further research into CRPs has since provided evidence of Mn and Ni within these features, often in the form of a shell surrounding a copper-rich core, highlighting that it is not just Cu that is influential in dictating RPV embrittlement.

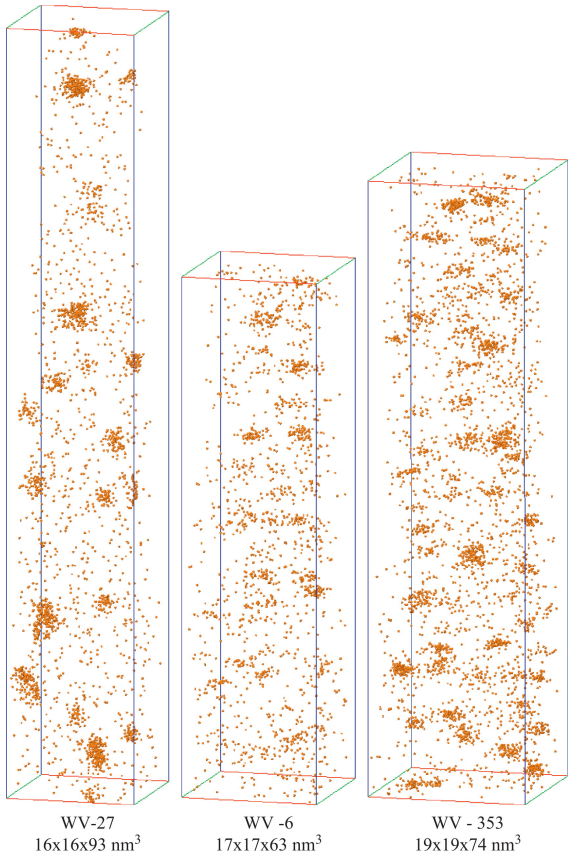

Figure 2.9: Atom map showing clusters of Cu atoms (orange) formed in high nickel, high copper RPV welds after irradiation. Other constituent elements have been removed for clarity. Reprinted from [28] © Copyright 2011, with permission from Elsevier.

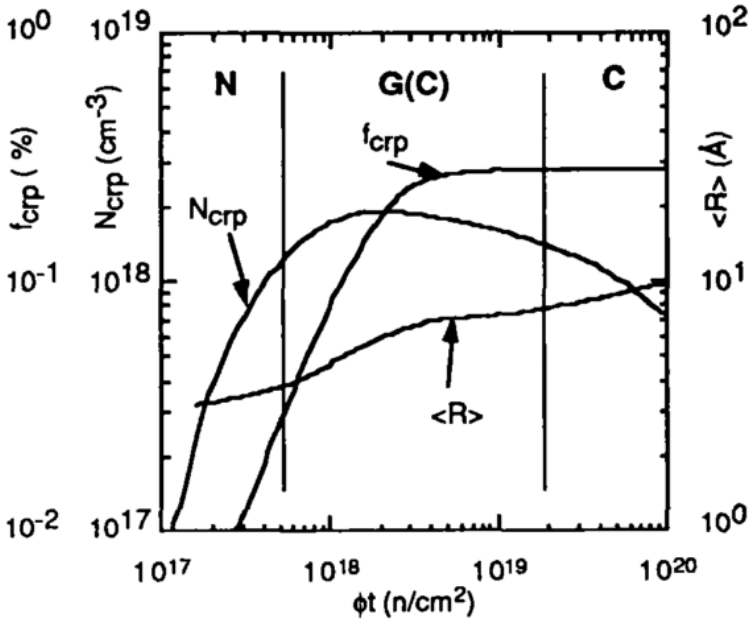

Figure 2.10: Plot demonstrating the change in Cu cluster density (N_{crp}), mean radius ($< R >$) and volume fraction (f_{crp}) with increasing neutron fluence. Reprinted from [59] © Copyright 1995, with permission from Elsevier.

Nickel

It is now accepted that Ni has an adverse effect on the sensitivity of steel to radiation-induced embrittlement [7, 13, 18, 47, 117], although the mechanisms behind its influence are not fully understood.

Initial suggestions proposed that Ni and Cu have a synergistic effect on embrittlement susceptibility [12, 14, 31, 40]. Hawthorne showed that increased Ni beyond 0.4wt.% caused Cu to display an enhanced hardening effect in plate RPV steel, following a 288°C irradiation, reportedly confirming this synergism [12]. However, Lambrecht et al. suggest that Ni (and Mn) only plays a limited, yet non-negligible, role in radiation sensitivity in low-copper steels, and further state that the hardening mechanisms associated with Cu and Ni are independent [46].

Due to the complex interplay between different solute concentrations in RPV steels, it is difficult to confirm for sure that the effect of nickel is linked in any way to copper, beyond alloying with CRPs. It therefore makes sense to evaluate its impact objectively; Ni influence on radiation hardenability needs to be studied where Cu effects have been minimised. Recently, these investigations have taken place, with Cu levels being closely controlled to <0.05wt.%, allowing the role of Ni to be studied more closely as an individual solute-effect [16]. In particular, recent work on ion-irradiated Fe-Ni and Fe-Mn model alloys demonstrated that RIS occurred in both alloys, with Ni and Mn clusters formed respectively, in the absence of a Cu stimulus [118]. This suggests that there is a driving force for Ni clustering.

One postulated influence of Ni on irradiation sensitivity is its role in enhancing grain boundary hardening, leading to a degradation in fracture toughness. This is a synergistic effect with phosphorus (which has consistently been shown to segregate to boundaries [18, 34, 58, 112, 119]), and demonstrated greater P diffusion to grain and ferrite-lath boundaries with increased Ni content [13, 18]. Based on this relationship, queries have arisen as to the influence of Ni on dictating the extent of non-hardening embrittlement, given the potential that heterogeneous nucleation of Ni features to grain boundaries could correspond to further enhanced P levels and thus greater intergranular toughness loss [37]. Furthermore, Miller proposed that hardening within the matrix could correspond to an increased importance of grain boundaries, as steel failure is often at the 'weakest link' [120]. Therefore, in steels where there is greater intergranular embrittlement due to Ni/P boundary diffusion, an observed difference in mechanical properties post-irradiation could result.

There have been contrary findings noting that in *superclean* SA508 Grade 4N forged steels (high-Ni but low- Mn, S, P and Si contents) neutron irradiation does not result in any significant reduction in the 47 J DBTT [121]. Burke et al. therefore carried out a comprehensive microstructural characterisation of forged SA508 Grade 4N in an attempt

to assess the impact of irradiation-induced changes to the steel microstructure [113]. By comparing high-Ni alloys, containing respectively approximately 0.3wt.% and 0.03wt.% Mn, they came to the conclusion that manganese is critical in stabilising the development of hardening solute-inclusions. As such, it may be wrong to single out Ni as solely causing a DBTT shift in high concentrations, rather Mn plays a complementary role. This postulation that Mn content is a controlling factor in determining embrittlement behaviour, when combined with Ni, is complemented by the findings of Lee et al. and Kang et al. [47]. It is therefore important to consider Mn as an influential element in irradiation hardening.

Manganese

Belkacemi-Rebrab et al. suggest that, based on ion-irradiated Fe-Mn and Fe-Ni model alloys, Mn segregates more strongly in Fe compared to Ni [118]. This is explained by the dual-diffusion method of Mn; both vacancy and self-interstitial diffusion is possible, compared to only vacancy-diffusion for Ni [122].

Furthermore, modelling has shown that Mn is capable of forming very stable mixed-dumbbells, not seen for Ni or Si [123]. These dumbbells can cluster via self-interstitial migration, in turn becoming sinks for further Mn dumbbells – and eventually Ni and Si atoms – allowing the formation of enriched solute clusters [67].

Phosphorus

Neutron irradiation has been show to enhance segregation of phosphorus atoms to grain boundaries in RPV plates [58, 119], forgings [34, 58] and welds [18, 58, 119]. Nishiyama et al. focused on the role of enhanced P diffusion in irradiation induced intergranular embrittlement, though the research does not indicate any correlative effect with Ni; rather, it is concluded that clusters play the greater role [124]. As expected, a higher bulk P content

corresponds to increased levels of segregation and hardening [88], however, Nishiyama et al. proposed that a reduction in the amount of intergranular fracture observed between the unirradiated and irradiated conditions suggests that P inclusion into hardening clusters mitigates any contribution of non-hardening boundary segregation to embrittlement. Notably, this P segregation effect has been shown to exhibit more strongly post-ion irradiation compared to neutron-irradiated [97].

The major role of phosphorus in irradiation clustering is likely a stabilising effect [97], linked to the formation of small solute-complexes caused by interstitial P migration [106]. This is attributed to the large P-vacancy binding energy [125]. P stabilising of point-defect clusters was also demonstrated in [126], where it was deemed to allow cluster development through the capture of Ni and Si, producing solute clusters. Phosphorus atmospheres were observed to be the only feature of forged, low-Cu RPV steels which exhibited a 31°C 41 J DBTT shift following neutron irradiation at intermediate fluence at operational temperatures [127]; this suggests that P clustering may be involved in early-stage embrittlement.

2.8 Atom Probe Tomography of Irradiated RPV Steels

As previously detailed, the nanoscale clusters formed as a result of irradiation are known to play a major role in RPV embrittlement. Modern day atom probe tomography (APT) has become an extensively used, powerful tool for developing an understanding of the role of clusters and solute segregation in irradiation hardening, by means of its high spatial resolution and elemental mapping.

Initial research into irradiation-induced clustering in RPV steels was undertaken using Atom Probe Field Ion Microscopy (APFIM), the forerunner to APT. APFIM was first used on fission reactor surveillance samples in 1981 [55]. Miller et al. observed the presence of

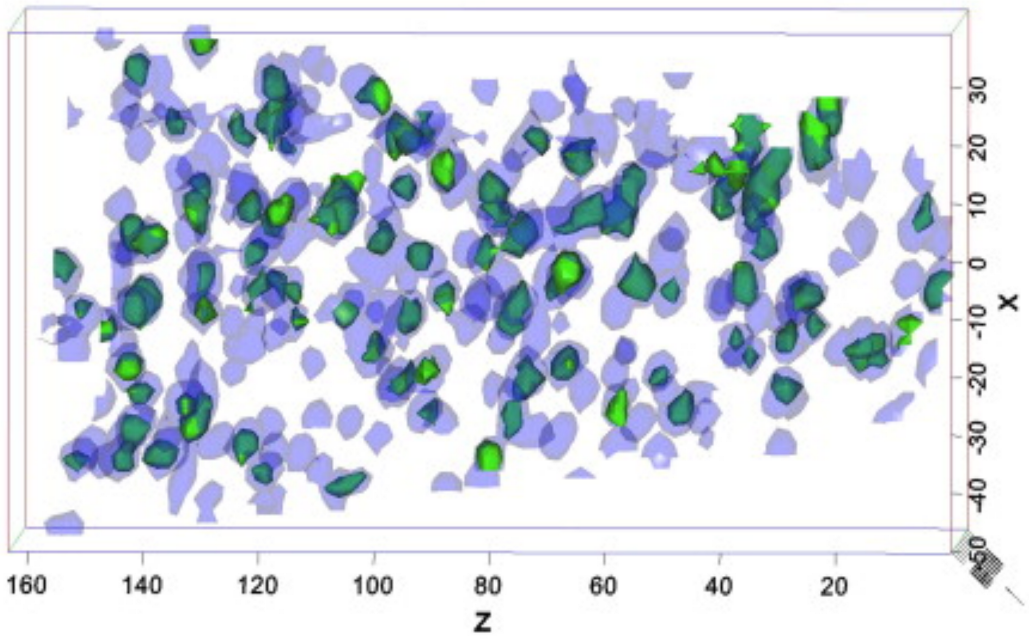

Figure 2.11: APT data set from high copper, high fluence RPV weld alloy. Regions (green) when Cu concentration is >0.5at.% within, superimposed over semitransparent outlines (blue) of regions of >4at.% Mn+Ni+Si. Reprinted from [132] © Copyright 2013, with permission from Elsevier.

ultra-fine, roughly spherical, precipitates, of both Cu and P majority types, which was later confirmed by additional APT studies [48, 58, 128]. Measurements of matrix composition also demonstrated significant Cu depletion in irradiated RPV steels [58], further supporting the existence of CRPs. Furthermore, APT was the first technique to provide evidence for the presence of Mn and Ni within Cu clusters [129], specifically the existence of the core/shell structures due to heterogeneous nucleation, in RPV base metals [57, 63, 130] and welds [28, 57, 131]. An example of this is shown in Figure 2.11.

Alternative techniques, such as scanning transmission electron microscopy - energy dispersive x-ray spectroscopy (STEM-EDX), can also provide chemical information at comparable resolution to APT and thus have the potential for complementary research. STEM-EDX is limited by totalling signals from the entire sample thickness, so true comprehensive spatial and compositional analysis is limited. Consequently, APT retains an

advantage in early-cluster detection and characterisation. APT is very sensitive to the early onset of clustering, whilst also providing information on the chemistry, size, number density distributions and interfacial chemistry of clusters identified. Nevertheless, a limited sampling size and restricted ability to determine structural information renders the use of complementary techniques critical to effective APT-focused research.

APT has helped shed light on many of the more debated aspects of RPV embrittlement, including the true nature and evolution of *late-blooming phases*. There is no consensus within the RPV community on the formation and growth of MNSPs, but the capability of APT to detect the earliest signs of cluster creation, and monitor their evolution, has allowed various studies to provide greater insight into their role.

2.8.1 APT of Mn-Ni-Si clusters

Many investigations into MNSPs have supported theories of heterogeneous nucleation on Cu clusters. An early study in 1993 by Pareige et al. used APFIM to observe Mn-Ni-Si clusters in irradiated low-Cu alloys [133]. They showed that Cu displayed very high local-enrichment, despite it making up a low percentage of the nominal composition; approximately 60% of Cu atoms were segregated to solute *clouds* within the matrix. It is worth noting that this study collected a total of 80,000 ions for analysis from a limited field of view. Modern day datasets gathered using 3D APT are often in the millions and include a direct image of the 3D distribution of elements, to which increasingly sophisticated data analysis algorithms can be applied, thus adding to their statistical relevance. Clear evidence of CRPs acting as nucleation sites was collected by Edmondson et al. from surveillance specimens taken from the R.E. Ginna reactor [111] - however, this was in a high-copper weld material so the conclusion may not apply for low-Cu alloys.

Wells et al. used APT to show that MNSPs still formed without the need for pre-

existing Cu clusters, where fluence was very high and Ni acts as the dominant stimulus for precipitation [63]. This was attributed to irradiation-induced defect-solute clusters acting as nucleation sites. These findings follow on from the work by Meslin et al., who conducted APT experiments that showed a high number density of Mn-rich clusters forming in irradiated, low-alloy ferritic steels [134]. It was also concluded that, due to Mn being under-saturated within the alloy at the irradiation temperature, thermodynamics was not sufficient to cause homogeneous cluster formation and therefore they must nucleate heterogeneously on radiation-induced point-defect clusters. These studies are in agreement that, in alloys containing non-negligible copper, Cu is the singular element super-saturated in iron at reactor temperature, indicating that Cu clusters can act as catalysts for MNSP nucleation where Cu content is sufficiently high.

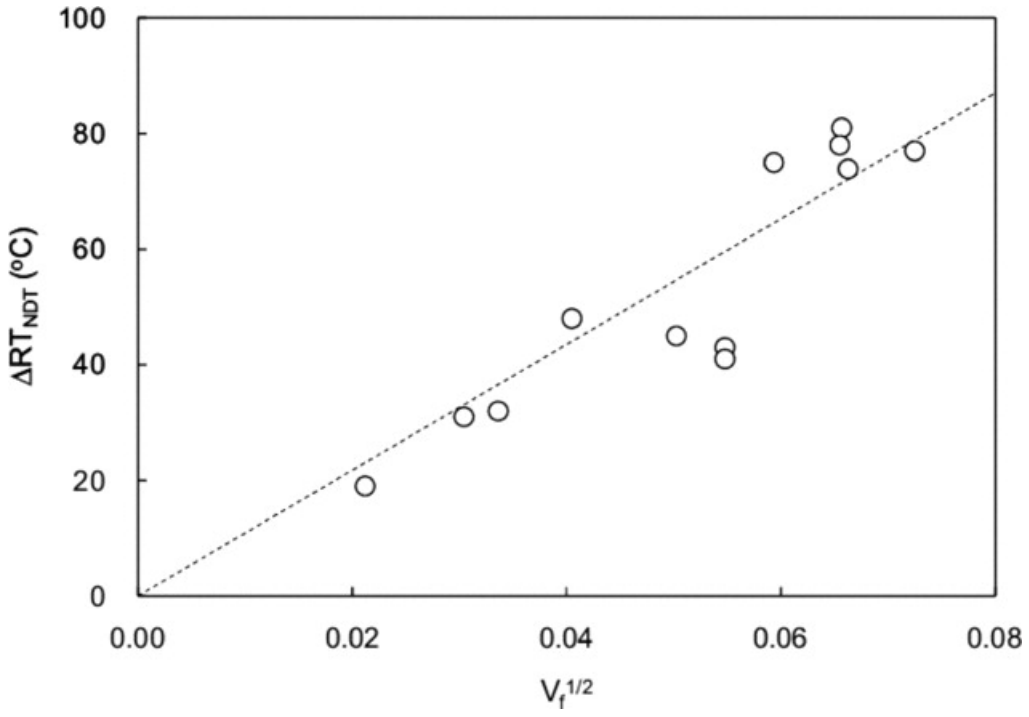

Figure 2.12: Plot showing the relationship between cluster volume fraction and DBTT shift in surveillance samples Image sourced from [45] © Copyright 2013, reprinted by permission of Informa UK Limited, trading as Taylor & Taylor & Francis Group, http://www.tandfonline.com

The extent to which MNSPs play a role in accelerating irradiation embrittlement late in the lifetime of a reactor is yet to be convincingly experimentally proven. Although a good correlation between cluster volume fraction and hardening has been shown in surveillance specimens (see Figure 2.12) [45]), linking any mechanical property changes to any *late-blooming phases* requires correlative mechanical testing and cluster classification from high fluence RPV irradiation data. Often these techniques are used independently, with studies claiming the presence of LBPs failing to report their consequential effects on mechanical properties, making determining of any accelerated irradiation effect difficult [54, 135]. Of those correlative studies that exist, only one has demonstrated a *late-blooming* effect (Bergner et al. [60]), however this was only observed in one alloy and researchers were unable to determine whether it was a LBP or change in existing cluster composition that caused this response. In contrast, a RPV weld APT study by Lindgren et al. identified Mn-Ni-Si features that continuously evolved throughout irradiations (new clusters nucleating, existing ones growing), with no evidence of an accelerated mechanical property change with fluence [74].

2.8.2 Cluster identification methods in APT

In order to identify and further analyse nanoscale solute clusters in APT data, a number of techniques have been utilised by different researchers. Despite some clusters produced during irradiations being sufficiently large to identify in atom maps with the naked eye, in order to process these clusters (and to identify smaller clouds) a computational method is required.

The most commonly used technique is the Maximum Separation Method (MSM) developed by Hyde [136] (procedure shown in Figure 2.13). The parameters used in this algorithm, N_{min}, d_{max} and L, are all dictated by the user. Therefore, if this method is applied,

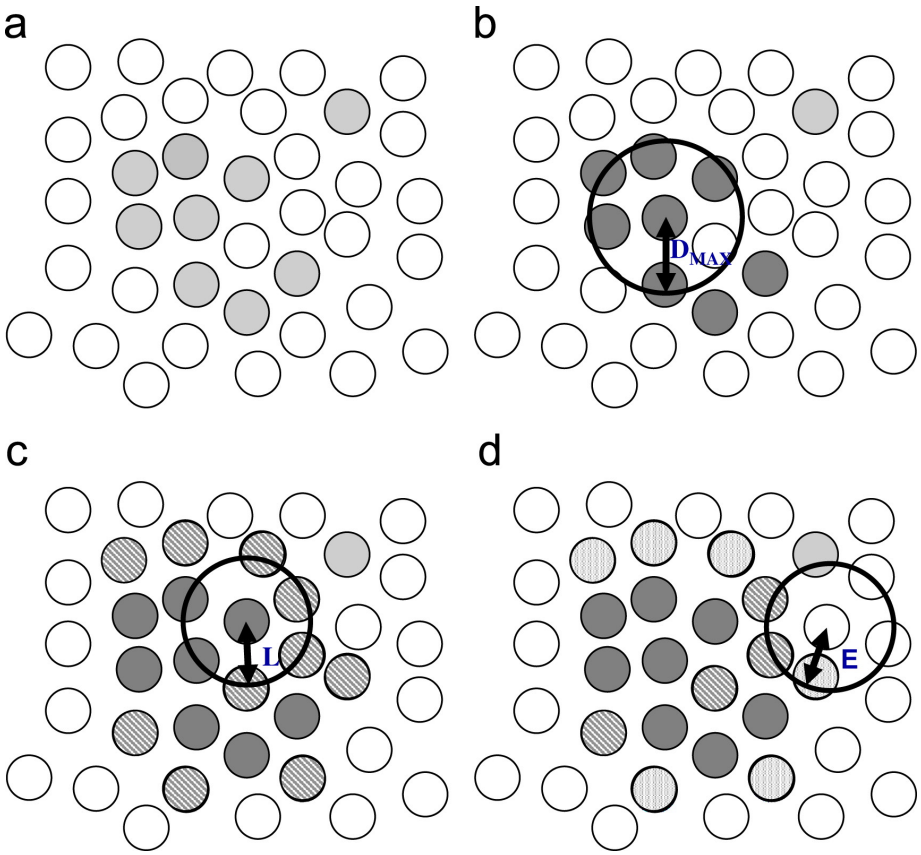

Figure 2.13: Schematic of the maximum separation method for cluster identification a) solute atoms (shaded) b) core solute atoms within D_{max} of each other are identified (dark shade) c) other atoms within L distance of the core atoms are highlighted (hatched) d) atoms within E distance of any other atom are eroded (dotted). Reprinted from [138], Copyright 2011, with permission from Elsevier.

it is the user-input that critically defines whether two atoms are clustered. Variation in chosen parameters can influence the results outputted by the algorithm. Furthermore, the procedure is based on first nearest neighbour distances, so is appropriate for fine-scale clusters but remains sensitive to local density changes and APT trajectory aberrations. An enhanced method of MSM, known as core-linkage, can be used where clusters are of a larger scale, such that it becomes appropriate to account for higher order nearest neighbours [137].

Cluster identification and characterisation capability has been an invaluable resource for enabling statistical analysis of clusters. The number density, composition and size

can all be quantified and attempts made to correlate this information with large-scale mechanical property changes. Additional measurements, such as the radius of gyration, can be calculated, allowing comparison to other cluster identifying techniques (e.g. SANS).

2.8.3 Presence of iron in RPV clusters

Clusters have been regularly reported with Fe compositions of up to 50at.% using APT [45, 48, 54, 75, 82, 100, 116, 139] - in fact, it was the standard to include iron as part of detected inclusions. However, there is a strong argument that these measured concentrations are erroneous, due to local magnification effects resulting in a mixture of matrix and solute atoms within clusters [74, 140–142]. As a result, Shu et al. suggests that all Fe present in copper-rich precipitates (and by extension MNSPs) is an artefact of APT, and clusters are without a significant Fe content [140]. This theory is supported by thermodynamic considerations and SANS data (where Fe is generally ignored from cluster identification based on assumptions the CRPs are non-magnetic) [140].

2.9 Scope for Further Work

Although over half a century of research has been conducted on the effect of irradiation on RPV steels, there are still areas where more work is required:

- The influence of specific alloying elements on irradiation hardening has been extensively researched, yet there is little existing literature on the role of microstructure morphology (i.e phase fraction, grain size, defect density) and the subsequent impact of alloy processing route.
- MNSP nucleation and growth mechanics are still not well understood. A universally recognised theory of their formation and nature is required to allow predictive models

to account for their role (if any) in in-situ RPV embrittlement.

- The use of ion irradiations as a surrogate for neutron irradiation is a useful tool to facilitate long-term simulation of reactor embrittlement mechanisms, but there is still scope for investigations as to their viability.

Chapter 3

Materials and Methods

3.1 Materials: SA508 Grade 3 Class 1 Steel

All materials studied as part of this research were SA508 Grade 3 Class 1 RPV steel [143], subjected to differing processing methods and thus displaying a range of initial microstructures. This MnNiMo low-alloy steel was first developed in the 1950s as part of the push to minimise Cu content (and thus Cu precipitation embrittlement) in RPV steel (as discussed in Chapter 2). SA508 steel was provided by Rolls Royce and is commonly used in RPVs.

Conventionally, RPVs are produced using forged steel, subjected to a heat treatment cycle consisting of quenching, tempering and stress-relief steps. This results in a microstructure comprised largely of lower bainite (though this may not hold across thick samples), with fine, bainitic laths incorporated within prior-austenite grains. Samples produced using the traditional forging procedure (taken from a thick section) will be referred to as LF (large

Table 3.1: Tensile data for conventionally forged SA508 sample (LF)

Temperature (°C)	UTS (MPa)	0.2% Proof (MPa)
20	613-618	472-474
354	560-571	399-406

forging). Table 3.1 shows the tensile properties of the LF sample.

The conventional heat-treatment process for the LF sample is shown below, with the exact timings and temperature not given due to corporate non-disclosure.

(a) austenisation

(b) water-quenched

(c) tempered at 600-650°C

(d) furnace-cooled

(e) stress-relieved

(f) furnace-cooled

The additional materials studied have similar composition to the LF, but have been subjected to one of two different forms of novel manufacturing: Hot Isostatic Pressing, or variation in tempering duration. Critically, these alternative processing routes give rise to non-standard heat treatments, particularly in the case of the HIPed alloy, which is likely to play a complex role in altering the resultant microstructure and subsequent performance. This effect is exacerbated by SA508-type steel being particularly sensitive to heat-treatment.

Table 3.2: Indication of the compositions in wt.% and at.%, bal. Fe, for the SA508 steel samples, as derived via chemical analysis at Rolls Royce of the as-received samples. For the HIPed sample, the analysis was conducted on the powder form. There are also trace amounts (<0.01wt.%) of S, V, As, Co, Nb, Sn, Ti, Sb and Ca across all samples.

		Composition										
Material		C	Mn	Ni	Si	Mo	Cr	Al	Cu	P	N	O
HIP	wt.%	0.16	1.24	0.86	0.21	0.51	0.10	0.02	0.03	0.012	0.018	0.014
	at.%	0.74	1.25	0.81	0.42	0.30	0.11	0.04	0.03	0.021	0.071	0.048
LF	wt.%	0.17	1.42	0.82	0.26	0.53	0.22	0.02	0.03	0.004	0.007	0.001
	at.%	0.79	1.43	0.78	0.51	0.31	0.24	0.04	0.03	0.007	0.027	0.003
B	wt.%	0.16	1.33	0.78	0.25	0.52	0.17	0.02	0.03	0.002	0.007	0.001
	at.%	0.74	1.34	0.74	0.49	0.30	0.18	0.04	0.03	0.004	0.030	0.007
C	wt.%	0.17	1.33	0.80	0.25	0.52	0.16	0.02	0.03	0.002	0.007	0.002
	at.%	0.79	1.34	0.76	0.49	0.30	0.17	0.04	0.03	0.004	0.026	0.007

Compositions for each of the sample types, as provided Rolls Royce, are shown in Table 3.2.

3.1.1 Variation in post-forging heat treatment

As part of a series of trial forgings at Rolls Royce, four SA508 alloys were produced in order to ascertain any effects of forging and heat treatment parameters on mechanical properties. For this research, the materials which demonstrated the greatest difference in toughness were selected; B and C. An air-cool, followed by high-degree of tempering gave rise to inferior toughness in Forging B, whereas a water-quench and low-degree of tempering produced superior toughness in Forging C. Figure 3.1 indicates the variation of tensile strength with temperature for each of the trial forgings produced.

The underlying cause of this disparity in toughness is likely the differing microstructure produced by these two heat treatment procedures. Whilst Forging C consists almost entirely of bainite, akin to the conventional SA508 forging, Forging B incorporates a significant fraction of polygonal ferrite.

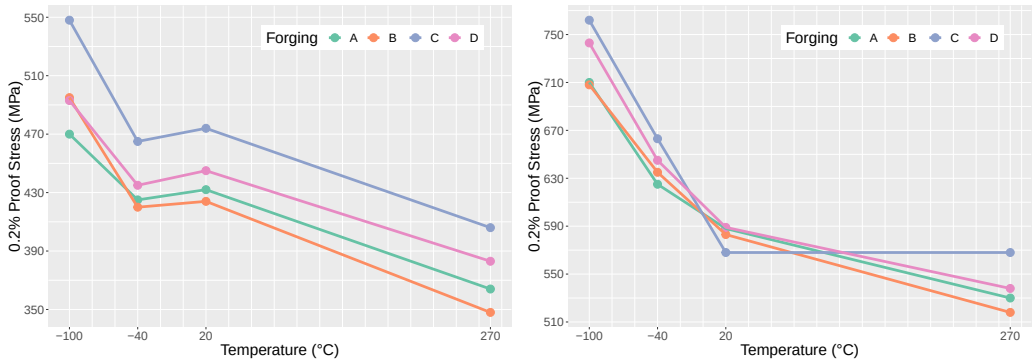

(a) 0.2% proof stresses at varying test temperatures

(b) Ultimate tensile strength values at varying test temperatures

Figure 3.1: Tensile test data for novel trial forgings of SA508 Grade 3 Class 1 Steel at various temperatures.

3.1.2 Hot Isostatic Pressing

Blocks of SA508 Grade 3 Class 1 steel were HIPed as part of an Electrical Power Research Institute (EPRI) development programme, with the initial aim of conducting a feasibility study into the use of the HIP process to manufacture large-scale ferritic components. HIP fabrication was performed by the EPRI, and subjected to mechanical testing by Rolls Royce prior to delivery.

The heat treatment applied to the HIPed samples are as follows:

(a) austenisation (1120°C)
(b) gas-quenched
(c) normalised (900°C)
(d) gas-quenched
(e) tempered (650°C)
(f) air-cooled

Micrographs in Figure 3.2 indicate the microstructure of HIPed SA508 in comparison to a conventionally forged sample. The HIP process subjects the alloy to a heat treatment which differs significantly from that typically experienced by SA508 steel, giving rise to a different microstructure. Of note is the presence of a significant fraction of polygonal, idiomorphic ferrite. For the sake of comparison between this polygonal ferrite and the lower bainite observed in HIPed SA508, from this point polygonal ferrite will be referred to simply as 'ferrite'.

Whilst the microstructural disparity between HIPed and forged steels is complex in nature and origin, as a starting focus, this high proportion of ferrite is of interest, in addition to comparisons between the bainitic features. The softness of ferrite compared to bainite is well recognised, and as such metallurgists developing materials for nuclear applications

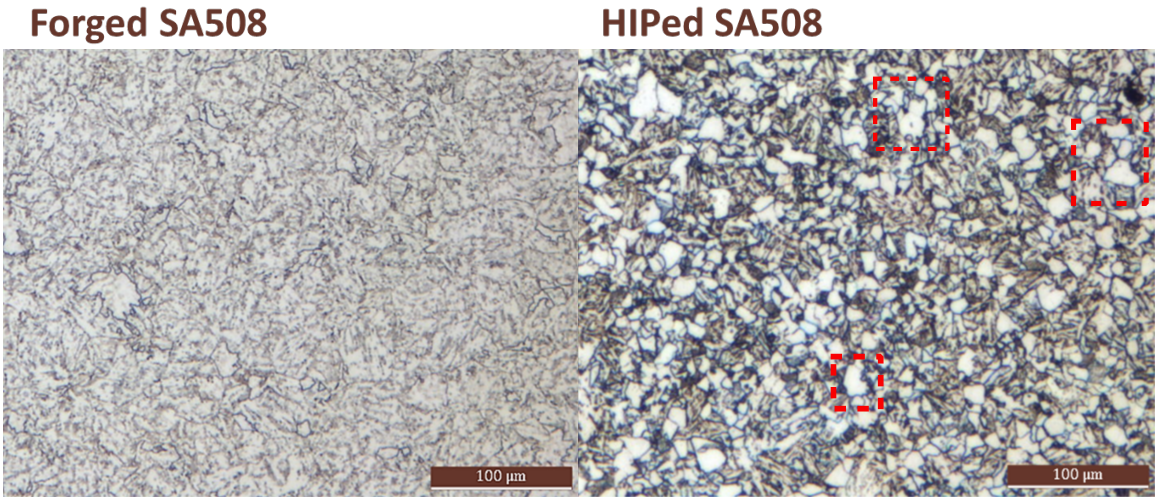

Figure 3.2: Optical micrographs of forged and HIPed SA508 steel following a nital etch. Ferrite grains within the HIPed microstructure are seen as white and highlighted by the red annotations.

have generally avoided its inclusion within RPV steel microstructures where possible. However, by comparing Table 3.1 and Figure 3.3 it can be shown that the mechanical properties of HIPed SA508 are still satisfactory when compared to its forged counterpart.

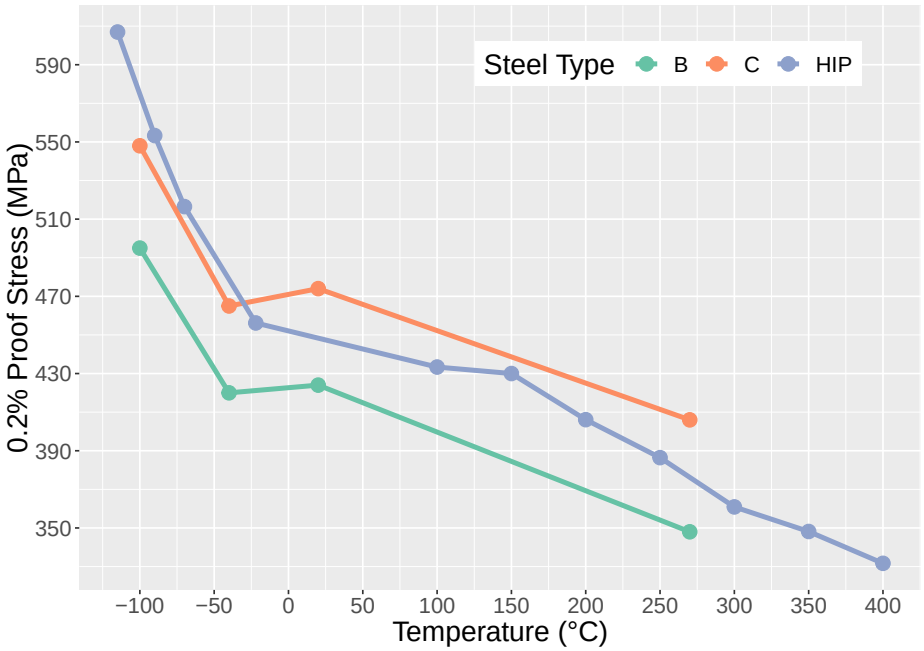

Figure 3.3: Comparison of the 0.2% proof test data obtained for Forgings B/C and HIPed SA508.

This is likely the result of interplay between the detrimental impact of ferrite and the benefits of HIP as a manufacturing route.

3.2 ANSTO Neutron Irradiations

Neutron irradiations were conducted in the Open Pool Australian Lightweight (OPAL) reactor at the Australian Nuclear Science and Technology Organisation (ANSTO). Of the samples available for investigation, the LF and HIPed steels were chosen for neutron irradiation. The LF sample acts as a control and provides a more conventional microstructure with which to compare the radiation-induced-enrichment of polygonal ferrite.

Disks (3 mm diameter, 0.5 mm thickness, and weighing ≈4 mg) of each sample were prepared using electro-discharge machining and ground with Struers® SiC paper of grit 800 and 1200. Discs (mounted in a bespoke aluminium irradiation rig) were irradiated within the gas-cooled fast flux (FFX-2) facility and positioned such that it was exposed to the irradiation conditions given in Table 3.3.

Table 3.3: OPAL reactor irradiation conditions for ANSTO neutron-irradiated samples. The temperature estimate came from fluid dynamics models predicting the extent of gamma heating and gas cooling for the can.

Fast Neutron Flux (E>1MeV)	Thermal Neutron Flux	Temperature
9×10^{12} cm^2s^{-1} ± 10%	1.1×10^{14} cm^2s^{-1} ± 15%	155±10°C

The OPAL set-up limits the possible irradiation temperature, causing it to be relatively low compared to in operating commercial reactors. Although this prevents direct comparison with investigations utilising temperatures typical of PWRs, it still allows like-for-like comparisons between the samples. The potential impact of this lower irradiation temperature is discussed as part of the experimental results.

The amount of neutron damage each disk was subjected to was dependent on the time spent in the reactor (fixed neutron flux). Each irradiation fuel cycle at OPAL is 28 days long, thus restricting the possible increments in radiation damage obtained. Ultimately, it was chosen to investigate the LF and HIPed samples after three-months (84 days) and six-months (168 days) of exposure. From Equation 3.1, the approximate damage for the exposure intervals is[144].

$$15 \text{ dpa} \approx 10^{22} \text{ n/cm}^2 \qquad \text{(for E > 1 MeV)} \tag{3.1}$$

Subsequently, a three-month long irradiation would correspond to approximately 0.1 dpa ($\approx 6.7 \times 10^{21}$ n/m^2), equivalent to roughly 25 years of operation in a civil power PWR. The six-month irradiation would thus mirror 50 years of use in a PWR.

Upon completion of each irradiation cycle, and conditional on sufficient cooling period prior to shipping, samples were transferred from ANSTO to the UK, where they were received by the Materials Research Facility (MRF) at UKAEA, Oxfordshire. Further activity measurements determined when each disk could be prepared for analysis.

Polishing was completed within MRF active gloveboxes by facility staff, using Struers® SiC paper grit 800, 1200, 2000 and 4000 followed by a 3 µm and 1 µm diamond polishing stage. For polishing a Struers® MD Nap cloth was used. A finish suitable for EBSD and SEM imaging was acquired.

3.3 Ion Irradiations at Dalton Cumbrian Facility

Ion irradiations used Fe^{4+} ions and were completed at the Dalton Cumbrian Facility (DCF), a research-base for the University of Manchester and part of the EPSRC National Ion Beam Centre. Fe^{4+} irradiations utilised the facility's larger accelerator (DAFNE). To



Figure 3.4: Image of the front face of the sample holder used for DCF ion-irradiations.

irradiate multiple samples simultaneously, a holder was constructed in which to mount 3 mm diameter disks (shown in 3.4). Prior to insertion, each disk was subjected to typical grinding (400, 800, 1200 and 4000 grit) and polishing (3 μm and 1 μm diamond solution on lapping cloth) procedure, up to a final colloidal silica stage. As ion irradiations give rise to damage as a function of depth from the surface, polishing post-irradiation was not possible.

3.3.1 Calculating ion irradiation parameters

The depth-damage profiles for each irradiation were obtained using the Stopping and Range of Ions in Materials (SRIM) simulation code, abiding by the best-practice described in [145]. A Kinchin-Pease displacement threshold energy of 40 eV and lattice binding energy of zero were used. By inputting the irradiation particle type and acceleration energy (5 MeV for Fe^{4+} ions), in addition to the composition of the target alloy, SRIM calculated the number of displacements per Angstrom across 2 μm in depth.

The SRIM displacement data was summed to include the total number of vacancies produced by both ions and recoils, then multiplied by 10^8 to give the total vacancies/cm (ν). The irradiation end-point is tracked by monitoring the total charge incident on the samples

(Q). For each ion irradiation, noting the value of ν at a desired depth gives the Q needed to give the requisite dpa at that depth, using Equation 3.2, where ρ is $8.42{\times}10^{22}$ atoms/cm^3 – the approximate atomic density of RPV steel – and n is the charge state of ion. Beam area is given in cm^2.

$$\begin{aligned} \Phi &= \frac{(\text{target dpa}) \times \rho}{\nu} \\ \text{No. of Ions} &= \Phi \times \text{Beam Area} \\ \Sigma\Phi &= \text{Ions} \times ne \end{aligned} \tag{3.2}$$

Knowing the total charge required allowed either the irradiation duration for a given accelerator current to be calculated, or the current required for the irradiation to take a specified amount of time.

3.3.2 SRIM profiles

Working with a combination of the SRIM vacancy data and the actual beam parameters recorded during irradiation, the simulated damage-depth profiles for each irradiation could be produced. An example is shown in Figure 3.5, indicating the typical shape of damage profiles produced by Fe^{4+} irradiation. These profiles help give an indication of the expected dpa at particular depths, which is an important consideration when fabricating APT samples – see Section 3.7.

3.4 Atom Probe Tomography

Atom probe tomography is a 3D spatial reconstruction technique used to reproduce nanoscale volumes of material based on the controlled evaporation of ions from a fine-tipped (R $\leq$100 nm) specimen under an high electric field ($\approx 10^{10}$ V/m). The electric field

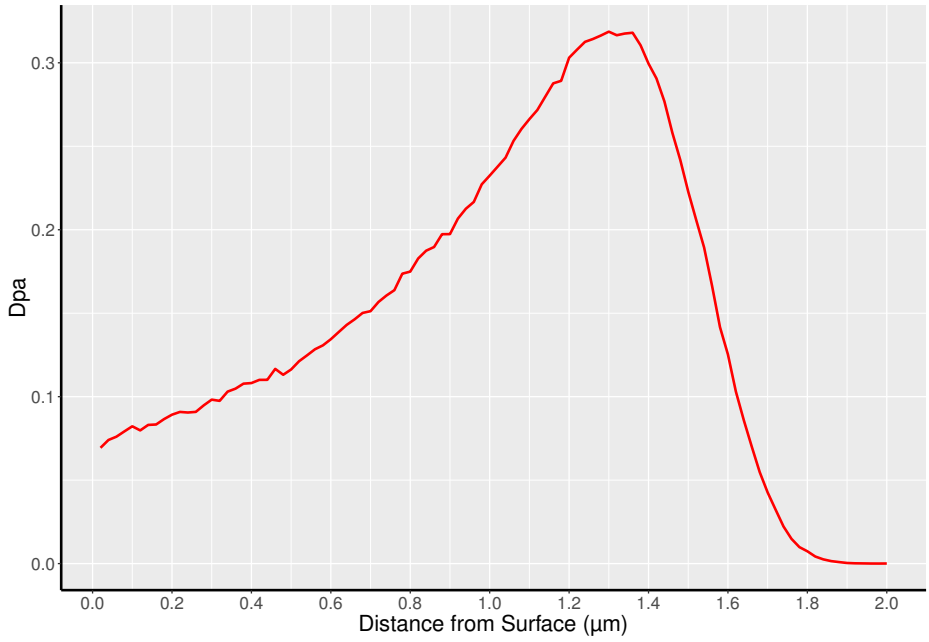

Figure 3.5: Damage profile into Fe^{4+} irradiated surface for a SA508 HIPed sample with target damage of 0.1 dpa at 500 nm depth.

(F) experienced at the tip of APT samples for a given voltage (V) is described by

$$F = \frac{V}{k_f R}. \tag{3.3}$$

The field factor, k_f, accounts for the shape of the specimen and electrostatic environment, and therefore influences the intensity of the electric field at the tip - it is treated as a constant for each dataset [146, 147]. For this project, APT was conducted in voltage mode, which entails the application of a standing DC voltage. The field produced lowers the activation energy (Q) required to ionise, and subsequently evaporate, atoms off the specimen's surface. Carefully controlled superposition of voltage pulses induce the ionisation of atoms from the tip in a controlled evaporation process. The pulsing mechanic allows the detected ion to be directly correlated to the specific pulse that triggered its evaporation. This enables time-of-flight (ToF) measurement, which is required for mass-to-charge-state determination. The schematic in Figure 3.6 gives an indication of the set-up used for a straight flightpath

instrument; this work used a reflectron atom probe (LEAP 5000XR), where an electrostatic mirror bends ion trajectories as a form of energy compensation whereby the flight path of lower energy ions is shortened (and lengthened for heavier ions) to reduced uncertainty in flight times and thus improve mass resolution [148, 149].

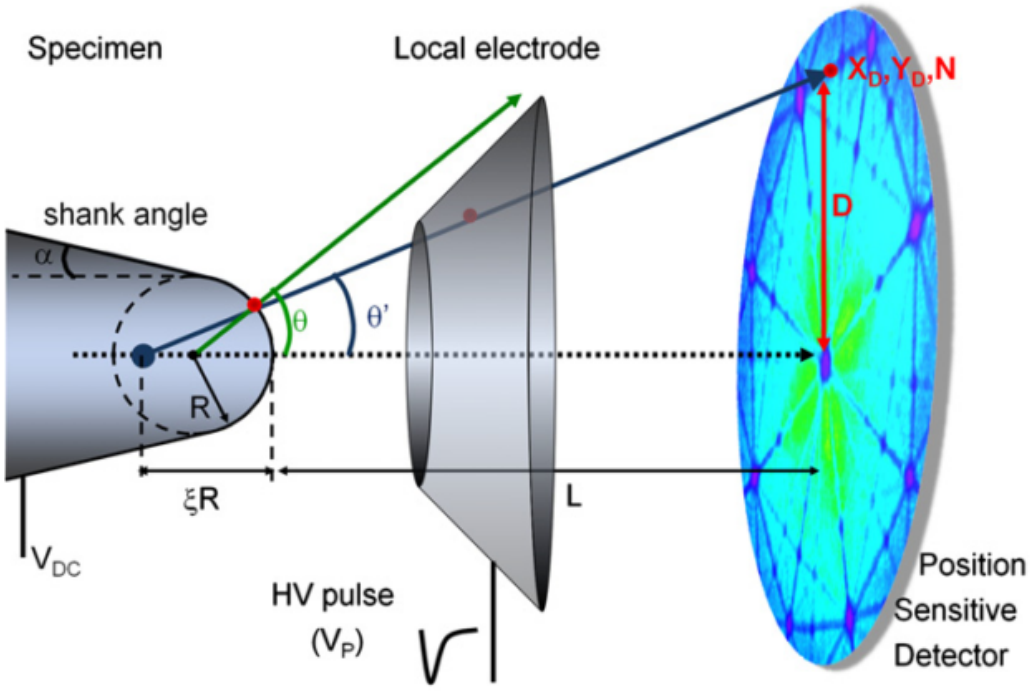

Figure 3.6: Schematic of a Local Electrode Atom Probe (not to scale – L ≫ R). Reprinted from [150] © Copyright 2011, with permission from Elsevier.

Evaporated ions are accelerated through the E-field (following field lines) to a position-sensitive multichannel plate detector, which converts ion impact into an electrical signal. This process assigns each incident ion a set of x-y Cartesian coordinates, with a point projection algorithm mapping these detector coordinates back to a position on the sample surface [150]. The evaporation sequence, together with a geometrical correction based on the radius of the specimen apex, is used to determine the approximate location in z of each ion, producing a complete set of 3D coordinates. By combining the positional information of each ion with time-of-flight mass spectrometry (ToF-MS), a 3D point cloud

can be reconstructed using software.

In APT there are a variety of experimental parameters that determine the conditions a sample tip is subjected to during data collection:

- Operation Mode – whether a voltage or laser pulse is used to trigger evaporation events.
- Pulse Frequency – the rate at which evaporation inducing pulses are applied to the sample.
- Pulse Fraction – the additional potential applied to the sample as a fraction of the standing DC voltage.
- Detection Rate – the fraction of ions detected per pulse, for instance 0.2% would correspond to 2 ions detected per 1000 pulses.

Voltage mode is generally chosen for irradiation studies due to the higher spatial resolution compared to laser-pulsing allowing enhanced detection of nanoscale features [151]. Furthermore, laser mode increased the extent of P and Si surface diffusion to crystallographic poles, often indicated by the formation of trilateral symmetric features centred on the 222 crystallographic pole in the reconstructed data [66].

Operation conditions were investigated, with a pulse frequency of 200 kHz, temperature of 45 K and pulse fraction (f_p) of 25% initially selected. This was a consequence of APT calibration studies on the as-received steel samples indicating reduced P/Si migration at 45 K compared to 50 K, and giving a Ni composition slightly nearer the nominal value when a f_p of 25% was used. Where yield diminished for the irradiated samples, a reduction in f_p to 20% was successfully utilised (akin to that conventionally used for these type of samples [151]). The data obtained using these different pulse fractions gave comparative compositional values.

3.4.1 APT mass spectrum

ToF-MS allows ion identification during APT. The ToF measurement for each detector event is converted into a corresponding mass-to-charge state (m/z) using Equation 3.4, which are plotted as a histogram to produce a mass spectrum for each APT sample analysed – m = mass, z = charge number of ion, q = elementary charge, V = applied voltage, t = flight time, and L = flight distance between specimen and detector.

$$\frac{m}{z} = \frac{2qVt^2}{L^2} \tag{3.4}$$

For each mass spectrum, ionic identities can be assigned to any peaks that exist at particular m/z values, in a process known as ranging. It is ranging which adds the chemical information to the spatial position for detected ions. Any ion which does not have a ranged mass-to-charge state is designated as a background detector event and thus does not appear in the reconstructed atom map. An example of a ranged mass spectrum is shown in Figure 3.7.

Ranging and peak-overlaps

The identification and peak ranging of mass spectrum in APT is a user-driven process, and thus liable to human-error if not treated with caution. Work in this area shows the impact of incorrect ranging on the outcomes of subsequent data analysis [152, 153].

To be consistent with the ranging applied to each mass spectrum, this project used the Full-Width-Half-Maximum (FWHM) method to dictate the range width for each peak. Each spectra was ranged individually based on a master range file for each type of sample, which was then adapted (peak widths changed, new species added, non-present species deleted etc.) by the user as appropriate. This ensured a baseline template for ranging

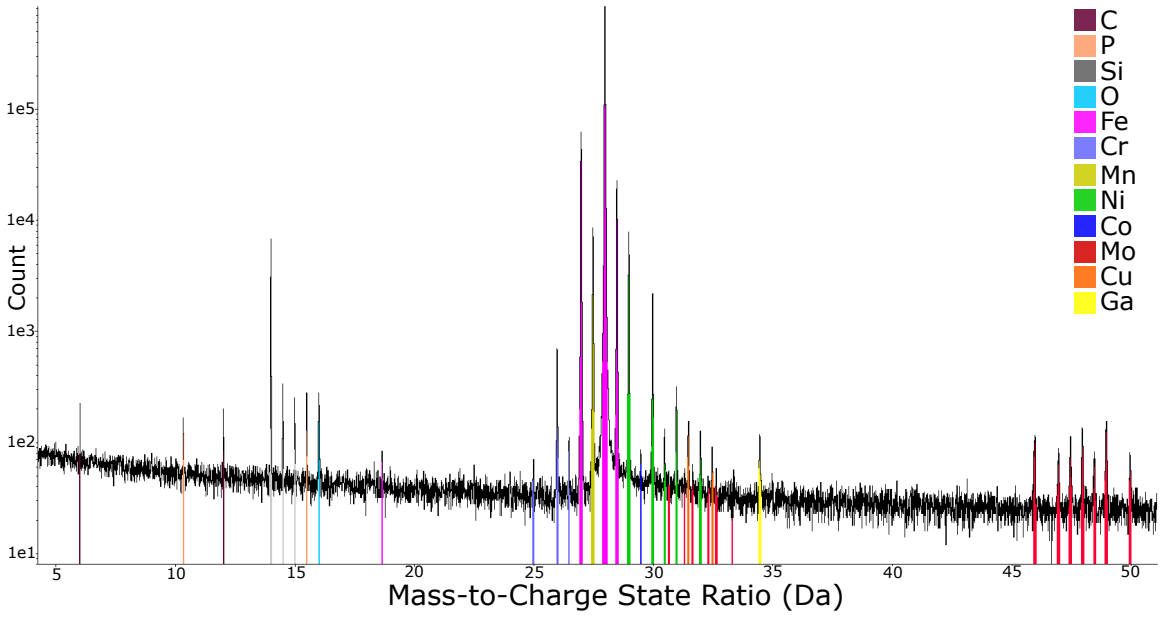

Figure 3.7: Example ranged mass spectrum from a neutron-irradiated HIPed SA508 Grade 3 Class 1 steel sample

kept continuity between spectra, whilst still placing impetus on the operator to ensure any changes between spectra were accounted for.

Whilst the mass spectra produced by the SA508 steel samples were not, relatively, complex, one area where caution must be applied is with the handling of peak overlaps. Overlaps occur where multiple ionic species share a mass-to-charge ratio, or are separated by a value less than the mass-resolving power of the atom probe, leading to peaks formed by the cumulative ion counts of these multiple species. This corresponds to an uncertainty in the amount of each species actually present within the analysed volume. There are various methods for deconvolving the count of each ion, the most common of which utilises the isotopic abundance ratios to give the expected values based on the count of isotopes of the same species present. Atom Probe Lab version 0.2.1 written by Dr Andrew London, and using methods detailed in [154], was used for bulk decomposition of ranged peaks to determine compositions.

In RPV steels the most significant peak overlap is that between the $^{58}Fe^{2+}$ and $^{58}Ni^{2+}$ ions, occurring at 29 Da (Figure 3.8). Ni is known to be a major solute involved in cluster formation, and thus understanding the true Ni content in clusters is critical. When determining the cluster compositions, the 29 Da peak was labelled as Ni, given the mass-spectrum lacked a large ^{56}Fe isotope peak (indicating a relatively low amount of Fe was present and ^{58}Ni would dominate contributions to that peak [66]). Deconvolution was then conducted using the IVAS deconvolution tool.

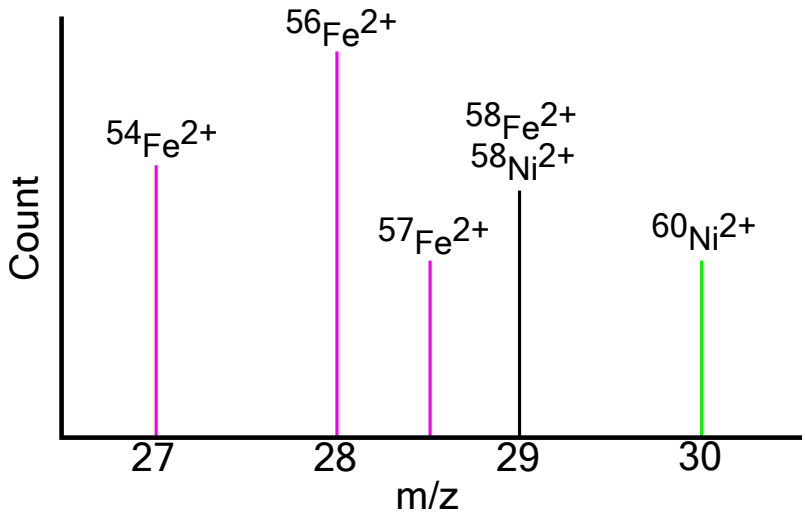

Figure 3.8: Schematic indicating the $^{58}Fe^{2+}$ and $^{58}Ni^{2+}$ ion peak overlap.

3.4.2 Hitmaps

Hitmaps in APT is a general term referring to desorption maps produced through the cumulation of ion impacts on the detector. These desorption images are two-dimensional histograms of ion-impact position across the face of the detector, and often indicate the low-density regions formed as a result of crystallographic features within an APT tip [147]. Observation of zone-lines and poles in a hitmap is a consequence of the faceting of atomic-planes at the specimen surface giving rise to high-field localities; this also produces

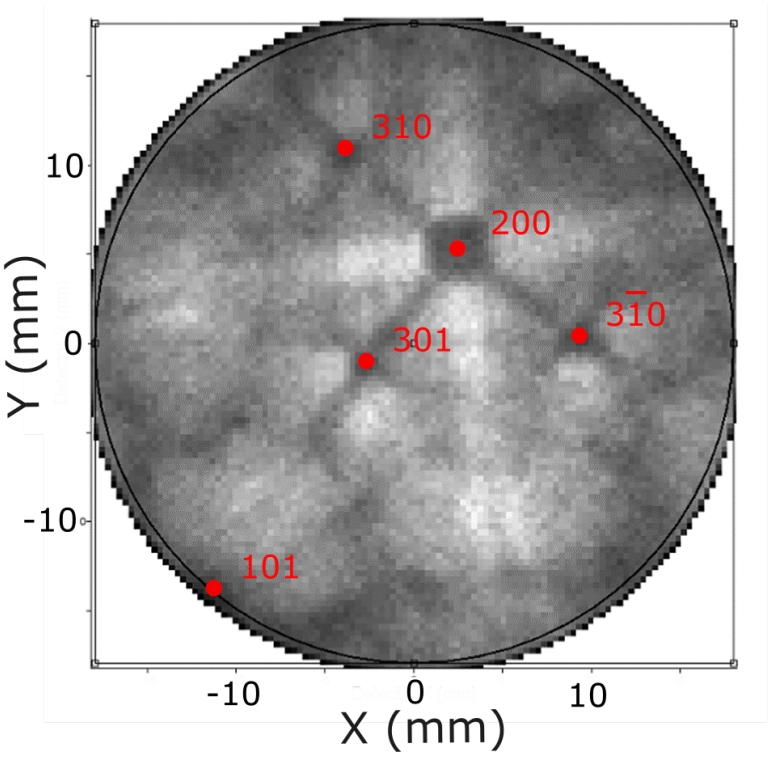

Figure 3.9: Example APT hitmap for SA508 steel (bcc) with major poles indexed.

highly localised curvature at the facet surface, which corresponds to reduced density at these features as a result of trajectory aberrations (discussed below).

An example hitmap for SA508 steel is shown in Figure 3.9. In this work, hitmaps were primarily used in an effort to enhance the accuracy of reconstruction parameters by indicating the presence of poles, which could be used to generate more accurate reconstructions based on calibration of interplanar spacing [155].

3.4.3 Trajectory aberrations

APT reconstruction algorithms are a form of modified point-projection [147], but, due to the nature of the evaporation process and the assumptions made, there arises a variety of spatial distortions. Of particular note is the assumption that the sample tip approximates as a hemispherical cap, which evolves during evaporation such that the tip radius, R, increases;

this allows R at a certain point in time to be estimated using the known applied voltage and Equation 3.3. Although a useful representation of the specimen under a small field-of-view, the assumption of a hemispherical cap begins to break down with increasing field-of-view (typically seen in modern day APT), due to a variety of factors detailed in [146].

Given this research focuses on the development of nanoscale features, it is important to understand the trajectory aberrations associated with phase inhomogeneity. There exists a critical interplay between radius of curvature, electric field, and magnification in APT reconstruction, hence any distortion in these areas gives rise to a non-physical representation of the sample within the reconstructed point cloud. This is due to the difference in evaporation field required to remove atoms from within the clusters compared to the alloy matrix giving rise to local variations in the radius of curvature, and thus the ions emitted from these volumes experience a flight-trajectory which differs from that assumed for a hemispherical cap [156] [157]. Small, low-field clusters evaporate ions prematurely when compared to the specimen bulk, locally flattening the evaporation surface, which corresponds to a decrease in the radius of curvature. This effectively acts to focus ions emitted from this region, such that their inwards trajectory gives an apparent increase in local ion hit density [158].

Trajectory aberrations are particularly consequential when determining the composition of radiation-induced clusters, as they can lead to Fe ions from the matrix being identified as part of the clusters, as discussed in Chapter 2 Section 2.8.3 [159].

3.5 Isosurfaces and Proxigrams

Some analysis in this thesis required the isolation of regions of an atom map based on local concentration. Isosurfaces define boundaries at which a specified element (or combination of elements) exists at a specific concentration, therefore allowing them to be

used to neatly delineate regions of higher solute concentration in the data [160].

Proximity histograms (proxigrams) can be used to calculate the changes in local composition in the proximity of a defined surface – in most APT cases, an implemented isosurface. Changing the extent of a proxigram allows a concentration profile to be constructed through the surface with varying start and end distances.

In this work, all isosurfaces and proxigrams were applied to atom maps with a voxel size of 1 nm^3, at a de-localisation of 3 nm.

3.6 Cluster Analysis

IVAS cluster analysis software was routinely applied to APT data as a primary method in determining the impact of irradiation on the SA508 steel samples investigated. Generally the following procedure was used to isolate solute clustering within atomic reconstructions:

- a frequency distribution analysis indicated whether any specific ionic species were displaying non-random behaviour. This was particularly useful in samples exposed to low levels of radiation damage, where segregation behaviour was not easily visible in atom maps
- cluster size and count distribution IVAS scripts were used iteratively to determine reasonable MSM parameters according to best practice (described below)
- chosen d_{max}, $N_{min}$and L values were imputed into the IVAS cluster analysis tool (which, in turn, provided cluster information data for further study)

Frequency distribution analysis is a method of assessing the randomness of atomic positioning within a dataset. By breaking-up the APT reconstruction into sub-volumes containing the same total number of ranged ions and counting the species present in each division, a histogram indicating the frequency at which each species occurs can be

produced [161]. For a randomly distributed element this histogram would resemble a binomial distribution. For species deviating from random solution, a statistical test, often a Pearson's analysis (μ) and determination of a p-value, indicates the extent to which non-random behaviour is being observed.

Where clustering was suspected as a result of the frequency distribution results, the reconstruction was then subjected to MSM analysis using IVAS 3.8.4. The key MSM parameters (defined in Table 3.4) were user determined, in-line with previous reports on the use of this algorithm [58, 136, 138, 158, 162, 163]. A complementary simulated dataset, in which the chemical identities of all the atoms have been randomly swapped to remove chemical-spatial correlations, was generated such to help accurately determine the amount of real clusters for a chosen d_{max} and N_{min} pairing.

Table 3.4: Description of key MSM parameters.

MSM Parameter	Description
d_{max}	the maximum separation between two solute atoms for them to be determined to belong to the same cluster
N_{min}	the minimum cluster size (used to prevent statistical fluctuations of atoms randomly within d_{max} separation from being included in cluster counts)
L	the maximum separation of non-solute elements
E	the erosion distance (atoms within E distance of matrix atoms are removed from the cluster)

For each dataset the finalised MSM parameters were chosen such that the number of clusters identified from the random comparator system was less than 5% of the total number of solute clusters identified in the real data [56]. The exact parameters used depended on the samples investigated, and are given alongside their respective APT results. The envelope (L) and erosion (E) parameters used in each case were equal to half of the selected d_{max}. This was in order to apply a systematic inclusion of surrounding solute atoms to the cluster

core across different analyses, whilst minimising the excessive addition of atoms from the matrix. Furthermore, it is generally noted as best practice to have E=L [138].

Where clusters are larger, a higher nearest-neighbour order (NN_{order}) can be used in order to better capture clusters in their entirety. Having high orders is undesirable for analysis of small clusters, as increasing NN_{order} increases the amount of random matrix fluctuations which are identified as clusters, thus dictating a higher N_{min} value to minimise over-classification, which, in turn, reduces the algorithm's sensitivity to small clusters [66]. This is why core-linkage was avoided, as cluster sizes were generally fine-scaled in this work.

For analysis, an open-source R code, courtesy of Dr Ben Jenkins, was used to extract the volume fraction (V_f) and number density (N_d) values of clusters. This method utilised edge-detection software, through use of an alpha-hull, whereby clusters detected as occupying space on the edge of reconstructed volume were recorded. This allows edge clusters to be treated as half a cluster in number density calculations. In addition, this script was used to eliminate edge clusters from subsequent cluster size calculations.

All cluster radii were calculated through the assumption that clusters are spherical, with a diameter formed by adjacent solute atoms of known volume. The limited detection efficiency of the atom probe (approximately 52% for the LEAP 5000XR) would have the effect of reducing the observed cluster size distributions, although the exact impact of this efficiency-degradation on measured APT cluster sizes is complex (described in [164]). Where cluster sizes were presented as a mean value (or used as a mean value in radii calculations), an approximate correction was applied, whereby the physical cluster size (in atoms) was calculated by dividing the cluster sizes yielded by the MSM algorithm by 0.52. Given the complexity of correcting for detection efficiency when considering a distribution of clusters, in this work such correction was not applied.

In all size calculations, Fe was not included, either as a contributor to the number of atoms included in a cluster, or in the estimation of the cluster diameter (using Equation

3.5), where ρ_{RPV} is the expected number of iron atoms in RPV α-Iron) [165].

$$V_{\mathrm{cluster}} = \frac{\text{Corrected Cluster Size}}{\rho_{RPV}}$$

$$r_{\mathrm{cluster}} = \left(\frac{3V_{\mathrm{cluster}}}{4\Pi}\right)^{\frac{1}{3}} \tag{3.5}$$

Equation 3.6 was used to calculated $\mathrm{V_f}$ and $\mathrm{N_d}$, where $\mathrm{X_{cluster}}$ is the number of solute atoms (Fe not included) in all the identified clusters, $\mathrm{X_{total}}$ is the total number of atoms in the APT dataset, $\mathrm{N_{clusters}}$ is the number of clusters detected, $\mathrm{N_{edge}}$ is the number of detected edge clusters, and $\mathrm{V_{total}}$ is the total volume of the dataset (adjusted to account for the LEAP detection efficiency and the atomic density of BCC-Fe).

$$V_{\mathrm{f}}(\%) = \frac{X_{\mathrm{cluster}}}{X_{\mathrm{total}}} \times 100$$

$$N_{\mathrm{d}} = \frac{N_{\mathrm{clusters}} - (0.5 \times N_{\mathrm{edge}})}{V_{\mathrm{total}}} \tag{3.6}$$

There are some instances in this work where segregation behaviour involved local-enrichment levels beyond the sensitivity of MSM. This was particularly true for the P-rich regions encountered in the early stages of ion irradiation. Here, as an alternative method of indicating where segregation was transpiring, local chemistry analysis was conducted, using the integrated algorithm, similar to that described in existing literature [166, 167], included in 3Depict v0.0.21 (a visualisation and analysis software for APT). The local chemistry of a selected species is computed about each atom in the dataset, with the value assigned to the point in question. This allows plotting of the variation of local chemistry, based on a given colour scale, or the filtering of atoms such that only those above a chosen concentration threshold are included in the plotted atom map.

3.7 Focused Ion Beam

Samples for APT were fabricated using Focused Ion Beam (FIB). The nature of this process depended on the substrate being investigated, but the typical procedure followed the standard APT lift-out protocol detailed in [168]. A focus on the role of ferrite within the HIPed structure stipulated the need for site-specific sample preparation, such to distinguish between ferritic and bainitic APT tips. This process is detailed in Section 3.7.1.

The majority of APT needles were produced using either the Zeiss NVision or Crossbeam560 DualBeam FIB at the University of Oxford. For radioactive samples sample preparation was completed using the Thermo Scientific™ Helios NanoLab™ DualBeam FIB at the MRF. All APT tips were formed by mounting individual wedges from the extracted liftout bar on Si-microposts. Tips of apex less than 100 nm were produced using annular milling at 30 kV 700 pA and 80 pA, followed by a 2 kV polish.

Where samples had been ion-irradiated, the depth-damage profile (shown in Figure 3.5) had to be considered when producing specimens of the desired dpa. Depth-sensitive APT tip fabrication, ensured the tip was located at a specific depth from the original sample surface. Rapid Pt-deposition was required (provided by the Crossbeam FIB) to produce 1 μm thick layer of protective platinum to cover the designated lift-out bar (initially delineated with a layer of electron beam carbon). Consequently, tips could be shaped and thinned such to retain a Pt capping-layer up until the final low-kV polishing stage, wherein the necessary amount of material could be removed. This technique allowed higher accuracy depth measurements for the final tip, as the retained Pt delineated the position of the original surface. Figure 3.10 gives an overview of the FIB lift-out process employed, whilst Figure 3.11 details the method used to produce APT tip apexes at a given depth from the self-ion irradiation surface.

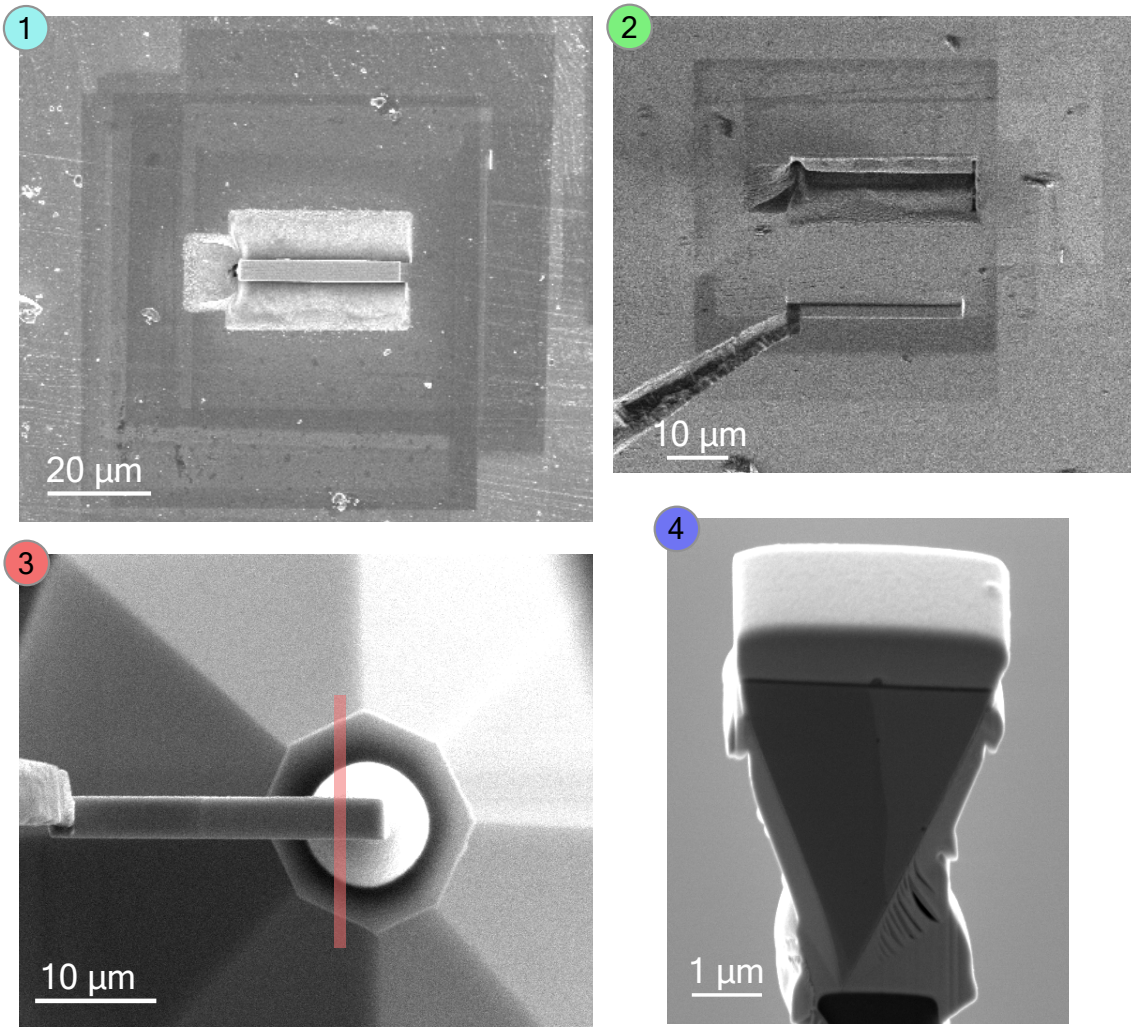

Figure 3.10: Outline of the FIB liftout procedure to produce APT samples. The steps are as follows: 1) a liftout bar is produced using Pt deposition to protect the surface and FIB milling to allow the bar to be released; 2) extraction of the bar from the substrate surface using a micromanipulator (this image is taken in FIB view); 3) attachment of liftout bar to Si micropost using a Pt weld (red area shows where the bar was cut following the weld); 4) resultant attached sample wedge, prior to tip shaping.

3.7.1 Site-specific FIB preparation of HIPed samples

In order to select ferritic regions for APT investigation, the site-specific capability of FIB preparation was utilised for chosen HIPed specimens. For the ion-irradiated samples, access to a FIB instrument with Electron Backscatter Diffraction (EBSD) capability (Zeiss Crossbeam) allowed ferrite grains to be identified via EBSD scans (70° tilt, 20 kV voltage). E-beam deposition was then used to highlight regions where a liftout bar could be placed such to produce both ferritic and bainitic wedges. This was particularly useful following ion irradiation, where the surface finish of the previously polished samples was negatively affected by the irradiation set-up. Thinned APT wedges (<200 nm) could then be checked using transmission kikuchi diffraction (TKD), which indicated whether it incorporated a ferritic, bainitic or mixed region. For this, a voltage of 30 kv, current of 2 nA and working distance of 12.5 mm was used, at a sample tilt of 70°. An example of this is shown in Figure 3.12.

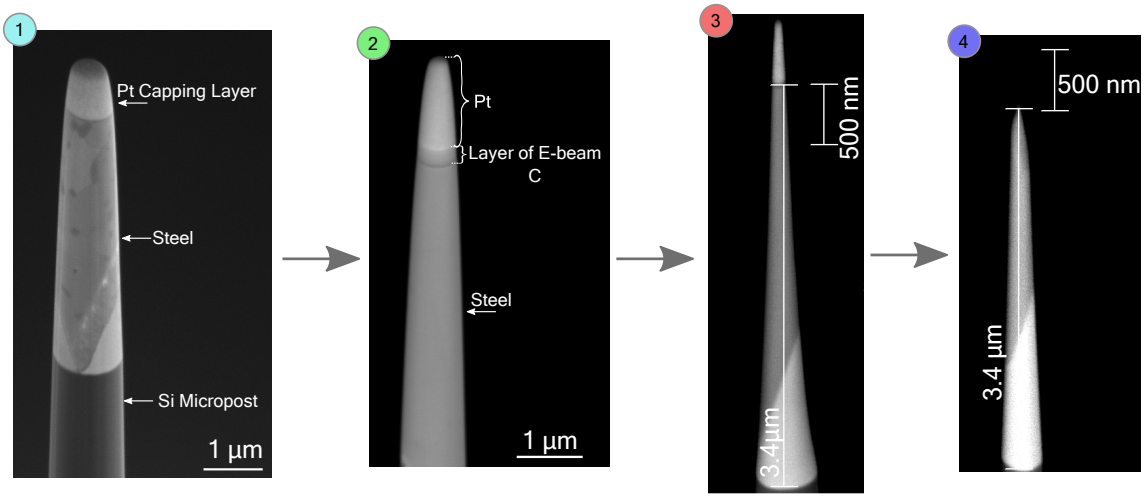

Figure 3.11: Process of producing APT tips with an apex at a chosen surface depth (used for self-ion irradiated samples). The initial tip in 1) is the product of 30 kV 700 pA shaping mill, with an 80 pA current used to produce the shaped tips in images 2) and 3). In this example a tip apex at a depth of 500 nm was targeted. A 2 kV 9.19 nA polish produces the final tip in 4).

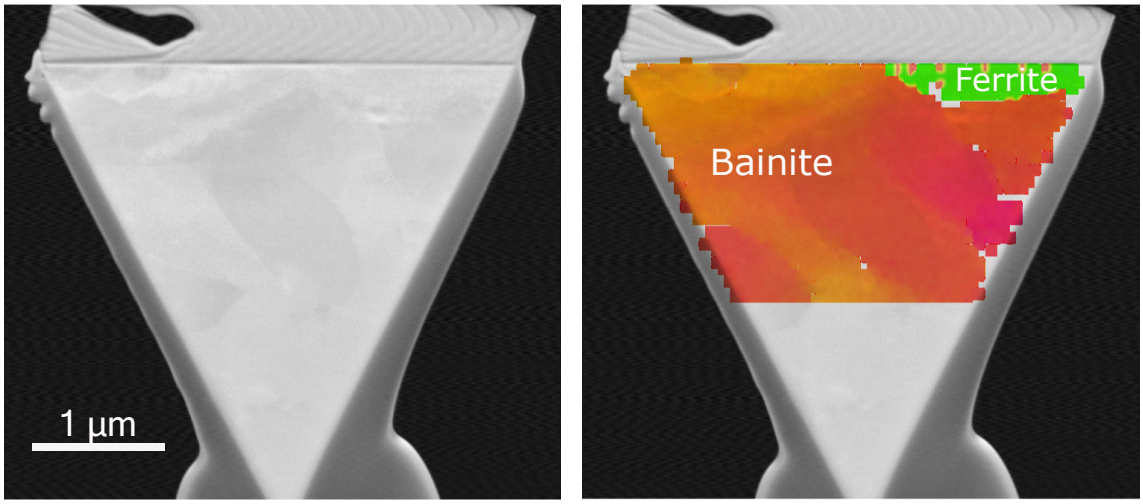

Figure 3.12: Example of a HIP SA508 steel APT wedge cross-section imaged using TKD.

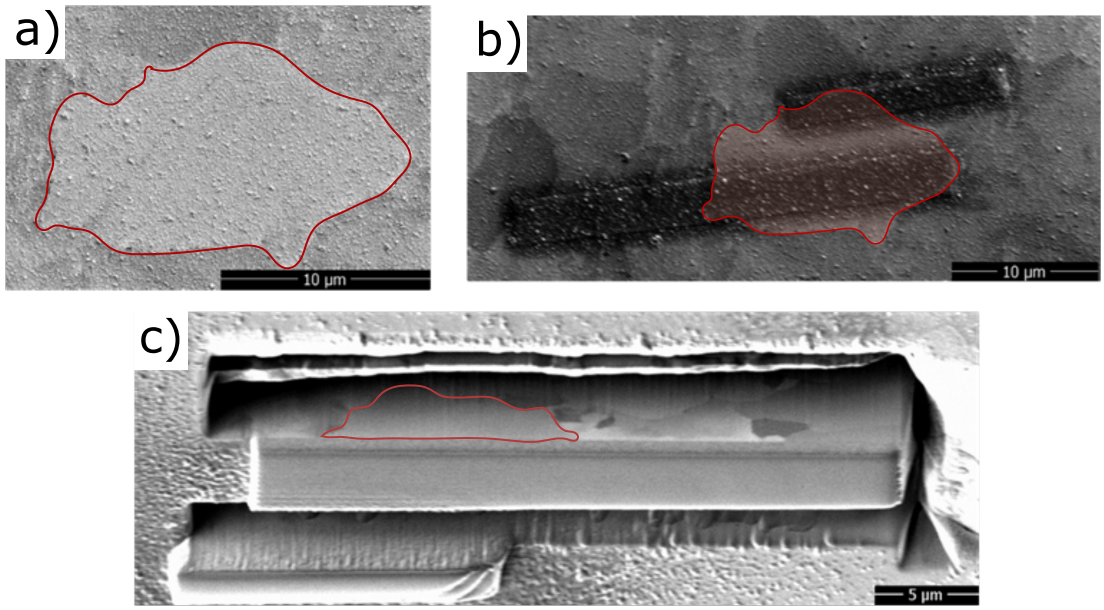

Figure 3.13: Selection and extraction of ferrite for APT analysis and TEM analyses using FIB-SEM. A ferrite grain (a) is identified, delineated by the red line, which is then incorporated into an atom probe and TEM liftout bar (b), with the location within the APT bar noted (c).

For neutron-irradiated samples, the method for ferrite grain identification was altered due to the MRF FIB not having an EBSD detector. The consistent damage profile of these disks allowed polishing post-irradiation (as the surface location within the irradiated volume is of no consequence). This allowed for visual identification of polygonal ferrite using SEM imaging, shown in Figure 3.13. Following APT liftout and mounting, the origin of each liftout wedge within the original bar was tracked, enabling an approximation of what microconstituent was contained within each APT sample (shown in Figure 3.14. A similar approach was used for one of the Fe^{4+} irradiated HIPed samples (5 dpa) which was etched prior to irradiation – this was a tentative investigation to see whether it would aid microstructure identification in future experiments of this type, and proved successful.

3.8 Nanoindentation

Nanoindentation of neutron-irradiated HIP and LF samples was completed at the MRF using the Agilent Nanoindenter G200, equipped with a Berkovich tip. Indent arrays were performed using Continuous Stiffness Measurement (CSM) mode (conditions given in Table 3.5) such to produce 80 indents in an 8×10 arrangement. CSM introduces a sinusoidal displacement rate to the indenter tip (of frequency f), which is used to continuously determine contact stiffness as a function of indenter depth [169]. All indents were performed perpendicular to the sample surface, at depths up to 2 μm (with displacement control).

Table 3.5: Nanoindentation CSM mode conditions.

Tip Frequency	Indent Separation	Surface Approach Velocity	Harmonic Displacement
45 Hz	40 μm	10 nms^{-1}	4 nm

To characterise the hardness of the ferritic and bainitic phases in the HIPed sample, EBSD maps were acquired on the nanoindented region. EBSD was performed using a

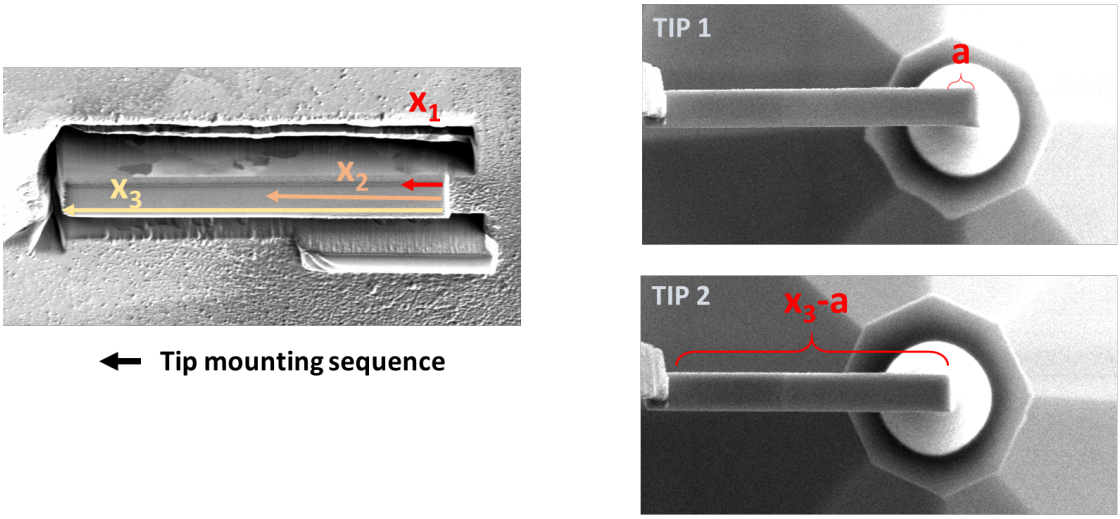

Figure 3.14: Tracking location of microconstituent grains in irradiated HIPed samples.

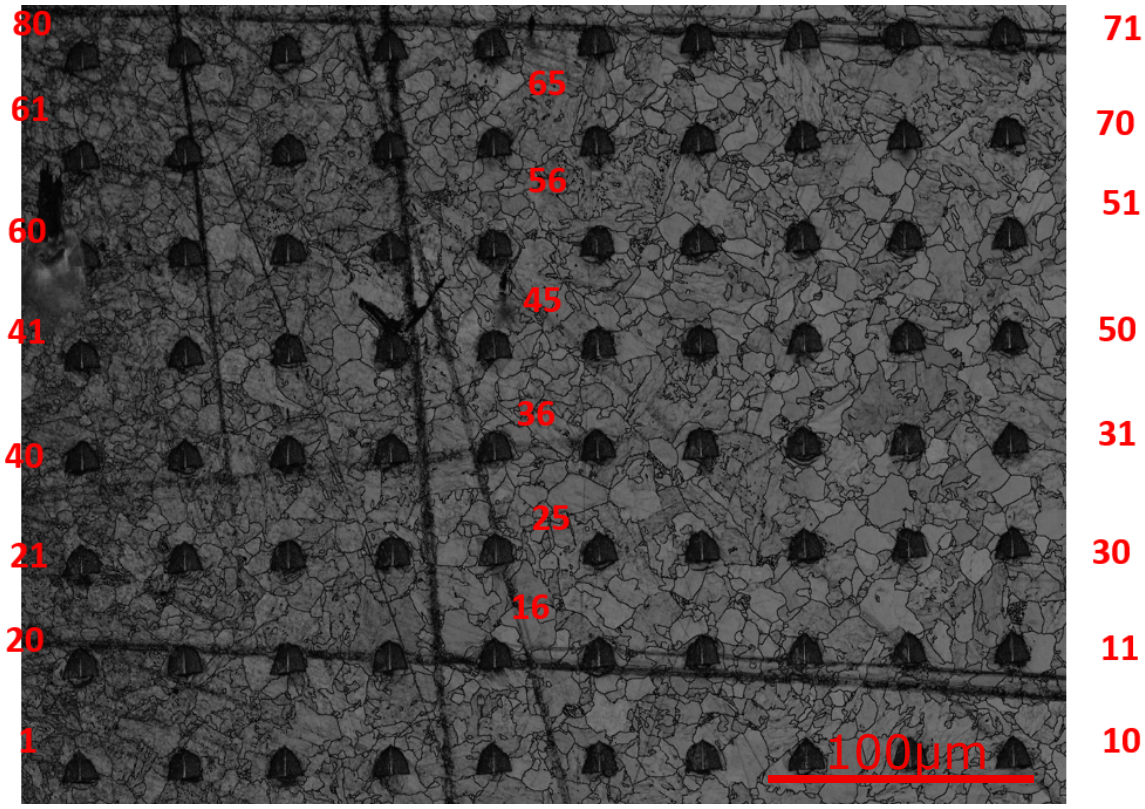

Figure 3.15: Example of a 80 nanoindent array in 0.1 dpa, neutron irradiated HIPed SA508 steel (shown using band contrast imaging, with 10°and 2°grain boundaries). The numbering indicates the indentation sequence.

TESCAN Mira3 XMH SEM at MRF with an Oxford Instrument NordlyS EBSD detector (70° tilt, 20 kV voltage). A step size of 230 nm and exposure time of 18 ms were used to analyse the sample surface post-indentation. EBSD patterns were plotted and analysed using Channel 5™ software with modules Tango™ (mapping) and Mambo™ (pole figure) from Oxford Instruments® HKL™. Using the images obtained, each indent was then assigned an identity; ferrite, bainite, or mixed. Any indents lying on scratched regions were ignored during analysis.

Chapter 4

Characterisation of As-Received SA508 Steel

Prior to irradiation studies, which induce a non-equilibrium environment on the target samples, it is important to have a baseline comprehension of the prior micro- and nano-structure which is being subjected to the enhanced diffusion and segregation mechanics associated with irradiation. This allows understanding of the role changes in material substructure have on mechanical properties.

This chapter discusses the use of characterisation techniques across various length scales (APT→TEM→SEM→optical microscopy) to analyse the nanostructures and microstructures of the as-received, un-irradiated forms of SA508 Grade 3 Class 1 steel being utilised in irradiation studies in this research.

Investigations of this type have been comprehensively conducted elsewhere on conventionally forged SA508 steel (discussed in Chapter 2). This work will focus on the HIPed material, with additional comparison to its conventional counterparts. Comparison is vital to acquire a more complex understanding of microstructural character, allowing the source of any potential differences in irradiation response to be highlighted.

4.1 HIPed Microstructure

Alternative reactor designs, such as SMRs, could facilitate the use of powder-processed alloys in the nuclear industry by incorporating the need for net-shape manufacturing or assembly-line components [170]. Prior to consideration for nuclear applications, a better understanding of the microstructure and mechanical properties of this form of metallurgy is required. Given this research focuses on comparison via APT, an APT study of pre-irradiation HIPed samples is required.

As shown in Section 3.1.2, the clearest difference in HIPed SA508 microstructure compared to that observed in the forged materials is the higher fraction of ferrite present. However, this is one aspect of the resultant microstructure; in reality, performance differences between forged and HIPed SA508 type steels will originate beyond solely the heightened presence of this ferrite microconstituent.

4.1.1 Determining ferrite fraction

To determine the approximate fraction of ferrite present in HIPed SA508, the simplest method available was using the etched optical micrographs in combination with the ImageJ "Morphological Segmentation" tool from the MorphoLibJ plug-in [171]. Optical micrographs were converted into 8-bit greyscale images, with contrast adjusted to give the sharpest possible image of the grain structure (Figure 4.1a). Morphological segmentation was then applied, with the 'object image' tool creating a domain map (Figure 4.1b) from the micrograph based on a chosen tolerance value (usually around 20, but this varied between images) and domain connectivity of 4. By manually merging domains which were deemed to be polygonal ferrite, a map indicating the ferritic regions could be produced (Figure 4.1c). By using the 'analyse regions' tool and selecting area, the area attributed to the labelled

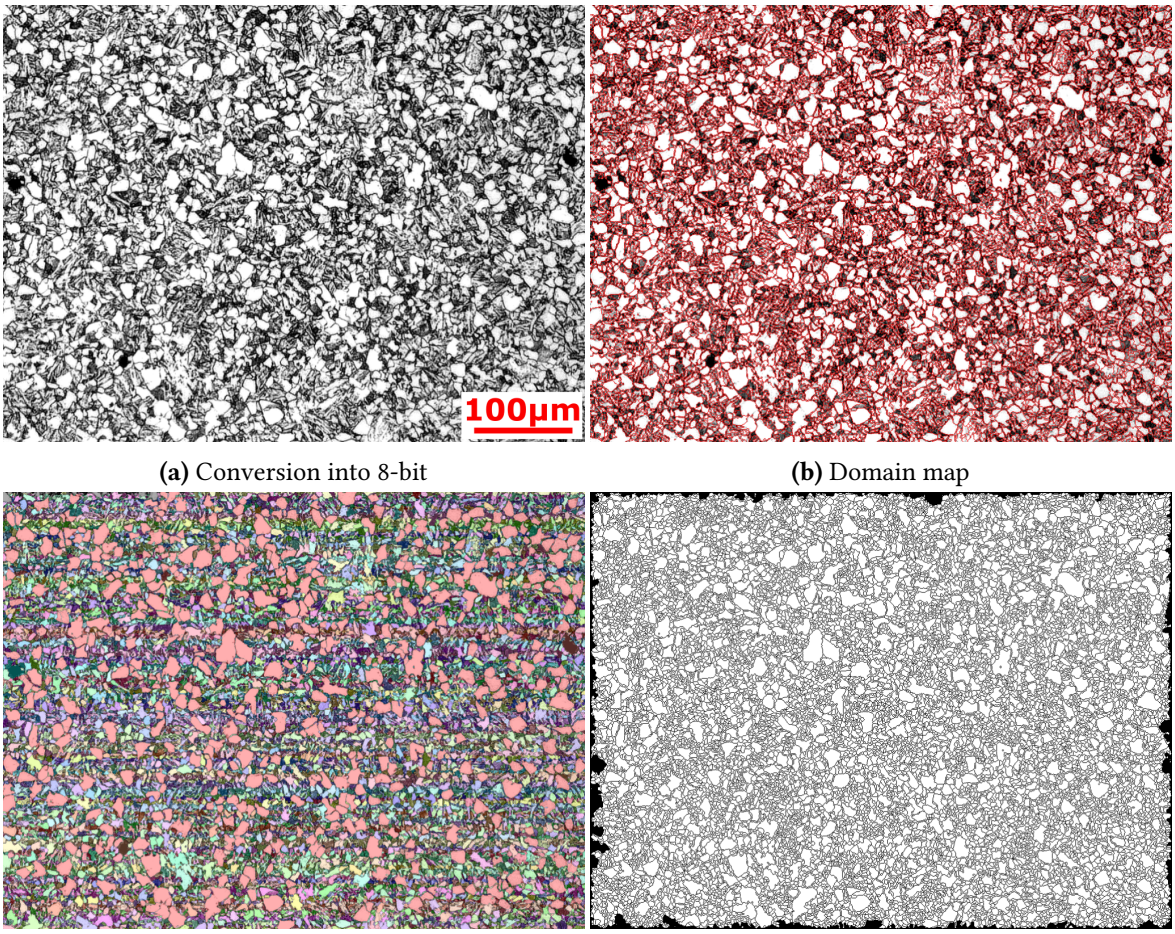

(a) Conversion into 8-bit

(b) Domain map

(c) Ferrite domains merged (red) in domain map

(d) Edge removal in area calculation

Figure 4.1: The process of using morphological segmentation in ImageJ to determine approximate ferrite fraction.

ferrite regions could be compared to that of the entire imaged surface (with border domains removed from the analysis to avoid missing partial ferrite grains) (Figure 4.1d).

This process yielded an area fraction of ferrite grains, as determined by manual grain selection. As the ferrite selection is a result of user choice, such to give a reasonable estimate of microconstituent fraction, area fraction calculations were conducted on three different optical micrographs (encompassing different areas of the sample surface) and with three different approaches to ferrite assignment; reasonable, underestimate and overestimate. The average of these approaches across the three sample areas gave an approximate ferrite

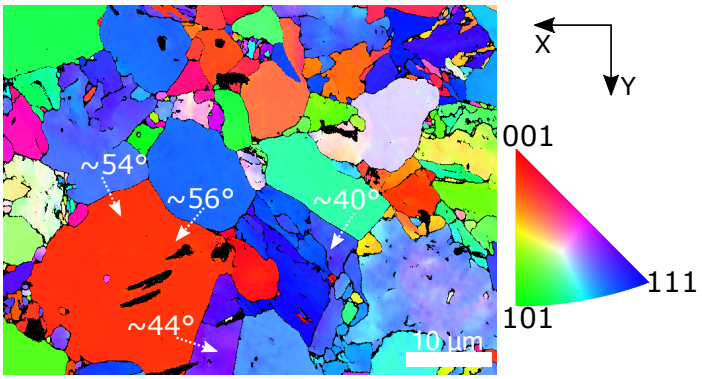

Figure 4.2: An EBSD map from as-received HIPed SA508 indicating the misorientation angles across various ferrite grain boundaries. The arrows lie across each boundary, starting in the first grain and pointing into the adjacent grain for which the misorientation was calculated. The IPF Z colour key is included.

fraction of 18% ± 2%. Whilst this method is reasonable in giving a good indication of the amount of polygonal ferrite present in HIPed SA508, it must be noted that it is not wholly accurate quantitatively.

4.1.2 EBSD and EDS mapping

Beyond optical imaging, EBSD mapping gives a good overview of the larger-scale microstructure of the samples. This was primarily used in determining the locations for site-specific FIB preparation, but was also useful in gaining an insight into the grain orientations and networks involved.

It is known that in bainitic-steel microstructures, specific low angle grain misorientations are primarily associated with lath boundaries [172], whereas higher misorientations are likely indicators of prior-austenite (PA) grain boundaries (remnants of the microstructural evolution involved in the production of lower bainitic steels). Whilst both types of boundary were present across all samples, the ferrite grain interfaces were of the high angle (PA) variety. An indication of the high grain boundary misorientation of a ferrite interface in HIPed SA508 steel is shown in Figure 4.2, as determined using the HKL Tango software.

An overall misorientation distribution comparing the HIPed and LF SA508 is displayed in Figure 4.3, produced using Channel 5™. Although a somewhat rudimentary method of comparing the grain boundary networks present in both samples, it is useful in indicating a relative increase in high angle boundaries (PA) in the HIPed steel, whereas low angle boundaries dominate in the forged steel. This may be of relevance in determining reasons behind segregation behaviour under irradiation, as high angle boundaries are associated with more free space in which solute atoms can sit compared to low angle ones. This could influence the diffusion dynamics in each alloy, as grain boundary diffusion is generally the most common mechanism of solute migration in polycrystalline materials [173].

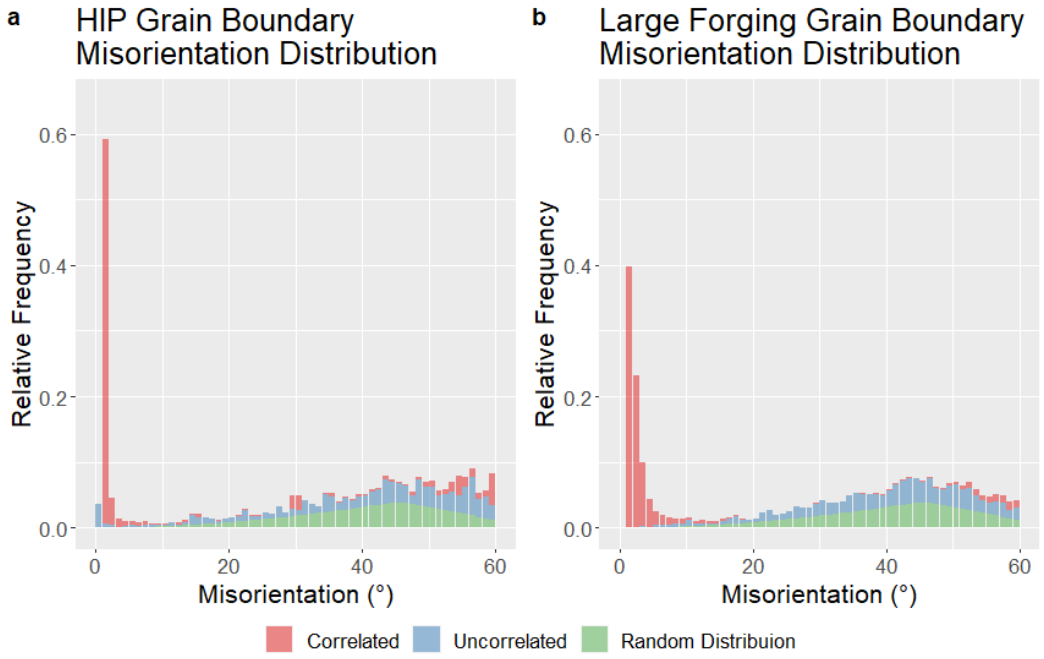

Figure 4.3: Frequency distribution of grain boundary misorientations in a) HIP and b) LF SA508 steel. Correlated counts correspond to the misorientation between two neighbouring grains, whilst uncorrelated counts are for misorientations between randomly selected points in the data. Bin size is 1°, and the random misorientation distribution is a MacKenzie plot [174] from the Channel 5™ software. The bars from each distribution are overlaid.

During FIB sample preparation, various inclusions can be discerned in the intermediate tip cross-sections, prior to final shaping. Whilst these features could not be easily identified

in the large surface imaging used at the beginning of the production process, they could be identified in SEM, which then prompted further investigation using energy dispersive spectroscopy (EDS). For the forged samples it was invariably the case that these features were carbides, however, in the HIPed samples, EDS revealed the presence of aluminium-rich oxide particles.

The method for investigating dispersoids via EDS analysis is shown in Figure 4.4; two Al-rich features were identified. Specifically, both were shown to incorporate raised levels of Al, O and Si compared to spectra taken from matrix regions. The limited compositional resolution of EDS means it is not valid to quantativly quote the compositions of these particles, however it is useful in giving a qualitative indication of the nature of these metallic inclusions.

4.2 APT Observations in As-received Samples

Initial APT analysis of the as-received SA508 samples is important in providing a baseline to which specimens in the post-irradiation condition can be compared. This encompasses the acquisition of expected compositional ranges for the alloy matrix and general investigations into the appearance of nanoscale volumes of these samples, incorporating any observed solute segregation or phases formed.

4.2.1 Matrix compositions

In RPV steels, this inhomogeneous solute distribution is often the result of secondary phase formation, normally carbides, which can result in either local enrichment or depletion of certain alloying elements, in addition to preferential solute segregation to phase interfaces. It is therefore important in APT studies to establish expected composition ranges for the matrix regions of investigated alloys to enable conclusions concerning the influence of

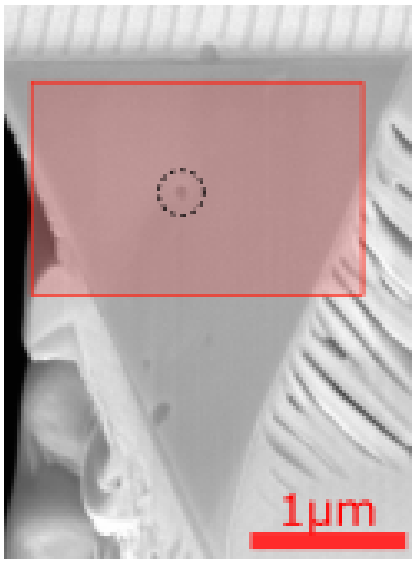

(a) Thinned APT wedge prior to EDS of inclusion features - inclusion indicated by black circle.

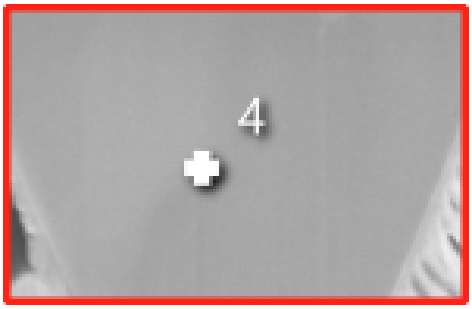

(b) Highlighted area from which EDS spectrum taken from apparent inclusion.

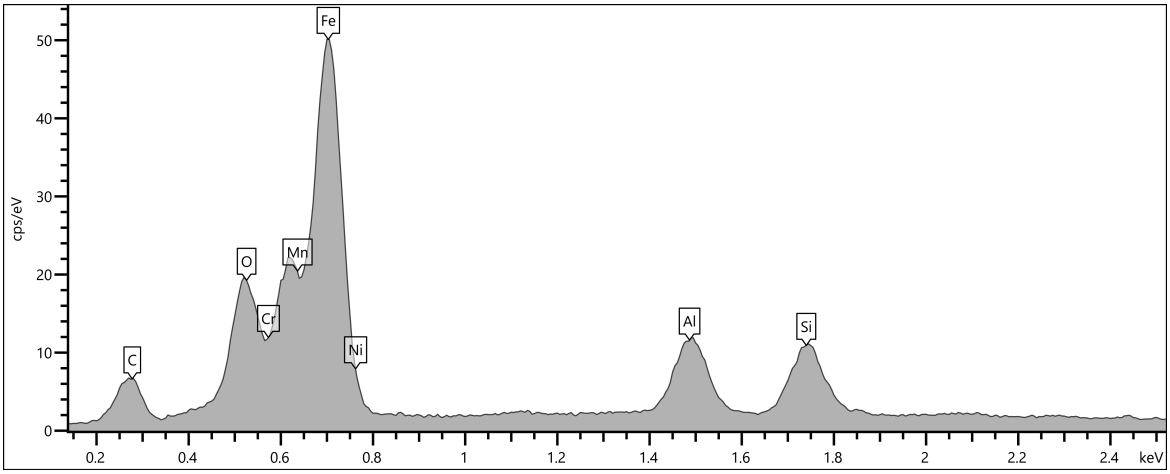

(c) EDS spectrum obtained from point 4, indicated in b), showing the prescence of elevated levels of Al, Si and O

Figure 4.4: Process of identifying potential metallic inclusion and extracting EDS information.

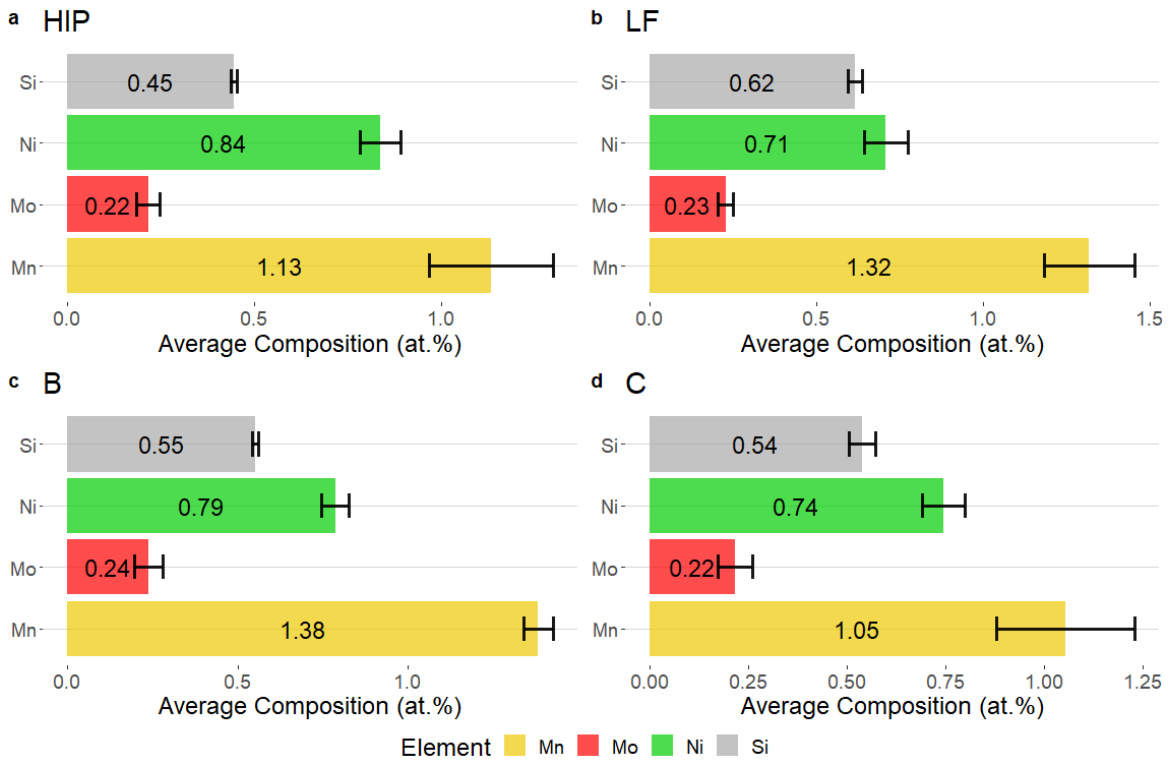

Figure 4.5: Bar plot of the average Si, Ni, Mo and Mn contents in each type of SA508 alloy, acquired using APT, with error bars equal to 1 standard deviation. The number within each bar indicates the average composition of that element across multiple APT datasets, for ease of comparison between the alloys.

irradiation on the distribution of elements within the material. Thus, given the volume-specific nature of APT experiments, the samples analysed rarely present the nominal composition of the material being investigated (a result of the microscale inhomogeneity impacting the distribution of elements).

In this work, all four types of SA508 steel were subjected to APT analysis in the as-received state. A number of matrix compositions were extracted, and graphs indicating the variation in major alloying elements (Ni, Mn, Mo, Si, P and C) are shown in Figure 4.5 and Table 4.1. The error values shown are equivalent to 1 standard deviation based on measuring the elemental composition across multiple APT datasets (5 HIP, 2 alloy B, 6 alloy C and 3 LF) of each alloy.

Table 4.1: Table showing the average P and C contents in each type of SA508 alloy, acquired using APT, with quoted errors equal to 1 standard deviation.

Element		HIP	LF	B	C
P (at.%)	Average	0.019	0.007	0.002	0.002
	Error (± at.%)	0.002	0.002	0.0001	0.0002
C (at.%)	Average	0.053	0.024	0.014	0.004
	Error (± at.%)	0.019	0.017	0.006	0.004

As shown in Figure 4.5, the greatest variation in species composition seen within APT samples was in Mn. This is likely a consequence of Mn-rich carbides heterogeneously distributing Mn throughout the alloy volume at the micro-scale, resulting in APT tips lying near carbides containing significantly less Mn due to the solute denuded zone. Given that Mn has been shown to participate in irradiation clustering, the distribution of this element relevant to APT sampling is an important consideration when interpreting irradiated datasets. Akin to the composition variance shown for Mn, that of C also experiences significant fluctuation, again a consequence of carbide formation and proximity. However, of note is that the average amount of carbon in the HIPed samples is greater than in the forged steels, suggesting a disparity between the alloys in the amount of carbon trapped within carbides. This effect is heightened by the increased amount of retained ferrite within the HIPed sample, reducing the relative number of cementite laths present in the alloy.

The elevated P content in the HIPed steel, shown in the nominal composition provided in Table 3.2 in Chapter 3, continues in the as-received atom probe data. Furthermore, there is a reduction in Si in the HIPed sample compared to the forged ones, which may be a consequence of Si being tied-up in the silicon-rich inclusions encountered using EDS.

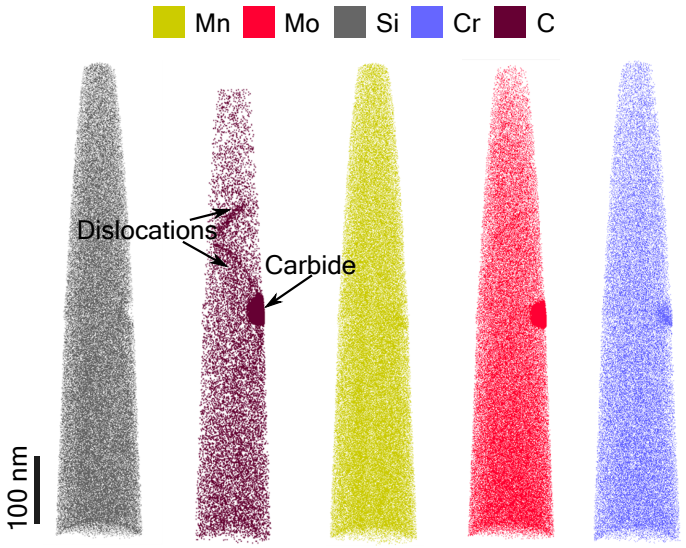

Figure 4.6: Solute segregation to a carbide and dislocations in as-received HIPed SA508.

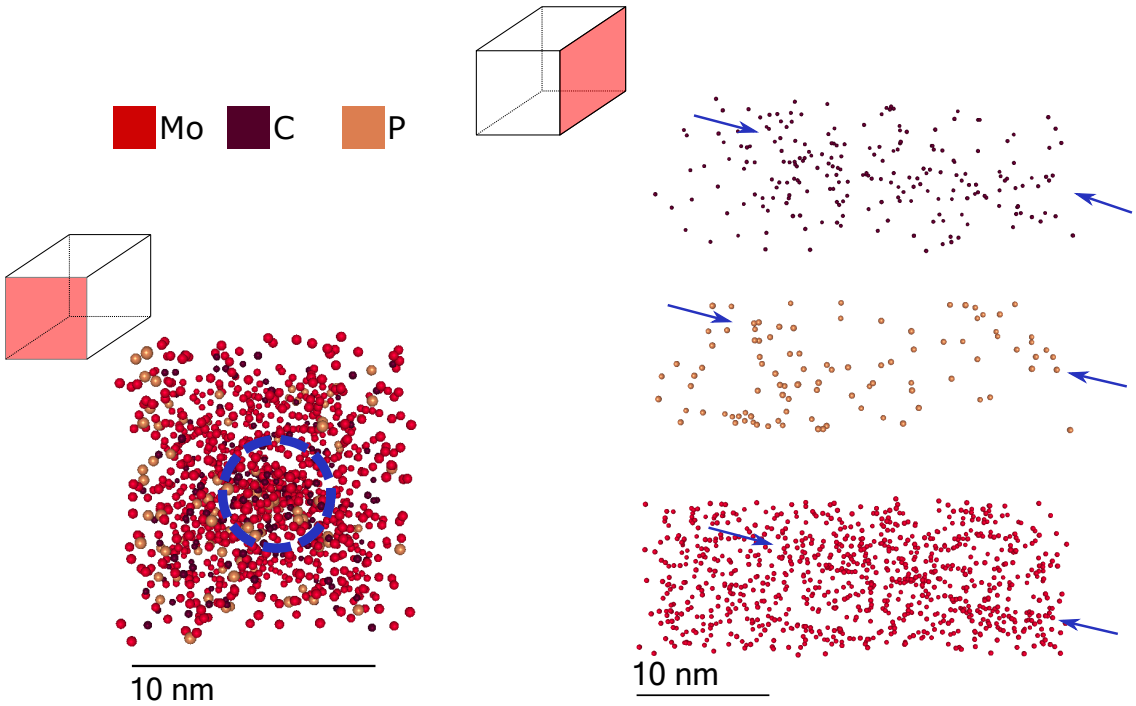

(a) View through the dislocation line

(b) View perpendicular to the dislocation line

Figure 4.7: Indication of solute clustering to a dislocation in an as-received HIPed SA508 sample in two planes at 90°. The solute atoms are represented as spheres, with the viewing plane shown in the adjacent 3D plans. The blue circle (a) and blue arrows (b) indicate the apparent dislocation location.

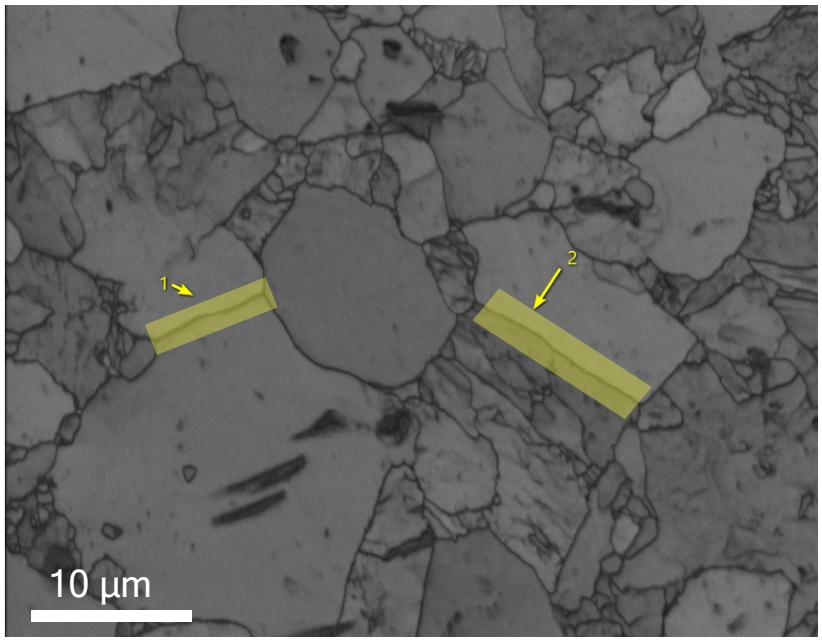

Figure 4.8: Band contrast map indicating regions (yellow) where prior-austenite grain boundaries for APT liftout were identified using EBSD.

4.2.2 Solute segregation to dislocations and grain boundaries

Decorated dislocations were observed across the four types of SA508 steel. Specifically, C and Mo segregation to dislocations was commonly seen in APT reconstructions, shown in Figures 4.6 and 4.7, in addition to P on some occasions, akin to what is often seen in forged samples. P segregation is less pronounced, on account of its trace contribution to the alloy composition.

Given the influence that processing can have on grain boundary networks in SA508, prior-austenite (PA) grain boundaries (specifically those adjacent to ferrite grains in the HIPed material) were investigated, having been isolated using EBSD mapping (Figure 4.8 and TKD. As previously discussed, it is in the relative frequency of high angle boundaries where HIPed and LF SA508 steel differ most notably in this aspect of microstructure.

An example of using TKD to isolate a PA grain boundary in as-received LF SA508 steel is shown in Figure 4.9.

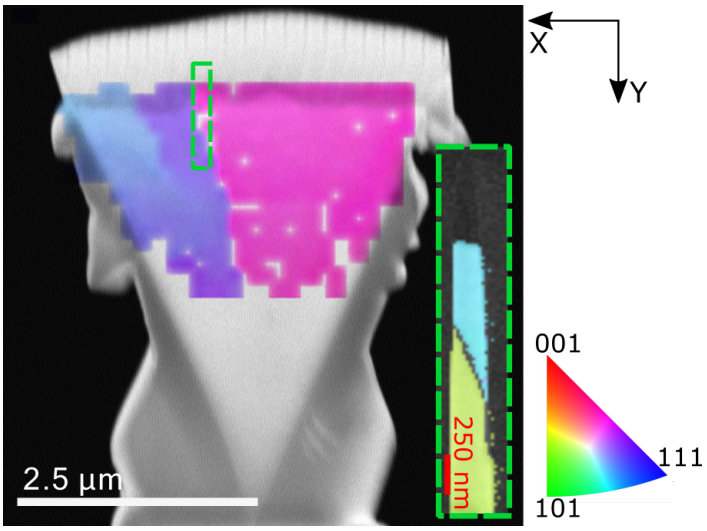

Figure 4.9: The isolation of a PAGB in as-received LF SA508 using TKD. The final APT tip shape (prior to a cleaning polish, where approximately 500 nm was removed) is shown in the green box. The IPF colours do not match between the larger wedge and the final tip on account of the images being taken in different sessions, such that the angle between the sample and EBSD camera was changed. Thus the IPF colour digram changed between images, despite showing the same mis-orientation.

Solute species previously known to segregate to interfaces [58] were also seen at grain boundaries. Perhaps due to the significantly higher free space at grain boundaries, the extent of segregation is greater at grain boundaries. A grain boundary from an APT run

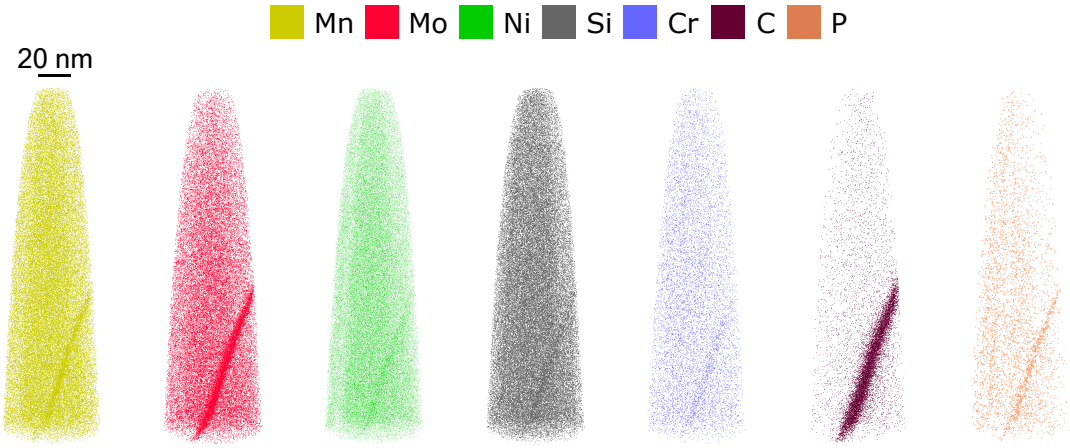

Figure 4.10: Indication of segregating species to a prior-austenite, ferrite grain boundary in as-received HIPed SA508 steel.

	C	Fe	Mo	Ni	Cr	Mn	Si	P
Bainite Grain	0.03	97.48	0.24	0.91	0.08	0.80	0.40	0.01
Ferrite Grain	0.26	97.94	0.14	0.75	0.04	0.72	0.37	0.00

Table 4.2: Grain compositions (at.%) in as-received SA508 HIPed Steel as determined by a 15×15×15 nm ROI cube in each grain. Error approximated to 0.01 at.%

of as-received HIPed steel is shown in Figure 4.10. Unfortunately, the five grain boundary regions isolated in the forged sample failed to run successfully in the atom probe, thus restricting grain boundary results to the HIPed material.

By considering the EBSD and TKD data for the tip in Figure 4.11 , the relative location of the ferrite and bainite regions can be determined; ferrite grains appear as one solid colour in the IPF figure, whilst bainite grains have graded colours. Subsequently, for this atom map, the larger grain region (above the boundary in Figure 4.11) is bainitic, whilst the lower grain is ferritic. Using this information, the composition of these different microconstituents can be determined, the results of which are shown in Table 4.2.

Despite elements such as Ni and Si appearing to segregate (as in Figure 4.10), the 1D concentration profile through the region (Figure 4.11a) shows this is not a clear-cut case. An appearance of segregation for these elements is as a result of the higher relative density (caused by a low evaporation field) of the boundary region, as shown in the volume render in Figure 4.11c, causing a local magnification effect [175, 176].

Gibbsian excess values (Γ_i) can be determined for individual grain boundaries (in this case using an R script provided by Dr Ben Jenkins). In this example, the apparent interface width was defined using the Mo counts across the boundary and measured approximately 5nm. It is important to show Gibbs excess alongside the compositions of the two grains present, such to better understand it in the context of the amount of each element present [165]. Table 4.2 indicates the compositions of regions further from the grain boundary,

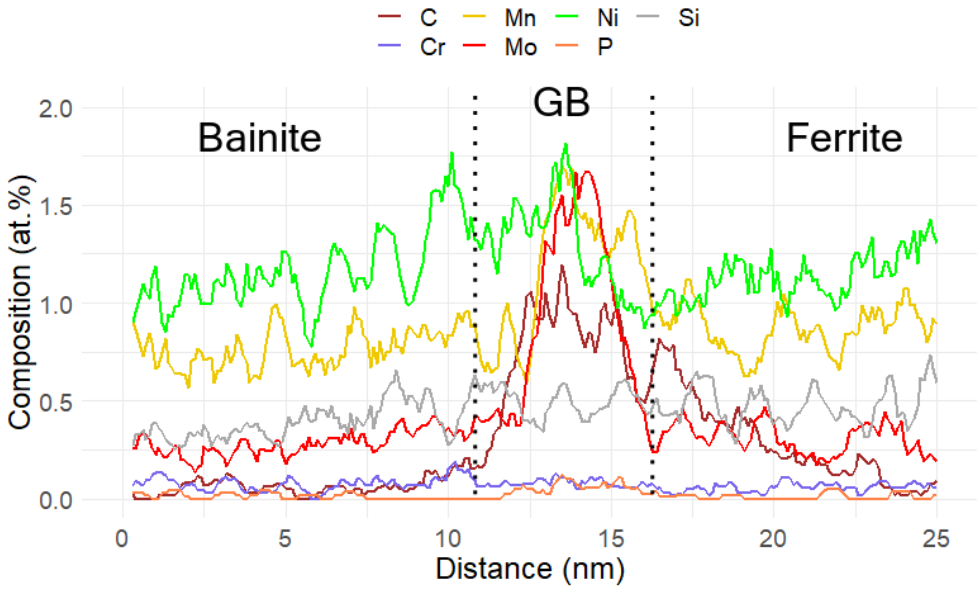

(a) 1D concentration profile through the region of interest in Figure 4.11b. The direction of analysis is indicated adjacent to the ROI included in Figure 4.11b.



(b) Location of the analysis region of interest (ROI) used to obtain a concentration profile perpendicular to the grain boundary interface. The analysis direction of the z-axis concentration profile is indicated by the 'z' arrow.

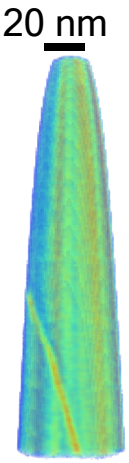

(c) Volume render indicating regions of higher density (red) and lower density (blue).

Figure 4.11: Analysis of solute segregation to grain boundary in as-received HIPed SA508 steel.

Table 4.3: Calculated Gibbs Excess values for the HIPed SA508 as-received grain boundary, including compositional values for the interface and adjacent volumes (with an error of ± 0.01%).

	C	Fe	Mo	Ni	Cr	Mn	Si	P
Gibbsian Excess (excess atoms/nm^3)	1.97 ± 0.57	-5.46 ± 1.10	2.01 ± 0.20	0.32 ± 0.03	0.13 ± 0.00	0.93 ± 0.22	-0.13 ± 0.13	0.15 ± 0.06
Interface Comp. (at.%)	0.80	95.54	0.77	1.15	0.09	1.08	0.46	0.06
Bainite Grain A Comp. (at.%)	0.07	97.25	0.27	1.11	0.06	0.78	0.41	0.02
Ferrite Grain B Comp. (at.%)	0.19	97.02	0.31	1.10	0.06	0.82	0.43	0.03

whereas those given in Table 4.3 are taken from the volumes directly either-side of the defined interface. Notably, the script used does not account for peak overlaps, thus the excess in Ni seen at the interface likely reflects an excess of the 32 Da peak (which is shared between the $^{64}Ni^{2+}$ and $^{96}Mo^{3+}$ species). This correlates with no notable Ni segregation being seen in the concentration profiles, compared to the clear Mo enrichment observed.

4.2.3 Carbides and carbide interfaces

In this work, when considering the solute available for clustering/segregation behaviour, an understanding of carbide types and interface profiles is important in inferring any influence on irradiation response. Given the size of these features, and that acquiring data on them was not a focus of this project, the results gathered on carbide inclusions was a result of random sampling in APT tip fabrication. As such, by chance both carbides found in the as-received state were in HIPed datasets; carbides from other steel types were found in the irradiation studies, and will be discussed where relevant.

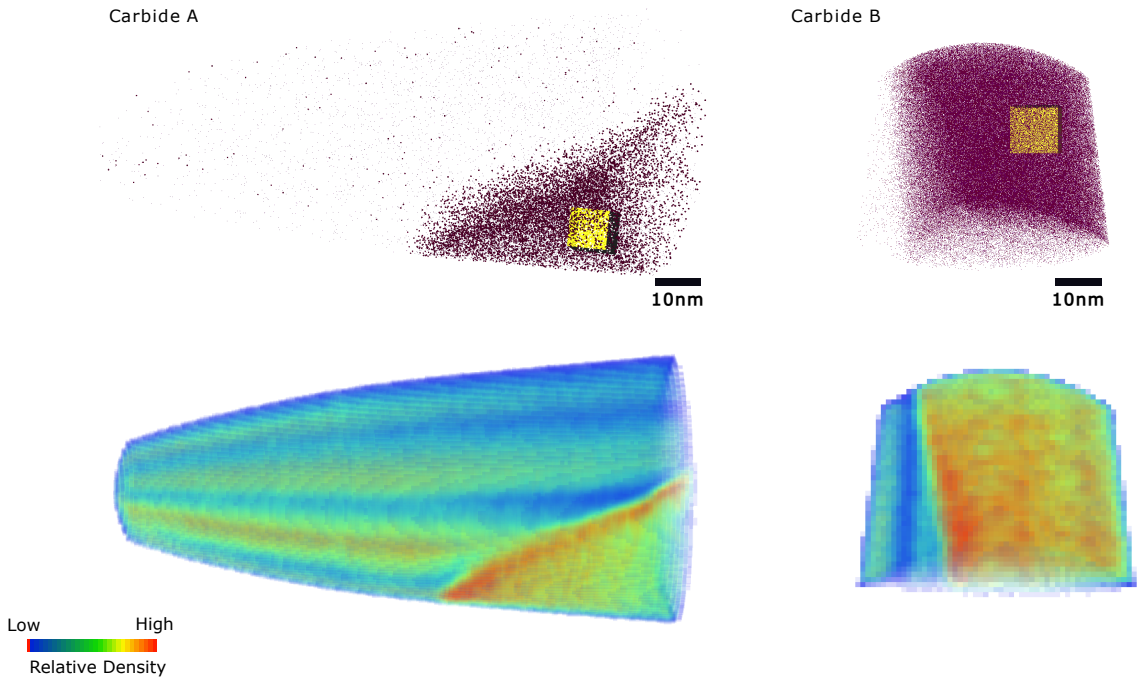

Figure 4.12: APT maps (showing C atoms only) of carbides found in as-received HIPed SA508 steel. The ROIs (yellow) are 10×10×10 nm and were used to extract carbide composition measurements. Density maps are shown, with the colour scale indicating the relative density of region of the APT reconstruction.

Carbide compositions

Shown in Figure 4.12 are carbides analysed in as-received APT runs. Regions of interest (ROIs) within the carbide allow the composition away from the interface region to be isolated. It should be noted that determining carbide concentrations using APT is complex. In many carbide types, there is significant C loss during atom probe detection – due to 'multi-hit' events (where multiple ion detection events occur within a very small time interval, preventing distinction of the signals [177]). However, specifically in the case of cementite, C overestimation can occur due to intricacies in peak ranging (detailed in [178]). The density maps in Figure 4.12 indicate these carbides are of apparent higher density than the surrounding matrix in the APT reconstructions, which implies they are low-field features.

Table 4.4: Carbide compositions (at.%) in as-received SA508 HIPed Steel. Error approximated to 0.01 at.%. Note the mass spectra used to determine these compositions was subjected to peak overlap deconvolution in an attempt to separate the peaks contributed by different carbon species.

	C	Fe	Mo	Ni	Cr	Mn	Si
Carbide A	30.50	59.50	0.60	0.25	0.30	8.88	n/a
Carbide B	26.61	58.91	2.01	0.31	1.40	7.70	n/a

Given they are low-field features, it is likely both are cementite (Fe_3C), with the derived compositions (shown in Table 4.4) impacted by loss of Fe during APT analysis. However, carbide A is richer in Mn and C, whilst carbide B is richer in Mo and Cr. As discussed in Section 4.2.1, incorporation of certain elements within carbides causes a significant reduction in the amount of that solute within the matrix, resulting in a reduction in the APT-derived composition compared to the nominal.

$$\text{Solute Reduction (\%)} = \frac{c_{\text{carbide}} \times f_{\text{c}}}{c_{\text{nominal}}} \tag{4.1}$$

Whilst the relative compositional differences between carbide A and carbide B may seem small, the slight change in a species' enrichment level between the carbides will impact the fraction of the total amount of that species in the alloy which is involved in carbide formation. This can be illustrated by considering Equation 4.1, which calculates the reduction in the amount of a given matrix solute due to a given carbide phase fraction (f_c). By assuming f_c is a constant for each alloy, inputting the concentration of an element in the carbide ($c_{carbide}$)

Table 4.5: Estimates of the fraction of key alloy solute elements trapped within carbides in as-received HIPed SA508 steel, based on the carbides identified in 4.12. Values are given to 2 significant figures.

	Mn	Ni	Mo	Cr
Carbide A	$7.2f_c$ %	$0.23f_c$ %	$1.2f_c$ %	$3.0f_c$ %
Carbide B	$6.2f_c$ %	$0.35f_c$ %	$4.0f_c$ %	$14f_c$ %

and dividing by the nominal alloy concentration of the same element ($c_{nominal}$) gives the matrix solute reduction for that element, for the chosen carbide type. Table 4.5 shows the amount of relevant alloying elements trapped in carbides for the HIPed SA508 steel, should all carbides be either the same composition as either carbide A or carbide B. The fraction is given as a percentage of the total amount of that element present, multiplied by f_c.

Carbide interfaces

Carbide interfaces act as segregation sites for certain solute species. Proxigrams (shown in Figure 4.13) across the interfaces of those carbides shown in Figure 4.12 indicate the distribution of elements across these surfaces. Carbide interfaces act analogously with grain boundaries, bar a couple of key differences. As shown in Figure 4.13, whilst grain boundaries exhibit sharp segregation behaviour, a carbide interface is wider, with elements generally shown to segregate to the neighbouring phases rather than the interface itself. The exception to this is P, which appears only at the interface region (akin to P segregation to grain boundaries), and Mo in Carbide A, which is at a clear peak concentration nearest the interface.

The behaviour of Mo at the carbide boundary seems to differ depending on the carbide composition. Those carbides found with lower relative Mo compositions, for example, in Carbide A and the secondary-phase-containing carbide discussed in the next section (see Table 4.6), exhibit a Mo profile which varies with distance into the carbide – suggesting Mo sits preferentially in the region nearest the interface, with the concentration highest directly at the phase boundary. In contrast, Carbide B contains significantly more Mo (approx. 2at.%), which is reflected in the stable concentration profile into the carbide region as Mo takes up a more uniform distribution within that phase. Observations of this nature highlight the important distinction between those elements which segregate to phase boundaries specifically, and those which simply lie at interfaces as a result of thermodynamically favourable partitioning to the adjacent phase.

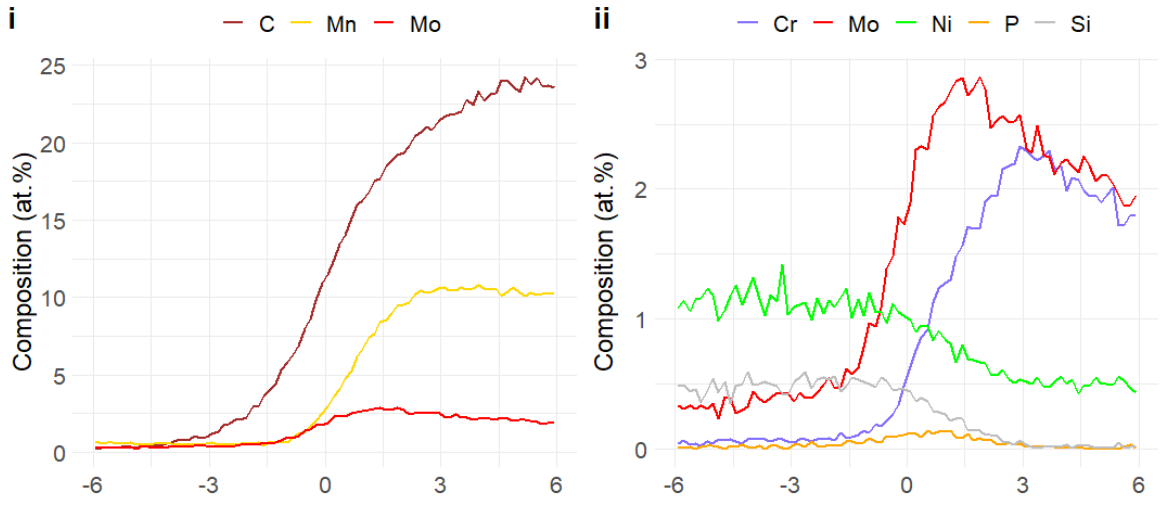

(a) Proxigram taken from 12% C isosurface across Carbide A

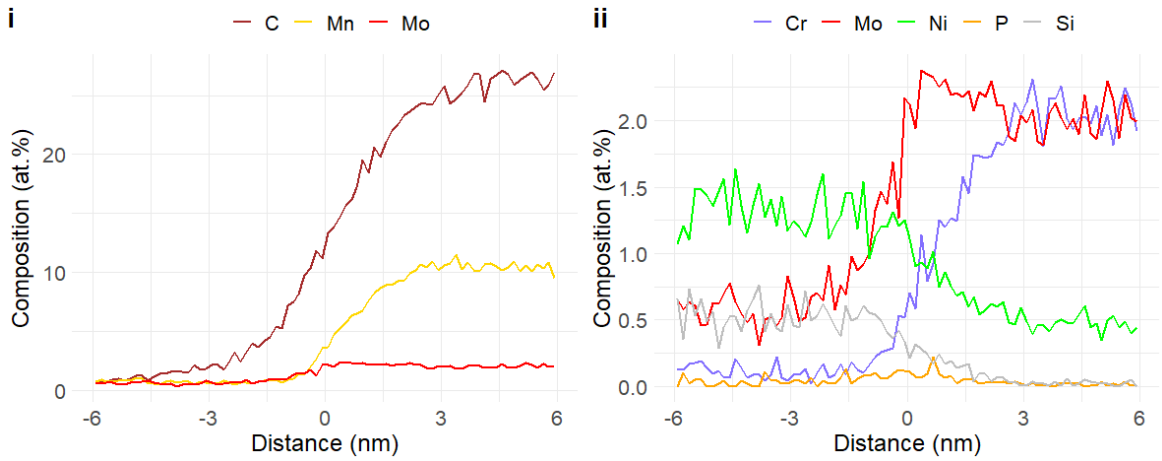

(b) Proxigram taken from 14% C isosurface across Carbide B

Figure 4.13: Proxigrams across carbide interfaces in as-received SA508 HIPed APT samples (original carbides shown in Figure 4.12)

4.2.4 Silicon inclusions within carbides

Perhaps an unexpected feature encountered during analysis of the as-received materials was the observation of Si-rich particles incorporated into a grain boundary carbide, shown in Figure 4.14. Inclusions of this nature are not commonly reported, with most intra-

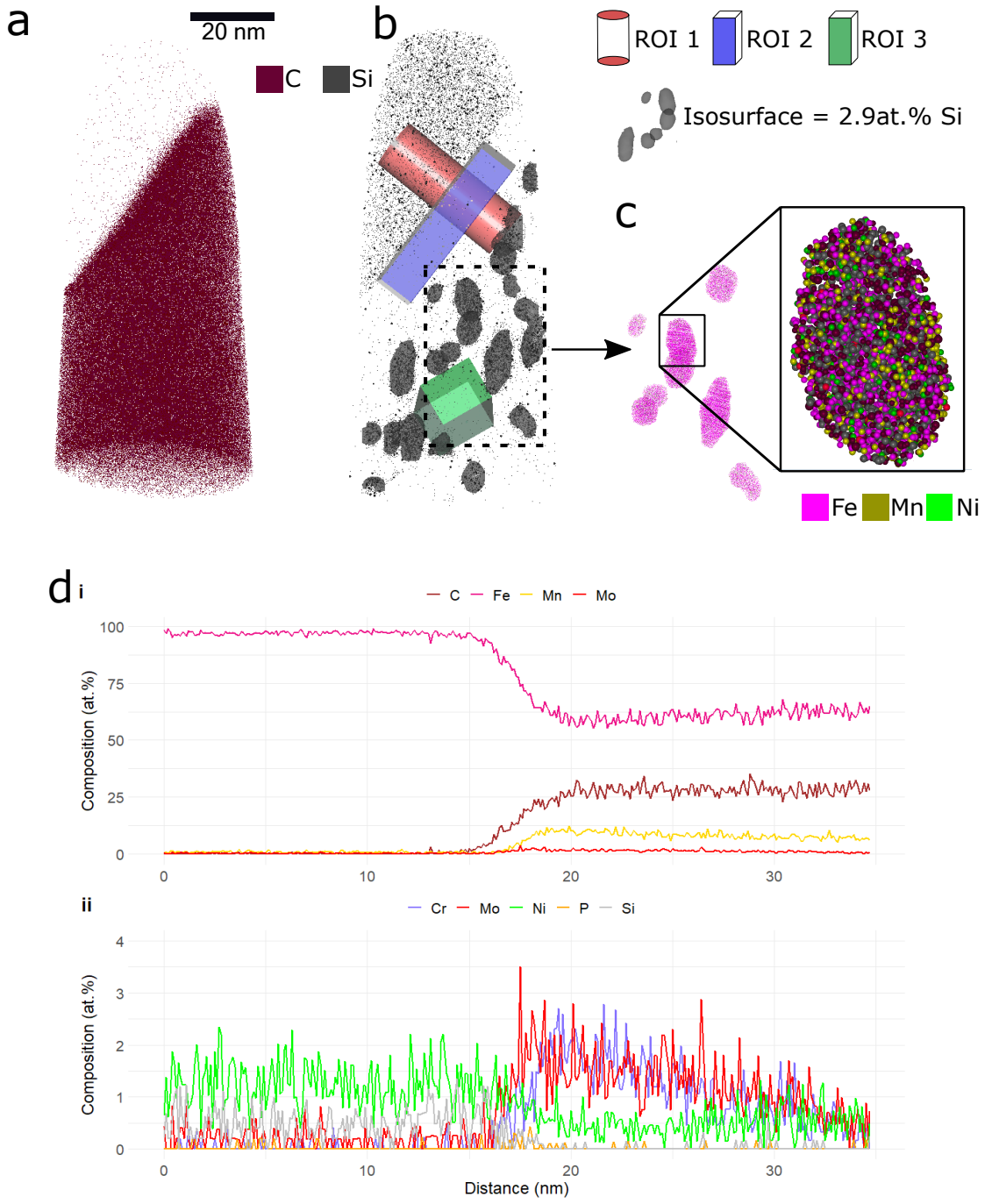

Figure 4.14: APT data indicating the presence of Si-rich secondary precipitates within a carbide in HIPed SA508: a) atom map showing carbon atoms; b) indication of the location of ROIs within a Si-only APT map; c) reconstruction of secondary precipitates for composition analysis (manually selected to avoid those incident with edge of dataset), including magnified image of lone precipitate, with main solute atoms represented as spheres; d) 1D concentration profile running down the long axis of RO1, indicating the compositional change across the carbide interface.

carbide secondary precipitates linked to segregation behaviour induced by irradiation or thermal ageing. On first observation, there is a precipitate-free region near the carbide-matrix interface, with the quasi-spherical secondary precipitates then present further into the carbide. Interestingly, closer examination of these inclusions reveals an apparent regular crystal plane spacing, the exact orientation of which varies slightly between the individual secondary precipitates. However, this may be a feature of the evaporation process, as opposed to a physical insight into plane structure, as the planes are all close to perpendicular with the analysis direction.

By isolating different regions of this dataset, compositional values from the carbide and secondary precipitates could be extracted; the ROIs used for this purpose are labelled in Figure 4.14. Two volumes, one adjacent to the carbide interface and one deeper into the carbide, were chosen in order to encompass both the region devoid of, and that in close proximity with, the secondary inclusions respectively. A selection of the intra-carbide precipitates were extracted using a Si isosurface of 2.9at.%, with a requisite that those chosen were fully encompassed within the reconstructed atom map to avoid edge-effects. The compositions of the ROIs, the secondary precipitates, and the entire carbide region (isolated using a 7at.% carbon isosurface), are shown in Table 4.6 (calculated using Atom

Table 4.6: Compositions of sub-volumes of the carbide containing secondary precipitates in HIPed SA508 APT samples (volumes shown in Figure 4.14). Where the Si content is given, note that for ROIs 2 and 3, this could correspond to N, due to a peak overlap, and the knowledge that Si is generally rejected from carbide phases. Approximate error in compositions of 0.01at.%.

	Fe	C	Si	Ni	Mo	Mn	Cr	P	Cu
ROI 2	58.58	29.27	0.03	0.29	1.38	8.91	1.50	0.02	0.00
ROI 3	62.76	30.59	0.00	0.35	0.30	5.86	0.13	0.00	0.00
Carbide	62.01	28.90	0.22	0.41	0.77	7.02	0.65	0.01	0.00
Secondary Precipitate	66.50	19.49	7.26	2.55	0.30	3.60	0.15	0.02	0.11

Probe Lab per-ion deconvolution [154]). For ROI 2 and ROI 3, the only 'Si' peak identified was at 14 Da, which could mean that the trace amount of species with 14 Da mass-to-charge corresponds to N in the carbide regions (given Si is usually rejected from carbide phases). In contrast, all major Si peaks (14 Da, 14.5 Da and 15 Da) were found in the overall carbide region (including the precipitates) and in the secondary precipitates, strongly reinforcing that it is Si that is found within these features.

The overall carbide composition implies it is of the M_7C_3 type, however this includes the secondary precipitates, and there are also the C loss/gain issues discussed earlier in this chapter. As with other carbides investigated, this one had a higher density in the APT reconstruction, thus is more likely of the cementite phase. If the inclusions are ignored, there is an apparent variation in solute ratio from near the carbide interface (an approximate $M_{12}C_1$ ratio, seen in ROI 2), into the more central carbide region ($M_{10}C_1$- seen in ROI 3). As with those carbides previously studies, Mo lies nearer the carbide interface, before plateauing to a lower concentration value which better reflects its presence within the entirety of the carbide (shown in Figure 4.14d). The secondary precipitates are enriched in Si and Ni and depleted in Fe, Mo, Mn and Cr, relative to the surrounding carbide phase.

4.3 TEM

Supplementary TEM characterisation was performed by Dr Jack Haley (University of Oxford) on three of the four SA508 alloys. Beyond surface imaging techniques previously used, TEM allows further investigation into the influence of manufacturing process on microstructure, on a scale between SEM and APT. From the images obtained from the HIPed, LF and Forging C – shown in Figures 4.15, 4.16 and 4.17 respectively – the overall takeaway is the presence of a largely inconsistent microstructure throughout the samples imaged. This is a result of the sensitivity of SA508 steel to cooling rate. It is not possible to

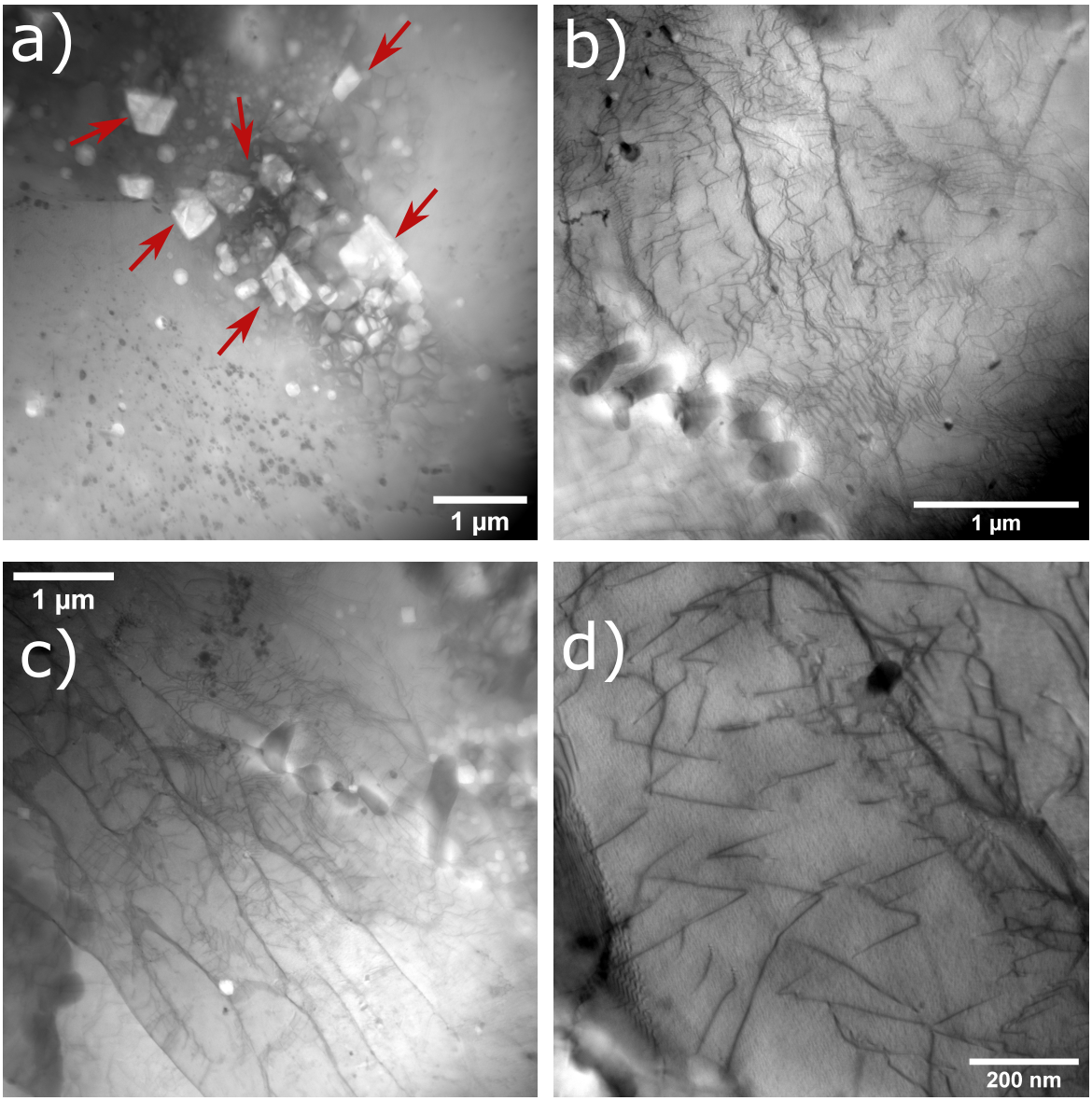

Figure 4.15: Bright field (BF) TEM images of as-received HIPed SA508. Red arrows in a) indicate low contrast, faceted inclusions.

maintain a consistent cooling rate across the entire cross-section of a larger scale forgings.

The steels contain a mixture of course and fine carbides. Larger carbides are commonly found along grain boundaries, often in distinct 'packets', whilst smaller carbides are found both on boundaries and seemingly homogeneously nucleated within grains. The larger carbides at boundaries are often elongated along the boundary line, indicative of preferable

carbide growth along the fast diffusion route provided by increased free volume.

Upon visual inspection there are regions of HIPed material which have both a significantly lower density of grain boundaries and dislocations when compared to the forged samples (see Figure 4.15a). This could correspond to the regions of ferrite grains observed with the optical microscope and SEM. If this is the case then it supports previous suggestions that idiomorphic ferrite contains fewer dislocations than bainite. Furthermore, Figure 4.15a indicates the presence of light contrast inclusions in the vicinity of ferritic grains. The lower contrast, faceted particles are likely the Al, Si and O rich features previously identified using EDS. Whilst Figure 4.15a shows these inclusions as larger (around 500-1000 nm) and cuboid in shape, Figure 4.15c contains a couple which are smaller and spherical. Although it is difficult to clearly discern, the smaller oxide particles in c) seem to lie on grain boundaries, in contrast to the cluster of larger particles in a) which do not have an obvious nucleation site.

In all these images it is difficult to identify the exact nature of the microstructures present. A lath structure typically expected in bainitic steels was not clearly identifiable

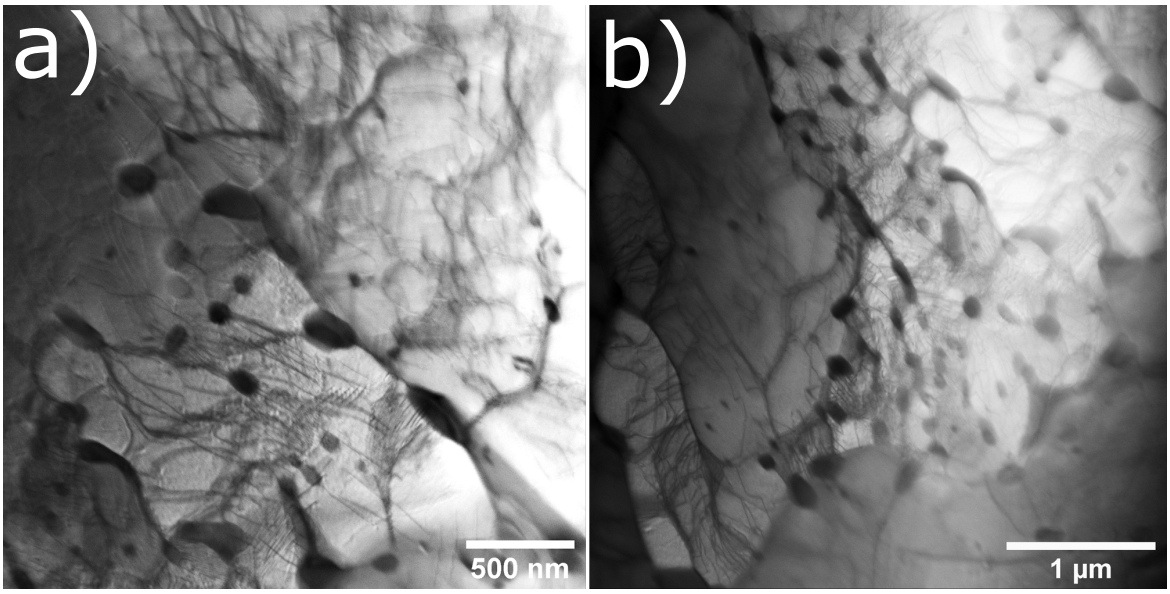

Figure 4.16: Bright field (BF) TEM images of the LF SA508 alloy.

during TEM imaging, nor was a distinction between ferritic and bainitic regions possible (even for the HIPed sample, where ferrite content was significantly higher).

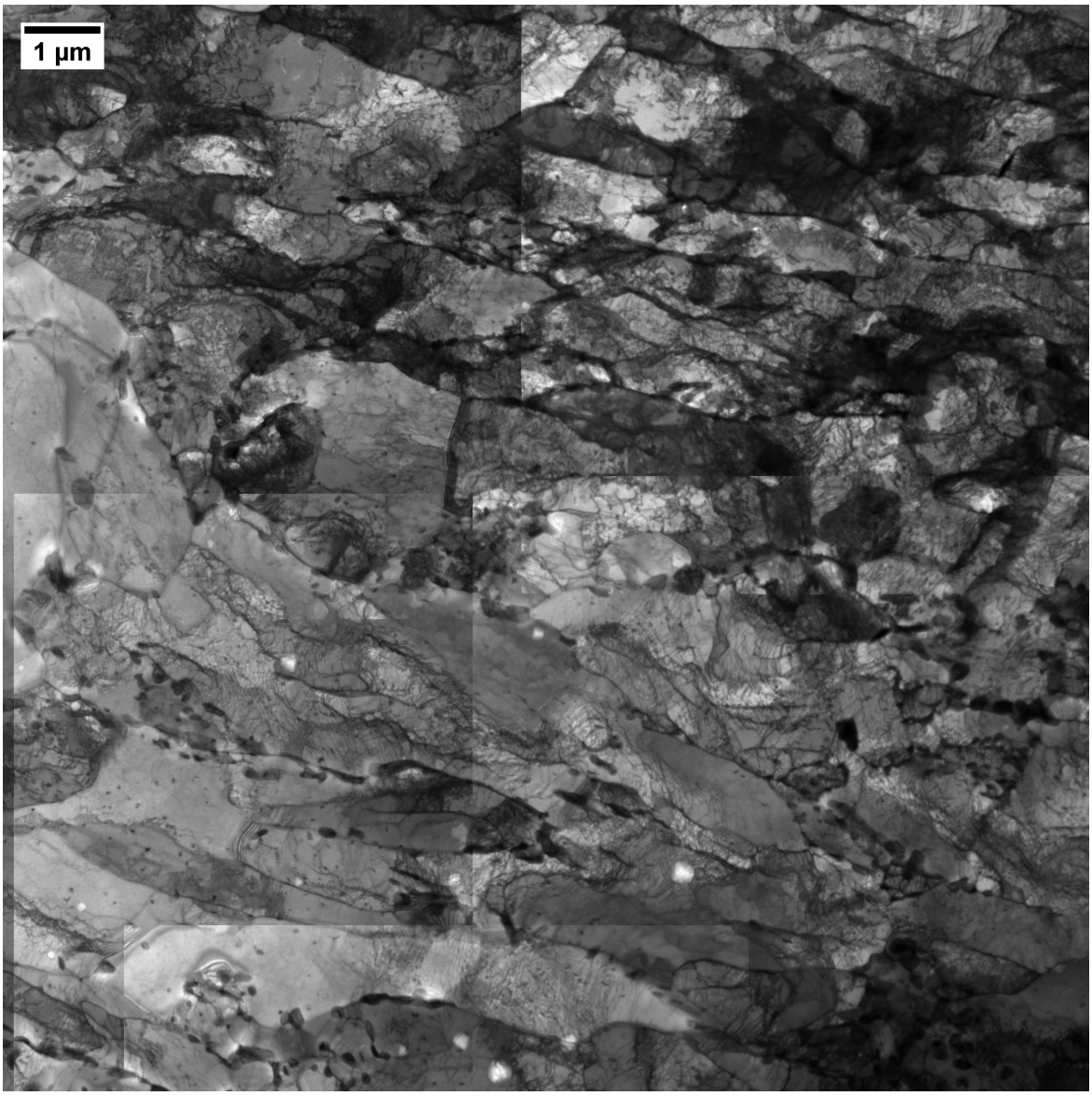

Figure 4.17: Bright field (BF) TEM image montage of the forged C SA508 alloy.

The best impression of the overall forged microstructure is provided by Figure 4.17, showing a digital montage of TEM images of alloy C. Here a directional, banded grain structure is more apparent, reflecting a morphology more in-line with expectations of

lower bainite. Notably there are regions of particularly high dislocation density, perhaps a reflection of its relatively short tempering duration [179].

4.4 Discussion

4.4.1 Characterisation of HIPed SA508

Initially, the most prominent difference between HIPed microstructure and that of the conventionally forged counterparts was thought to be the existence of high fractions of ferrite. This microstructural feature was readily shown via EBSD and optical imaging. However, nanoscale features, such as the Al-enriched particles observed, are most surprising with respect to distinctive microstructural differences. The presence of alumina-type inclusions, as observed with EDS imaging and TEM, is likely a result of the powder-processing. It has been suggested that this manufacturing method gives heightened levels of oxygen [180], as initially shown in the as-received compositional information provided in Section 3.1 and replicated here in Table 4.7, triggering the formation of non-metallic inclusions (in this case, alumina particles).

Given that current understanding suggests elements such as Al and O play little part in radiation-induced embrittlement, the implication is that the formation of these inclusions is likely to be of little consequence to radiation stability of this alloy. However, the addition of Si to these inclusions may have a small impact on the amount of solute available for cluster formation via RED, thus potentially influencing the size and composition of any clusters formed.

Table 4.7: Indication of the compositions in wt.% and at.%, bal. Fe, for the SA508 steel samples, as derived via chemical analysis at Rolls Royce of the as-received samples. For the HIPed sample, the analysis was conducted on the powder form. There are also trace amounts (<0.01wt.%) of S, V, As, Co, Nb, Sn, Ti, Sb and Ca across all samples.

		Composition										
Material		C	Mn	Ni	Si	Mo	Cr	Al	Cu	P	N	O
HIP	wt.%	0.16	1.24	0.86	0.21	0.51	0.10	0.02	0.03	0.012	0.018	0.014
	at.%	0.74	1.25	0.81	0.42	0.30	0.11	0.04	0.03	0.021	0.071	0.048
LF	wt.%	0.17	1.24	0.82	0.26	0.53	0.22	0.02	0.03	0.004	0.007	0.001
	at.%	0.79	1.43	0.78	0.51	0.31	0.24	0.04	0.03	0.007	0.027	0.003
B	wt.%	0.16	1.33	0.78	0.25	0.52	0.17	0.02	0.03	0.002	0.007	0.001
	at.%	0.74	1.34	0.74	0.49	0.30	0.18	0.04	0.03	0.004	0.030	0.007
C	wt.%	0.17	1.33	0.80	0.25	0.52	0.16	0.02	0.03	0.002	0.007	0.002
	at.%	0.79	1.34	0.76	0.49	0.30	0.17	0.04	0.03	0.004	0.026	0.007

4.4.2 Dislocations, interfaces and carbides

Dislocation segregation behaviour in the four steel types was dominated by C and Mo, with some P enrichment at these features also observed. Of the main dislocation segregating elements, shown in Figure 4.7, it is phosphorus which is known to be subjected to the most significant radiation enhanced segregation [181]. If some phosphorus is already lying at linear defects prior to irradiation, there is the potential for the degree of its segregation to be influenced by the extent it is already sitting at low-energy features.

Furthermore, there is clearly pre-existing interface segregation in the HIPed steels; an observation which would also be expected for the forged materials, given the propensity for carbide and grain boundary solute segregation across many types of steels. Whilst lath-type grain boundaries are rarely visible using APT, the higher misorientation angles of PA boundaries gives rise to solute segregation, causing them to be delineated in atom

maps by certain species. Investigation of PA boundaries in the as-received HIPed alloy has shown high levels of Mo, Mn and C enrichment, whilst the relative composition changes at the boundary for P and Cr implies these elements also segregate.

The difference in interface segregation width (i.e. the distance over which segregated solute exhibits a changing concentration profile) between grain boundaries and carbide-matrix interfaces is likely a consequence of the thermodynamic reasoning driving solute diffusion to these interfaces; for grain boundaries, the drive comes from the lowering of energy by sitting in a narrow region of increased free volume, whereas for carbides, the drive is to sit within an entire phase where solubility is greater.

The key takeaway from this section of work is that a nominal composition, provided by macro-scale chemical analysis, is not indicative of the true amount of solute available for cluster formation during irradiation, particularly in the case of Mn (trapped in carbides) and P (significant enrichment at interfaces and dislocations). An awareness of the impact of compositional inhomogeneity is critical in APT studies, where variance in local solute contents plays a large role in dictating the confidence with which small volume cluster and composition data can be presented.

4.4.3 Secondary intra-carbide precipitates

Although only one example of this carbide feature was found, it is impossible to say whether secondary carbide precipitates are unique to SA508 samples formed by HIPing. Their likeness have not previously been documented in as-produced steel, but similar features have been described following the thermal ageing of RPV steel [182]. Given their observation in the as-received condition, they are a clear product of the manufacturing process. It is those species with a low solubility in cementite which have precipitated out of the carbide phase, notably Si, Ni and Fe. Subsequently, assuming these features precipitated

within existing carbides rather than nucleating prior to carbide formation, it is likely that the precipitates form during the ageing process, whilst carbide formation is generally associated with cooling post-austenisation (where there is a large carbon supersaturation).

There is also a significant increase in Cu content in this phase compared to that of both carbides and matrix regions seen in as-received APT samples. The concentration of Cu within the HIPed APT matrix reconstructions was found to very closely match the nominal of 0.03at.%, so this relative increase in the secondary precipitate seems to be localised on this region, and not indicative of wide-spread Cu segregation in general.

4.5 Conclusions

This chapter has demonstrated the influence that different manufacturing processes have on the microstructure of the alloys under investigation. The HIPed sample is the most unconventional in nature, incorporating metallic inclusions and a significant ferrite fraction. There is also local variation within the forged samples, likely the result of carbide distributions.

TEM imaging highlights the inhomogeneity in microstructure present in each of the different alloys, likely a result of inconsistent cooling through the sample sections. Carbides were shown to be present both at grain boundaries and within grains, though those at boundaries were generally larger and often elongated along the boundary line. EDS and TEM analysis also highlighted the presence of Al, Si and O enriched, faceted particles within the HIPed microstructure.

The intra-carbide Si inclusions are not a feature previously identified, and seem unusual in as-produced steel. It is likely that they are a result of the heat treatment pathway HIPed metal is subjected to, prompting intra-carbide precipitation of elements with a low-solubility in the cementite phase.

Chapter 5

Neutron Irradiation of SA508 Steel

This chapter presents work completed on neutron-irradiated SA508 steel samples, as detailed in Chapter 3, Section 3.2. In order to assess the credibility of proposals for novel materials in nuclear construction, investigation into neutron response is critical. This process would be aided by comparison to conventional alloys which are already commonly used in identical applications. For this project, HIPed SA508 Grade 3 Class 1 steel is compared to its forged counterpart, with a focus on the role of polygonal ferrite and the influence of manufacturing route on bainitic hardening. In particular, APT is used in correlation with nanoindentation data to investigate the role played by Mn, Ni and Si enriched defect clusters on irradiation embrittlement. All sample fabrication and nanoindentation was completed at the UKAEA Materials Research Facility, with production of the six-month irradiated samples possible as a result of funding provided by the National Nuclear User Facility (NNUF). This work is also part of a wider collaboration investigating the use of the OPAL reactor at ANSTO, to accelerate and economize neutron-irradiated sample production.

5.1 Three-month HIPed SA508 ANSTO Irradiation

Investigations centring on this sample focused primarily on the role of ferrite and bainite microconstituents on the response of HIPed steel under neutron irradiation. This was the only sample subjected to combined APT, TEM and nanohardness investigations.

Characterisation conducted by TEM in bright-field mode (BF) on the three-month irradiated HIPed sample did not show any visible irradiation-induced damage features; black dots visible on the surface were later identified as surface oxide (Fe_3O_4) by centred dark field (CDF) imaging and selected area diffraction patterns (SADPs). STEM-EDS was also utilised, and suggested an uneven distribution of Mn, Ni and Fe, however, this observation was subtle and no indisputable evidence of cluster formation could be derived. The TEM results and a brief discussion are given in Appendix A.

These initial TEM investigations highlighted the role that atom probe tomography would play in this work, as any more quantified solute cluster analysis would require improved chemical detectability limits.

5.1.1 Nanoindentation

Following the nanoindentation protocol described in 3.8, individual indents could be attributed visually as incident on ferrite or bainite, based on the location of each indent within the EBSD map (see Figure 5.1). It was found that an overlaid image comprised of the 2° and 10° grain boundaries, alongside to band contours, best distinguished the two microconstituent phases.

Hardness readings were acquired up to a displacement depth of 2 μm, enabling hardness vs displacement curves to be plotted, as shown in Figure 5.2a and 5.2c. As expected, the pyramidal indenter tip produced an apparent decrease in hardness with increasing

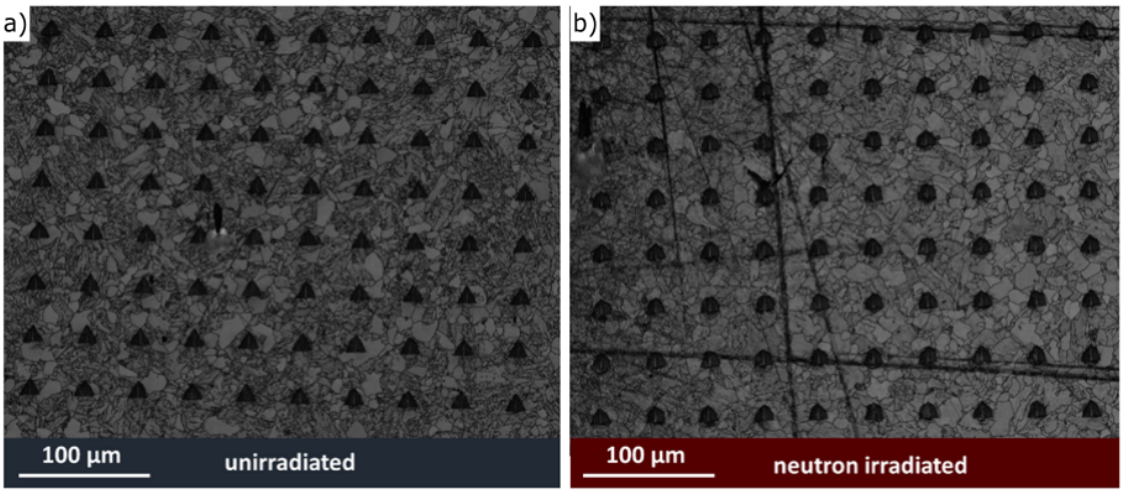

Figure 5.1: EBSD images of nanoindent arrays showing band contrast and grain boundaries (10 degrees and 2 degrees) of: a) unirradiated; b) three-month neutron-irradiated HIP SA508 Grade 3 steel

indentation depth [97].

In order to illustrate both the overall extent of hardening and the relative hardness of the ferrite and bainite respectively, an 'absolute' hardness value for each indent was extracted from the chosen displacement interval of 100 nm-200 nm. Errors are given by the standard deviation in hardness reading within this depth interval (reflecting the distribution in the measured hardness). This indent depth was selected to account for the uncertainty regarding the extent to which microconstituent grain types seen on the surface penetrated into the sample, to minimise the potential influence of neighbouring, sub-surfaces grains.

Neutron irradiation induced a significant amount of hardening in the steel. Figure 5.2b indicates that a similar hardness was reached by bainite and ferrite microstructures after neutron irradiation. The hardening of the irradiated bainite and ferrite grains with respect to depth is shown in Figure 5.2c; this illustrates the average hardness for indents incident on purely ferritic or bainitic grains. Hardness values for each grain type are shown in Table 5.1, with the change in hardness with neutron irradiation illustrated in Figure 5.2d.

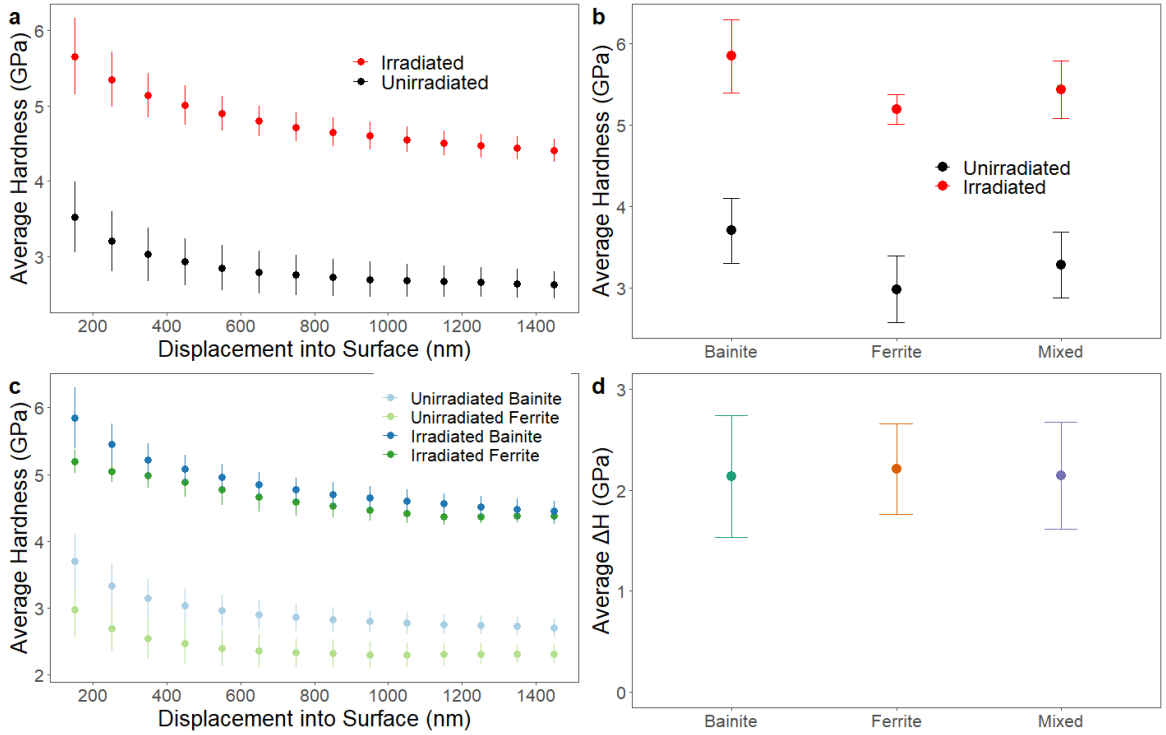

Figure 5.2: Nanohardness data acquired in CSM mode on unirradiated and three-month neutron-irradiated samples: a) average hardness versus indenter displacement into surface; b) average hardness (sampled at 100 – 200 nm displacement interval) of indents incident on bainitic, ferritic or mixed microstructures; c) average hardness of bainitic and ferritic indented grains with depth from the unirradiated and neutron-irradiated samples; d) average irradiation hardening, ΔH, due to neutron irradiation for bainitic, ferritic and mixed bainitic/ferritic grains (sampled at 100 – 200 nm displacement). All error bars shown are equal to ± 1 standard deviation.

Table 5.1: 0.1 dpa neutron-irradiated HIPed SA508 steel hardness (GPa) according to sampled microconstituent.

Grain	AR Hardness (GPa) (3sf)	0.1dpa Hardness (GPa) (3sf)
Bainite	3.70 ± 0.40	5.84 ± 0.45
Ferrite	2.98 ± 0.41	5.19 ± 0.18
Mixed	3.28 ± 0.41	5.43 ± 0.35

5.1.2 Atom probe tomography

APT investigation of the HIPed samples utilised the ferrite/bainite isolation method detailed in Section 3.7.1. For the three-month irradiated sample, APT tips from multiple

ferrite grains were able to be extracted, along with tips produced from bainitic regions adjacent to each grain. This allows both comparison between the grain types and across different ferrite grains.

Clusters were extracted using the maximum separation method; equivalent to core linkage, but where the nearest-neighbour order (NN_{order}) value is 1. This was due to the clusters being small, diffuse and poorly defined within the matrix, meaning a higher order did not improve cluster extraction. For these samples, d_{max} values ranged from 0.4-0.6 nm. Ni, Mn, Si and P species were included as the clustering solute, with the 29 Da peak ranged as Ni. In total, 31 FIB samples were produced and, of these, 18 yielded usable APT datasets; 9 from bainitic regions and 9 from ferritic regions.

Cluster analysis

Evidence of neutron irradiation induced solute clustering was provided by APT. Representative atom maps produced by analysis of site-specific APT samples taken from ferrite and bainite regions are shown in Figure 5.3. All clusters are of the Mn-Ni-Si (MNS) type. Visually, the distribution and nature of clusters in bainite and ferrite appear similar. This apparent

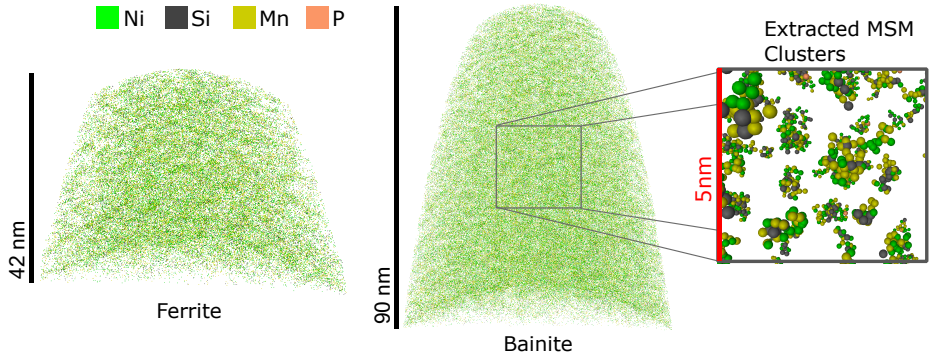

Figure 5.3: Representative APT atom maps indicating the presence of fine-scale neutron irradiation induced solute clusters in SA508 RPV steel ferrite and bainite samples, following neutron irradiation to 100 mdpa at 155°C. An example of the clusters extracted using the Maximum Separation Method is included for the bainite sample, with only the solute atoms shown (for clarity).

uniformity in cluster distribution for bainite and ferrite is supported in further analysis based on cluster composition and volume fraction (V_f). These clusters appear very small in scale, likely owing to this irradiation regime producing a population of clusters at the very early stages of their nucleation and growth evolution. Cluster radii averaged approximately 1 nm, as determined using the assumptions and method detailed in Chapter 3, Section 3.6.

Volume fraction → Figure 5.4 compares the cluster V_f of samples measured from within the bainite and ferrite phases, respectively, against the overall amount of solute atoms (Mn, Ni, Si, P, Cu) contained within each reconstruction. The mean volume fractions are shown in Table 5.2. There appears to be only limited variation between the microconstituents with respect to average cluster V_f. In these samples, greater spread of measured cluster V_f is seen within the bainitic reconstructions. However, this spread in clustering does not seem to affect hardness – assuming there exists some form of correlative effect between the

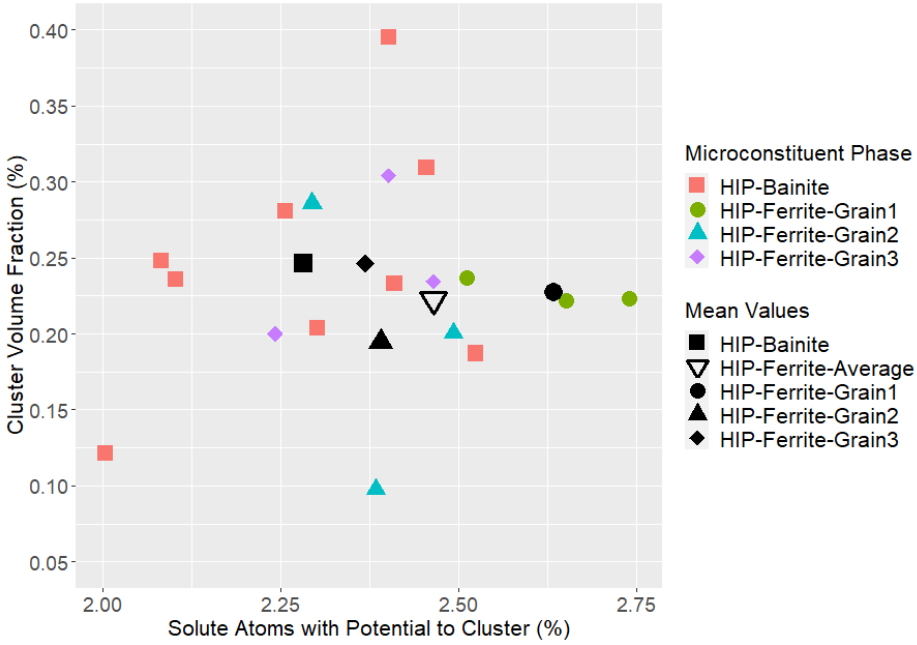

Figure 5.4: Plot detailing the volume fraction of clusters vs the total number of solute atoms involved in clustering present for each atom probe dataset of the three-month irradiated HIPed SA508 steel. The mean values for ferrite and bainite region reconstructions are shown in black.

Table 5.2: Average cluster volume fractions and number densities for the microconstituents in 0.1 dpa irradiated HIPed SA508 steel.

	Average Cluster Volume Fraction (%)(3sf)	Average Cluster Number Density (m^{-3}) (3sf)
Bainite	0.246 ± 0.073	$4.07\times10^{24} \pm 1.46\times10^{24}$
Ferrite	0.223 ± 0.055	$3.73\times10^{24} \pm 1.04\times10^{24}$

number of clusters and the observed hardness - since the clusters were observed within very small areas therefore giving large variance, whilst hardness tests are taken over a larger area and therefore any small area deviations are averaged out.

The generally lower clustering-solute content in bainitic samples is shown to coincide with a reduced Mn content within the tip, as shown in Figure 5.5. In this plot, Mn content is shown relative to the tip Ni content, as Ni concentration across the tips remain relatively constant (approximately that of the nominal alloy Ni composition), whereas Mn varies such as to be either higher or lower than the Ni content.

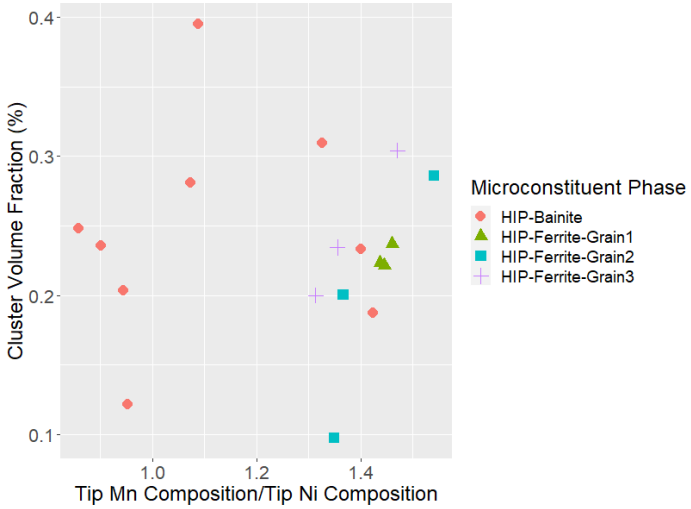

Figure 5.5: Plot indicating the relationship between the cluster volume fraction observed in samples and the relative Mn content, with respect to Ni, for the three-month irradiated HIPed ANSTO samples.

Cluster compositions → The measured distribution of cluster compositions taken from each of the APT datasets are shown in Figure 5.6; Fe has not been included in the composition calculations. It is apparent that there is greater consistency in compositions within the ferrite samples, mirroring that seen with the volume fractions.

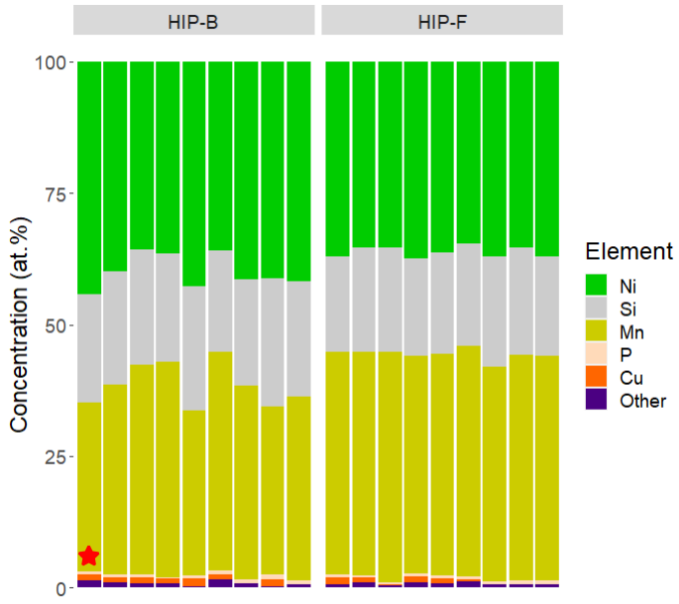

Figure 5.6: Plot showing the composition of clusters (averaged) in each APT dataset of 0.1 dpa HIPed SA508 steel. The red star indicates Run 8834, which contains a carbide and is discussed below.

An alternative visualisation of the cluster compositions can be seen in Figure 5.7. Here, the average cluster composition obtained from each APT dataset is shown, with respect to solute known to contribute to clustering (Mn, Ni, Si, P and Cu). In this format, the ratios of each of the key clustering elements can be better compared between datasets and with respect to the thermodynamically-predicted G and Γ_2 phases. From this, it can be noted that the compositions do fall near the proposed 'G' and 'Γ_2 phases ($Ni_{16}Mn_6Si_7$ and Ni_3MnSi respectively) [63], but with higher Mn contents. The influence, if any, of Cu and P on the observed solute ratios can also be determined, due to them often being of interest in RPV steel clustering. However, it is clear from Figure 5.7 that there is no obvious compositional

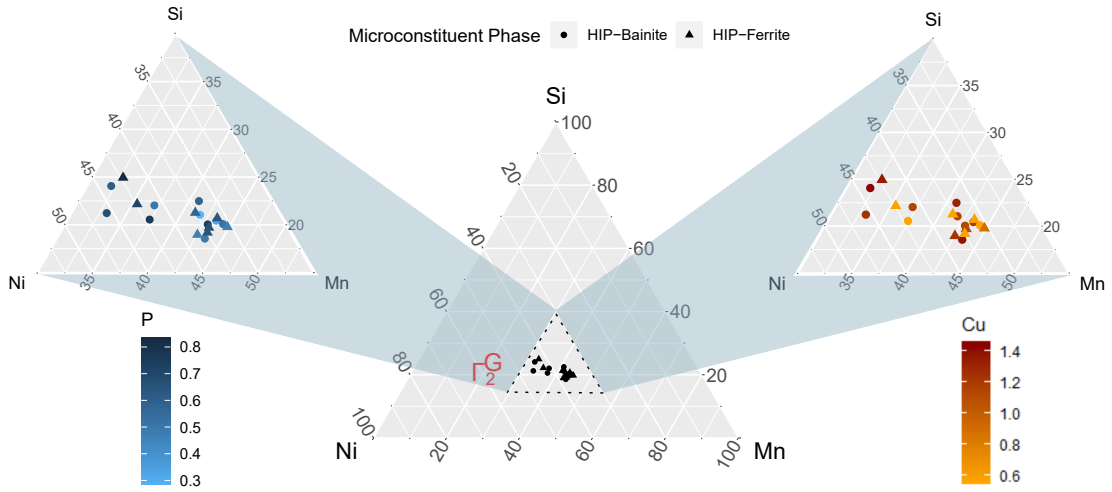

Figure 5.7: Ternary diagrams showing the average cluster compositions within APT samples taken from 0.1 dpa HIPed ferrite and bainite grains. The compositions of the proposed G and Γ_2 phases are denoted in red. The close-up ternary regions indicate the P (left) and Cu (right) concentrations.

influence of these two elements with regards to the Mn:Si:Ni ratio of clusters in this case.

APT tip matrix compositions

The average matrix compositions for the ferritic and bainitic APT reconstructions are shown in Table 5.3. This data was obtained by extracting the clustered solute from each APT tip (following cluster analysis) and then deconvolving the composition of the remaining matrix volume. The relative lower overall tip Mn concentration of the bainite samples translates to both a reduced amount of Mn in the matrix and in the clusters themselves.

5.2 Three-month Forged SA508 ANSTO Irradiation

For the forged samples, work focused on the role of local variation in chemistry and microstructure, typical of that seen in forged steel samples. APT was particularly useful for this investigation, as it allows differences across very small volumes to be observed.

Table 5.3: Extracted average matrix and cluster compositions for 0.1 dpa HIPed SA508 steel.

	Average Composition (at.%)						
	Fe	Mn	Ni	Si	P	Cu	Other
Ferrite Matrix	97.33 ±0.31	1.06 ±0.08	0.72 ±0.06	0.39 ±0.02	0.01 ±0.00	0.03 ±0.01	0.45 ±0.12
Ferrite Clusters	—	42.40 ±4.95	36.18 ±2.56	19.49 ±1.60	0.53 ±0.15	0.56 ±0.50	0.73 ±0.22
Bainite Matrix	97.61 ±0.28	0.85 ±0.16	0.75 ±0.04	0.38 ±0.02	0.01 ±0.00	0.02 ±0.01	0.36 ±0.13
Bainite Clusters	—	36.21 ±3.53	39.94 ±2.46	21.56 ±1.66	0.63 ±0.13	0.89 ±0.49	0.77 ±0.35

5.2.1 Nanoindentation

The nanoindentation data for the as-received and three-month irradiated (0.1 dpa) LF samples is presented in Figure 5.8. As with the previous specimens, hardness data was taken from the 100-200 nm displacement region. For the 0.1 dpa forged SA508 Grade 3 Class 1 steel, an average hardness of 5.27 ± 0.40 GPa was determined, which corresponds

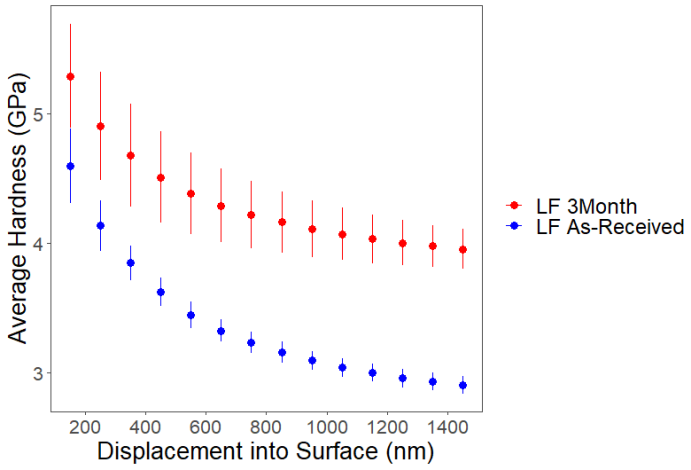

Figure 5.8: Variation of measured nanohardness with indent depth for the as-received and 0.1 dpa forged SA508 samples. The error bars indicate ± 1 standard deviation.

to an approximate hardening of 0.69 ± 0.49 GPa.

5.2.2 Atom probe tomography

For the forged 0.1 dpa ANSTO samples, 12 FIB-fabricated tips were run in the atom probe. Of these, 6 yielded usable data.

Cluster analysis

Of the six APT datasets from the three-month irradiated forged sample, five contained MNS clustering. Interestingly, one dataset showed no evidence of segregation behaviour, either upon visual inspection or following cluster analysis. Figure 5.9 shows an example of the clusters extracted from one of the datasets. As with the three-month irradiated HIPed sample, cluster analysis used the MSM (NN_{order} = 1), as use of higher orders missed the small, dilute clusters identifiable in this low-dose irradiation. D_{max} values ranged from 0.5-0.56 nm, and N_{min} ranged from 16-20 atoms.

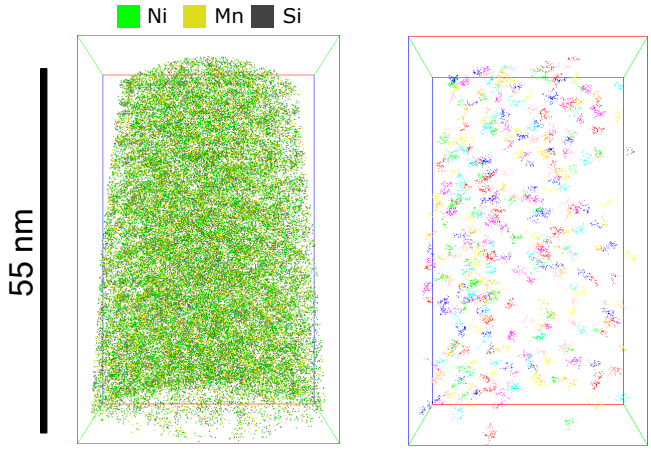

Figure 5.9: APT maps of 0.1 dpa forged SA508 Grade 3 Class 1 steel; Mn, Ni and Si atoms shown (left) alongside clusters extracted from cluster analysis (right).

Volume fraction → Again, all clusters found were of the Mn-Ni-Si type. The average cluster V_f and number density (N_d) across the five samples containing clusters is shown in Table 5.4. Fe was not included in cluster calculations. The spread in V_f with clustering solute was also investigated, however, as was seen in the HIPed samples, the bainite showed a lot of variation in measured clusterable solute without revealing any definitive link between the amount of Mn, Ni, Si and P and the cluster V_f for each tip.

Table 5.4: Average cluster volume fractions and number densities for the microconstituents in 0.1 dpa irradiated forged SA508 steel.

Average Cluster Volume Fraction (%) (3sf)	Average Cluster Number Density (m^{-3}) (3sf)
0.283 ± 0.065	$4.40\times10^{24} \pm 1.12\times10^{24}$

Cluster compositions → As with the HIPed samples, the clusters formed were very small, again indicating an early stage in MNS cascade-cluster-complex growth. The average cluster compositions for each dataset are shown in Figure 5.10. Each solute concentration remains relatively steady across the five datasets. Mn and Ni alternate in which is the majority element per sample (maximised at around 40at.%), with a reduction in Si not consistently corresponding to an increase in one of Ni or Mn (rather it appears random).

Tip compositions

A better understanding of the changing cluster compositions could come from comparison to the tip compositions, given that forged samples have been shown to exhibit a large range in solute content in the as-received APT samples; likely a consequence of the more irregular substructure of bainite and large variance in local chemistry in forged samples (a result of the irregular, imperfectly-controlled cooling process).

For the forged samples, a closer look at the influence of tip chemistry on cluster formation

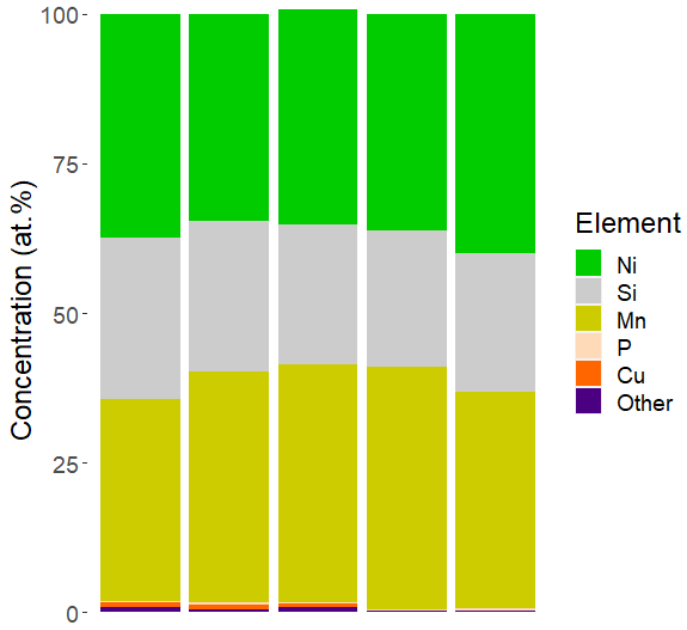

Figure 5.10: Plot showing average cluster compositions for each APT dataset obtained for the three-month irradiated forged SA508 sample.

can be obtained by investigating any link between the cluster ratios observed in the tip and those in the clusters it contained. By calculating the average ratio of a matrix of element pairs (Mn:Ni, Mn:Si, Ni:Si), the relative amounts of each element within both the clusters and the overall tip can be determined. Subsequently, the relative difference between the ratio for each dataset and the average ratio across all samples could be determined, allowing the influence of any deviation from the average solute ratio in the tip to be linked to the observed variance within the clusters. For example, where the Mn:Ni relative difference is negative, there are more Ni atoms in that cluster population compared to the average; accordingly, this can be linked to the tip as a whole also containing relatively more Ni.

Figure 5.11 shows the results of these calculations, plotted as bar charts for visual clarity. As expected, where a set of clusters is diminished in a particular species, this corresponds to the tip containing less of that species. Interestingly, the relative amount of Mn and

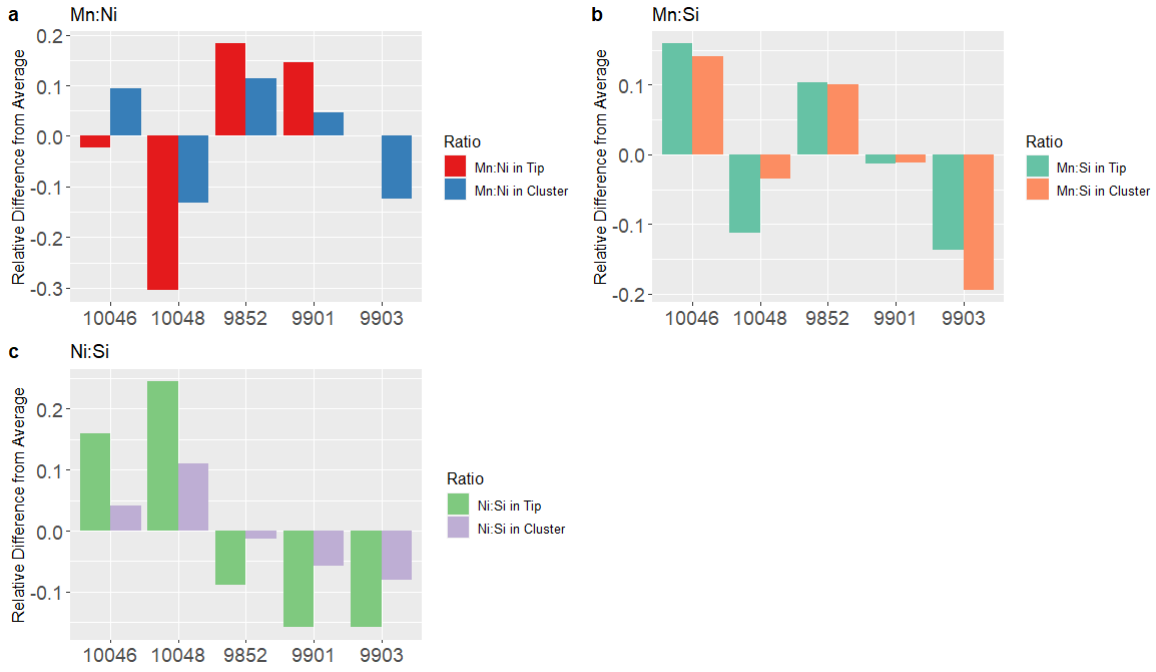

Figure 5.11: Plot showing volume fraction of clusters vs the total number of solute atoms involved in clustering present for each atom probe dataset (represented by the experiment number on the x-axis) of the three-month irradiated forged SA508.

Si within the tip seems to have the strongest influence on the relative amount of those elements which are involved in cluster formation.

The tip matrix compositions were extracted from those APT tips which contained clusters, in addition to the tip composition for Run 10043, in which no clusters were observed. This data is shown in Table 5.5. The formation of clusters translates into the overall tip composition being higher than that of the extracted matrix for those elements integrated into clusters.

Comparing Run 10043 to the other APT runs, there is not any notable reduction in clusterable solute, which would potentially explain the lack of clustering in this sample. Hence, the extent of clustering does not appear to be tied to the local composition in this case, rather there is another potential variable playing a role in randomising whether clustering does or does not occur in specific volumes. One postulate is the local point

Table 5.5: Extracted average matrix and cluster compositions for 0.1 dpa forged SA508 steel

	Average Composition (at.%)						
	Fe	Mn	Ni	Si	P	Cu	Other
Matrix (clustered Runs)	97.12 ±0.30	1.08 ±0.16	0.79 ±0.06	0.57 ±0.05	0.01 ±0.00	0.02 ±0.00	0.42 ±0.07
Clusters	—	37.64 ±2.47	36.76 ±1.86	24.32 ±1.57	0.24 ±0.07	0.51 ±0.32	0.53 ±0.28
Whole Tip (clustered Runs)	96.52 ±0.40	1.19 ± 0.16	1.01 ±0.14	0.63 ±0.03	0.01 ±0.00	0.02 ±0.01	0.54 ±0.37
Matrix (Run 10043)	96.04	1.45	1.04	0.67	0.01	0.02	0.78

defect density; the vacancies required for RIS may have been absorbed by other defect sinks in the vicinity, rather than forming the stable MD regions or solute-vacancy complexes needed to promote segregation.

5.3 Six-month HIPed SA508 ANSTO Irradiation

The six-month irradiation produced samples with 0.2 dpa of damage. It is expected that more damage corresponds to a higher level of hardening, with an increase in the extent of segregation seen in the APT samples. As with the three-month irradiation samples, the behaviour of the ferrite and bainite grains under irradiation will be compared.

5.3.1 Nanoindentation

Nanoindentation of the six-month irradiated (0.2 dpa) HIPed sample mirrored that completed on the three-month irradiated sample; again, indents were identified as lying within ferrite, bainite or mixed grains, and a displacement interval of 100-200 nm was chosen to give the hardness change value. Figure 5.12 shows the bainite, ferrite and mixed

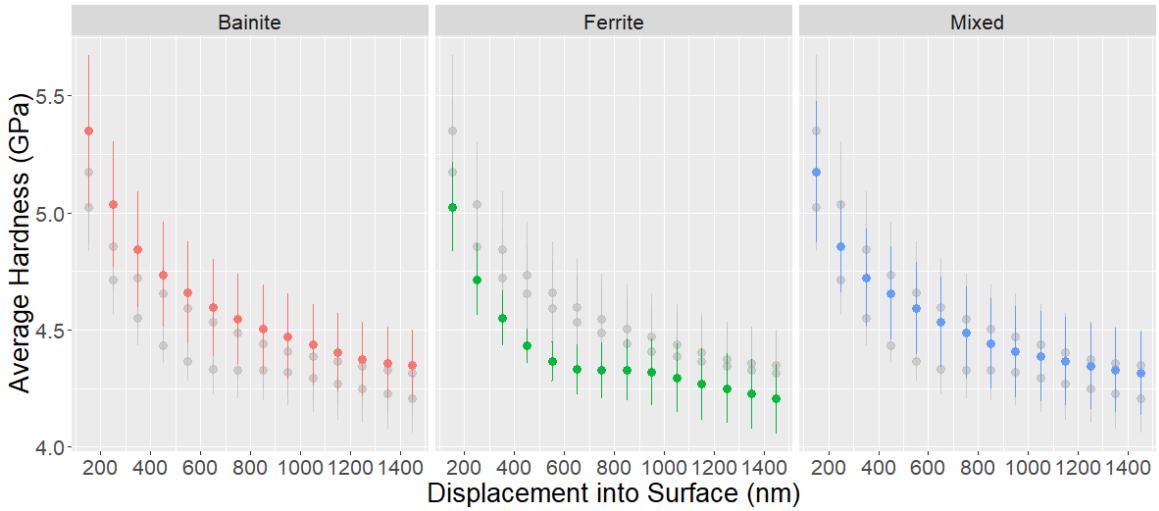

Figure 5.12: Variation of the measured nanohardness with indentation depth for the 0.2 dpa HIPed SA508 steel, for each microconstituent phase. In each plot the highlighted (bright coloured) points represent the data from the named phase type, whilst the grey points represent the data from the other two indent locations. This allows easier comparison between the microconstituents. The error bars indicate ± 1 standard deviation.

grain results, as a function of displacement depth. The 0.2 dpa irradiation produced the following average hardness values for each of the microconstituent phases at 100-200 nm indentation depth: ferrite, 5.03 ±0.19 GPa; bainite, 5.35 ±0.33 Gpa; mixed ferrite and bainite, 5.17 ±0.30 GPa.

Notably, these values are lower than those produced following the three-month irradiation, which is unexpected. It may be physical, but also could be a consequence of the uncertainties associated with the nanoindentation process. There is an overlap in the 0.1 dpa and 0.2 dpa values when errors are accounted for, thus it is difficult to determine whether the measured hardness decreased or remained approximately the same. Both possible scenarios deviate from what would be expected for the irradiation of RPV steels, especially given the increase in cluster V_f for these samples, discussed below.

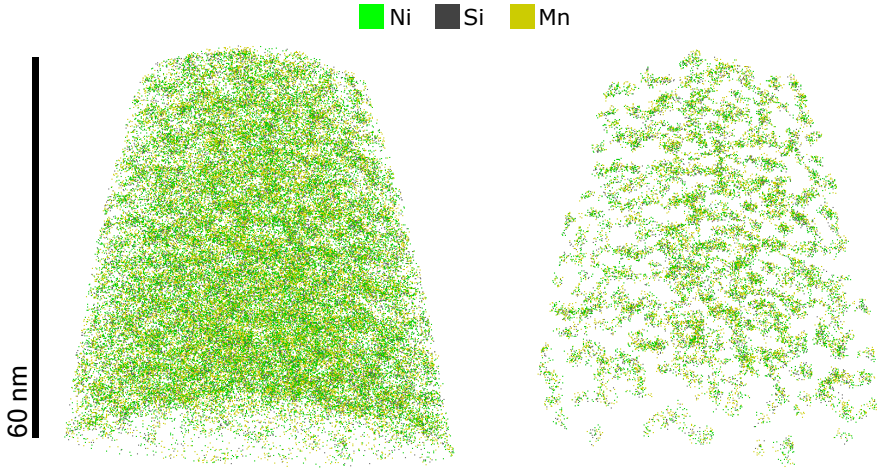

Figure 5.13: Representative APT atom maps of neutron irradiation induced solute clusters extracted from site-specific RPV steel samples neutron-irradiated to 0.2 dpa at 155°C. Left is the atom map prior to cluster analysis, right is a Mn,Ni and Si atoms identified as being part of clusters.

5.3.2 Atom probe tomography

In total, 30 APT FIB tips were produced, however only 13 yielded datasets larger than 1 million atoms. Usually a lower limit of 2 million ions was used to delineate usable APT data, but, given the sample loss encountered, smaller datasets were used in order to improve statistics.

Targeting the different microconstituent grains yielded 8 samples from ferrite and 5 from bainite.

Cluster analysis

The Mn-Ni-Si clusters seen in the 0.1 dpa samples were again observable in the 0.2 dpa HIPed APT atom maps. Again, the clusters are not visually very defined, and, rather, comprise of a high number of diffuse, higher solute density regions. In this case, MSM parameters ranged between 0.5-0.58 nm for d_{max} and 18-26 atoms for N_{min}.

Volume fraction → Examples of clusters are shown in Figure 5.13. On first impression, they appear larger than in the 0.1 dpa samples, although, again there appears to be no definitive difference in clustering between bainite and ferrite. Table 5.6 gives the average cluster N_d and V_f values for each grain type, for each dpa of neutron-irradiated HIPed steel.

Within uncertainty, the difference between 0.2 dpa and 0.1 dpa neutron-irradiated HIPed SA508 is both a higher number (N_d) and increased volume (V_f) of irradiation-induced clustering. On average, the N_d of MNS clusters approximately doubles with the doubling of irradiation duration, implying a quasi-constant rate of cluster nucleation across both irradiation durations. However, the V_f of clusters increases by more than a factor of two, suggesting the growth of existing clusters contributes a greater volume of cluster solute than the nucleation of new clusters.

As with the three-month irradiated samples, there is no appreciable difference in the extent of clustering seen in ferrite and bainite. Figure 5.14 indicates the variation of cluster V_f with the fraction of atoms within the total APT tip volume which are known to act as clustering solute (Mn, Ni, Si, P and Cu). Bainitic grains again display a greater variance in the amount of solute available for cluster formation. The ferrite samples appear to show a more positive correlation between the amount of solute atoms able to cluster and the V_f of clusters, both compared to the 0.2 dpa bainite samples and to that seen in the

Table 5.6: Average cluster volume fractions and number densities for the microconstituents in 0.2 dpa irradiated HIPed SA508 steel.

	Average Cluster Volume Fraction (%) (3sf)	Average Cluster Number Density (m^{-3}) (3sf)
0.1 dpa Bainite	0.246 ± 0.073	$4.07\times10^{24} \pm 1.46\times10^{24}$
0.1 dpa Ferrite	0.223 ± 0.055	$3.73\times10^{24} \pm 1.04\times10^{24}$
0.2 dpa Bainite	0.659 ± 0.055	$7.38\times10^{24} \pm 1.11\times10^{24}$
0.2 dpa Ferrite	0.701 ± 0.128	$7.12\times10^{24} \pm 1.09\times10^{24}$

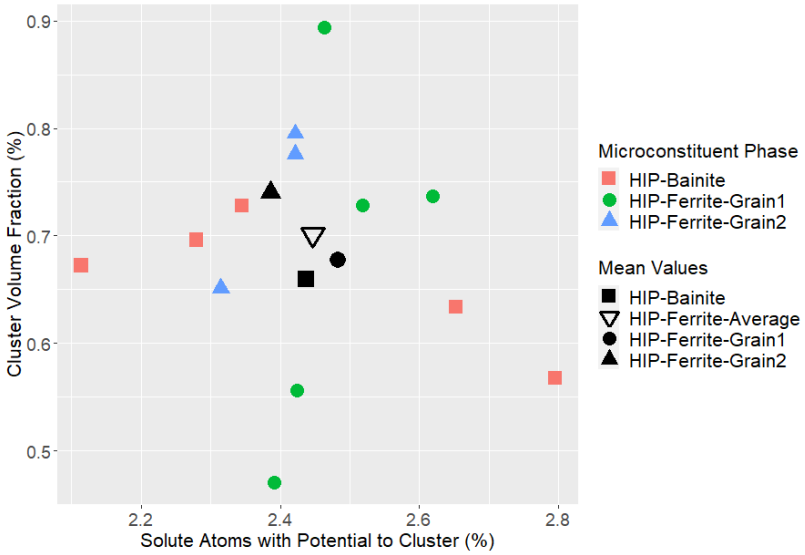

Figure 5.14: Plot detailing the volume fraction of clusters vs the total number of solute atoms involved in clustering present for each atom probe dataset of the 0.2 dpa HIPed SA508 steel. The mean values for ferrite and bainite region reconstructions are shown in black.

ferrite data from the 0.1 dpa HIPed tips.

In contrast to the 0.1 dpa samples, here it is the ferrite tips which produce a greater spread in V_f, even within the same grain. Thus, differing to what could be implied from the three-month irradiated HIPed APT reconstructions, the extent of clustering across the different microconstituents does appear random, with the potential sources of nucleation and the rate of growth having no discernible link to the grain type.

Cluster compositions → Figure 5.15 indicates the fraction of each solute type within the clusters present in each APT tip. In this case, mirroring that seen in the 0.1 dpa data, the amount of Mn in the bainitic samples is lower than that in the ferritic clusters, likely a result of greater proximity to carbides. As with the 0.1 dpa HIPed samples, any variation in P and Cu within the clusters did not appear to be influenced by the microconstituent phase. Generally, there is a reduction in the fraction of non-MNS solute within the clusters, indicating that the diffusion of Mn, Ni and Si as a contribution to cluster growth dominates

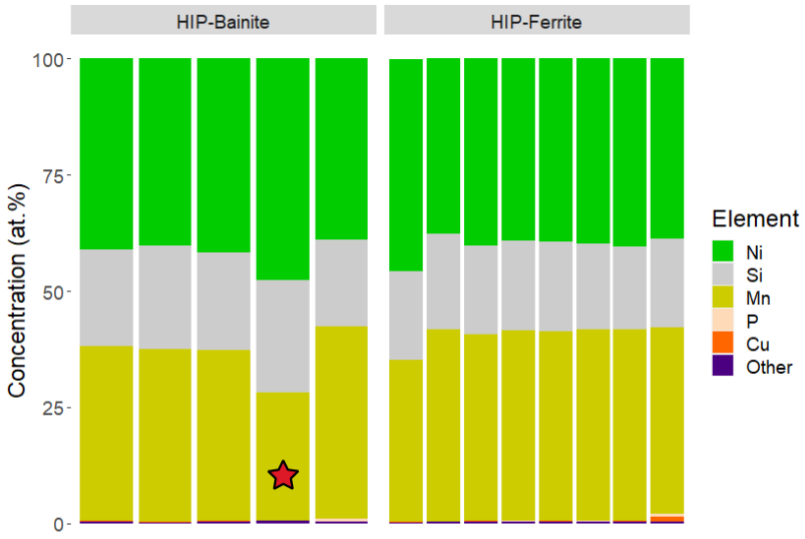

Figure 5.15: Plot showing the composition of clusters (averaged) in each APT dataset of 0.2 dpa HIPed SA508 steel. Star denotes the average solute concentration of clusters found in Run 10643, which contained a carbide.

as clusters grow.

Given the increased length of irradiation for these samples, it is likely that the local chemistry has had more time to influence the make-up of the clusters. Focusing on the key species, Figure 5.16 indicates how the tip composition correlates to cluster composition for these samples. As indicated by a significant p-value (<0.01), for the 0.2 dpa HIPed samples the correlation between tip Mn content and the Mn content of the clusters is pronounced.

APT tip matrix compositions

For reference when considering the cluster compositions provided for the 0.2 dpa HIPed samples, the APT tip matrix compositions are shown in Table 5.7. Compared to the 0.1 dpa HIP samples, the non-clustered matrix contains less Mn, Ni, and, to a lesser extent, Si. This illustrates how a greater fraction of these elements are involved in clustering at the higher dose.

5.4 Six-month Forged SA508 ANSTO Irradiation

The forged SA508 Grade 3 Class 1 steel was subjected to 0.2 dpa of damage after the six-month neutron irradiation. Nanoindentation and APT analysis was conducted in order

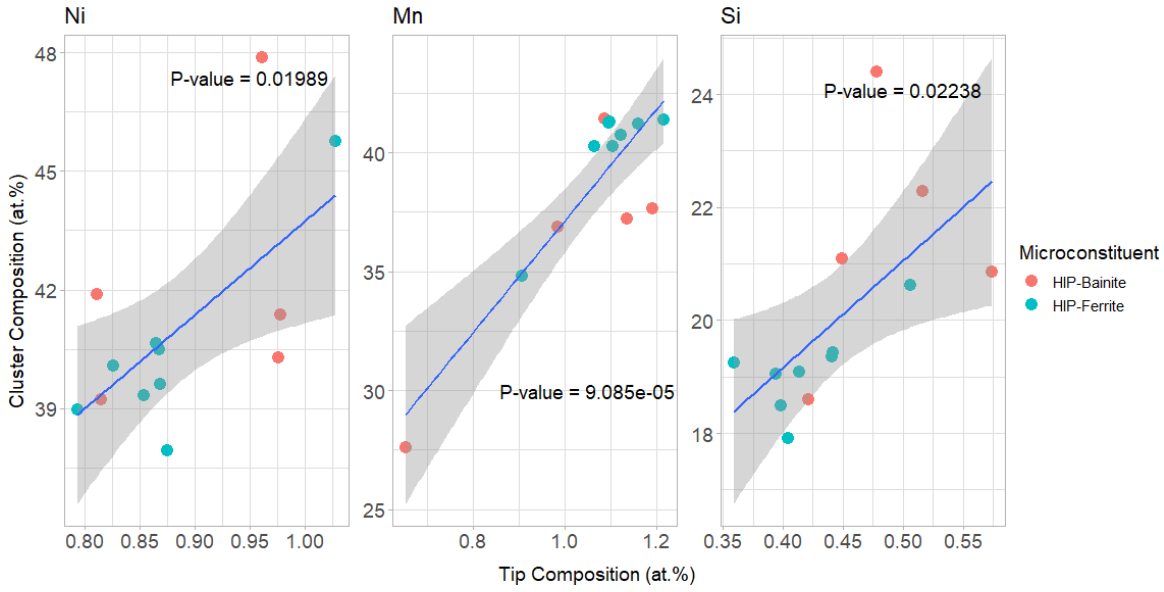

Figure 5.16: Plot correlating the tip composition with cluster composition in the 0.2 dpa HIPed sample.

Table 5.7: Extracted average matrix and cluster compositions for 0.2 dpa HIPed SA508 steel.

	Average Composition (at.%)						
	Fe	Mn	Ni	Si	P	Cu	Other
Ferrite Matrix	97.84 ±0.18	0.82 ±0.06	0.58 ±0.08	0.30 ±0.04	0.02 ±0.00	0.02 ±0.00	0.43 ±0.05
Ferrite Clusters	—	39.98 ±2.05	40.19 ±2.20	19.07 ±0.74	0.11 ±0.18	0.23 ±0.33	0.40 ±0.07
Bainite Matrix	97.75 ±0.41	0.77 ±0.17	0.61 ±0.08	0.36 ±0.07	0.01 ±0.00	0.02 ±0.00	0.49 ±0.12
Bainite Clusters	—	35.99 ±4.58	41.95 ±2.97	21.35 ±1.88	0.15 ±0.23	0.13 ±0.03	0.43 ±0.10

to give insight into the influence of this dose on material hardness and Mn-Ni-Si cluster formation, also allowing comparison with the lower dose forged sample and with the bainitic region of the 0.2 dpa HIPed sample.

5.4.1 Nanoindentation

The nanoindentation results for the six-month irradiated forged ANSTO sample reveal an increase in hardness across all indentation depths (shown in Figure 5.17). The average hardness in the near-surface displacement interval of 100-200 nm was 6.11 ± 0.38 GPa. This gives a change in hardness of 0.82 ± 0.55 GPa between the three-month and six-month irradiation at the same displacement.

5.4.2 Atom probe tomography

For the forged samples, there were 9 successful (>1 million ions) runs out of 20 APT tips produced. Again, these samples tended to fracture earlier than usual into APT analysis, hence the reduction in the lower limit for usable reconstruction sizes.

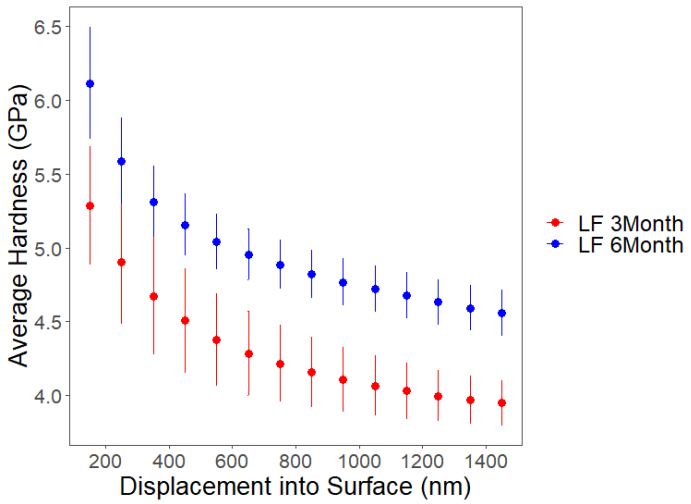

Figure 5.17: Variation of measured nanohardness with indent depth for the 0.1 dpa and 0.2 dpa forged SA508 samples. The error bars indicate ± 1 standard deviation.

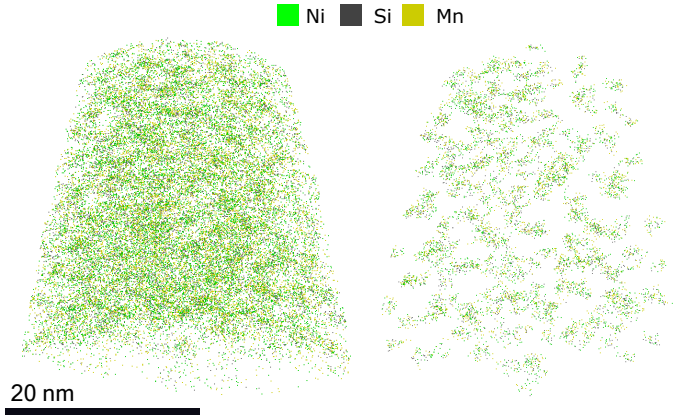

Figure 5.18: APT maps of 0.2 dpa forged SA508 Grade 3 Class 1 steel; Mn, Ni and Si atoms shown (left) alongside clusters extracted from cluster analysis (right).

Cluster analysis

Cluster analysis used the Maximum Separation Method, with d_{max} values ranging from 0.52-0.56 nm and N_{min} values between 16 and 25 atoms. The appearance of the clusters matched that seen in the HIPed 0.2 dpa reconstructions.

Figure 5.18 shows a typical 0.2 dpa, forged APT atom map, with the extracted clusters produced through application of MSM.

Volume fraction → The extent of clustering seen in the six-month irradiated forged samples is higher than that seen in the three-month irradiated material. Table 5.8 gives the average V_f and N_d data across those APT maps containing clusters, with the values from the 0.1 dpa LF samples included for reference. There is an approximate doubling of V_f with doubled dose, whilst N_d increases by just under a factor of two. Although difficult to fully determine, due to the spread of values obtained, this reduced increase in N_d could correspond to the second three months of radiation contributing more to cluster growth than further nucleation. This generally mirrors that seen in the HIPed 0.2 dpa samples, where the relative V_f increased more than the N_d.

Table 5.8: Average cluster volume fraction and number density for 0.1 dpa and 0.2 dpa forged SA508 steel.

	Average Cluster Volume Fraction (%) (3sf)	Average Cluster Number Density (m^{-3}) (3sf)
0.1 dpa	0.283 ± 0.065	$4.40\times10^{24} \pm 1.12\times10^{24}$
0.2 dpa	0.570 ± 0.118	$6.27\times10^{24} \pm 1.45\times10^{24}$

Unlike in the 0.1 dpa forged samples, here there is a clearer link between the amount of solute able to cluster (Mn, Ni, Si, P and Cu) within the entire tip volume and the fraction of tip that is clusters, as shown in Figure 5.19.

Cluster compositions → The average cluster compositions for each dataset are shown in Figure 5.20. With increasing irradiation dose, the composition of the clusters is further dominated by Mn, Ni and Si, with the fraction of other solutes reduced in comparison to the 0.1 dpa condition.

As with the 0.1 dpa forged samples, the influence on local chemistry was analysed by

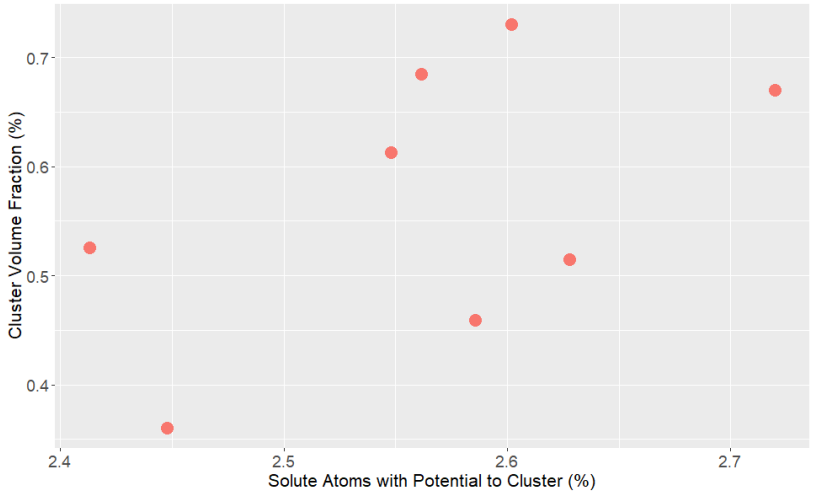

Figure 5.19: Plot detailing the volume fraction of clusters vs the total number of solute atoms involved in clustering present for each atom probe dataset of the six-month irradiated forged SA508 steel.

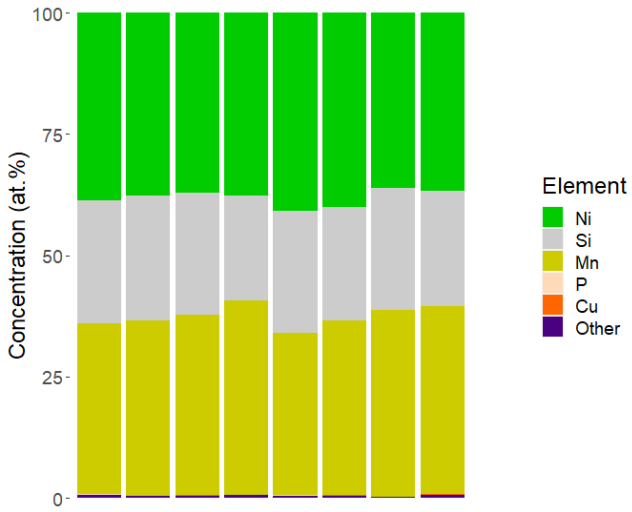

Figure 5.20: Plot showing the composition of clusters (averaged) in each APT dataset of 0.2 dpa forged SA508 steel.

determining the relative difference between the key solute ratio (Mn:Ni, Mn:Si and Ni:Si) of each tip and the average of each ratio across all APT samples, for both the overall tip composition and that of the clusters. Figure 5.21 shows these relative differences. Compared to 0.1 dpa forged samples (Figure 5.11), the relative difference in the solute ratios of the clusters corresponds well to that for the tips for all three solute permutations. This suggests that deviation from the average solute ratios in the tips translates more strongly to any deviation from average in the clusters. This implies that local composition is having a greater influence on cluster solute content as irradiation time increases for these samples, which is in agreement with the results presented for the 0.2 dpa HIPed steel.

APT tip matrix compositions

Cluster compositions are compared to the matrix composition (with clustered atoms removed) in Table 5.9. As with the 0.2 dpa HIPed samples, there is a reduction in Mn, Ni and Si in the tip matrices compared to the 0.1 dpa forged matrices.

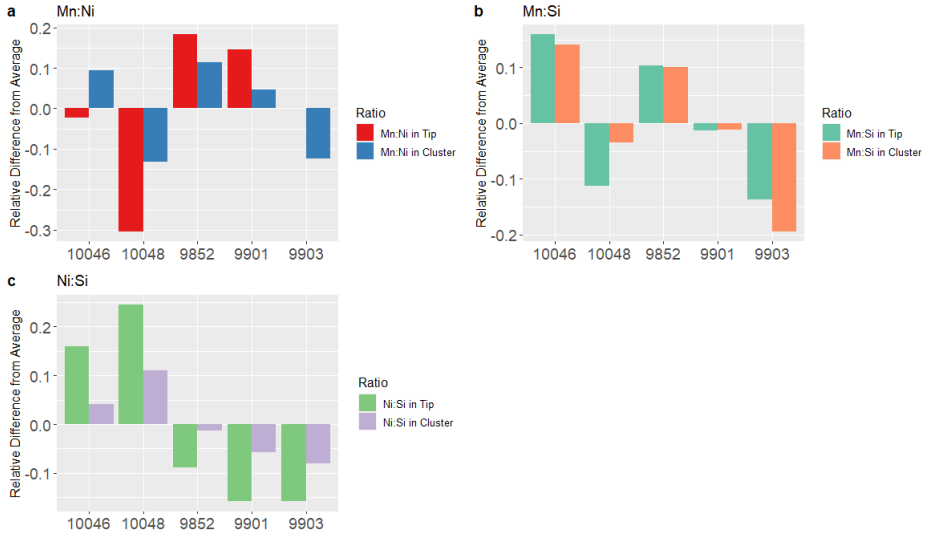

Figure 5.21: Plot showing volume fraction of clusters vs the total number of solute atoms involved in clustering present for each atom probe dataset of the six-month irradiated forged SA508.

Table 5.9: Extracted average matrix and cluster compositions for 0.2 dpa Forged SA508 steel.

	Average Composition (at.%)						
	Fe	Mn	Ni	Si	P	Cu	Other
Matrix	97.49 ±0.14	0.87 ±0.07	0.63 ±0.04	0.46 ±0.03	0.00 ±0.00	0.02 ±0.00	0.52 ±0.07
Clusters	—	36.88 ±1.98	38.11 ±1.52	24.42 ±1.29	0.02 ±0.02	0.13 ±0.05	0.46 ±0.13

5.5 Carbides and Interfaces

Although carbides and grain boundaries were not targeted during the APT FIB liftouts, they were encountered by chance on six occasions across both irradiation durations; five carbides and one grain boundary.

0.1 dpa HIPed SA508 carbides and grain boundary

Carbides were found within two of the 0.1 dpa HIPed APT datasets, with one having a MnSi-rich appendage.

Figure 5.22 shows the carbide and Mn-Si segregation region. The compositions (shown in Table 5.10) of these features were determined using an 11at.% C isosurface (for the carbide region, cropping the top part where the appendage attaches) and a targeted ROI (for the Mn-Si appendage). Based on the solute stoichiometry (and low evaporation field), the carbide appears to be of type M_3C, enriched in Mo and Mn. No clusters were found within the carbide. However, there is evidence of Ni segregation to the carbide interface (shown visually in Figure 5.22), with a small zone depleted in Ni adjacent to the boundary. Notably, those clusters extracted from the carbide-adjacent region contain one of the lowest amounts of Mn of all the APT datasets; the Run 8834 average cluster composition is highlighted by the red star in Figure 5.6. This illustrates the impact that a carbide near a cluster population can have on their composition.

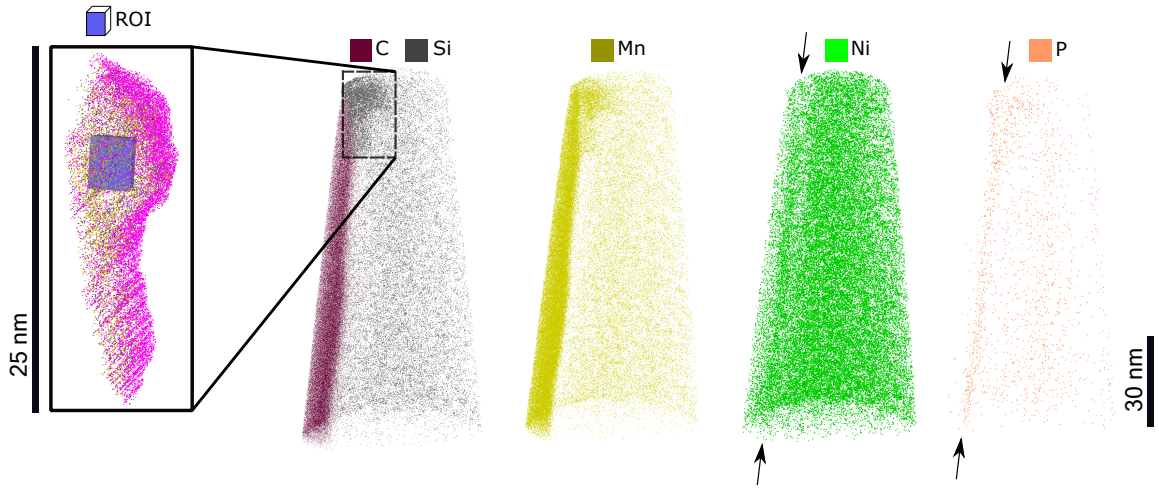

Figure 5.22: APT maps of carbide found in 0.1 dpa HIPed bainite sample, Run 8834. MnSi rich inclusion is highlighted, as well as the ROI used to isolate the composition away from the Fe-rich matrix interface.

Table 5.10: Compositions of the carbide and Mn-Si appendage in 0.1 dpa HIPed steel, Run 8834. Error approximately ± 0.01%.

	Composition (at.%)						
	Fe	C	Mn	Si	Ni	Mo	Cr
Carbide	61.44	26.14	9.12	0.06	0.28	1.18	1.76
Mn-Si Region ROI	16.60	0.16	46.65	35.98	0.45	—	—

The nature of the appendage is uncertain. Features of this type were not observed in the as-received steel, although this may be a consequence of the small size and limited APT sampling volume. Given it is largely comprised of Mn and Si, both elements known to exhibit RED, it is not unreasonable to suggest that this feature is a consequence of the irradiation process. The relatively high solubility of Mn in cementite means the solute is more likely to have precipitated out of the matrix, rather than the carbide. As seen with the Si-rich intra-carbide precipitate features shown in Chapter 4, Si has poor carbide solubility and thus in this case could have been rejected from the carbide. The question arises as to whether this was before or after irradiation. This gives rise to two scenarios: a Si-rich region was present prior to irradiation, which acted to promote Mn segregation; or, both Si and Mn diffused to the carbide interface under irradiation.

A second carbide was found during Run 9753. As shown in Figure 5.23, this carbide lies on a grain boundary region (which is discussed below). Similar to other carbides observed, although APT compositional information suggests it is near the M_7C_3 type, it is more likely cementite due to the appearing with a higher density (lower evaporation field) in the reconstruction. The carbide is enriched in Mo, Mn and Cr. Given the proximity of most of the matrix region to solute sinks (in the form of the carbide and grain boundary), it is understandable that in this analysis the cluster V_f was significantly less compared to the other datasets (0.0164%). Furthermore, the positioning of the grain boundary made

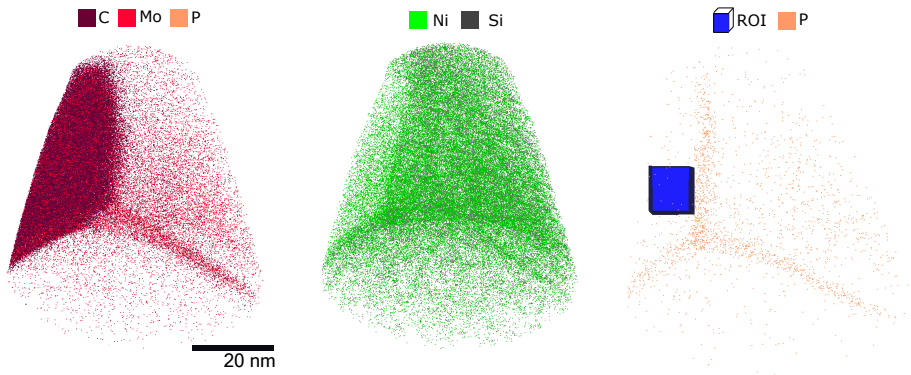

Figure 5.23: APT maps of carbide and grain boundary found in 0.1 dpa HIPed bainite sample, Run 9753. The ROI used to isolate the composition away from the Fe-rich matrix interface is shown in blue.

it difficult to determine whether the sample was bainitic or ferritic in origin, hence it is discussed as a standalone dataset here, rather than being included in the comparison above. The compositions of the clusters is comparable with that seen in previous samples, though the Si content (23.4at.%) is significantly higher and Mn content (31.85at.%) is significantly lower than average. This may be a result of reduced Mn availability due to carbide proximity, indicating that those datasets which also showed this lower Mn concentration in clusters could also have been affected by carbides just beyond the APT sampling volume.

0.1 dpa HIPed SA508: grain boundary (Run 9753)

The grain boundary shown in Figure 5.23 was isolated in order to calculate Gibbsian excesses for each element. Γ_i values are shown in Table 5.11. There are positive values for C, Mn, Mo, Ni, P and Si. The nature of this boundary is unknown (i.e crystallographic misorientation angle), thus it is potentially problematic to make direct comparisons to the as-received boundary analysed in Chapter 4. However, a few broad comparisons can be made. For this irradiated sample, the Γ_i values increase for C ($\sim 3\times$), Ni ($\sim 2\times$) and P ($\sim 2\times$). The increase in the interface carbon composition could be a result of the conjunction of the

Table 5.11: Calculated Gibbs Excess values for the 0.1 dpa HIPed SA508 grain boundary (Run 9753), including compositional values for the interface and adjacent volumes (with an error of ± 0.01%).

	C	Fe	Mo	Ni	Cr	Mn	Si	P
Gibbsian Excess (excess atoms/nm^3)	7.06 ± 0.47	-10.90 ± 0.55	2.56 ± 0.02	0.65 ± 0.17	-0.29 ± 0.14	0.54 ± 0.23	0.09 ± 0.13	0.27 ± 0.19
Interface Comp. (at.%)	1.53	95.53	0.58	1.08	0.06	0.67	0.42	0.10
Grain A Comp. (at.%)	0.37	97.28	0.21	1.03	0.07	0.65	0.37	0.01
Grain B Comp. (at.%)	0.45	97.19	0.21	1.01	0.09	0.62	0.39	0.04

boundary with a carbide, providing a fast diffusion path for C within the carbide to segregate to the boundary. There also appears to be more carbon in the surrounding matrix, despite the increase at the interface, compared to the as-received sample. The increase in Γ_{Ni} seems to result from a decrease in the concentration of Ni in the adjacent grain regions rather than a change in the concentration at the boundary itself, thus resulting in an apparent higher excess. Generally, whilst some discussion points arise, there does not seem to be a marked change in grain boundary segregation behaviour with irradiation at this low neutron dose.

0.2 dpa HIPed SA508 carbide (Run 10643)

Run 10643 contained a section of carbide, adjacent to a volume containing MnNiSi clusters. In Figure 5.24a, the ROI used to extract the carbide composition is shown, alongside the positions of the Mn, Ni and Si atoms. The composition of this carbide is shown in Table 5.12, and this, combined with it being a low-field phase, suggests the carbide is cementite, enriched in Mo, Mn and Cr (the same as seen in Run 8834).

No evidence of intra-carbide segregation was found in this case, however the proxigram

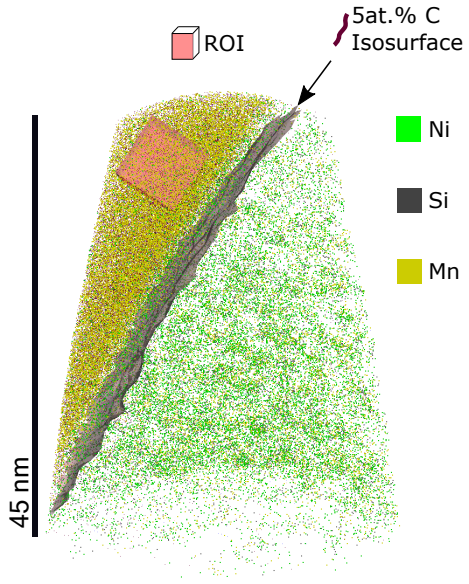

(a) APT map of carbide found in 0.2 dpa HIPed bainite sample, Run 10643. The ROI (7 nm x 7 nm x 7 nm) shown was used to obtain the carbide composition.

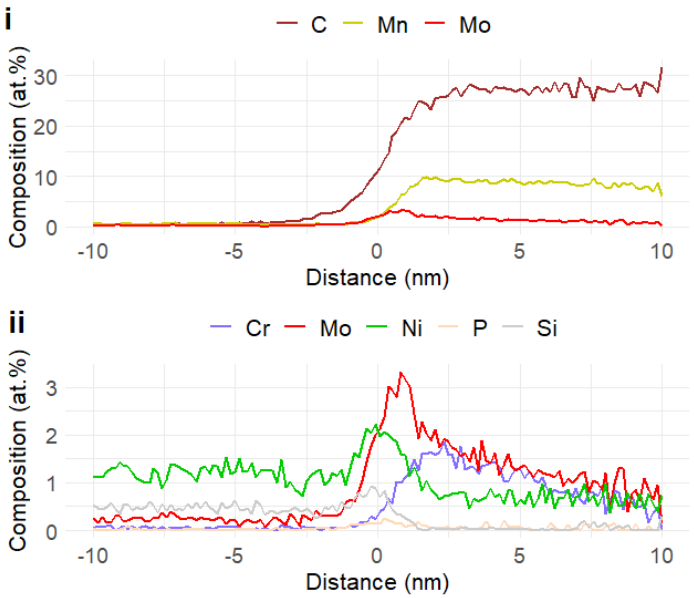

(b) Proxigrams showing the compositional variation at the carbide interface found in 0.2 dpa HIPed bainite sample, Run 10643.

Figure 5.24: Atom map and isosurface proxigram (15at.% C) for the carbide found in Run 10643 (0.2 dpa HIPed SA508)

shown in Figure 5.24b indicates segregation to the carbide interface of Mo, Ni, Si and P. This phenomenon was only seen for Mo and P in the as-received samples (see Section 4.2.3), suggesting that this increase in Ni and Si at the carbide interface is a consequence of irradiation.

Table 5.12: Compositions of the carbide found in Run 10643 of the 0.2 dpa HIPed SA508 steel (shown in Figure 5.24a). Error approximately ± 0.01%.

	Composition (at.%)						
	Fe	C	Mn	Si	Ni	Mo	Cr
Carbide	56.36	32.34	8.60	0.03	0.33	1.25	1.03

Table 5.13: Compositions of the carbide and inclusions found in Run 10649 of the 0.2 dpa forged SA508 steel (shown in Figure 5.25). Error approximately ± 0.01%.

	Composition (at.%)						
	Fe	C	Mn	Si	Ni	Mo	Cr
Carbide	55.50	29.91	11.60	0.01	0.26	0.89	1.81
Inclusion	62.57	20.76	6.10	7.15	2.19	0.72	0.37

0.2 dpa forged SA508 carbide (Run 10649)

The carbide found in a 0.2 dpa APT sample of forged SA508 differed from that seen previously in these samples. As can be seen in Figure 5.25, there are Si-rich features present within the carbide, comparable to those seen in the as-received HIPed carbide discussed in Section 4.2.4. However, unlike in that case, these inclusions are rich in Mn and Ni as well, and appear to be less regularly present throughout the carbide. The composition of both the carbide and the inclusions are shown in Table 5.13.

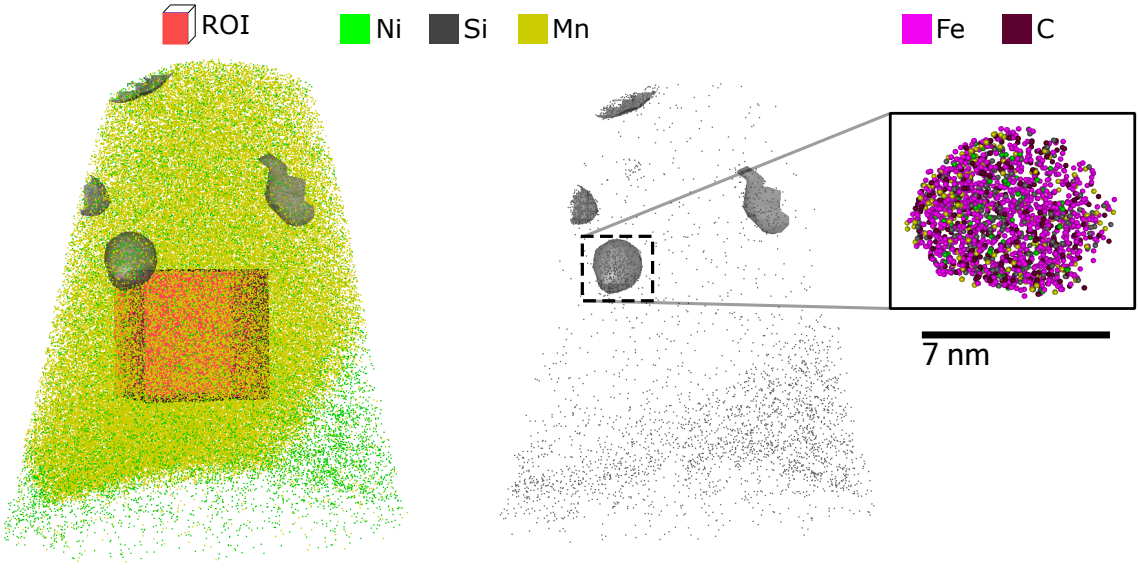

Figure 5.25: APT maps of the carbide and Si inclusions found in 0.2 dpa forged bainite sample, Run 10649. The ROI used to isolate the composition away from the Fe-rich matrix interface is shown in red, and the Si inclusions are highlighted using a 2.5at.% Si isosurface.

Again, this carbide is of the type M_7C_3. Interestingly, this is the only dataset found to contain V, in a very small amount restricted to the carbide region. A trace amount of vanadium was suggested to be present (<0.01at.%) in the nominal chemistry results provided by Rolls Royce, so appears it may only be present in specific carbides within the alloy.

With respect to the intra-carbide inclusions observed, given these are enriched in all three of the solute elements shown to exhibit RIS/RED in these samples, it is implied that they were, at least in part, formed due to the impact of irradiation. However, considering intra-carbide features were not observed in any of the other carbides encountered in the ANSTO samples, it may be that the origins of these particles lie in the manufacturing process (akin to what was suggested when this type of particle was observed in an as-received alloy). This reflects work by Zelenty et al. who observed similar features within carbides in thermally aged RPV steel, implying their formation may originate in heat treatment [182]. Neutron bombardment processes could then have enhanced diffusion of Mn to the features, causing the Mn content to increase relative to that seen in the as-received inclusions.

5.6 Cluster Size Distribution and Fluence

By considering the data gathered across both sample types and irradiation durations, the impact of neutron fluence on cluster size can be investigated. As alluded to in the results for the 0.2 dpa cluster volume fractions and number densities, further irradiation can lead to both the nucleation of new clusters or the growth of existing features; the relative amounts of each phenomena can be approximated by considering the size distribution of clusters after each irradiation.

Combining all of the cluster data from each APT reconstruction allows the cluster size distributions (based on the number of detected atoms, with Fe atoms removed) to be plotted for the 0.1 dpa and 0.2 dpa samples. This data is shown in Figure 5.26, and summarised in

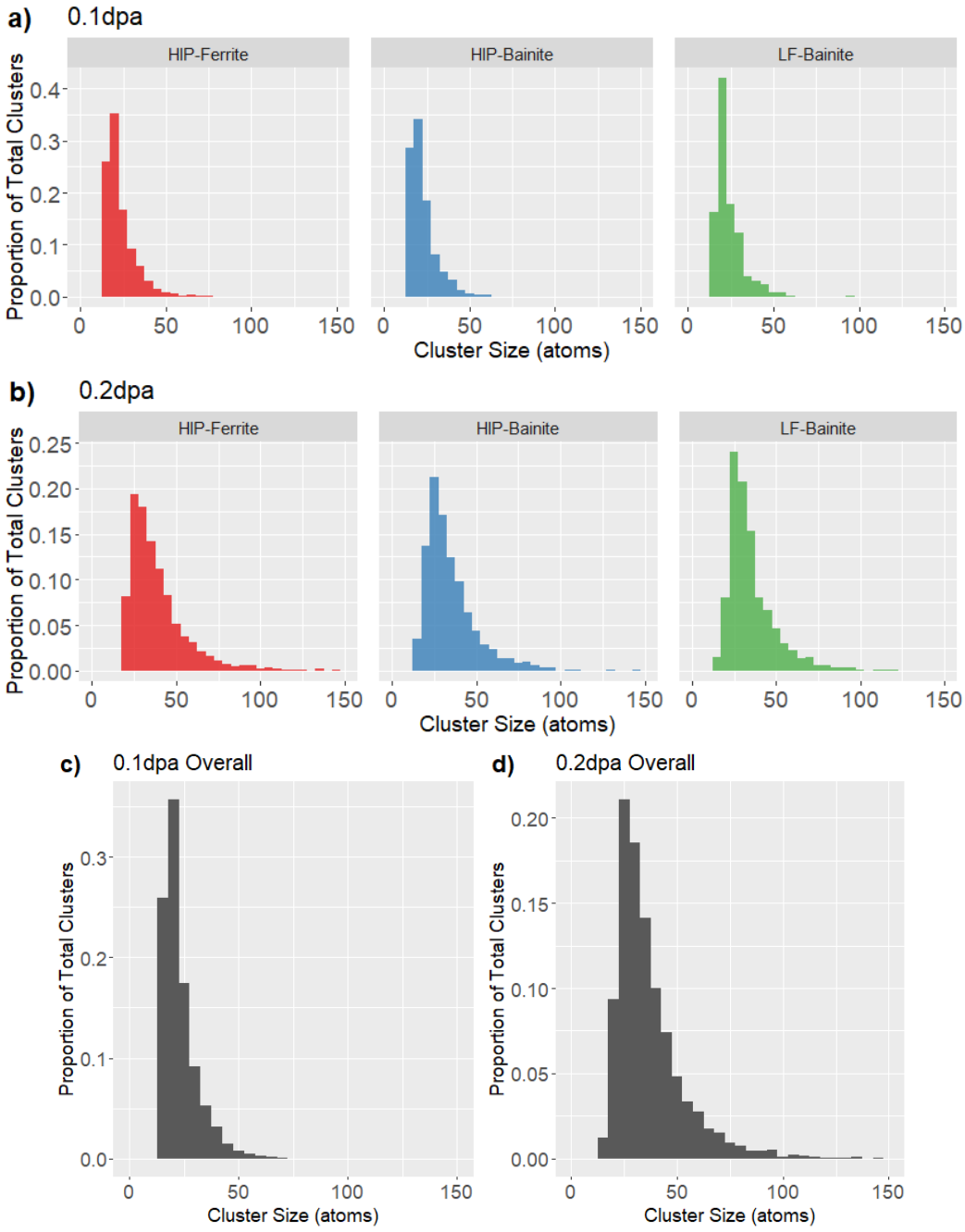

Figure 5.26: Cluster size distributions for the 0.1 dpa and 0.2 dpa ANSTO SA508 steel samples, ignoring Fe atoms and edge clusters. The count values for each bin are scaled such that the total area is equal to 1, and the y-axis used is then equal to this density multiplied by the binwidth, such to give the number of clusters in each size-range as a proportion of the total number of clusters (%). The binwidth in this case is set to 5 atoms, allowing comparison across the different sample sizes. Histograms a) and b) show the size distributions for each type of microstructure analysed, whilst c) and d) show the overall size distribution for the three-month and six-month irradiated samples.

Table 5.14. Clearly there is a broadening of the cluster size distribution with increasing dose. Furthermore, the forged bainite contains a reduced proportion of the smallest cluster sizes compared to the HIPed material (this is true across both irradiation lengths).

Table 5.14: Average corrected cluster size (atoms) for each of the ANSTO materials.

Dose	Origin	Average Cluster Size (atoms) (2sf)	Standard Deviation (atoms) (2sf)
0.1 dpa	HIP-Ferrite	45	17
	HIP-Bainite	43	15
	LF-Bainite	46	16
0.2 dpa	HIP-Ferrite	75	34
	HIP-Bainite	67	31
	LF-Bainite	68	28

It is also possible to see how the composition of clusters changes with increasing size. Ternary diagrams illustrating the Mn, Ni and Si concentrations of clusters are shown in Figure 5.27, where each dot represents a cluster produced in the ANSTO irradiations (Fe atoms have been removed from the cluster sizes and composition calculations). Given the results for each form of steel showed little distinction between the clusters produced by the different processing routes, all clusters have been grouped together such to give the general influence of size across all of the data.

The data shown in Figures 5.27 and 5.28 clearly indicates the tending to a given cluster composition as the cluster size increases. With Mn, Ni and Si, this is a tendency towards occupying the Mn:Ni:Si ratio shown in the high density areas of the ternary plots (particularly visible for those clusters larger than 100 detected atoms).

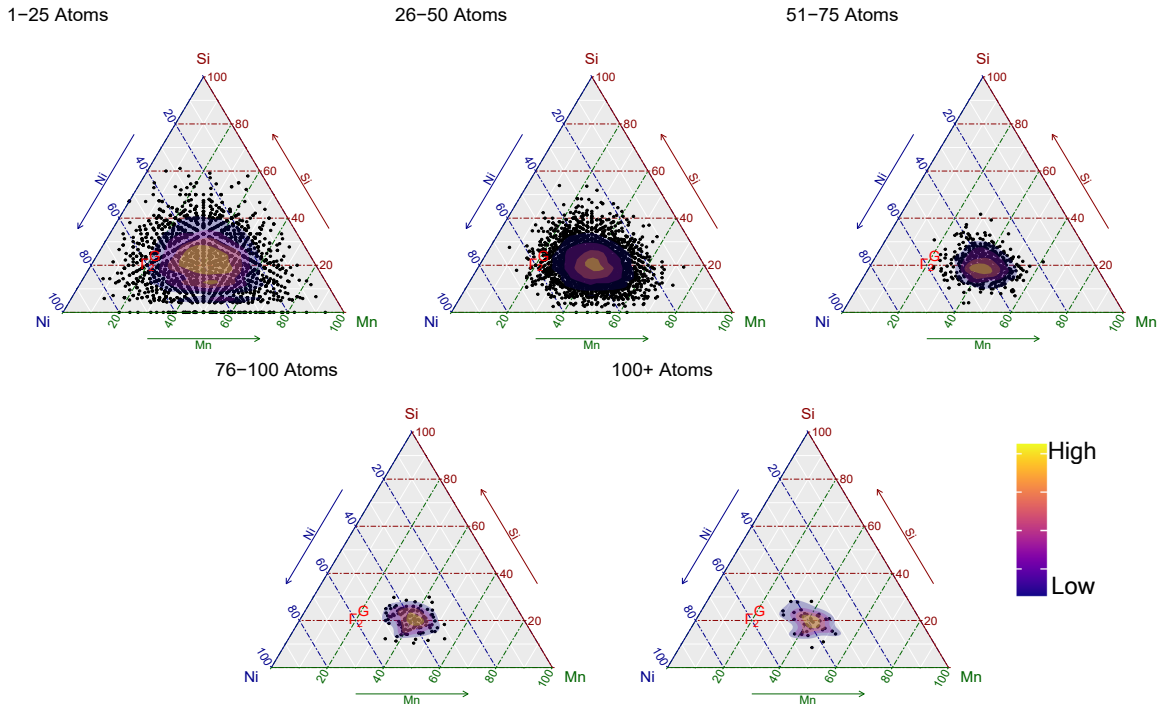

Figure 5.27: Ternary composition diagrams for a series of cluster size (equal to number of detected solute atoms) divisions across all clusters seen in ANSTO neutron-irradiated steel APT datasets.

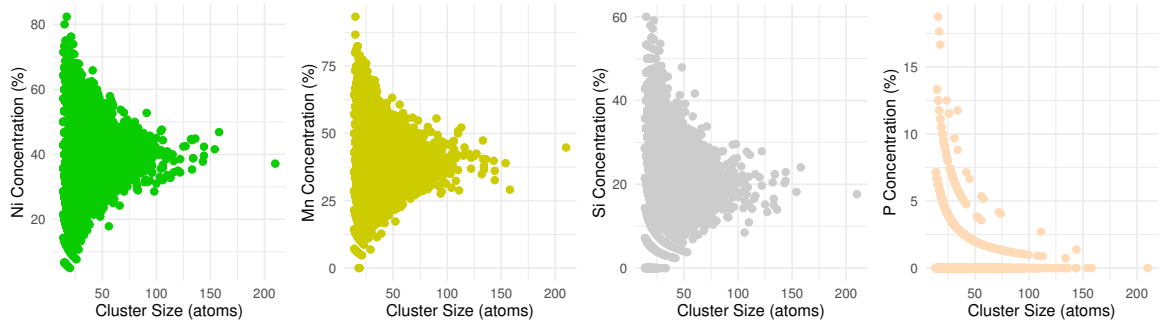

Figure 5.28: Plot of cluster size against solute concentration for the key clustering solute across all clusters seen in the ANSTO neutron-irradiated steel APT datasets.

5.7 Discussion

A summary of the key results presented in this chapter is given in Table 5.15.

The significance of the results presented in this chapter are best discussed when broken down into distinct areas: the successful observation of clustering within steel irradiated in the OPAL reactor; the impact of neutron fluence on the mechanical properties of the irradiated steel; the nature and influence of radiation-induced clustering identified.

Of importance when considering the results derived from the ANSTO experiments in the context of conventional RPV studies, is the need to account for the lower irradiation temperature utilised as a consequence of the OPAL reactor set-up. Whilst it is still of interest to identify any influence of original microstructure on neutron radiation response, as is the focus of this chapter, caution must be used when comparing cluster densities and compositions to those findings from experiments conducted at typical RPV operational temperature. The irradiation temperature of 155°C is likely to have impacted the cluster formation kinetics, density and compositions significantly, as a consequence of more stable point defects, as shown in previous low-temperature studies [76, 84, 183].

Furthermore, as mentioned previously, any disparity in the microstructural features exhibited by HIPed and forged samples goes beyond the heightened ferrite fraction; rather, there is likely more fundamental, complex differences due to differing temperature pathways during production. Comparison of the bainitic features was thus another way to capture some of the ways these alloys may respond differently under irradiation, such to incorporate another aspect of the microstructure which is significantly affected by heat treatment.

Table 5.15: Summary of ANSTO irradiation results.

Sample	V_f (%) (3sf)	Observations
0.1 dpa HIPed	Ferrite: 0.223 ±0.055 Bainite: 0.246 ±0.073	• Increase in hardness from as-received samples • No compositional influence of P and Cu on the cluster volume fraction or cluster compositions • Bainitic samples contained less Mn, likely due to increased number of local carbides compared to in ferrite • No apparent difference in clustering behaviour between ferrite and bainite
0.1 dpa LF	0.283 ±0.065	• Increase in hardness from as-received samples • Ratio of Mn to Si in the APT tip influences the Mn:Si ratio in the clusters
0.2 dpa HIPed	Ferrite: 0.701 ±0.128 Bainite: 0.659 ±0.055	• Lack of observable hardening with irradiation (most probably a result of experimental error) • Increase in cluster size, number density and volume fraction compared to 0.1 dpa samples • No apparent difference in clustering behaviour between ferrite and bainite • Pronounced correlation between tip Mn content and cluster Mn content • Relative increase in V_f greater than relative increase in N_d
0.2 dpa LF	0.570 ±0.118	• Increase in hardness compared to three-month irradiated LF samples • Increase in cluster size, number density and volume fraction compared to 0.1 dpa samples • Relative increase in V_f greater than relative increase in N_d • Influence of tip composition on cluster composition greater than for 0.1 dpa LF samples

5.7.1 Observation of early-stage neutron-induced clustering

A key aspect of this work was a proof-of-concept study into the use of an adapted medical isotope reactor for use in nuclear materials research. By taking the observation of MNS clusters as an indicator that neutron-bombardment has influenced material nano-structure, in combination with (generally) an increase in hardness, it is clear that this study has successfully irradiated alloys using the OPAL reactor. Consequently, it would be reasonable to propose this form of study as an alternative to the use of established material test reactors.

With respect to the reduced T_{irr} of the OPAL reactor, there does not appear to be a significant impact on the type of early-onset damage observed, in the form of small MNS clusters. Instead, the effect was primarily on the N_d of solute clusters produced. Both the 0.1 and 0.2 dpa irradiations contained MNS clusters with N_d on the order of 10^{24} m^{-3}, of average diameter in the range of 1 nm. Taking recent work by Wagner et al. as a comparator, the OPAL irradiations appear to produce clusters with higher N_d than that found in an A508 RPV steel irradiated at higher temperature to a higher fluence [79]. Given the Wagner et al. higher fluence irradiation had lower cluster radii ($\approx$ 0.8 nm) and a smaller V_f ($\approx$ 0.05 %) than the ANSTO samples, this relative difference in N_d is not a result of cluster coarsening with increased fluence. Although this comparison does not exactly match other important parameters, such as flux and steel composition, it does yield conclusions in-keeping with existing theories; reduced T_{irr} causes an increase in the amount of matrix damage, corresponding to more sites for solute cluster development, and reduced diffusion, limiting cluster growth [83].

The clusters shown in this chapter were all relatively small in scale. This, combined with the clusters lacking the clearer interface definition seen in more developed 'precipitates' made it difficult to confirm that those extracted from the APT atom map constituted all that were truly present in each tip. However, APT itself proved an invaluable technique

for an investigation of this nature, as TEM alone proved insufficient as a method for detecting these early-stage clusters.

As would be expected from the small sampling volume in APT, combined with the inhomogeneous microstructures present in both materials, there was large spread in cluster V_f across all the successful APT runs. This was also amplified by the uncertainties surrounding cluster identification. Although there was a strong focus on keeping the manner in which user-determined parameters were chosen consistent, given the sensitivity of MSM to the d_{max} and N_{min} values, it was clear that the results of this method should not be used as 'definitive' values; for example, a small change in d_{max} can, and did, change the amount of identified clusters significantly. It was therefore important to gain cluster V_f and composition averages across multiple datasets for each category of sample, such to give improved representative data and give greater confidence in comparisons between the different materials.

Despite these uncertainties concerning the nature of clusters observed, it is the small size of the clusters which yield this uncertainty. The scale of the clusters seen across both irradiation durations suggests that this is an early-stage in cluster development when compared to higher damage neutron-irradiation studies [66, 111]. This supports the premise that Mn-Ni-Si clusters closely resemble cascade cluster-solute complexes at low fluence [2], and, contrary to CRPs, require a relatively high fluence to form larger volume fractions. Even at this early stage, all three MNS cluster forming elements are integrated into the clusters, this suggests there is no dominating element in early cluster growth. The amount of Ni and Mn present is often roughly equal.

5.7.2 Irradiation hardening

In RPV steel irradiation studies, the expectation is that embrittlement during neutron bombardment can be linked to an increase in hardness (and corresponding yield stress) with increased dose. The hardness changes for this work are shown in Figure 5.29. The errors in all nanoindentation work conducted in this chapter are given as ± 1 standard deviation, and are large as a result of the local variations in microstructure between indents.

Whether a consequence of the unexpected physical response of HIPed SA508, or a product of systematic error within the 0.2 dpa set of nanohardness measurements, the HIPed steel did not show an increase in hardness for the higher fluence sample. Given the expectation that increased dose gives increased hardness, combined with the evidence of increased cluster V_f (known to correspond with greater hardening) in the six-month irradiated HIPed sample, the latter suggestion (an error in the indentation data) is the

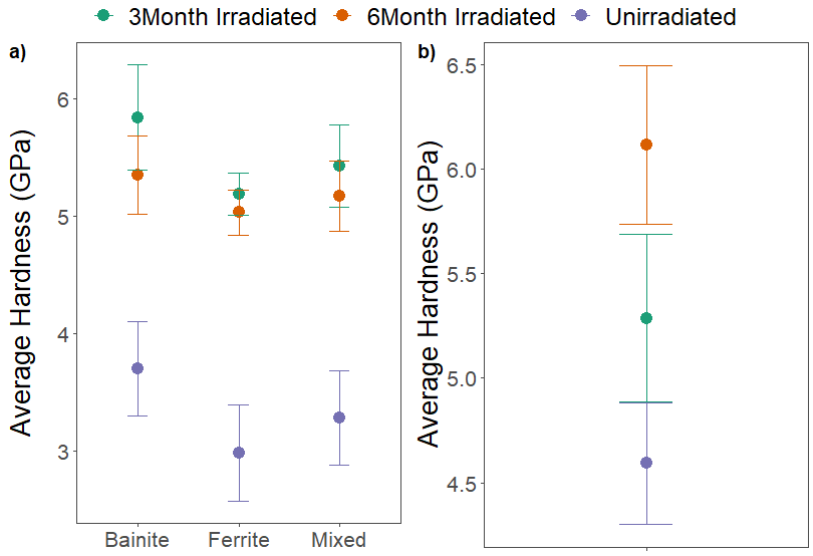

Figure 5.29: Plot of the average hardness (at a depth interval of 100-200 nm) of the ANSTO LF samples, going from the as-received state, through to 0.2 dpa of damage. The results from the HIP samples are shown in a), whilst the LF results are shown in b). The error bars indicate ± 1 standard deviation.

more likely occurrence.

Notably, the nanohardness results on the as-received samples illustrate a higher initial hardness for the LF material compared to the HIPed. There was also a smaller increase in hardness for the LF alloy after three months of neutron irradiation. Thus, although there was only a small difference in the hardening of bainite and ferrite (discussed below) in the HIPed sample, overall there is an aspect of the HIPed microstructure which makes it more susceptible to irradiation hardening. The forged SA508 behaved more in-line with expectations, exhibiting hardening behaviour which increased with neutron fluence.

The Rice-Stoller equation for correlating nanohardness with change in yield stress ($\Delta\sigma_y$) is shown in Equation 5.1 [42]:

$$\Delta\sigma_y = 274 \times \Delta H_n \tag{5.1}$$

Using a similar structure and approach to that adopted by Rice and Stoller, Gasparrini et al. produced an adapted formula based on the HIPed material used in this project, shown in Equation 5.2 [43]. Calculated $\Delta\sigma_y$ is given in MPa.

$$\Delta\sigma_y = 226 \times \Delta H_n \tag{5.2}$$

Given the latter formulation was shown to be better correlated to results from the HIPed samples, it was used to produce estimates for the $\Delta\sigma_y$ values in this work, shown in Table 5.16.

Cluster-induced hardening

In those datasets studied, all of the irradiation-induced features found were solute clusters, known to contribute to hardening embrittlement of RPV steels. As with most studies of this type, it is difficult to definitively link any hardening behaviour solely with

Alloy	$\Delta\sigma_y$ (MPa) (3sf)
0.1 dpa HIP	490 ± 235
0.1 dpa LF	157 ± 112
0.2 dpa LF	344 ± 108

Table 5.16: Change in yield stress (as estimated using Equation 5.2) for the neutron-irradiated SA508 samples.

the observation of nanoscale clusters; there are additional contributors to hardening in RPV steels beyond cluster/precipitate development, such as matrix damage (dislocation loops voids etc), which cannot be identified with APT. Compared to self-interstitial dislocation loops and voids, MNS clusters are weak obstacles to dislocation movement, however, it is likely the relatively high incidence of these clusters which dictates their role as the more significant source of hardening [184].

Using the results from the $\Delta\sigma_y$ conversion formula (Equation 5.2) discussed above, a plot of $\Delta\sigma_y$ against the square-root of cluster volume fraction ($\sqrt{V_f}$) can be produced. This is a well-established relationship found to exist in irradiation-hardening across broad irradiation conditions [45, 185]. For this work, the relationship between $\Delta\sigma_y$ and $\sqrt{V_f}$ is shown in Figure 5.30. Although there appears slight positive correlation, there are too few data points to determine whether the predicted linear relationship is exhibited in for these results. In addition, the lack of clear hardening between the 0.1 dpa and 0.2 dpa samples of the HIPed steel prevents a study of the correlation between clustered V_f and hardening in this case.

Although the LF sample hardened less than the HIPed following a three-month irradiation, there was little notable difference in the number or nature of MNS clusters seen in APT reconstructions of each alloy type.

In a DBH model of the type [186]:

$$\Delta\sigma_y = \alpha \times M \times \mu \times b \times \sqrt{Nd} \tag{5.3}$$

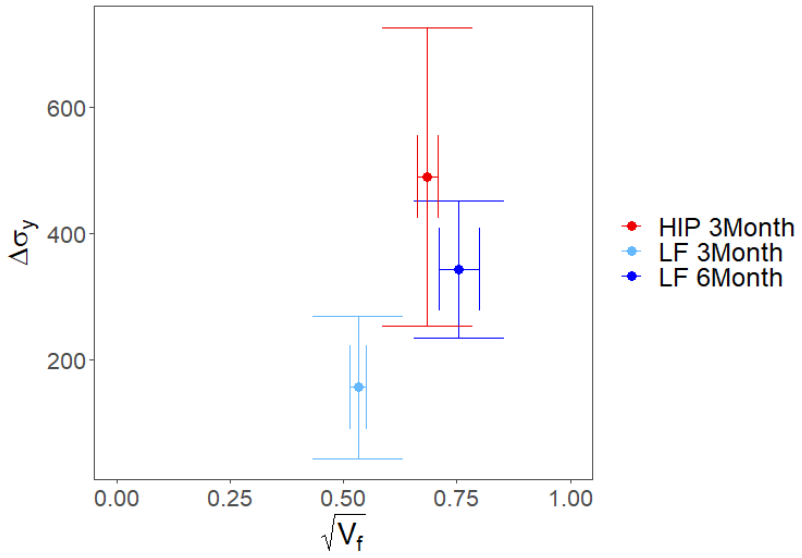

Figure 5.30: Plot of the average $\Delta\sigma_y$ against $\sqrt{V_f}$ for neutron-irradiated samples from the three-month irradiated (0.1 dpa) HIP and LF alloys, and the six-month irradiated (0.2 dpa) LF alloy.

where α is the obstacle strength, M is the Taylor factor and is considered equal to 3.06 for both bcc and fcc lattices [187], μ is the shear modulus (80 GPa for ferritic steel) and b is the Burgers vector length (0.2485 nm in bcc ferrite). N and d are the number density and the diameter of the features. For low-Cu RPV steels, an α value of 0.1 has been given as a reasonable estimate for the obstacle strength of solute clusters [79, 188].

In an attempt to correlate the results from APT and nanohardness with this existing model, only the observed MNS clusters could be input as a source of hardening. Although this is likely not the case, it would allow a comparison between the measured change in σ_y and the theoretical contribution of these clusters. For the three-month irradiations, cluster diameter averaged 1.0 nm, whilst they averaged 1.2 nm in the six-month samples. Using Equation 5.3, the DBH model would give a $\Delta\sigma_y$ of approximately 62 MPa for 0.1 dpa HIPed SA508 and 93MP for the 0.2 dpa HIPed SA508 steel (with the N and d values used produced by averaging values from both microconstituents). The calculated DBH $\Delta\sigma_y$ for LF were 66 MPa and 87 MPa for the 0.1 dpa and 0.2 dpa alloys respectively. These estimates are

significantly less than the $\Delta\sigma_y$ calculated for these materials based on nanoindentation data; either implying a different obstacle strength than assumed, or the presence of additional hardening features which cannot be quantified with APT.

The latter suggestion is an example of strengthening super-position [41], and can be applied to a combination of relatively weak obstacles induced by irradiation, such as dislocation loops and voids, or to pre-existing strong obstacles which contribute different amounts to the change in yield stress based on their distribution within the different grain types. Unfortunately, given the difficulties encountered in detecting radiation damage with TEM due to the presence of surface oxide, which produced black dots contrast, it was not possible to detect any other source of radiation damage at this stage, therefore applying the root-sum-square (RSS) [189, 190] model to calculate the impact of multiple weak obstacles is not possible. However, in this work it is strong, dispersed obstacles ($\alpha > 0.6$) in the alloy which are more likely to have influenced the difference in hardening experienced by ferrite and bainite. Here, strong obstacles likely take the form of carbides (and the oxides observed with STEM-EDX), which interact with the fine-scale weaker MNS clusters induced by neutron irradiation, altering the resultant dislocation-obstacle interactions and thus impacting the observed $\Delta\sigma_y$ according to a linear sum (LS) model [41]. Thus, any difference in carbide densities between microconstituents could influence $\Delta\sigma_y$, making the hardening dependent on the unirradiated material. The two possibilities (differing α values for clusters in ferrite and bainite, and the role of super-positioned hardening features) need to be further assessed.

Hardening in HIPed ferrite and bainite

Across all nanoindentation data, there is little evidence of a significant difference in the amount of hardening experienced by bainite and ferrite in the SA508 HIPed steel. The error bars are large both in the nanohardness data and cluster data from APT, so firm conclusions

cannot be derived on the behaviour of the two microstructures. However, the relative hardness change for the 0.1 dpa material was 0.58 ±0.16 GPa for bainite and 0.74 ±0.16 GPa for ferrite, indicating that the ferrite hardens more relative to its initial hardness. This greater relative hardening can be explained by the fact that it was softer before irradiation than the bainite. The similar hardness response obtained from the two microstructures may be related to the fact that hardening is more influenced by irradiation-induced defects than other microstructural features.

Hardening of HIPed bainite and Forged bainite

One source of comparison when looking at the hardening behaviour of the HIPed and forged samples would be the response of the bainite within each microstructure. The bainite in the HIPed samples was initially softer, and then hardened to a greater extent compared to the forged bainite (mirroring that seen when considering the samples as a whole). The difference in the relative increase in hardness at 0.1 dpa between the two bainite forms was significant, with the HIP-Bainite exhibiting a 0.58 (±0.16) relative increase compared to 0.15 (±0.11) for the LF-Bainite. This further enforces a fundamental difference in the hardenability of the bainite seen in HIPed SA508 compared to that produced by conventional forging - this is a product of the heat treatment pathways each alloy was subjected too. It could be that a higher density of dislocations and carbides in the forged bainite gives rise to greater initial hardness due to a high amount of possible dislocation impedance; the amount of hardening could be less impacted by cluster formation if dislocation motion was already inhibited significantly prior to irradiation.

5.7.3 Clustering behaviour of HIPed and Forged SA508

All clustering characterised was of the Mn-Ni-Si type. As with other irradiation studies into low-Cu RPV steels, there was no evidence that pre-existing Cu clusters were required for cluster nucleation. Many clusters showed no Cu content, and visually there were no clusters displaying an Cu-appendage on which heterogeneous nucleation may have occurred. It is therefore likely the primary method for cluster nucleation was radiation induced segregation, with Ni, Mn and Si the primary species subjected to enhanced diffusion towards defect-solute clusters formed during irradiation. An increase in irradiation duration (and associated damage level) corresponded to an increase in the MNS cluster V_f.

Extent of clustering

HIPed SA508 → Figure 5.31 shows the variation of cluster V_f with clusterable solute for both the three- and six-month irradiated HIP samples. In the three-month irradiated sample, the ferrite grains, on average, appeared to contain a greater amount of clusterable solute, i.e. solute atoms of elements that are actively associated with irradiation-induced

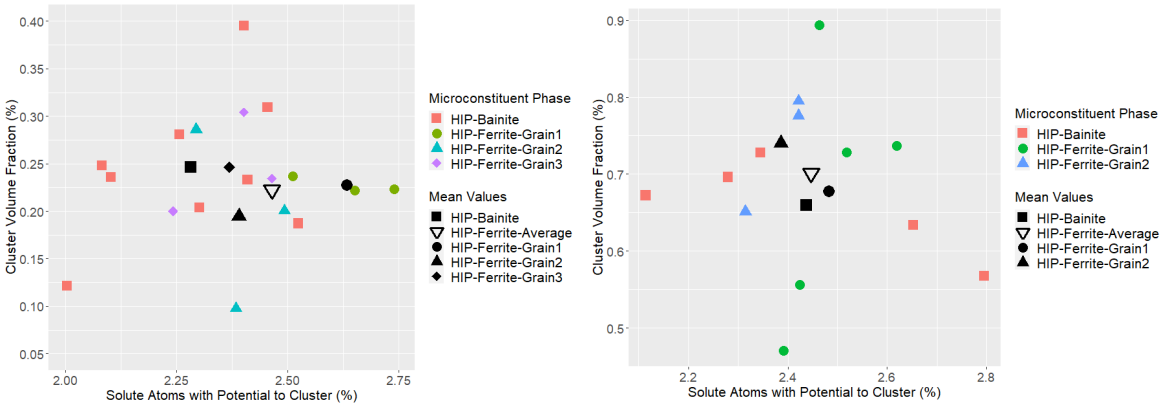

(a) 0.1 dpa HIPed **(b)** 0.2 dpa HIPed

Figure 5.31: Plot detailing the volume fraction of clusters vs the total number of solute atoms involved in clustering present for each atom probe dataset of the 0.1 dpa and 0.2 dpa HIPed SA508 steel samples. The mean values for ferrite and bainite region reconstructions are shown in black.

cluster formation, within the samples analysed (although it is acknowledged that the spread in data does give overlap in these cluster count distributions). Perhaps counter-intuitively, this does not correspond with a higher cluster V_f or N_d in the ferrite. In contrast, there is a much less significant difference in the amount of clusterable solute between bainite and ferrite in the six-month irradiated samples. Although ferrite tips still contained, on average, more solute with the potential to form clusters, both microconstituents were more similar in this regard. In addition, whilst in the 0.1 dpa results there appeared to be a greater spread in the measured cluster V_f and N_d levels within the bainitic reconstructions compared to the ferrite, the opposite was apparent for the 0.2 dpa samples.

Radiation induced segregation is known to involve the diffusion of solute atoms to point defects, although usually the majority of point defects attributed to hardening behaviour are assumed to be induced by neutron-induced displacement cascades [32]. Given this, any spread in cluster density between the different microconstituents could be a result of a difference in pre-existing defect density in that microstructure, for example, dislocations. This effect would play a more significant role at lower fluences, earlier in the stages of heterogeneous cluster nucleation. Given that bainite possesses a more defected microstructure, this amplified role of defect density at low doses could have led to the more pronounced variance in the degree of bainitic clustering seen at 0.1 dpa compared to at 0.2 dpa. As dose increases, the role of microstructure lessens and the cluster-vacancy (MD) defects induced by neutron irradiation dominate. The above postulation could also explain why ferrite possessing a greater amount of clustering solute does not translate into higher cluster volume fractions after three months of irradiation; the cluster N_d is limited by the number of available point defects (due to both neutron damage and pre-irradiation microstructure).

Forged SA508 → A link between the amount of clustering solute and the cluster V_f was not clearly present for the forged ANSTO samples. Although there was a suggestion of

increased V_f with increased solute available for clustering in the six-month irradiation samples, it was not enough to definitively link these two measures in this case. As such, it is reasonable to conclude that the distribution of clusters within specific sub-volumes of neutron-irradiated forged SA508 is erratic. This observed randomness may be linked to underlying variation in defect levels present, as discussed above.

Cluster compositions

Based on the results obtained from the irradiated ANSTO samples, ternary diagrams illustrating the variation in Mn:Ni:Si ratio for each set of clusters could be produced across the two difference irradiation durations. Figure 5.32 illustrates the shift in compositions with increased dose.

The cluster composition results provided two key findings; the first is that Mn, Ni and Si dominate the cluster compositions, with the amount of other species decreasing as dose increases; the second is that bainitic samples in the HIPed steel contain less Mn than the ferrite, whilst the forged samples, on average, lie between the two HIPed microconstituent with respect to Mn content. By considering Figure 5.32, it can also be

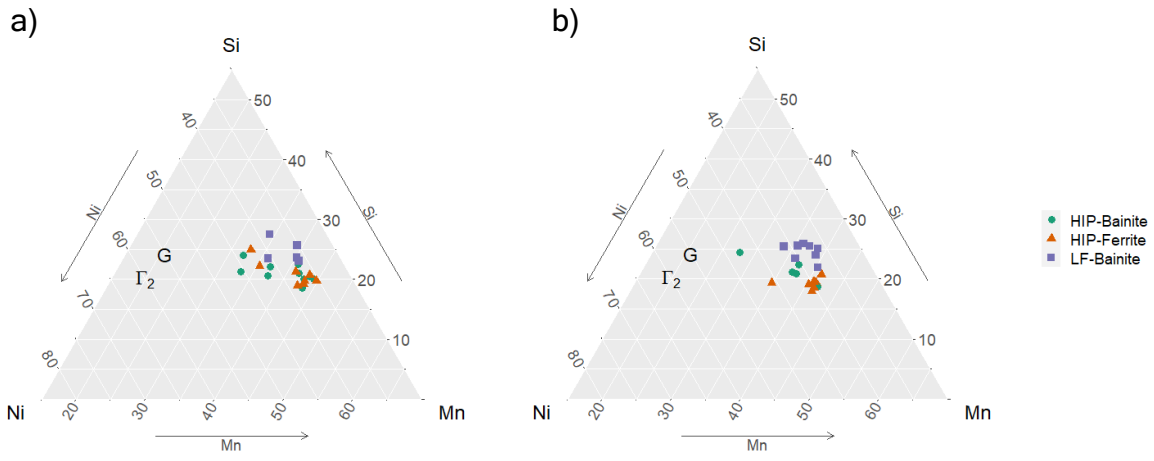

Figure 5.32: Average Mn, Ni, Si content (%) for clusters extracted from APT reconstructions of a) 0.1 dpa and b) 0.2 dpa neutron-irradiated HIPed and forged SA508 steel

seen that the compositions generally shifted to the left as the irradiation duration doubled, which corresponds to a relative increase in Ni content. As an empirical formula, these more developed clusters approached a ratio best described as Ni_2Mn_2Si.

When comparing the two bainitic microstructures (the HIPed bainite and the forged bainite), they are not as similar in composition as may be expected. Instead, the HIP-bainite more closely resembles the HIP-ferrite in composition, with the forged clusters generally containing a higher Si content. Based on the APT studies of the as-received samples, this reduction in Si for the HIPed clusters could be a consequence of the Al/Si/O rich inclusions found (discussed in Chapter 4).

Influence of tip composition on clustering

Beyond the influence of the combined solute content of the APT tips, the variation in specific elements within each tip should also be considered as a factor in both the V_f and cluster compositions. Graphs comparing these relationships, across all ANSTO materials, are shown in Figure 5.33 and Figure 5.34.

One would perhaps expect an increase in the amount of clustering solute within the tip (or the amount of one 'dominant' species) to also correspond to an increase in the amount of that element available for cluster formation, thus an observed linear increase in cluster V_f. Significantly ($p < 0.01$), this is not the case for any of Ni, Mn, Si or P, suggesting there is a more complex interaction between tip solute content and cluster V_f; likely the impact of irradiation conditions and dose on the efficiency of solute cluster formation.

There is clearly a strong link between the tip compositions and the cluster compositions produced. Figure 5.34 illustrates that the Mn, Si and P tip compositions have a linear relationship with the fraction of those elements in the 0.1 dpa clusters (ignoring Fe), whilst the same is true for Ni, Mn and Si in the 0.2 dpa clusters. This indicates that, for these elements, an increased presence within the tip translates into an increased presence within

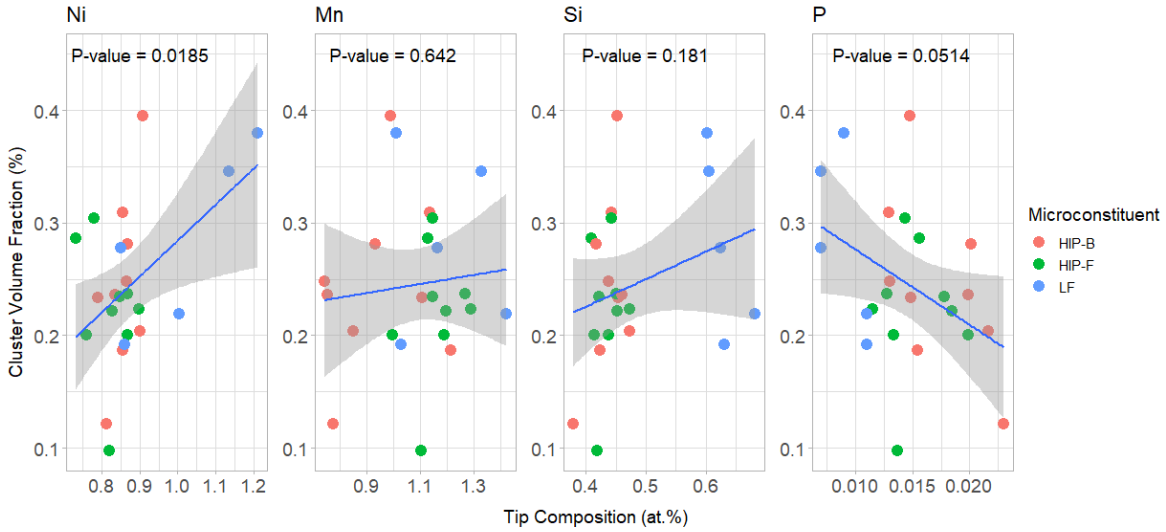

(a) 0.1 dpa

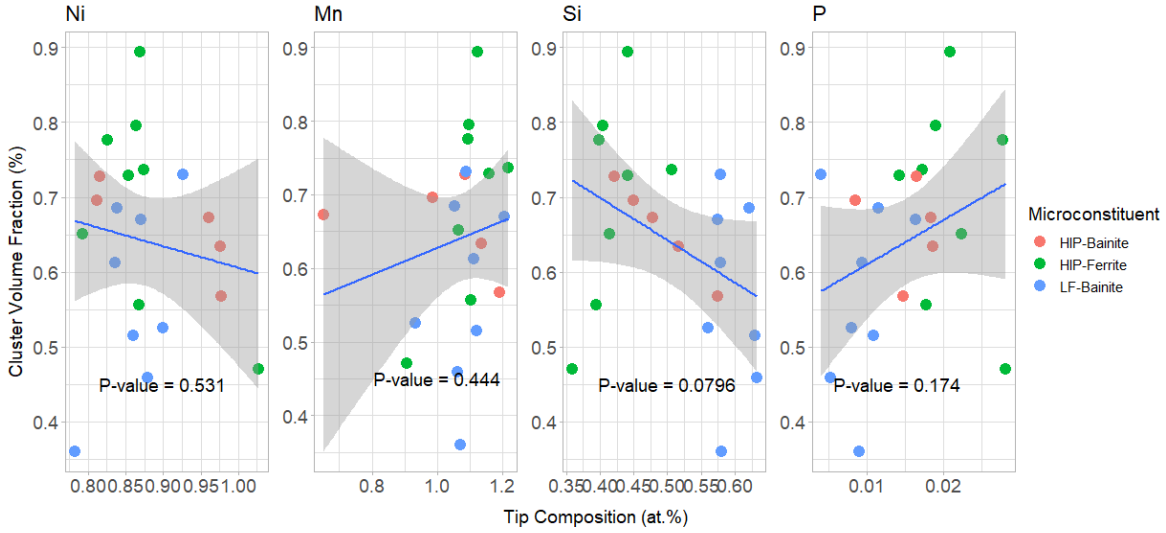

(b) 0.2 dpa

Figure 5.33: Plot of the cluster volume fraction each dataset against the corresponding overall tip composition, for both the three-month (0.1 dpa) and six-month (0.2 dpa) ANSTO irradiations.

the clusters. This seems an intuitive result, and one which would be expected for the key solutes across the different fluences. Ni not displaying this proportionality in the 0.1 dpa sample may be a result of the anomalously high Ni contents of the 0.1 dpa HIP-Bainite clusters. These compositional trends are observed early in cluster development, and thus, as the cluster compositions in this case are given as a fraction of the total clustering solute

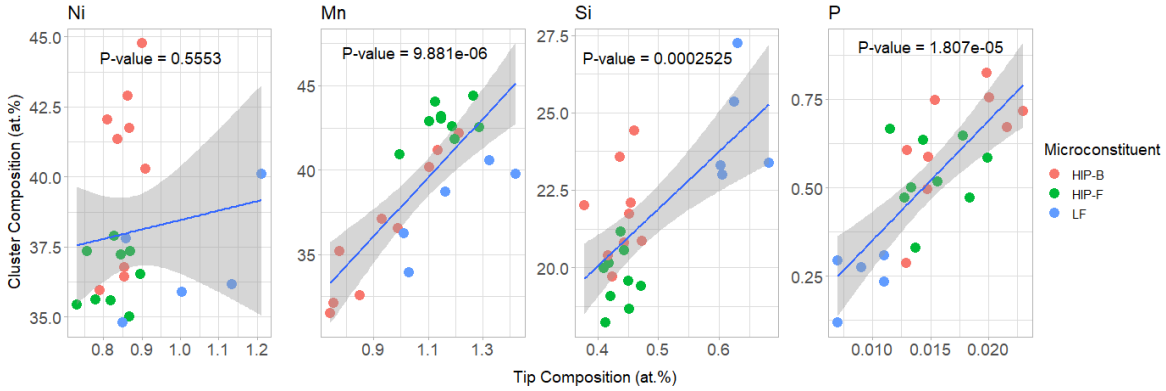

(a) 0.1 dpa

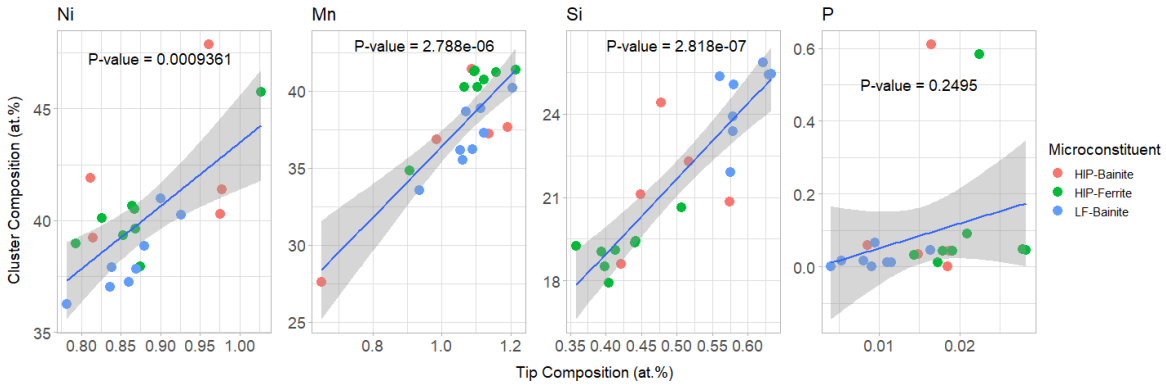

(b) 0.2 dpa

Figure 5.34: Plot of the average cluster compositions of each dataset against the corresponding overall tip composition, for both the three-month (0.1 dpa) and six-month (0.2 dpa) ANSTO irradiations.

(Mn, Ni, Si, P and Cu), the extent to which this trend would continue with increased cluster growth is debatable. For example, if there exists a thermodynamically-favourable phase for clusters to develop into, then the ratio of each solute element present in each cluster would reach a set value, after which any increase in available solute would not influence the cluster concentrations.

The link between tip composition and cluster content mirrors another clear takeaway from the cluster composition data; the observed greater Mn variation in bainitic samples. This is a result of the reduction in Mn within certain APT volumes which were extracted in the vicinity of carbides, and is a clear example of the local chemistry (including the tip and

beyond the APT volume investigated) impacting the make-up of the clusters observed. In this case, it is the irregular, lathed sub-structure of bainite which increases the possibility of sampling from regions near a carbide compared to the more homogeneous ferrite grains seen in the HIPed material.

Cluster size distribution and fluence

The cluster size distribution results shown in Section 5.6 clearly demonstrate a broadening of cluster size distribution with increased irradiation dose. From this, it is clear in this work that cluster nucleation is continuing with neutron exposure, though at a slower rate than cluster growth. The forged samples containing fewer of the smallest clusters perhaps indicates that cluster growth beyond nucleation was slightly more effective in these samples compared to in the HIPed steel.

As cluster growth continues, the composition of the clusters are tending to a ratio slightly higher in Mn than the thermodynamically suggested G and Γ_2 phases. There is also a reduction in the fraction of P present within clusters. Data shows that this is a result of the number of P atoms not increasing as the clusters grow, causing the overall fraction to decrease as the contribution of this species to cluster size dwarfed by the that of Ni, Mn and Si. This implies that P plays a less significant role in cluster development as size increases (unsurprising, given its notably lower contribution to the nominal alloy compositions).

Given that the primary size-effect of increased dose is a broadening of the size distribution, if one wanted to link the cluster compositions shown in Figure 5.27 to fluence, it would be reasonable to assume that as the cluster size increases more of those clusters shown are from the longer irradiation duration (six-month). From this, it becomes clear how the nature of clustering could change beyond this low-dose profile, into the more defined clusters seen in higher dpa experiments. However, this suggestion for evolution does not account for the role of other factors, such as flux and temperature, and thus it

may be unphysical for samples irradiated in this particular set-up to exhibit comparative clustering behaviour to that seen in more conventional experiments.

5.8 Conclusions

This chapter has shown the results obtained from subjecting SA508 Grade 3 Class 1 steels produced by different manufacturing pathways to neutron irradiation. The relatively low fluence resulted in the formation of nanoscale, dilute Mn-Ni-Si clusters, which were observed using APT, alongside the corresponding hardening effect, as measured by nanoindentation. The key conclusions from this work are:

- Comparisons made within the HIPed microstructure suggest that ferrite exhibits no detrimental performance under irradiation compared to bainite within the same material; this may be a critical justification in the use of alternative fabrication methods for nuclear steels, as the inclusion of idiomorphic ferrite does not impact a materials' susceptibility to hardening.
- Cluster V_f and N_d values increased with increasing neutron dose for both forms of SA508 steel, with the N_d increasing by a smaller factor than V_f.
- The Mn cluster content of bainitic samples was impacted by increased likelihood of carbide proximity, lowering the Mn content relative to that seen in ferritic clusters.
- For the forged SA508, an incremental increase in hardness was found to be associated with the increase in dpa. Unfortunately, the data from the HIPed six-month irradiated samples fail to show this expected trend, despite an apparent increase in hardening clusters. Based on the 0.1 dpa results, the LF alloy exhibited less radiation-induced hardening that the HIPed sample.
- The estimated changes in yield stress caused by irradiation (calculated with the DBH model) are not fully explained by the presence of the MNS clusters observed with

APT. There are hardening phenomena involved which could not be quantified in this work.

- There was a clear change is cluster-size-distribution with fluence; broadening indicates the growth of existing clusters, whilst the continued existence of smaller cluster sizes indicates continued cluster nucleation. These findings support the V_f and N_d values obtained.
- As clusters grew in size, the variation in cluster composition narrowed, approaching a more consistent Mn:Ni:Si ratio and tending to zero in those solutes with either less tendency for segregation or with reduced concentration within the material (shown to be the case for P). The relative amounts of Ni, Mn and Si in the larger clusters were approaching the empirical formulae of the thermodynamic G and Γ_2 phases suggested in literature, but with higher Mn contents than would be expected, such that they are better described empirically as Ni_2Mn_2Si. The small deviation from these values is likely a result of the temperature and fluence effects.

Chapter 6

Ion Irradiation of SA508 Steel

This chapter presents results from the mechanical and microstructural characterisation obtained from four SA508 Grade 3 Class 1 steels produced by different manufacturing routes and subjected to self-ion irradiation. Ion irradiation of materials can act as a surrogate to give microstructural effects induced by neutrons. In comparison, ion irradiation provides increased flexibility, allowing a greater variation in dose and temperature when irradiating samples. In this study, across a range of doses, the HIPed, Large Forging, Forging B and Forging C materials are compared based on their response to the irradiation conditions. This enables a study grounded in the influence of metallography and microstructure on the irradiation response of steel. All self-ion irradiations were undertaken at the DCF using a 5 MeV accelerator (DAPHNE). Three cartridges, containing 3 mm TEM disks of each alloy, were ion-irradiated; the letter attributed to the cartridge will be used as an identifier for each set of irradiation conditions (A, B and F). APT samples were then produced via FIB for each alloy type, including isolated ferrite and bainite grains from the HIPed samples in Irradiation B and F, where increased irradiation damage allowed easier comparison between microconstituent phases.

6.1 A: 0.1 dpa Fe^{4+} 300°C

All four different SA508 steel samples experienced a 5 MeV Fe^{4+} ion irradiation, with the irradiation conditions shown in Table 6.1. The damage profile for this irradiation, as calculated using SRIM (method described in Chapter 3), is shown in Figure 6.1.

Table 6.1: Fe^{4+} Irradiation A condition. *at target depth.

Target Depth	Dpa*	Average Beam Current	Beam Area (cm^2)	Dpa rate* (dpa/s)	Temperature (°C)
240 nm	0.1	34.2 nA	4.73(± 0.5)	2.49(±0.14) $\times 10^{-6}$	301.1 ± 2.3

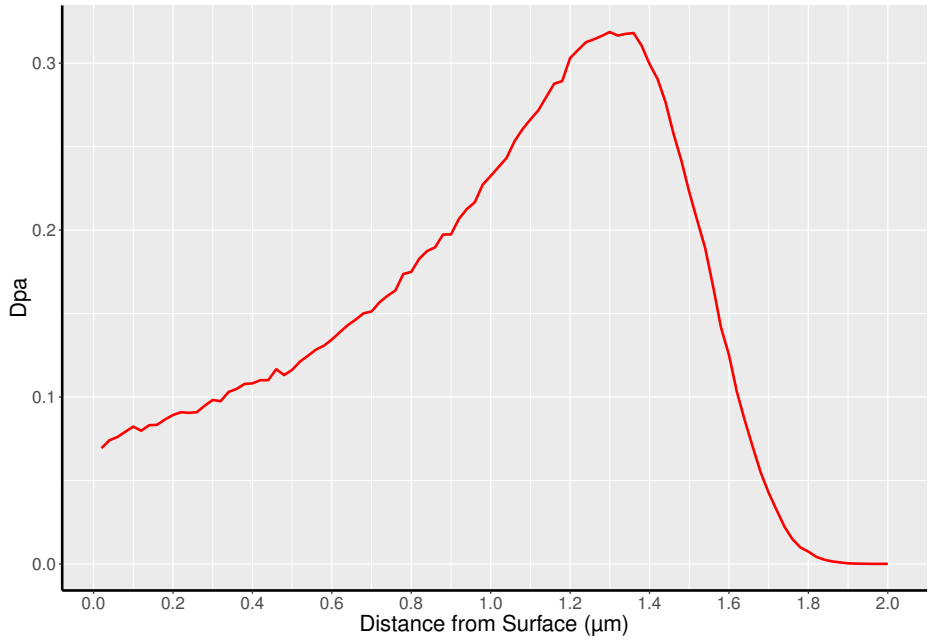

Figure 6.1: Damage profile into Fe^{4+} irradiated surface for a SA508 HIPed sample with target damage of 0.1 dpa at 500 nm depth.

By making APT samples from 240 nm, 500 nm and 1 μm depths, a variety of damage levels could be investigated (0.09 dpa, 0.12 dpa and 0.23 dpa respectively). In total, 43 tips

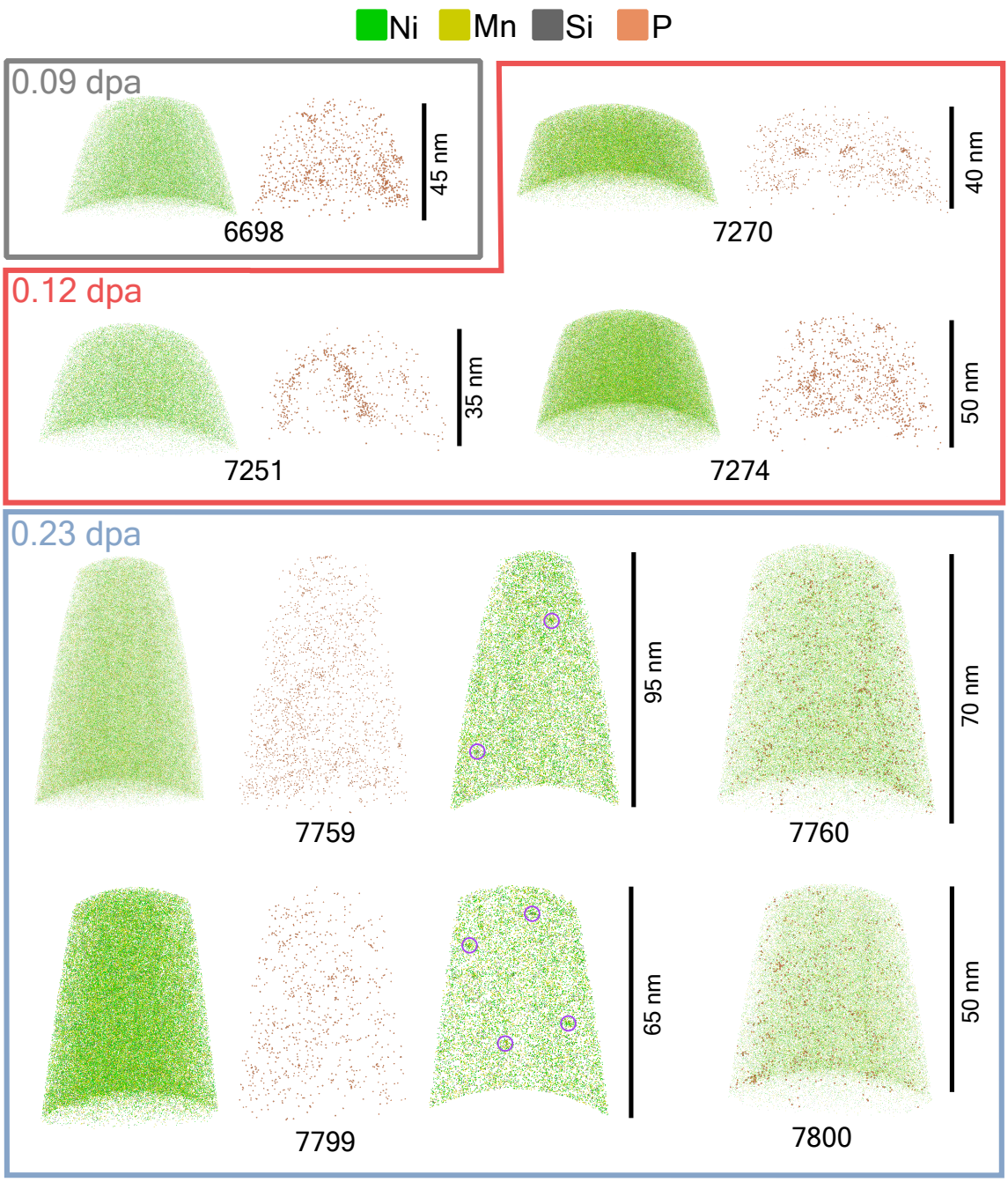

Figure 6.2: Overview of APT representative atom maps obtained from the Cartridge A Fe^{4+} irradiation of HIP SA508 Steel. For each sample (run number shown in figure), an image of Mn, Ni and Si atoms are shown, alongside evidence of the type of segregation observed. For the 0.09 dpa and 0.12 dpa reconstructions, an image of P atoms is included to illustrate the P segregation occurring. Where an additional image is included for the 0.23 dpa reconstructions, a 5 nm slice of the atom map is shown, used to better visualise MNS clustering (examples shown within purple rings).

were ran in the atom probe, which produced 32 viable datasets.

Figure 6.2 shows representative atom maps obtained from the HIPed sample at each depth/dpa, with the notable features highlighted.

In the case of the HIPed steel reconstructions, there appears to be a dose-dependent relationship, where at low dpa there is enrichment of certain regions only by P atoms, and at larger dpa there is nucleation of small, distinct Mn-Ni-Si clusters. Given the indistinct nature of these P regions, and large distances between the P atoms involved relative to the inter-atomic separations in BCC iron, this thesis will refer to them as P 'atmospheres'. Data across all four steel types shows this trend to be the case for the LF sample, although it does not hold true for every HIPed and LF sample investigated. Interestingly, the same progression was not observed at all in the forged B and C steels.

The P segregation and MNS cluster-forming behaviours are discussed in more detail in Sections 6.1.1 and 6.1.2, however, for a more general assessment of the inconsistency seen between samples it is beneficial to account for the changing local chemistry common in the nano-volume APT datasets. Figure 6.3 shows how the composition of each atom probe reconstruction changes between samples, and how this correlates to the observed segregation behaviour. Mn, Ni and Si are shown in relation to the detection of MNS-type clusters and regions of high P concentration (either in the form of atmospheres or segregation to dislocations).

There is a significant amount of variation in the concentrations of each relevant solute between datasets, most notably:

- the forged samples contain significantly higher Si concentrations compared to the HIPed samples
- Mn concentrations vary across all samples
- there is increased Ni concentration at the highest dpa, which also correlates to a

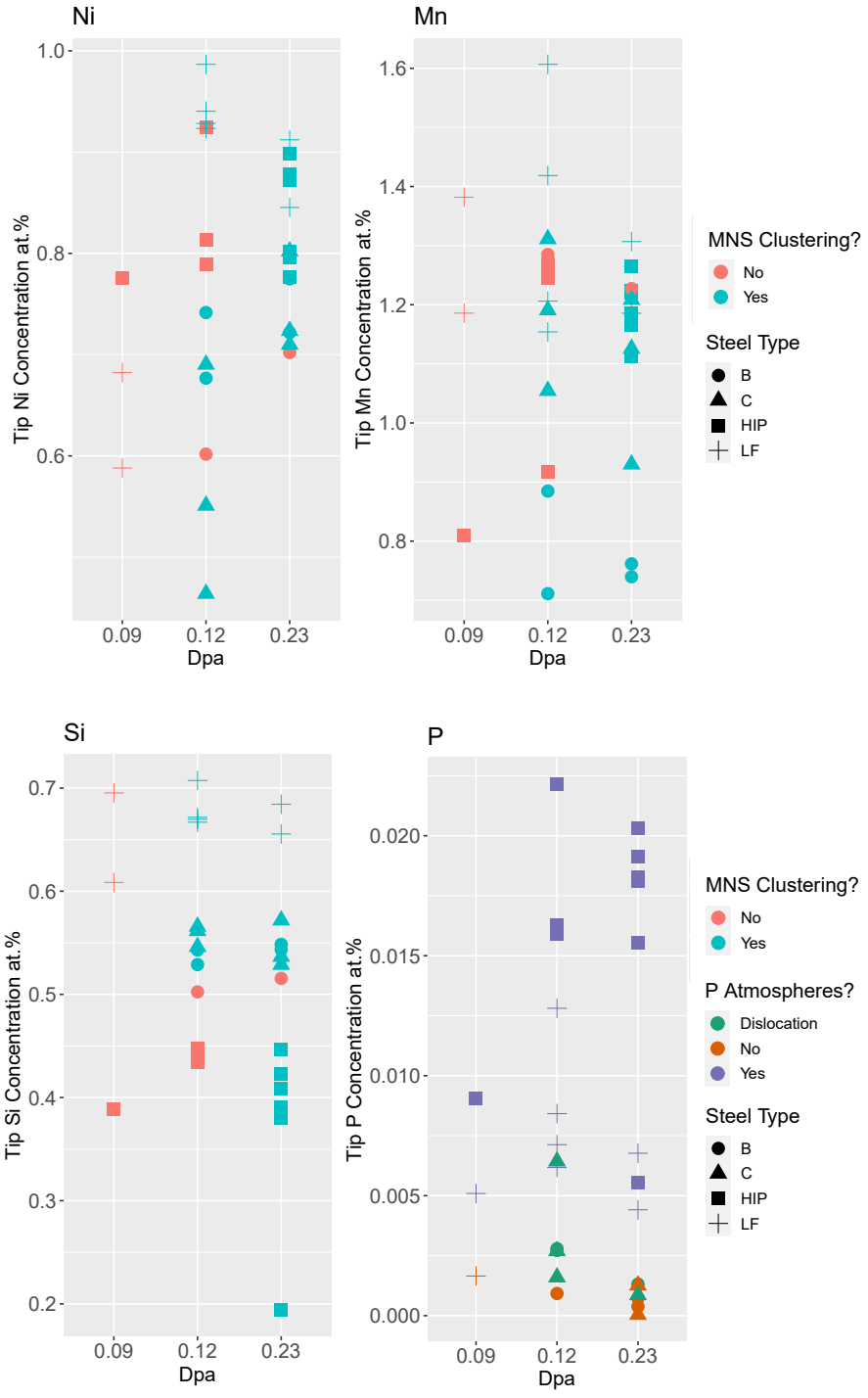

Figure 6.3: Plots illustrating the impact of Mn, Ni, Si and P composition in APT tips on the nature of segregation observed following self-ion Irradiation A. Each plot gives the tip content of a single element, with each data point representing an APT tip volume of a given dpa. The shape of the data point indicates the alloy of origin, whilst the colours refer to the whether MNS clustering (in the Ni, Mn and Si plots) and/or P atmosphere formation (for the P plot) is observed.

higher incidence of MNS-type clustering

- materials B and C contain less P, which links to no atmospheres being observed

Some of the observed compositional fluctuations are expected in these particular samples. The presence of Mn in carbides commonly results in large Mn variation and there is less Si in the HIPed samples on account of the presence of Si-rich secondary precipitates (the HIPed dataset with particularly low Si may be adjacent to one of these particles). However, it is also important to consider the holistic impact of damage level and tip composition in determining whether particular forms of irradiation-induced segregation is observed.

6.1.1 Phosphorus segregation

Regions of high local P concentration (not seen in the unirradiated samples) were primarily found in the HIPed and LF samples, likely a result of the higher nominal phosphorus content of these two alloys compared to the novel forgings B and C (see nominal compositions given in Chapter 3 Section 3.1). Due to the very low P content of the steels, denser regions of P atoms can be identified visually when inspecting the atoms maps. However, for clarity, local concentration mapping was useful in highlighting these regions of locally high P content. Examples of the P local chemistry atom maps are shown in Figure 6.4

Datasets where these atmospheres are observed are discussed in this section, separately from instances where there is only P segregation to interfaces or dislocations (see Section 6.1.3), as these are specific instances of RIS and RED behaviour respectively. As seen in Figure 6.4, it is at dislocations where the P is found within the forged B and C steels, without accompanying evidence of P atmospheres. Whereas P decoration of boundaries and dislocations is observed in non-irradiated alloys, distinct, quasi-spheroidal volumes of higher P concentration seem to be a feature induced by ion irradiation.

The diffuse nature of the P atmospheres makes characterisation difficult; whilst they are

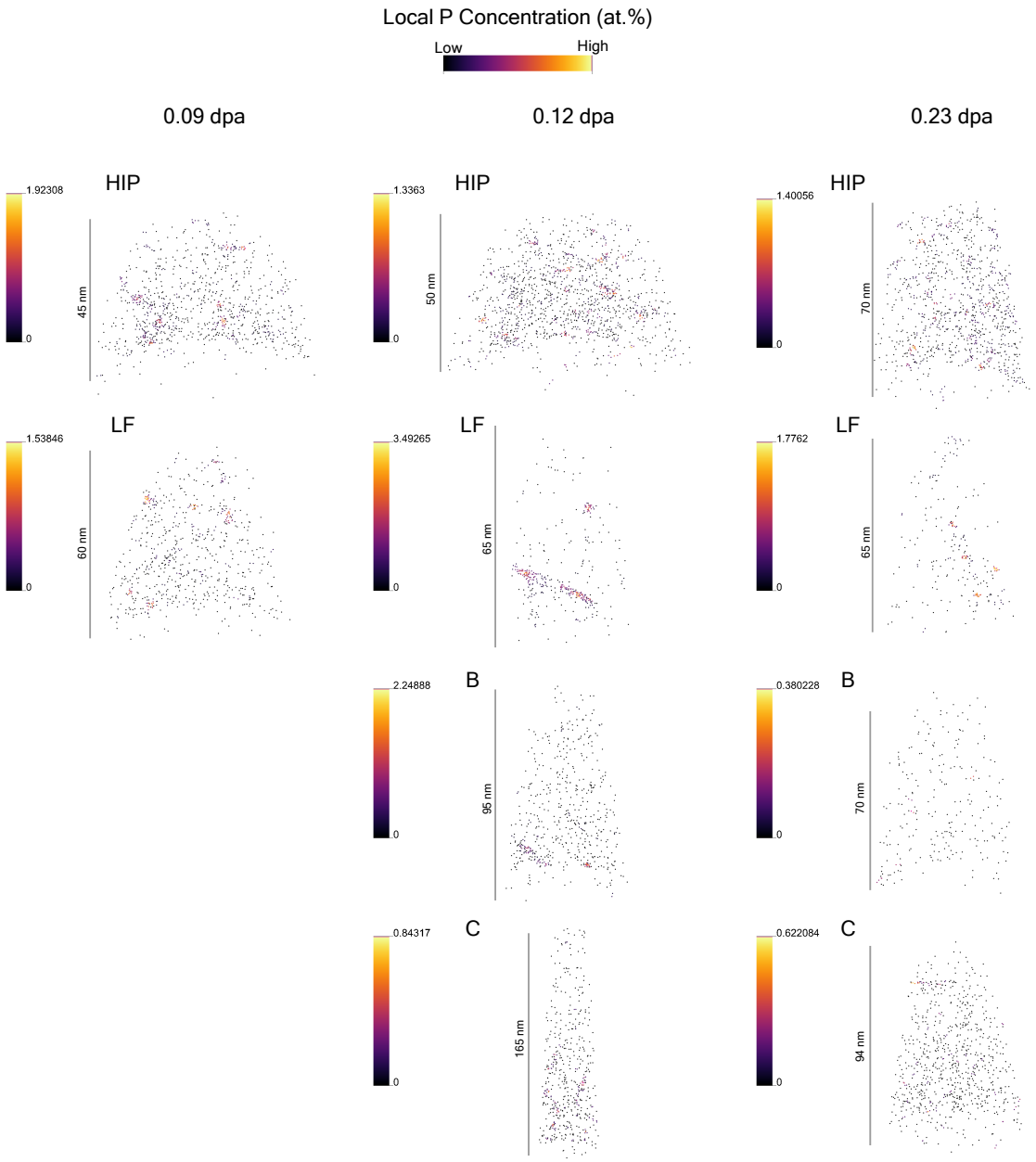

Figure 6.4: APT reconstructions showing only the P atoms present in each Cartridge A Fe^{4+} irradiated sample, with the included colour map indicating the local P concentration about each P atom. Some P segregation is in the form of P atmospheres (circular, high local concentration regions), whereas some is in the form of dislocations (linear features with relatively high P local concentration)

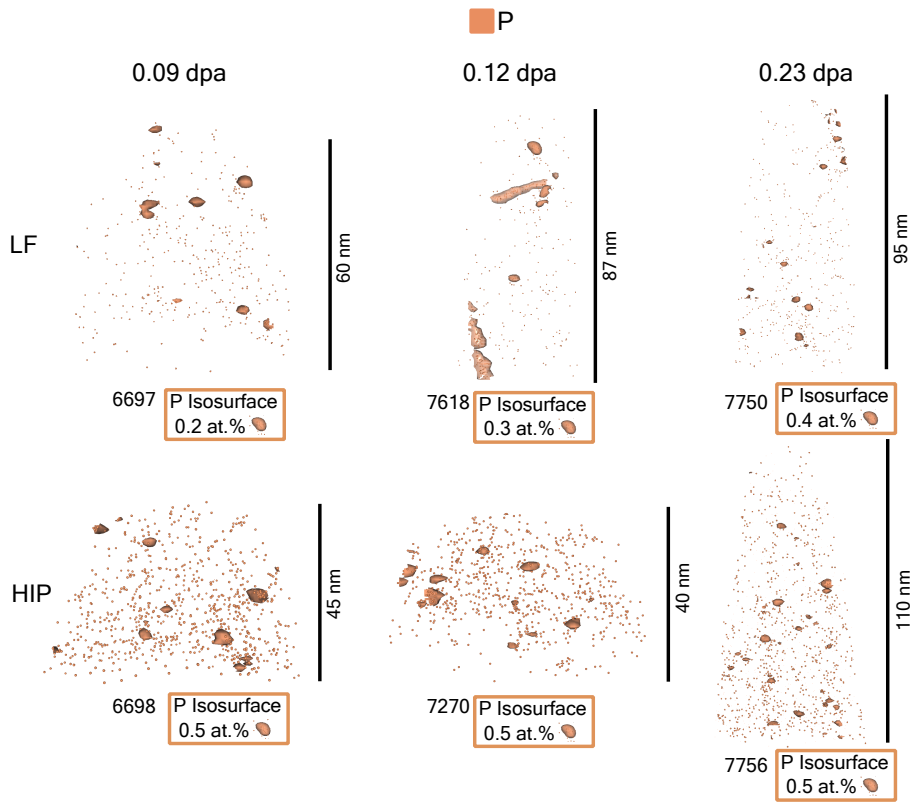

Figure 6.5: P atmospheres in HIPed and LF Fe^{4+} irradiated samples, at 0.09 dpa, 0.12 dpa and 0.23 dpa, 300°C. The regions of higher P concentration are highlighted by isosurfaces, ranging from 0.3-0.5 at.% P.

visible within APT datasets, extracting them for further analysis is non-trivial. As shown in Figure 6.5, isosurfaces (which range from 0.3-0.5 at.%) are a good way of illustrating the existence and approximate locations of these clusters, and match well with the segregation seen in atom maps. However, although they can provide an approximate local concentration value for P it is limited in its ability to accurately discern both the chemistry and morphology of these atmospheres.

One alternative method is to calculate the local concentration about each P ion, as shown in Figure 6.4, then filter datasets to only include those atoms with a local concentration above a given threshold. This then gives the extracted atoms, where P concentration is higher, although they are not grouped into distinct atmospheres during analysis.

A potential approach to clearly define the locality of individual atmospheres is MSM, considering only P atoms as solute. The intricacies and limitations of the application of this method to P atmospheres are detailed in Appendix B.

Providing more conventional values associated with cluster quantification, such as volume fraction (V_f) and size, is not straightforward, as there is uncertainty, particularly at higher dpa, in the extent to which other solute elements (particularly Mn, Ni and Si) are incorporated into the high P regions. As dose increased, Mn, Ni and Si were more clearly displaying segregation, increasing the likelihood that these species were incorporated into solute-rich regions which already contained P. Due to this uncertainty as to what stage a P atmosphere has some correlation to a part of a Mn-Ni-Si cluster, number density (N_d) calculation is more appropriate when considering only P atmospheres.

For consistency, and taking into account that the local concentration analysis appeared to better capture the P regions visible in reconstructions, atmospheres were counted based on the number of regions where P content was higher than 0.4% for the HIPed samples and 0.3% for the forged (accounting for the higher P content of HIPed causing more, randomly high concentration fluctuations which could be captured at lower isoconcentration values). The average N_d for each dpa is presented in Table 6.2, as calculated by dividing the number of observed P atmospheres in each dataset by the total volume of that atomic reconstruction. There is not a clear trend correlating the amount of phosphorus atmospheres with manufacturing route or irradiation dose, but an idea of their distribution is gained.

Table 6.2: Number densities of P atmospheres in HIPed and LF samples from Irradiation A.

Material	P Atmosphere Number Density (m^{-3}) (2sf)		
	0.09 dpa	0.12 dpa	0.23 dpa
HIP	1.2×10^{23}	$1.8\pm0.5\times10^{23}$	$2.0\pm 0.6\times10^{23}$
LF	3.6×10^{22}	$1.8\pm0.8\times10^{23}$	$1.0\pm0.35\times10^{23}$

6.1.2 Early stage MNS clustering

For Irradiation A, the lack of APT-detectable defect features, in the form of MNS clusters or dislocation loops, implies a low level of damage experienced by the samples. As a first-pass analysis, on datasets with carbides and/or grain boundaries removed, the use of frequency distribution analysis indicated which, if any, ions were displaying a non-random arrangement. The elements of interest were those where p <0.001, and these typically included C and Mo, due to dislocation segregation, and Mn, Ni, Si and P. For determination of MNS-type clustering, any of Mn, Ni or Si which were shown to display heterogeneous distribution were included as solute atoms in the MSM chosen parameters. In this case, P was not included where a random distribution was identified, as these instances were linked to the P atmospheres and thus P was treated separately. There were some cases where the segregation occurring was beyond the sensitivity of the MSM algorithm, which

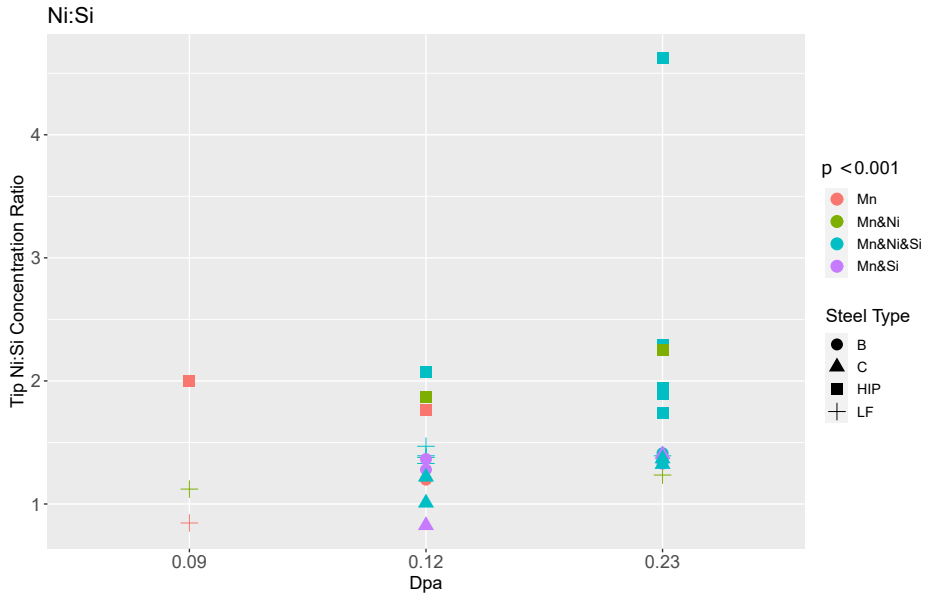

Figure 6.6: Plot indicating the Ni:Si ratio in each APT tip from the Irradiation A samples, with data-point colour indicating the results of frequency distribution analysis on that tip (indicative of the non-randomly distributed solute) and shape showing the alloy origin.

produced no statistically significant clusters for these datasets.

Where solute clustering was found, capturing them using the Maximum Separation Method was difficult; in some cases visual clusters in the reconstructions could be correlated with those extracted with MSM in an attempt to assess the validity of the parameters chosen. A detailed discussion of the method for choosing MSM input parameters in this case is given in Appendix B. Ultimately, as with the neutron samples, a NN_{order}= 1 seemed most suitable where very little segregation was occurring. The d_{max} ranged from 0.40-0.58 nm, and the N_{min} varied from 9 to 19 atoms.

Using frequency distribution analysis prior to the MSM, demonstrated that, whilst MNS-type clustering was occurring, it was not necessarily producing clusters of all three expected elements. Frequency distribution calculations often showed datasets where only one or two of the species were involved in solute clustering, for example Mn and Si, or just Mn, had p <0.001. Figure 6.6 shows the variation of non-random solute with alloy type and dpa, in relation to the ratio of Ni to Si in the tip. This ratio was chosen because all reconstructions showed Mn inhomogeneity, suggesting the interplay between Ni and Si played a more nuanced role.

Table 6.3: Average number density and volume fractions of MNS clusters in samples produced in Irradiation A.

Material	(0.12 dpa)		(0.23 dpa)	
	Number Density (m^{-3})	Volume Fraction (%)	Number Density (m^{-3})	Volume Fraction (%)
HIP	—	—	$1.87\pm1.29 \times10^{23}$	0.009±0.006
LF	$1.04\pm0.60 \times10^{23}$	0.006±0.003	$2.03\pm1.01 \times10^{23}$	0.017±0.009
B	$1.43\pm0.95 \times10^{22}$	0.001±0.000	$3.31\pm0.03 \times10^{22}$	0.001±0.001
C	$1.46\pm1.63 \times10^{23}$	0.005±0.006	$3.42\pm0.60 \times10^{22}$	0.001±0.000
Overall	$8.81\pm5.49 \times10^{22}$	0.004±0.002	$1.14\pm0.80 \times10^{23}$	0.007±0.007

This concept can be further developed by looking at the nature of solute clustering detected in each reconstruction. Using the cluster analysis results, the average number densities for each alloy were extracted for each dpa where solute clustering was present. These results are shown in Table 6.3. On average, there is the expected increase in N_d with dose, however this is within error. This illustrates how the cluster number densities provided should be treated with caution, as in most instances where clusters were found there were very few per dataset, and this inhomogeneous dispersion belies an increased likelihood

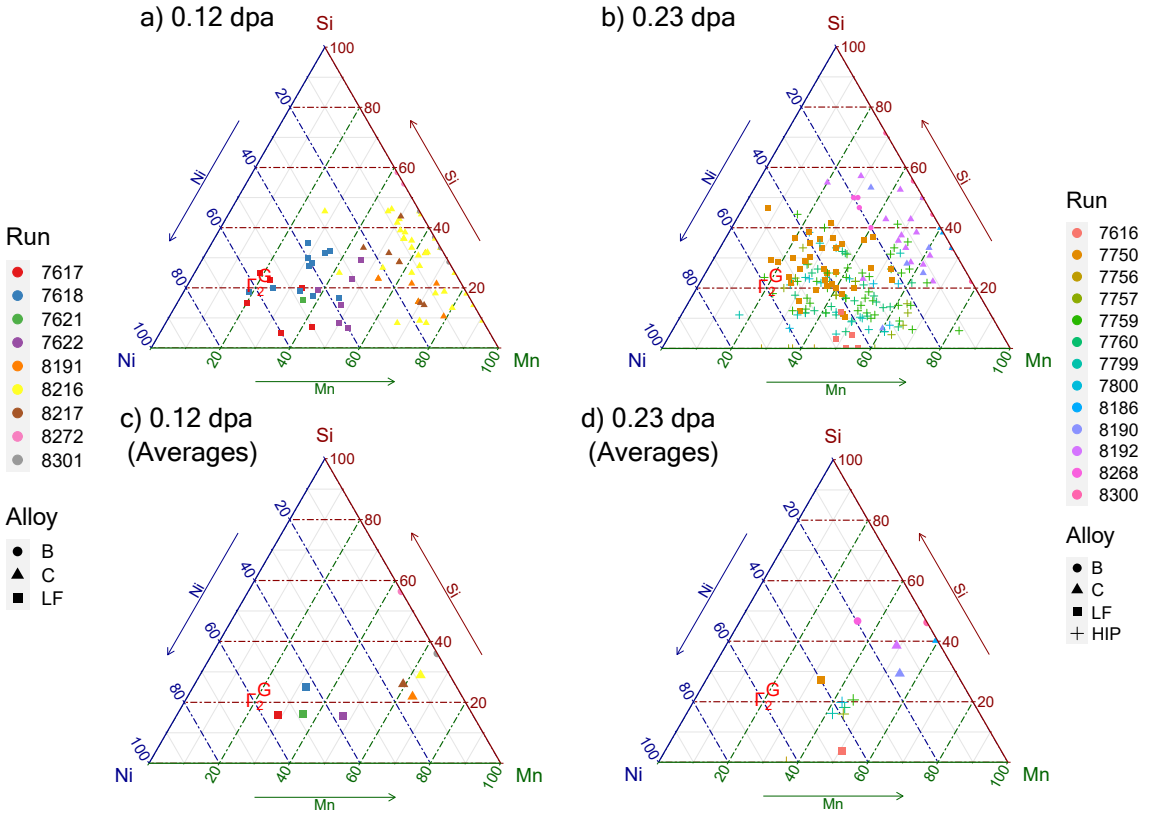

Figure 6.7: Ternary diagrams illustrating the relative fractions of Mn, Ni and Si in the clusters extracted from samples subjected to Irradiation A, according to the dose received. Colour varies with atom probe run number and shape varies with the form of alloy the clusters originate from. In plots a) and b) each point corresponds to a cluster, indicating the spread in cluster composition within datasets, whereas the mean compositional values for the clusters found in each reconstruction are shown in plots c) and d). The compositions of the proposed G and Γ_2 phases are denoted in red.

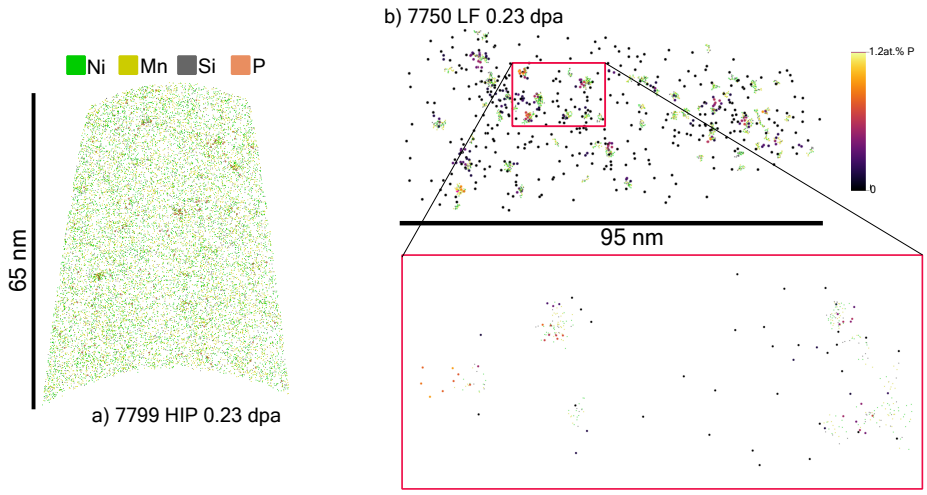

Figure 6.8: Two methods of matching MNS cluster location to regions of P enrichment: a) 5 nm slice of APT reconstruction, where P atoms are shown alongside visible Mn/Ni/Si-rich volumes; b) local concentration heat map for P atoms in APT reconstruction (high local concentration = yellow, low local concentration = black) overlaid with results of cluster analysis (MSM), where P atoms are larger for clarity and only the Mn, Ni and Si atoms within the identified clusters are included.

of detectable clusters in those reconstructions containing a higher number of ions. For example, no MNS clustering was found in the 0.12 dpa HIPed sample, however, this may be a product of a reduced amount of collected ions compared to the other materials at this dose.

The cluster compositions were also calculated for each reconstruction, with the cluster Mn, Ni and Si relative contents shown as ternary plots in Figure 6.7, indicating how the cluster compositions varied from dataset to dataset, and within different alloy types. The average cluster size for all detected MNS clusters was 43 atoms, which corresponds to an approximate radius of 1.0 nm, using the method explained in detailed in Chapter 3.

There is also evidence that some MNS clusters seen at higher dpa correlate spatially with previously formed P atmospheres, as shown in Figure 6.8, which shows both P atoms in near-proximity to apparent MNS clusters, and overlaps clusters found by MSM with a local concentration atom map for P. Here, regions of locally higher P concentration coincide with apparent MNS clusters.

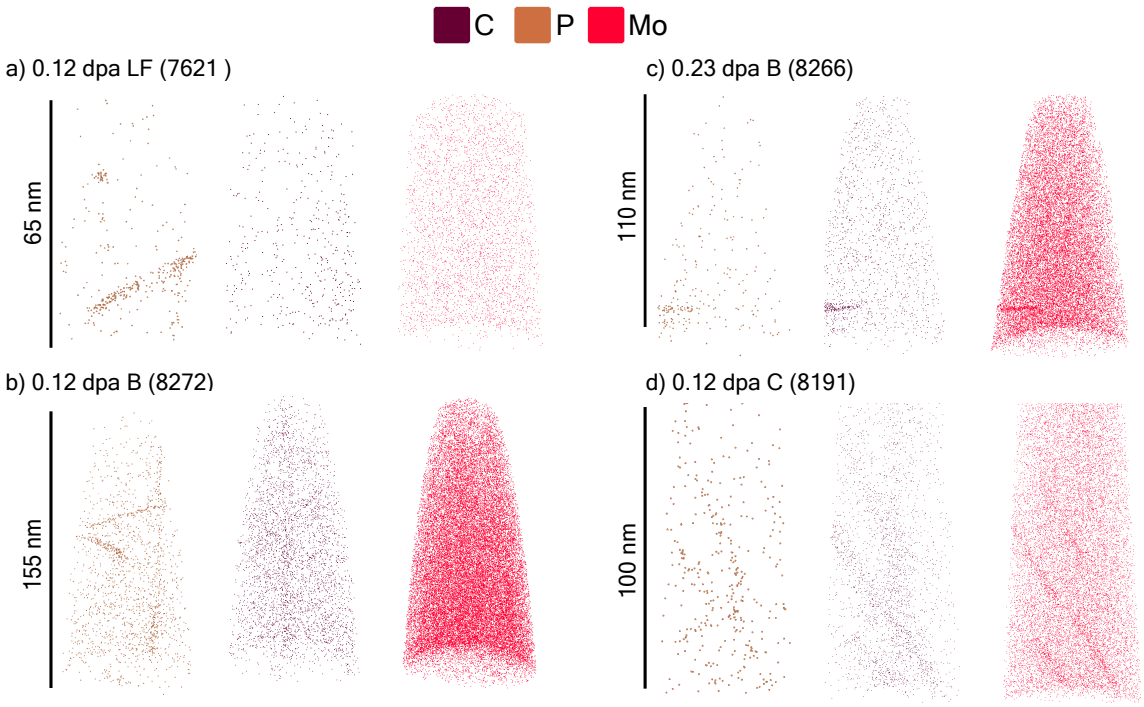

Figure 6.9: C, P and Mo decorated dislocations in SA508 samples following Irradiation A.

6.1.3 Dislocations

Even at low dose, there is evidence of segregation to dislocations under irradiation. Whilst dislocations are commonly seen in unirradiated samples, they can be induced by ion bombardment, hence there are two forms of dislocation segregation taking place; solute diffuses to both existing dislocations and to those newly formed under irradiation. Using APT, there does not appear to be a consistent method of distinguishing between these two forms of segregation. Multiple samples contained decorated dislocations, however there was variation in the solute involved and in prevalence. Whilst forgings B and C did not contain P atmospheres, they did exhibit a relatively high number of P-decorated dislocations (some of these were shown in Figure 6.9).

Closer inspection of the dislocations found in these datasets showed that some were

decorated by Mo and C (in addition to P), and some were not (as indicated in Figure 6.9).

6.2 B: 0.6 dpa Fe^{4+} 150°C

In Irradiation B, a 5 MeV Fe^{4+} ion beam was applied using the conditions detailed in Table 6.4. With these conditions, combined with the SRIM vacancy calculations, the dose graph shown in Figure 6.10 was produced, indicating an approximate damage of 0.6 dpa at 500 nm depth.

Table 6.4: Fe^{4+} Irradiation B condition. *at target depth.

Target Depth	Dpa*	Average Beam Current	Beam Area (cm^2)	Dpa rate* (dpa/s)	Temperature (°C)
500 nm	0.6	203.46 nA	5.4(± 0.5)	2.13×10^{-5} $\pm \approx 10^{-11}$	150.2 ±2.0

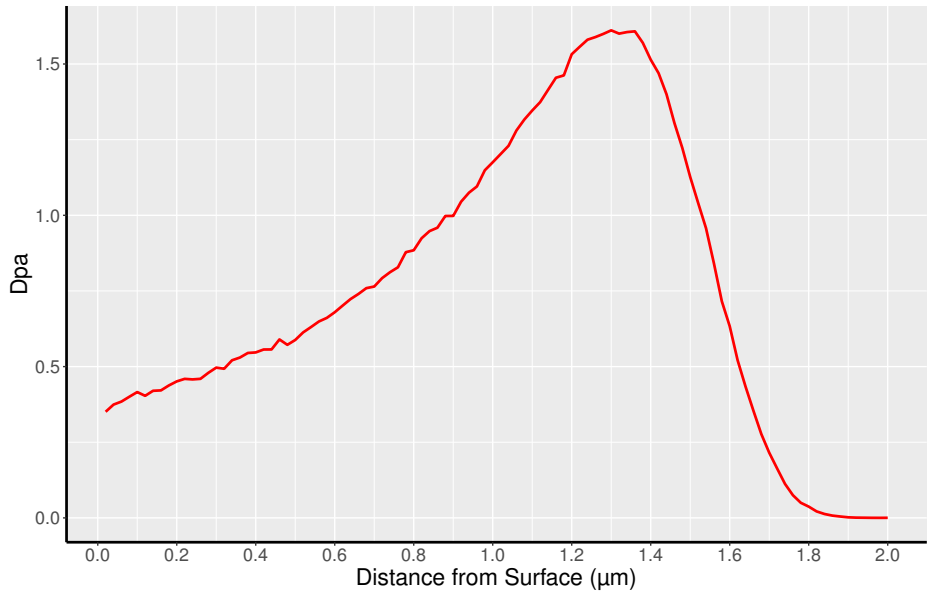

Figure 6.10: Damage profile into Fe^{4+} irradiated surface for a SA508 HIPed sample with target damage of 0.6 dpa at 500 nm depth.

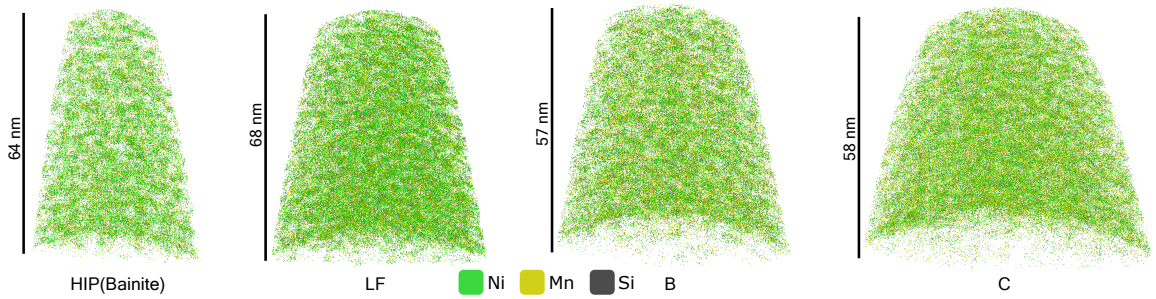

Figure 6.11: Example atom maps from the Irradiation B SA508 steel samples. Only Mn, Ni and Si atoms are shown to highlight solute clustering behaviour.

Following irradiation, 39 APT samples were fabricated, of which 27 yielded data appropriate for further analysis. Representative atom maps from each material type are shown in Figure 6.11. In this set of self-ion irradiation conditions, the primary defect induced was Mn-Ni-Si clustering. For reference, the average compositions of the reconstructed APT tip volumes are given for each alloy type in Table 6.5.

Table 6.5: Table showing the average APT tip compositions of Irradiation B samples, separated by alloy origin.

	Fe	Mn	Ni	Si	Cr	Mo	C	P	Cu	Other
HIP	97.33 ±0.19	0.97 ±0.16	0.97 ±0.06	0.43 ±0.02	0.09 ±0.02	0.18 ±0.04	0.06 ±0.06	0.02 ±0.00	0.02 ±0.00	0.04 ±0.03
LF	96.86 ±0.19	1.20 ±0.13	0.80 ±0.10	0.59 ±0.01	0.22 ±0.05	0.18 ±0.04	0.04 ±0.03	0.01 ±0.00	0.02 ±0.00	0.09 ±0.04
B	97.12 ±0.15	1.02 ±0.11	0.80 ±0.05	0.62 ±0.01	0.13 ±0.03	0.16 ±0.03	0.04 ±0.04	0.00 ±0.00	0.02 ±0.00	0.08 ±0.02
C	96.84 ±0.22	1.23 ±0.17	0.85 ±0.05	0.57 ±0.02	0.16 ±0.04	0.22 ±0.04	0.02 ±0.01	0.00 ±0.00	0.02 ±0.00	0.09 ±0.03

6.2.1 MNS clustering

All of the datasets from Irradiation B contained clear MNS clustering, with a more defined, spherical morphology than seen at lower dpa, although still fine in scale.

Table 6.6: Average cluster volume fractions and number densities for the APT samples of 0.6 dpa self-ion-irradiated (Irradiation B) SA508 steel.

	Average Cluster Volume Fraction (%)(3sf)	Average Cluster Number Density (m^{-3}) (3sf)
HIP-Ferrite	0.557 ± 0.091	$6.74\times10^{24} \pm 0.99\times10^{24}$
HIP-Bainite	0.578 ± 0.163	$7.15\times10^{24} \pm 2.19\times10^{24}$
LF	0.524 ± 0.095	$5.66\times10^{24} \pm 0.78\times10^{24}$
B	0.361 ± 0.156	$4.66\times10^{24} \pm 2.30\times10^{24}$
C	0.399 ± 0.064	$4.77\times10^{24} \pm 0.47\times10^{24}$

Cluster analysis showed a mid-to-high number density of fine-scale clusters, with ill-defined spatial extents. Using the MSM method (NN_{order} of 1), with d_{max} ranging from 0.48-0.54 nm and N_{min} ranging from 14-23 atoms, the average cluster number densities and volume fractions were extracted (shown in Table 6.6). Across the alloys, the average amount of detected solute clustering was of similar orders of magnitude, yet, there was broader distribution in the HIP-Bainite and Forging B. This is a result of those alloys containing outlier datasets which had either considerably higher or lower cluster densities, rather than a larger general scatter. Comparison to the local tip compositions of these datasets, showed that where N_d/V_f was lower there was no significant deviation from the average solute contents of those samples. Thus, it is more likely these anomalies are a product of random volume sampling in APT.

Average cluster compositions for each APT dataset are displayed in Figure 6.12. The compositions are strongly centred on a region where the Mn:Ni ratio is slightly higher than in the thermodynamically predicted G and Γ_2 phases.

The average cluster size across all 0.6 dpa samples produced by Irradiation B is 61 (±26) atoms (accounting for the number of ranged solute atoms in each non-edge cluster, modified by the LEAP 5000XR detection efficiency, with Fe atoms removed). This gives an

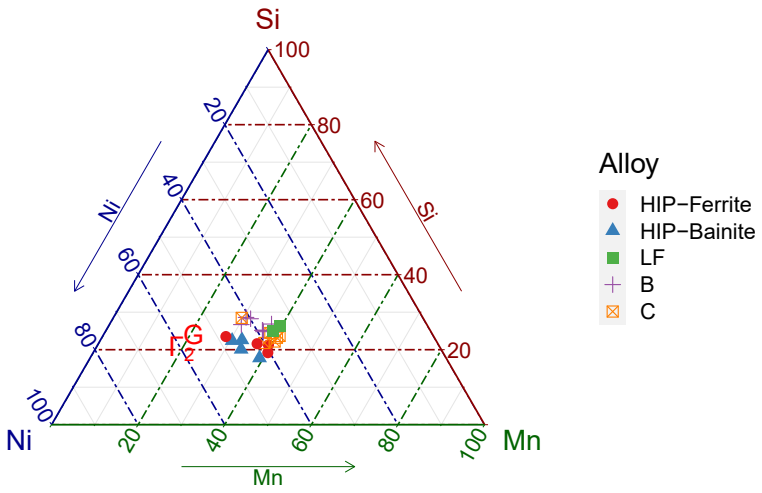

Figure 6.12: Ternary diagrams illustrating the relative fractions of Mn, Ni and Si in the clusters extracted from samples subjected to Irradiation B. Colour and shape indicate the material origin of the average cluster compositions represented by each data-point.

approximate average cluster diameter of 1.1 nm, using the Equation 3.5 in Section 3.6.

6.2.2 Case study: influence of depth-damage profile on defects observed in Large Forging

To investigate the effect of damage levels around the intended 0.6 dpa dose, the LF sample was used to produce FIB lift-outs from above and below 500 nm into the irradiated surface. Whilst the aesthetic of clusters extracted from APT remained consistent with dose, the cluster N_d and V_f did change (illustrated in Figure 6.13). As expected, on average there was an increase in both N_d and V_f as the sampling distance from the irradiation-surface increased.

Segregation to dislocations

In some APT atom maps, there is visual suggestion of the existence of network dislocations decorated with Mn, Ni and Si (in addition to the C, Mo and P seen in the unirradiated or lower dose samples). Whilst there is uncertainty as to the extent the linear features observed

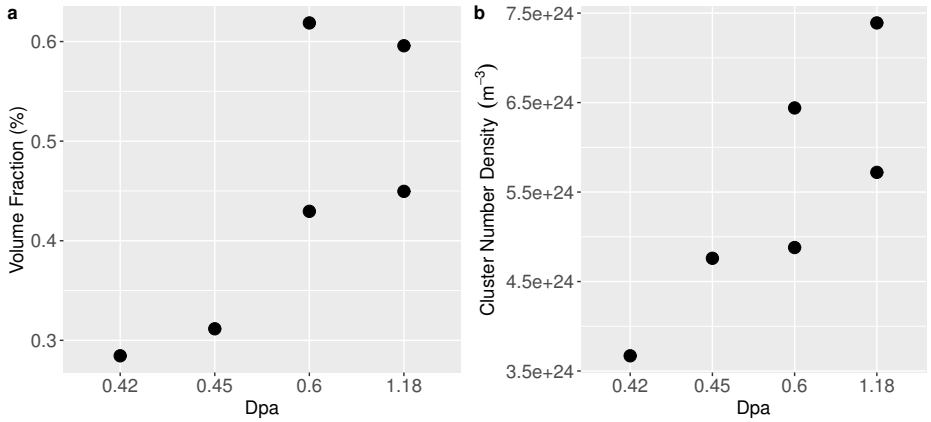

Figure 6.13: Variation of N_d (a) and V_f (b) in LF samples at various dpa (from Irradiation B).

in the 0.6 dpa samples are physical, or a result of random cluster distribution, within the higher damage (1.18 dpa) LF samples these decorated dislocations are significantly more easily discernible (Figure 6.14). The presence of dislocations decorated with the same solute species involved in solute clustering has been shown to complicate the cluster identification

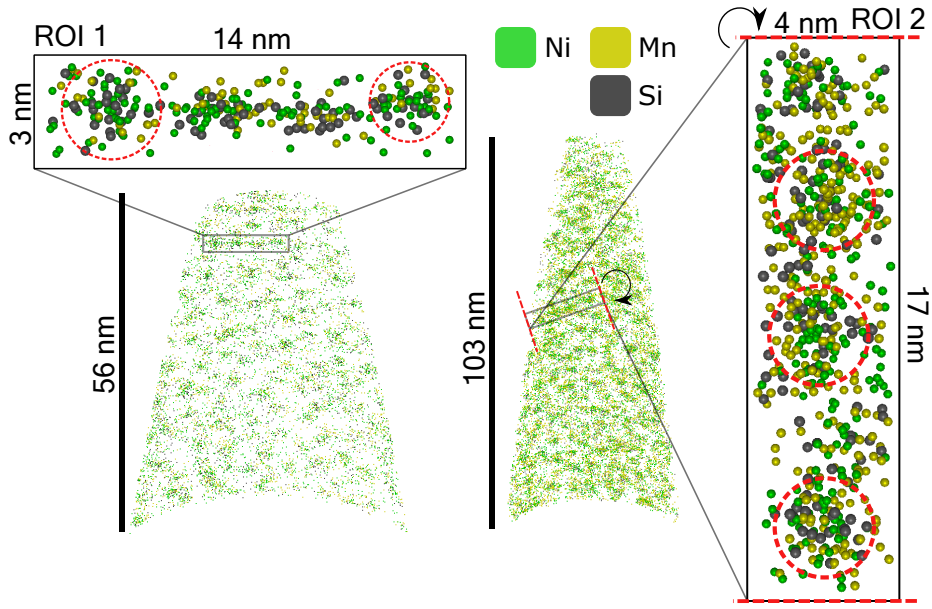

Figure 6.14: Mn, Ni and Si decorated dislocations in two 1.18 dpa self-ion-irradiated LF SA508 steel. ROIs show the isolated dislocation regions, whilst the red circles depict where clusters appear to lie upon the dislocation line.

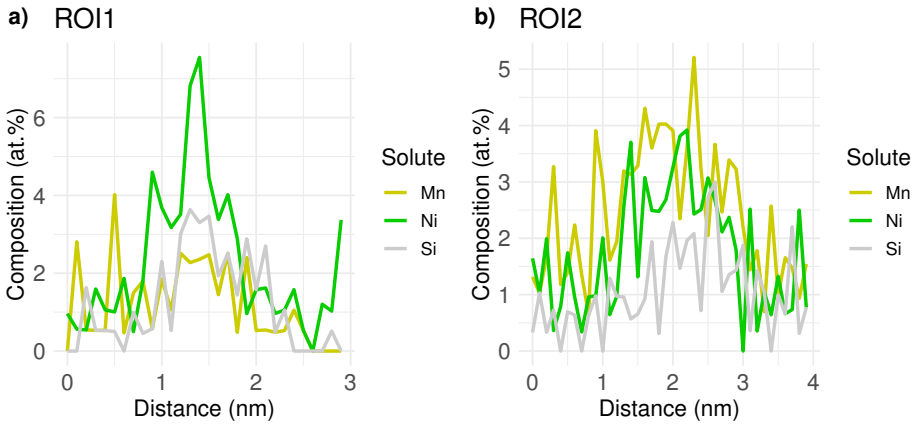

Figure 6.15: Concentration profiles indicating Mn, Ni and Si enrichment at dislocation lines in 1.18 dpa LF samples from self-ion Irradiation B. The profiles are taken through the entirerity of the ROI volumes encompassing dislocations (defined in Figure 6.14).

process, as segregation blends with MNS cluster formation, such that clusters appear to lie on the linear, enriched features.

In the case of the extractable dislocations in the elevated damage subset of LF samples, a concentration profile taken through each dislocation ROI volume allows a reasonable estimate of the extent of local enrichment present on these defects. From the plots in Figure 6.15, there is clear evidence of local enrichment of Ni, Mn and Si on the isolated dislocation lines, although the levels vary between the two dislocations sampled.

6.3 F: 5 dpa Fe^{4+} 300°C

A higher dose takes irradiation-induced and irradiation-enhanced behaviour to a point where the outcome is amplified, with the aim of comparing between the materials at a stage where a significant amount of the possible irradiation effects have been allowed to occur.

Table 6.7 shows the 5 MeV Fe^{4+} ion irradiation conditions utilised in this experiment. This resulted in 5 dpa of damage at a depth of 500 nm, as shown in the dose profile (Figure 6.16).

Table 6.7: Fe^{4+} Irradiation F condition. *at target depth.

Target Depth	Dpa*	Average Beam Current	Beam Area (cm^2)	Dpa rate* (dpa/s)	Temperature (°C)
500 nm	5	1.01 µA	5.4(± 0.5)	1.09×10^{-5} $\pm \approx 10^{-11}$	304.2 ±11.8

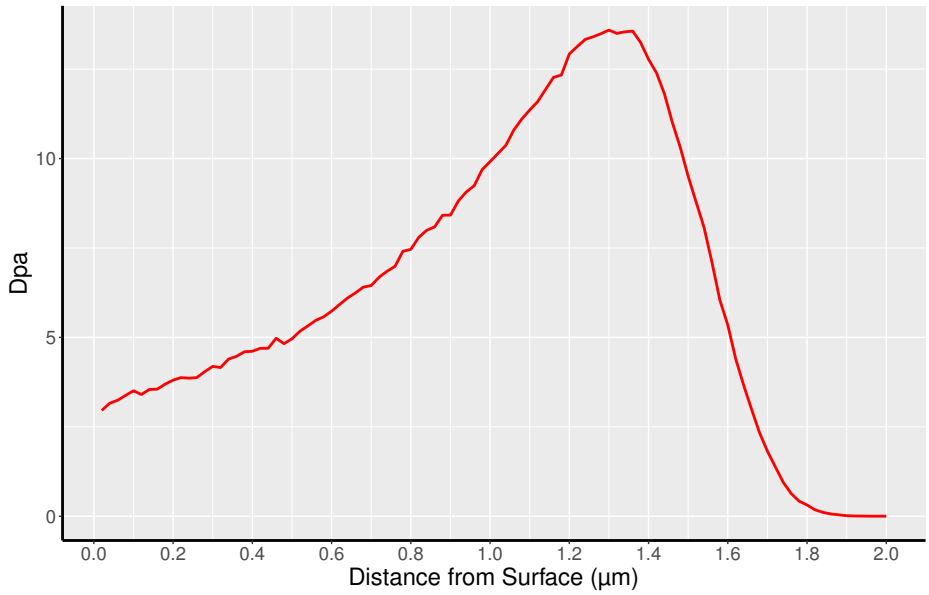

Figure 6.16: Damage profile into Fe^{4+} irradiated surface for a SA508 HIPed sample with target damage of 0.5 dpa at 500 nm depth

In total, FIB was used to produce 36 APT tips, resulting in 23 usable atom maps across the four alloy types. The reconstructions from Irradiation F were significantly more diverse in appearance than those of lower dpa; a result of more distinct segregation features. The average compositions of the reconstructed APT tip volumes are given for each alloy type in Table 6.8. Interestingly, compared to the as-received samples there is an increase in the amount of C following Irradiation F.

An APT specimen overview is shown in Figure 6.17, with only Mn, Ni and Si atoms shown to highlight the variety of segregation behaviour. On first inspection, the main features induced by Irradiation F are: large, MNS clusters; smaller clusters with a higher

Mn:Ni ratio; and enriched dislocation regions (including loops).

Table 6.8: Table showing the average APT tip compositions of Irradiation F samples, separated by alloy origin.

	Fe	Mn	Ni	Si	Cr	Mo	C	P	Cu	Other
HIP	97.31 ±0.34	1.01 ±0.16	0.78 ±0.13	0.40 ±0.08	0.10 ±0.02	0.18 ±0.02	0.14 ±0.07	0.01 ±0.01	0.02 ±0.00	0.05 ±0.02
LF	96.97 ±0.38	1.08 ±0.12	0.75 ±0.14	0.63 ±0.08	0.21 ±0.03	0.16 ±0.03	0.09 ±0.03	0.03 ±0.03	0.02 ±0.00	0.10 ±0.02
B	97.67 ±0.67	0.82 ±0.30	0.58 ±0.20	0.41 ±0.17	0.12 ±0.04	0.17 ±0.03	0.11 ±0.03	0.00 ±0.00	0.01 ±0.00	0.11 ±0.02
C	95.95 ±0.04	1.04 ±0.05	0.68 ±0.10	0.57 ±0.05	0.17 ±0.00	0.26 ±0.04	0.22 ±0.03	0.00 ±0.00	0.02 ±0.00	0.10 ±0.02

6.3.1 MNS clusters

The inclusion of large MNS clusters alongside highly enriched dislocations and dislocation loops, increased the difficulty of extracting cluster information. Whilst some reconstructions contained primarily stand-alone (not on dislocations) MNS clusters, many were significantly more complex, incorporating a mixture of homogeneously and heterogeneously nucleated clusters. With the influence of nucleation site on the size, composition and morphology of the clusters being of particular interest in these samples, a method of isolating each category of cluster for analysis was required.

Unfortunately, the methodology of the MSM algorithm does not lend itself to distinguishing between those solute atoms segregated to dislocations and those involved in clusters attached to those same dislocations. An example of the complexity of this problem is shown in Figure 6.18, where the standard MSM procedure has been applied to a HIPed dataset containing multiple, interwoven RIS features. Here it is clear that applying MSM without further data filtering stages would lead to false identification of dislocation

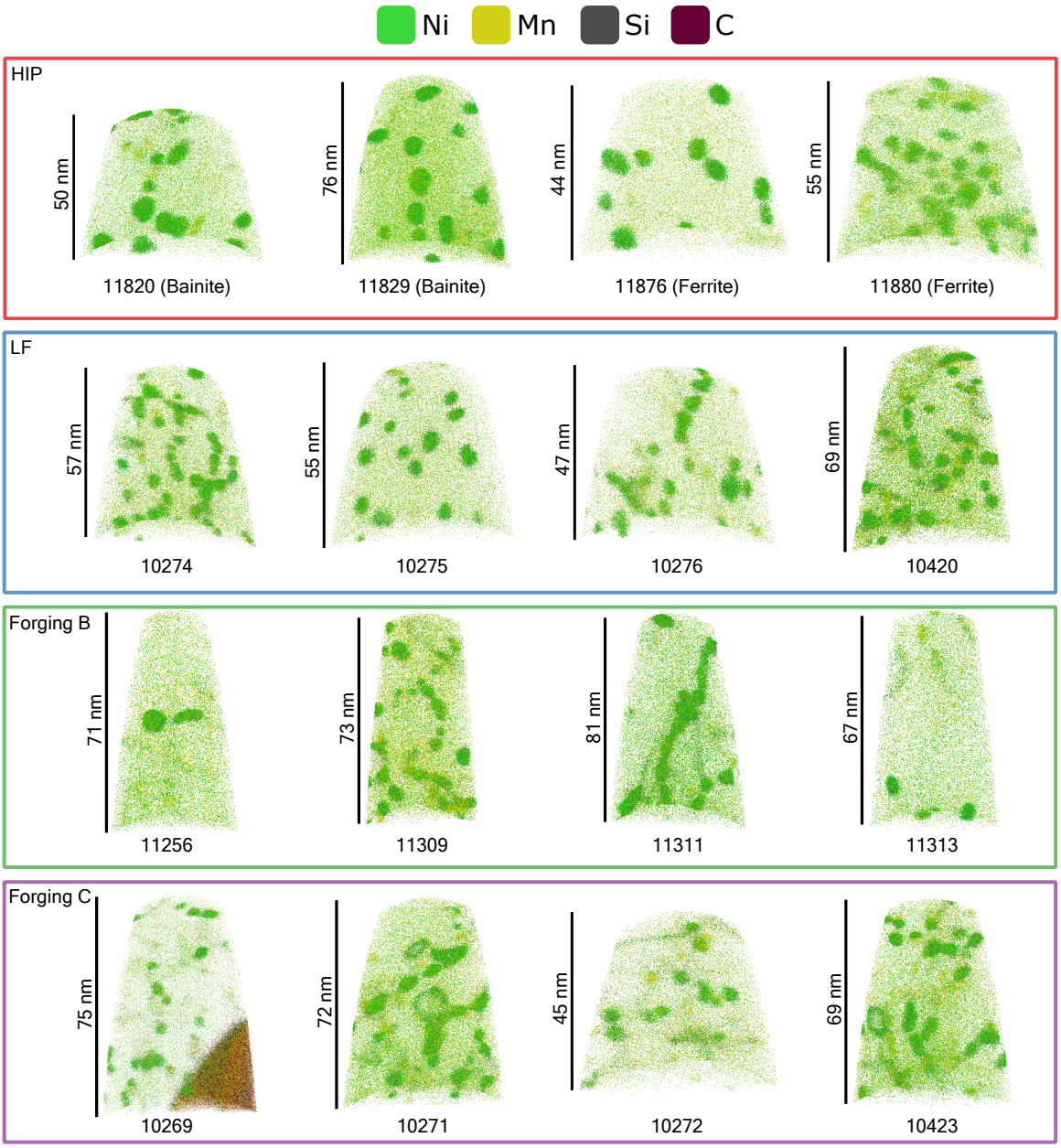

Figure 6.17: Overview of APT maps from samples produced by Irradiation F. Only Mn, Ni and Si atoms are shown for clarity (with the exception of the C in forging C, sample 10269).

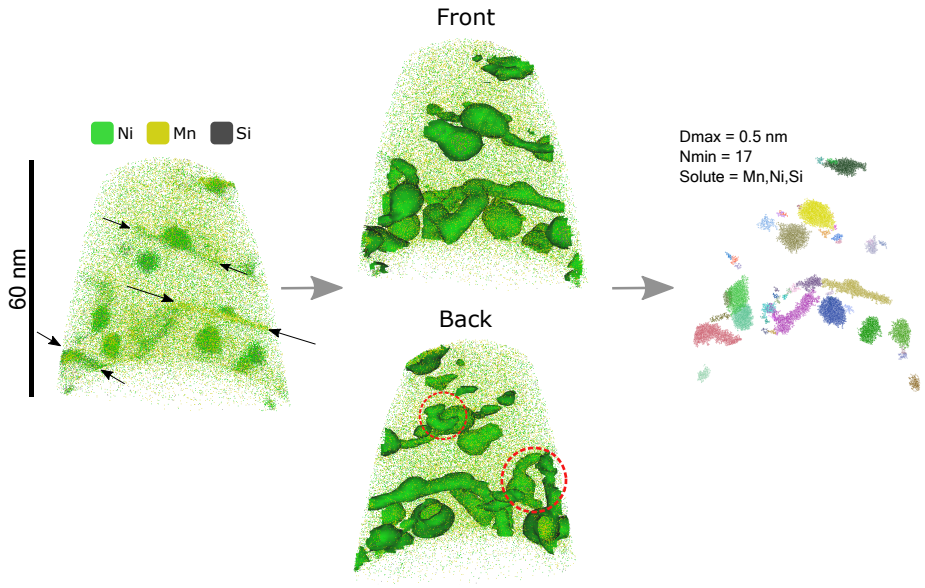

Figure 6.18: Application of the standard MSM procedure (previously utilised in this work) to an APT dataset from a SA508 sample produced by Irradiation F. D_{max} = 0.5, N_{min} = 17, with chosen solute ions of Mn, Ni and Si. Arrows indicate the presence of dislocation in the dataset, further highlighted using an isoconcentration surface for Mn, Ni and Si atoms.

enrichment as Mn-Ni-Si clustering. Dislocations are highlighted using an isoconcentration surface for Mn, Ni and Si atoms.

Subsequently, the method used for Irradiation F samples was multi-stage, as illustrated in Figure 6.19. Given dislocation segregation primarily involved Mn, MSM was firstly conducted using only nickel and silicon atoms defined as solute, such to minimise the number of dislocation regions extracted. A large N_{min} (generally $\approx$ 50) was selected in order to isolate the large Mn-Ni-Si clusters visible in each atom map and reduce the amount of small dislocation regions identified as clusters, and the erosion step was not implemented (distance set to zero), such to avoid removal of Mn atoms at the cluster peripheries.

Following application of the Maximum Separation Method, any remaining dislocation features were then manually removed from the datafile. From here, the extracted clusters were compared to the atom map, such that the nucleation site for each cluster could be identified for future analysis. Clusters were deemed to lie on dislocations where they clearly

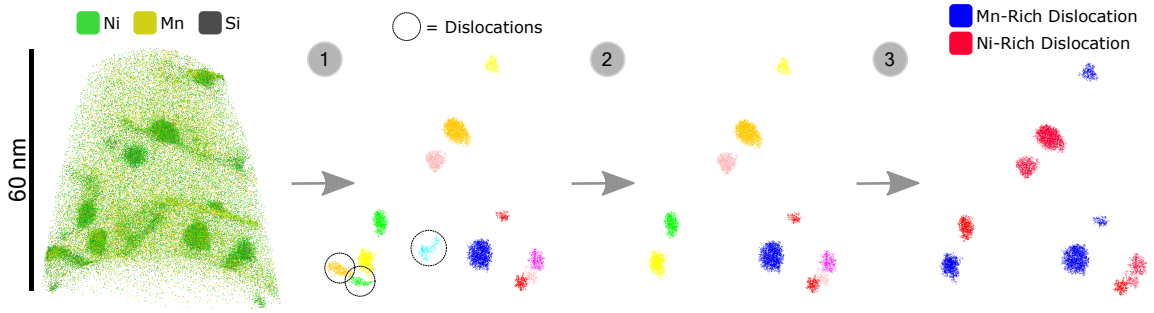

Figure 6.19: Process for the extraction of large Mn-Ni-Si clusters from Irradiation F APT datasets. Starting with the original reconstruction (far left), MSM using Ni and Si as the named solute, with d_{max} = 0.4-0.5 nm and N_{min} > 50, is used to isolate clusters (Step 1). Through comparison to the original atom map, clusters which are actually part of dislocations (highlighted by circles in second-from-left image) are removed (Step 2). Finally, the type of nucleation site for each cluster is recorded - shown visually by the cluster colouring in far-right image.

lay on a decorated dislocation line within the dataset - this could either be a significantly enriched dislocation, or a more subtle decoration. For ease of comparison, clusters found attached to Mn-rich clusters were labelled accordingly. At this point it is unknown whether the Mn cluster acted as a nucleation site for the MNS cluster, the MNS cluster as a nucleation site for the Mn cluster, or if the effect was a phenomenon associated with MNS cluster growth. However, such to clearly distinguish between those clusters without associated features and those within the proximity of Mn enrichment, Attached to Mn Cluster was included in the list of nucleation sites.

Where clusters were designated as homogeneously nucleated, this is true to the extent that visible nucleation sites could not be seen in the APT atom map. However, it simplifies the initial assumption that all matrix clusters can be described as nucleating heterogeneously on atomic-scale defect clusters (induced by irradiation). In this case, 'homogeneous' is used to describe the situation where there are no clear microstructural features acting as nucleation sites, such as dislocations or interfaces. Furthermore, given the fact that non-decorated dislocations cannot be seen in atom probe, it is impossible to conclusively rule out that heterogeneous nucleation occurred.

Table 6.9: Average cluster volume fractions and number densities for the APT samples of 5 dpa self-ion-irradiated (Irradiation F) SA508 steel.

	Average Cluster Volume Fraction (%)(3sf)	Average Cluster Number Density (m^{-3}) (3sf)
HIP-Ferrite	1.13 ± 0.34	$2.05 \pm 0.92 \times 10^{23}$
HIP-Bainite	0.84 ± 0.29	$9.29 \pm 2.83 \times 10^{22}$
LF	1.01± 0.18	$3.08 \pm 0.82 \times 10^{23}$
B	0.63 ± 0.32	$1.21 \pm 1.1 \times 10^{23}$
C	0.68 ± 0.14	$2.03 \pm 0.25 \times 10^{23}$

The measured average number density and volume fractions of the MNS clusters found in Irradiation F samples are shown in Table 6.9.

Cluster compositions

Figure 6.20 shows the relative Mn, Ni and Si compositions of clusters extracted from the Irradiation F datasets with respect to alloy origin. There does not appear to be significant variation in composition with manufacturing route.

As discussed above, the complexity of isolating these clusters may have impacted the accuracy of extracted compositions, and thus the compositions given are approximate. Using isoconcentration surfaces as a method to define composition was also considered, however, the variety of cluster sizes and interface profiles meant no consistent isoconcentration values accurately defined the boundary of every cluster in a given dataset. Once the amended MSM procedure was shown to give similar cluster compositions as those using isosurfaces, it was used on account of its improved practicality.

On average, the clusters studied contained less Mn than in the predicted G and Γ_2 phases, with correspondingly higher Si contents. This reduction in Mn may link to the presence of separate Mn-rich phases found within some datasets (Section 6.3.2).

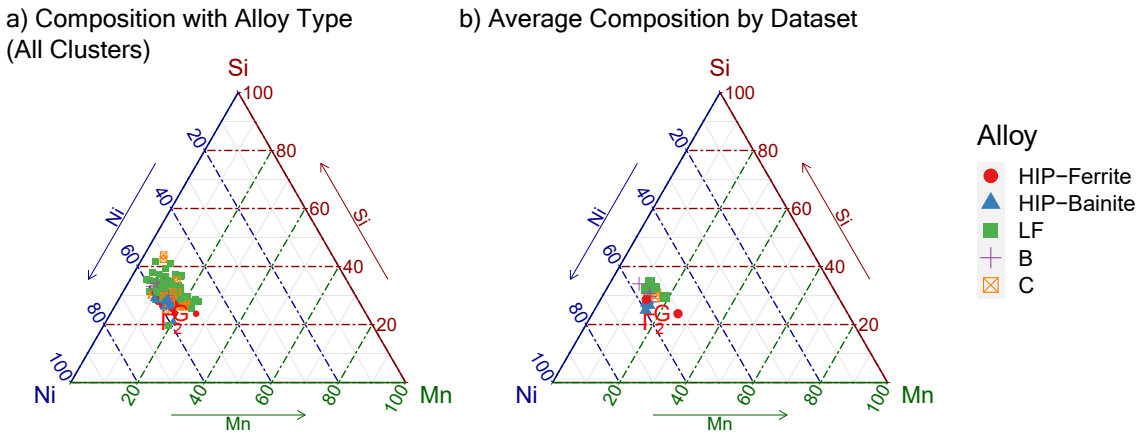

Figure 6.20: Ternary plot indicating the Mn:Ni:Si ratios of clusters found in samples from Irradiation F. Figure a) gives each extracted cluster a datapoint, whereas b) shows the average Mn, Ni, Si content for each reconstruction. The alloy of origin for each datapoint is indicated by the colour and shape.

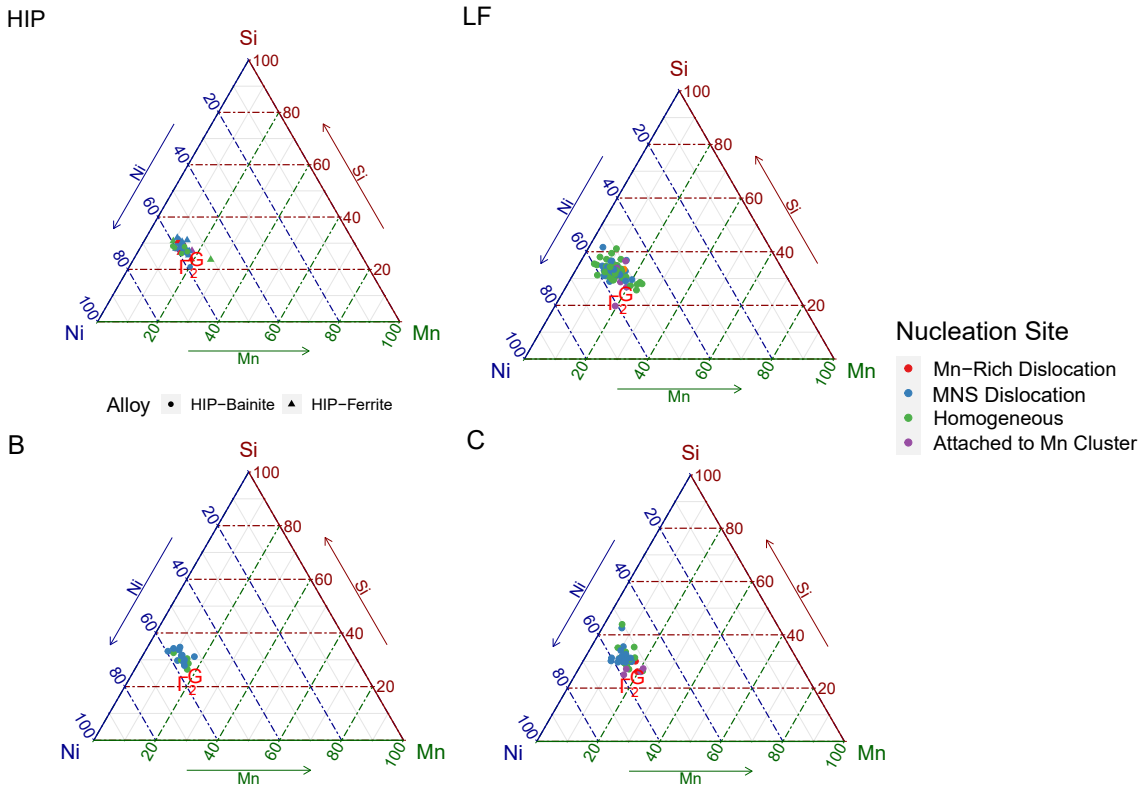

Figure 6.21: Each ternary plot indicates the Mn:Ni:Si fractions of clusters found in each of the alloy types investigated with Irradiation F. Each datapoint is an individual cluster, with its designated nucleation site indicated by colour.

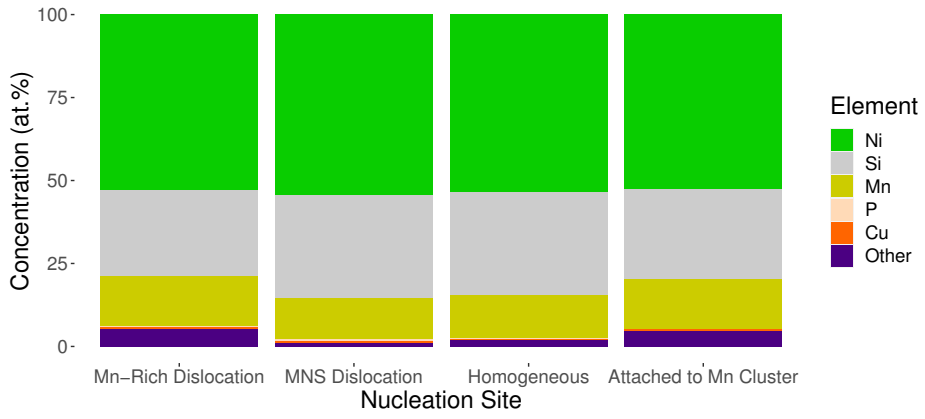

Figure 6.22: Plot of average cluster compositions in Irradiation F sample, according to classified cluster nucleation site.

Compared to the lower dpa irradiations, in the case of Irradiation F, it was the variety of cluster origins which stood-out in the APT reconstructions. As discussed above, a lack of standardised method meant that these nucleation sites were user-determined, although in most cases they were relatively clear when inspecting the atom maps. Figure 6.21 indicates the Mn:Ni:Si ratio of individual clusters from each of the alloy types, denoting the observed nucleation site, and the average relative amount of Mn, Ni and Si for each cluster origin. Although there is not much compositional variance between nucleation sites, there is a greater spread of compositions in the clusters thought to have nucleated homogeneously.

Figures 6.20 and 6.21 only consider the Mn-Ni-Si ratios of the clusters identified, which risks overlooking the amount of other solute. To demonstrate the extent to which other species are influenced, Figure 6.22 shows the average overall cluster compositions by nucleation site.

The homogeneous clusters and MNS-dislocation clusters have, on average, very similar compositions. There appears to be a greater amount of 'other' solute contained within those clusters adjacent to features enriched in Mn, in addition to comparatively higher Mn contents (14.8% and 14.9% for clusters on Mn-Dislocations and Mn clusters, respectively,

compared to 12.5% and 13% for those on MNS-dislocations and homogeneously nucleated). The identities of these additional elements are discussed in Section 6.3.2 below.

Cluster size distributions

The high damage level following Irradiation F (5 dpa) produced a wide variety of cluster morphologies and sizes; this is illustrated in Figure 6.17. Whilst morphology is difficult to accurately comment on in APT reconstructions, due to spatial resolution uncertainties, of note is that larger clusters appeared more elliptical in shape than smaller ones. In addition, some of the smaller clusters attached to dislocations were elongated along the dislocation line.

When calculating cluster sizes, care was taken not to include any falsely merged clusters. Unlike for previous irradiations, establishing an approximate cluster dimension was not suitable in this case, as many of the larger clusters could not be described as quasi-spherical.

Size distributions for each nucleation site are shown in the form of a Violin plot in Figure 6.23. Here a kernel function has mapped the changing probability density for cluster

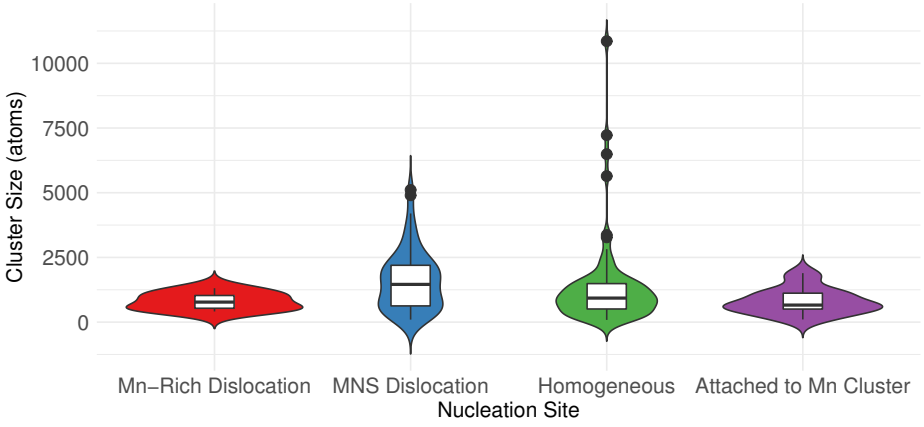

Figure 6.23: Violin plot [191] illustrating the detected cluster size distributions for Irradiation F SA508 samples, categorised by nucleation site. The breadth of the filled areas indicates the probability density of cluster sizes, smoothed using a kernel function, and an inlaid box plot illustrates the median, quartile and outlier values for each cluster type.

size, based on the size data extracted from all the SA508 steel samples. Overlaid box-plots indicate the median, quartile and outlier sizes for each nucleation site.

It is the homogeneous clusters which show the greatest spread in size, ranging from some of the smallest features through to the largest. Those clusters associated with Mn-rich features tended to similar median sizes, with relatively limited variance. The largest median size was attributed to clusters which nucleated on MNS-type dislocations.

Figure 6.24 maps the changing of composition with size for Irradiation F samples. Points of interest from these plots are the apparent tending to certain concentrations of Ni, Si and Mn as cluster size increases, the presence of P in the largest 'homogenously' nucleated clusters and many of those on MNS-decorated dislocations, and further evidence of elevated amounts of additional solute species in clusters on Mn-rich features. The largest scatter in composition occurred for smaller clusters, although the Mn-based clusters (red and purple points on graphs) showed a more consistent Mn concentration, which was generally

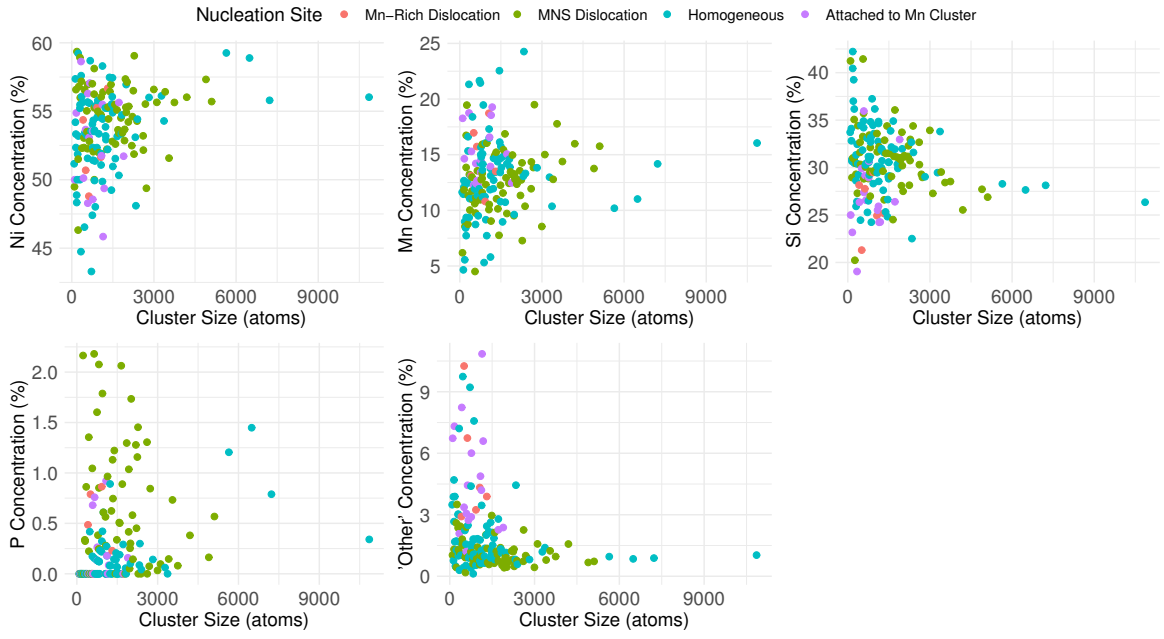

Figure 6.24: Variation of cluster composition with cluster size (as-detected), with data point colour denoting the determined nucleation site of each cluster.

higher than that in other cluster types of similar size.

6.3.2 Mn-rich solute clustering

In addition to the large MNS clusters in the specimen atom maps, smaller, Mn-rich clusters could be visually identified. These clusters were fewer in number compared to MNS clusters, and were not present in every dataset analysed. Clustering behaviour of this type, where clusters notably different in composition to MNS clusters are found within the same dataset, have not been documented previously. Generally, it was found that they took two possible forms; they were either standalone, apparently homogeneously nucleated features, or they appeared adjacent to MNS clusters. Examples of both these instances are shown in Figure 6.25.

As previously seen in MNS clusters attached to Mn-dislocations or clusters, those regions where Mn is particularly enriched, in the relative absence of Ni and Si, correspond to elevated levels of other solutes not commonly the focus of radiation enhanced diffusion in RPV steels. Evaluation of the atom maps revealed high local C, Mo and Cr concentrations coinciding with the regions where there was Mn enrichment without MNS formation. A

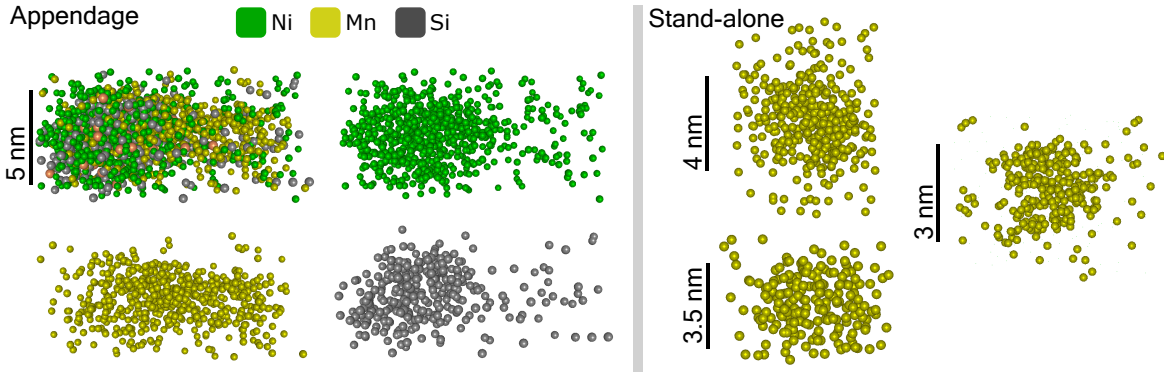

Figure 6.25: Examples of the different forms of Mn-rich solute clustering present in Irradiation F samples. Mn, Ni and Si atoms are represented as spheres, with other elements not included for visual clarity.

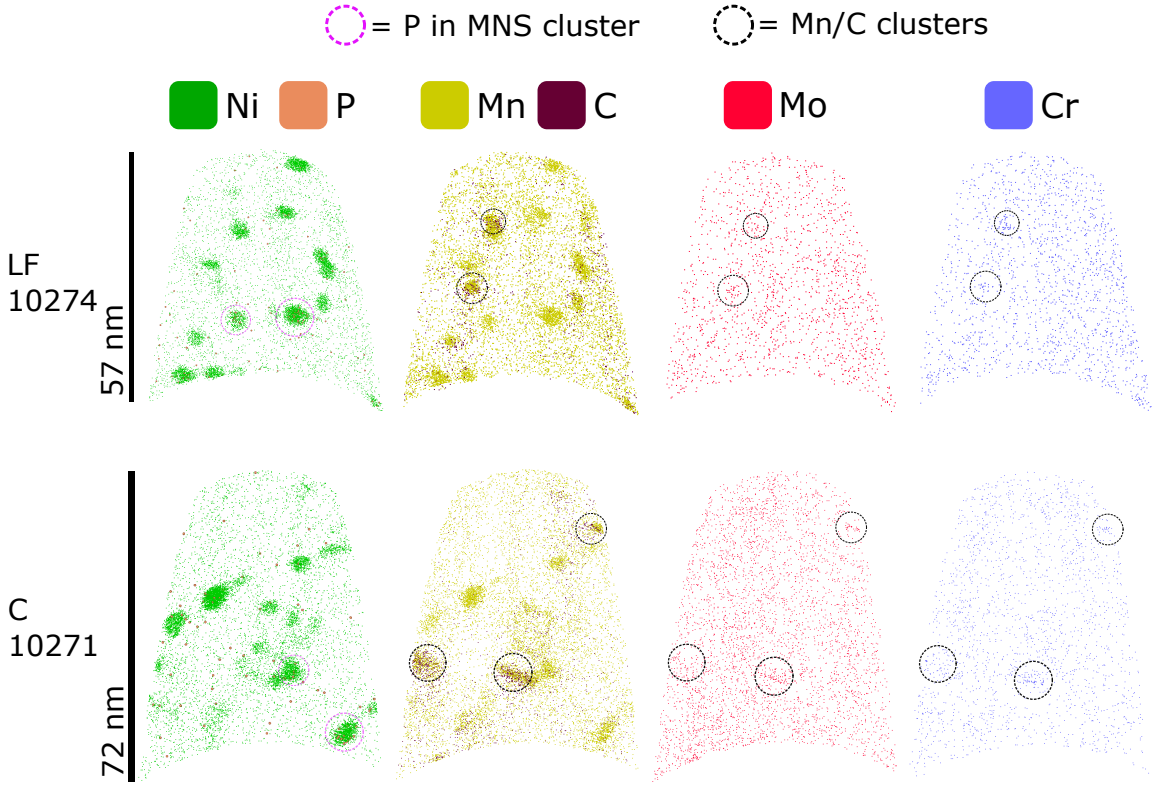

Figure 6.26: Atom maps from Irradiation F samples illustrating the correlative segregation of various elements to regions of primarily Mn-enrichment. Examples of clusters are circled, indicating those containing P atoms and those where Mn and C segregation coincide.

series of example atom maps best illustrate this behaviour (shown in Figure 6.26). The circles indicate key regions of the 8 nm slices; examples of Mn/C/Mo/Cr segregation, and also evidence of P segregation only to the fully developed MNS clusters. Interestingly, the Mo and Cr segregation does not occur in every region of coupled Mn and C enrichment.

Extracting the lone clusters (without MNS appendage) presented a problem, as they were not systematically identified using MSM. Such to gain an insight into the general composition of these features, Mn clusters from multiple datasets were manually extracted using a ROI, with that sub-volume then subjected to MSM analysis, with Mn, Ni, C, Mo and Cr included as core atoms. Using the collective data, the Mn-enriched features were found to contain approximately, on average, 56% Mn, 20% C, 14% Ni, 4% Cr, 4% Mo, plus

trace elements (with Fe atoms removed).

6.3.3 Dislocations and dislocation loops

There is significant decoration of dislocations across all the Irradiation F alloys. Visually, in the APT reconstructions these linear enrichments appeared to consist of two distinct types; one of typical MNS decoration (with Mn, Ni and Si present), and one solely (significantly) enriched in Mn.

Due to both the morphology of the dislocations and the cluster appendages, accurate determination of the degree of enrichment at these features was not possible. However, in some cases either proxigrams or concentration profiles perpendicular to straight regions of the dislocation line were used to get approximate maximum solute concentrations. For the Mn-rich dislocations, the Mn content appeared to average in the core region at about 10at.%, peaking at 16-20at.% (this is based on comparing multiple Mn-rich dislocations). There was also notable C segregation present on these linear features ($\approx$ 3at.%). The Mn enrichment was similar for the MNS-type dislocations, but with increased corresponding Ni (around 20at.%) and Si (around 14at.%) contents, respectively.

Dislocation loops were also observed following Irradiation F; refer to Figure 6.27. These appeared either relatively small and circular, or larger and elliptical. Enrichment of Mn, Ni and Si was notable in both cases. Generally, the larger loops measured approximately 14-20 nm along the longest axis, whilst the smaller ones were less than 12 nm in diameter. There was no definite trend in the prevalence of loops within the analysed microstructures, although in the randomly sampled volumes analysed, there was a higher incidence rate amongst the forged samples.

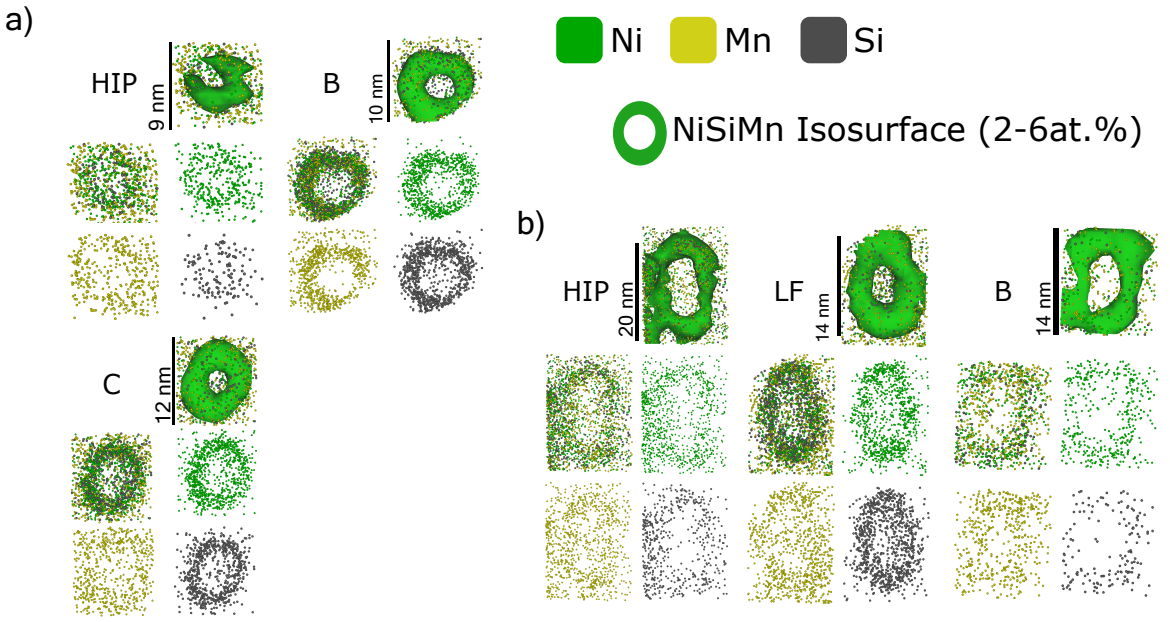

Figure 6.27: Dislocation loops found in Irradiation F samples. Loops are categorised by morphology: loops in a) are smaller and circular, whereas those in b) are larger and elliptical. Isosurfaces encompassing each loop are included, as well as atom maps for Mn, Ni and Si.

6.4 Self-Ion Irradiation Induced Segregation to Interfaces

Solute segregation to interfaces is a reported consequence of ion-irradiation, and, although not a targeted feature of this work, random sampling yielded several APT samples containing enriched interfaces. These were either in the form of carbide-matrix interfaces or grain boundaries. In both cases there was significant segregation of solute species detected.

6.4.1 Carbide interfaces

Figures 6.28, 6.29 and 6.30 show instances of matrix-carbide interface solute segregation present after each of the different irradiations.

With increasing damage, the extent of segregation to these interfaces changes. Initially,

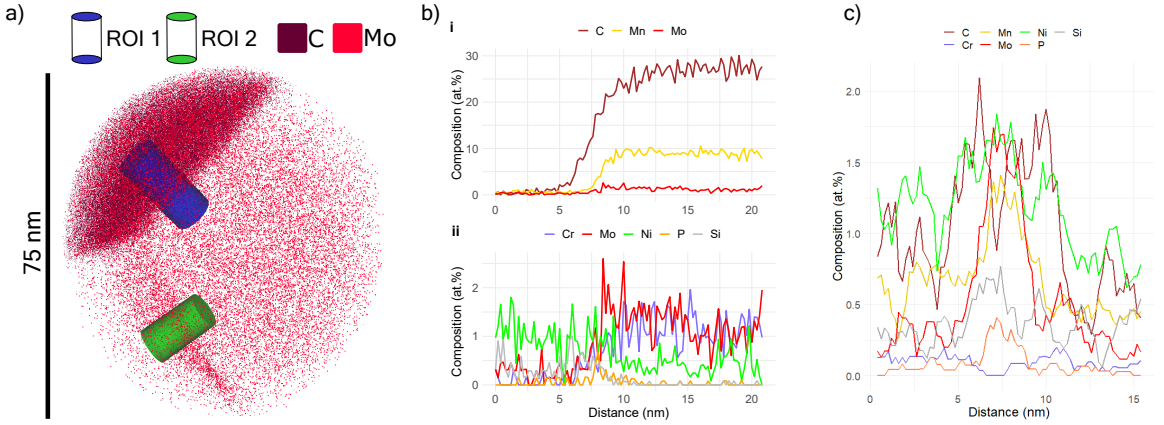

Figure 6.28: 0.09 dpa (Irradiation A) HIPed dataset showing segregation of certain species to a carbide interface and a grain boundary: a) Overview of the interfaces, with the ROIs used for extracting concentration profiles shown; b) the concentration profile (split according to maximum solute content for visual clarity) across the carbide interface using ROI 1; c) concentration profile through the grain boundary, using ROI 2.

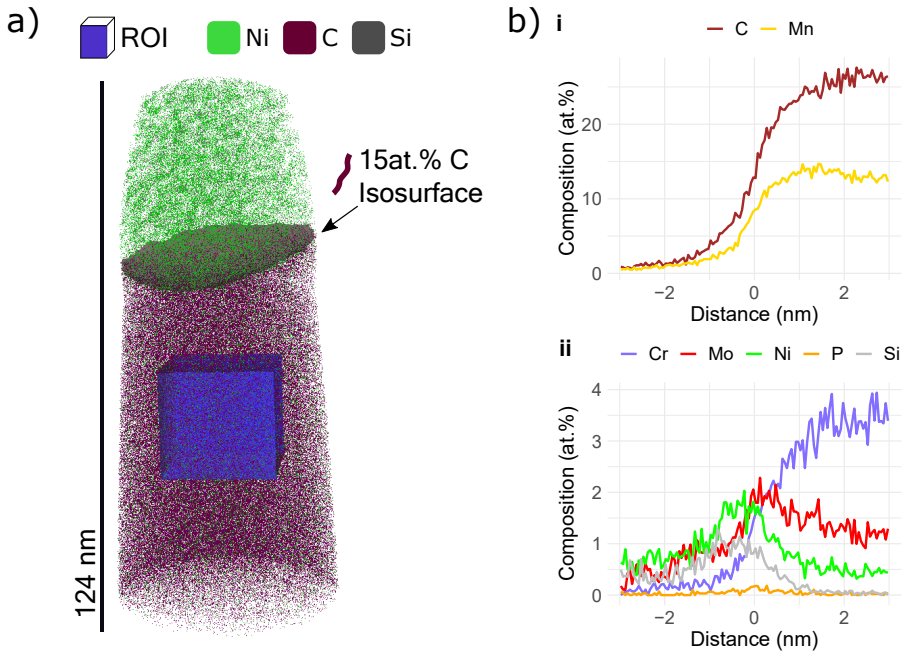

Figure 6.29: Carbide found in a 0.6 dpa (Irradiation B) forged B APT dataset. An overview of the atom map is shown in a), with selected species shown for clarity, whilst b) is a proxigram taken through the 15at.% C isosurface, indicating which elements are exhibiting segregation behaviour.

carbide found in a HIPed Irradiation A (0.09 dpa) sample showed only notable enrichment of Mo and P, with a faint local maxima in Si. For Irradiation B (0.6 dpa), there was a much clearer indication of Si and Ni interface segregation, with the local concentration of these elements increasing up to threefold for the carbides in Irradiation F.

For carbide interfaces at lower dpa, asymmetric Si enrichment is often observed about the interface, with Si locally higher on the matrix-side of the boundary, a result of the diffusion of Si out of the carbide phase, where solubility is low. This behaviour is also noticeable, but to a lesser extent, for segregated Ni atoms. As damage level increased this phenomenon became indistinct, with the positioning of the carbide interface less defined by a peak in Mo, owing to the concentration of Ni and Si atoms at the interface exceeding that of the Cr and Mo. In fact, by 5 dpa, based upon the proxigram analysis it could be interpreted that there is no clear Mo segregation to the interfaces.

As expected for the forged samples, given they contain less P, there is a reduced amount of P-enrichment at carbide-matrix interfaces compared to those found in the HIPed material, even where dpa is higher.

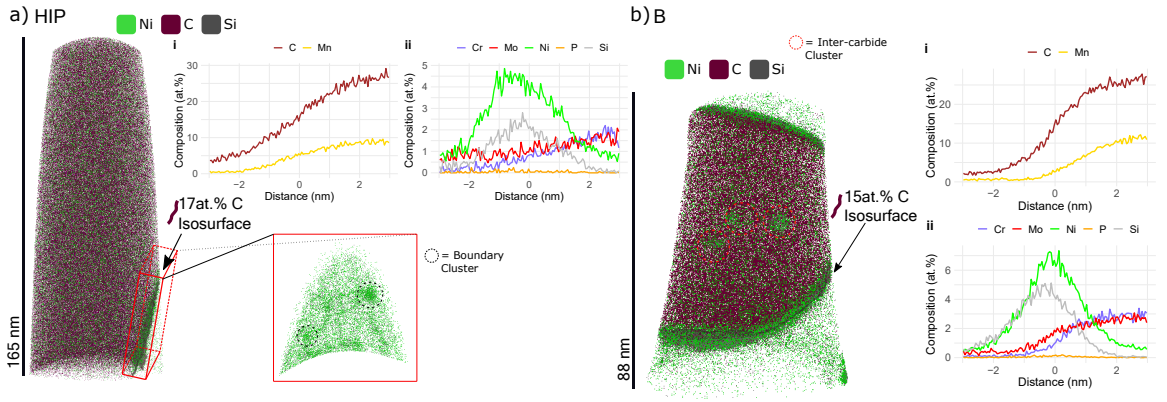

Figure 6.30: Carbides found in Irradiation F samples of a) HIPed SA508 and b) forged B SA508. Proxigrams across the carbide interfaces indicate the solute enrichment present at these boundaries. In a) clusters within the interface are circled, whilst in b) inter-carbide clusters are circled. Only Ni, Si and C atoms are shown for visual clarity.

Unique to Irradiation F is evidence of solute clustering within the carbide boundary and within the carbide itself (circled in Figure 6.30). These clusters were primarily comprised of Ni and Si atoms, and, where present at the boundary, they were spatially confined to the interface region, attached to linear enriched features. A higher incidence rate of observing these features within an APT analysis would be required to conduct a comprehensive study, potentially through carbide and grain boundary targeting, but this is beyond the scope of this work.

6.4.2 Grain boundary segregation

Increased solute segregation to grain boundaries was also observed; Figure 6.28 shows the atom map and ROI locations for a volume of 0.09 dpa HIPed SA508 (Irradiation A), containing both a carbide and grain boundary, alongside concentration profiles through each of the interfaces.

Segregation is more defined in the grain boundary concentration profile (Figure 6.28c), where there is a distinct increase in P, Ni, C, Mo, Si, Mn and P at the grain boundary. To better quantify the extent of segregation, the Gibbsian Excess values for this grain boundary, and another found in a 0.23 dpa Forged C sample (Irradiation A), are given in Table 6.10.

As previously noted, where the nature of the boundaries is unknown (as is the case here), direct comparisons to the as-received boundary analysed in Chapter 4 introduces uncertainties. However, the Γ_i values for these ion-irradiated boundaries display a clear difference to those seen in the as-received samples, and, taking into account the grain compositions, is likely beyond that which a variation in misorientation angle could cause. There is a clear increase in the excess amounts of Ni, Mn, Si and P post-irradiation, which can be visualised in a ROI normal to the 0.23 dpa boundary, presented in Figure 6.31.

A grain boundary found in an Irradiation F reconstruction also showed segregation

Table 6.10: Calculated Gibbs Excess values for the grain boundaries encountered in Irradiation A, including compositional values for the interface (with an error of ± 0.01%).

(a) 0.09 dpa HIPed Grain Boundary - calculated interface width ≈ 2.3 nm

	C	Fe	Mo	Ni	Cr	Mn	Si	P
Γ_i (excess atoms/nm^3)	3.30 ±0.54	-11.66 ±1.65	3.38 ±0.36	1.92 ±0.33	-0.08 ±0.01	1.81 ±0.26	0.65 ±0.06	0.39 ±0.01
Interface Comp. (at.%)	1.55	93.54	1.45	1.48	0.04	1.08	0.57	0.24
Grain-A Comp. (at.%)	1.04	95.94	0.48	1.21	0.09	0.72	0.36	0.06
Grain-B Comp. (at/%)	0.74	96.85	0.28	1.03	0.09	0.57	0.33	0.05

(b) 0.23 dpa Forged C Grain Boundary - calculated interface width ≈ 2.3 nm

	C	Fe	Mo	Ni	Cr	Mn	Si	P
Γ_i (excess atoms/nm^3)	2.34 ±0.27	-11.11 ±1.52	3.58 ±0.40	1.25 ±0.23	-0.14 ±0.01	2.23 ±0.35	0.70 ±0.07	0.28 ±0.01
Interface Comp. (at.%)	1.16	94.48	1.56	0.55	0.04	1.14	0.61	0.14
Grain-A Comp. (at.%)	0.53	96.88	0.57	0.42	0.09	0.76	0.39	0.02
Grain-B Comp. (at/%)	0.38	97.72	0.35	0.29	0.10	0.57	0.36	0.01

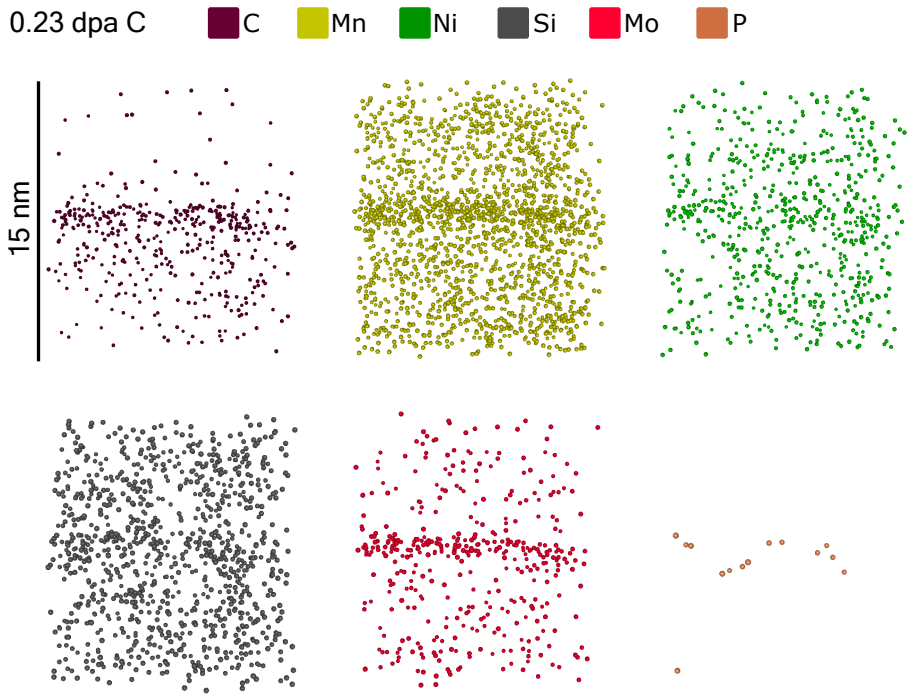

Figure 6.31: Solute segregation to a grain boundary observed in 0.23 dpa alloy C, visualised using an ROI perpendicular to the boundary plane.

of these key species, although in this case there was also evidence of inter-boundary solute clustering. Unfortunately the boundary area was too small, and too near the dataset boundary for thorough analysis.

It is thus a consequence of the Irradiation A and F conditions, and, by extension, ion irradiation in general, that segregation of Ni, Mn, Si and P to grain boundaries occurs. There also seems to be an increase in C, both as an enrichment of the interface and in the sections of grains adjacent. Upon visual inspection of the interfaces, the width of C segregation at the interface appears broader in the ion-irradiated samples, and, given the interface was defined by the more distinct increase in Mo, this area of higher concentration would lead to an increase in the calculated C composition of the adjacent volumes.

Table 6.11: Summary of Fe^{4+} ion irradiation results.

Irradiation	Temperature	Target Dose	Observations
A	300°C	0.1 dpa	• P clustering/segregation at low dose • Onset of MNS clustering as dpa increased with depth (small and diffuse) • Segregation to dislocations (P, Mo, C)
B	150°C	0.6 dpa	• MNS clustering (small, diffuse) • Segregation to dislocations
F	300°C	5 dpa	• MNS clustering (mixture of large, ellipitical clusters and smaller, spherical ones) • Solute segregation to dislocations and dislocation loops observed • Mn-rich features • Inter-interface solute clustering

6.5 Discussion

An overview of the completed self-ion irradiations can be seen in Table 6.11.

6.5.1 Early-onset P segregation

In the low-dose, 300°C, regime of Irradiation A, P was shown to exhibit high mobility, visually segregating to dislocations and forming P atmospheres, prior to the onset of defined MNS clustering. The formation of atmospheres was limited to the HIPed and LF samples, as the lower P content of materials B and C reduced the amount of P available, particularly where segregation to dislocations in these samples appeared more favourable. The N_d of P atmospheres did not appear to greatly increase with increasing dose; beyond having the lowest value at 0.09 dpa, the number densities thereafter did not vary significantly, implying some degree of saturation of these features. Despite the amount of P differing by a factor of four in the HIPed and LF alloys, this did not seem to translate to a difference in the amount of P segregation, rather it influenced the increase in local concentration in these regions

(this was higher for HIPed samples, where P content was relatively greater).

The reasoning behind this high P mobility under irradiation, at this temperature (300°C), has been proposed in existing literature, and largely entails favourable migration mechanisms being possible for P in Fe, allowing segregation to cascade damage regions (which are, in turn, stabilised [97]). This includes a strong solute-vacancy interaction energy [125], which promotes diffusion via vacancy dragging [192, 193], and a propensity to form mixed interstitial atoms (MIAs), the high mobility of which is deemed to be the dominant cause of RIS of phosphorus [194, 195]. Work done on FeCr alloys by Gómez-Ferrer et al. showed very similar results to those presented here; P clustering essentially saturated after 0.1 dpa of Fe^{2+} irradiation and coincided with observed non-random Ni and Si distributions (attributed to them displaying RIS, but at a reduced rate) [196]. Interestingly, the P content of the alloys shown to contain P clusters by Gómez-Ferrer et al. was higher than that for those in this work, whereas the alloys nearer the P content of the forged samples studied here were not reported to exhibit P clustering. This aligns with the observations made for forgings B and C, but prompts the question as to why the only slightly higher P content of the large forging gave rise to P atmospheres. This either suggests that a P concentration lower-limit for P clustering/atmospheres is more in-line with the 0.004at.% value for LF, or that there is a microstructural influence occurring in the large forging which is neither present in the FeCr model alloys studied by Gómez-Ferrer et al. nor the B and C forged materials in this work. However, there is insufficient information concerning how the manufacturing processes and sampled microstructures compare to yield a clear theory as to the influencing factors involved.

Given P atmospheres have been identified in Irradiation A reconstructions where there are no MNS clusters, the question is raised as to what mechanism is in effect. There are two possibilities; the P is moving first, forming solute-vacancy cluster complexes which then act as Mn, Ni and Si diffusion sinks, enhancing MNS nucleation; or, the high mobility of P gives

a faster rate of pairing with the irradiation-produced point defects but does not influence Mn, Ni or Si, as these species would diffuse to these defects regardless, just at a slower rate. Considering that the 0.1 dpa results showed MNS clusters not at P enriched sites, it makes more sense that the latter suggestion holds true, whereby RIS of Mn, Ni and Si is not a synergistic effect of P-rich-atmosphere formation. Furthermore, a reduced P concentration in alloys B and C was shown to not correlate with an absence, or reduced N_d, of MNS clusters.

6.5.2 Impact of varying irradiation conditions

As would be expected, there is a significant increase in both the diversity and the amount of detected damage present in the ion-irradiated samples as dose increased. Even allowing for temperature variation, there is a clear sequential nature to the formation of certain defects (at least with respect to their detectability using APT) with increasing dpa. Small, ill-defined clusters of Mn, Ni and Si form first, prior to any significant solute decoration of dislocations, evolving into more distinct MNS clusters as the target dose rose.

Early-stage MNS clusters (Irradiation A)

The frequency distribution results for APT datasets of Irradiation A samples indicated the subtle onset of inhomogeneous solute distribution prior to MNS clusters being detectable. Whilst all data showed non-random Mn distribution, there was variance in whether Ni and/or Si inhomogeneity was also present. In particular, the results indicate that where Si content was reduced with respect to Ni, there is an increased likelihood that Si would not be detected as segregating. This is particularly noticeable at the intermediate dose level (0.12 dpa). In addition, as dpa increases, Si is more likely to be incorporated into clusters, even where concentration is low. It is apparent that there is some form of complex phenomenon occurring, whereby the tip composition influences the solute clustering

process but the impact is beyond that of the absolute amount of each solute present, rather there is an interplay dictated by diffusion mechanics and solute behaviour under irradiation.

The detection of some non-random solute distributions without associated solute clustering is a strong indication that the early stages of MNS clustering were present in the Irradiation A samples; with specific elements acting first in the nucleation of solute clusters through formation of very local regions of increased concentration centred on solute-vacancy clusters, prior to further diffusion-led growth as dose is increased. At this very early stage, heterogeneous nucleation on irradiation-induced matrix damage (vacancy complexes and dislocation loops) is the dominant (lowest activation energy) process, alongside enhanced diffusion to existing features such as dislocations and interfaces. In order to better characterise the development of MD at this low dose, further work utilising TEM may aid identification of the changing defect densities based on dislocation loop observations.

Cluster compositions

The different average cluster compositions in all APT datasets (based on Mn, Ni, Si ratios) are presented in the ternary plots in Figure 6.32.

The clusters appear to start with a higher Mn content at low dpa, which reduces as

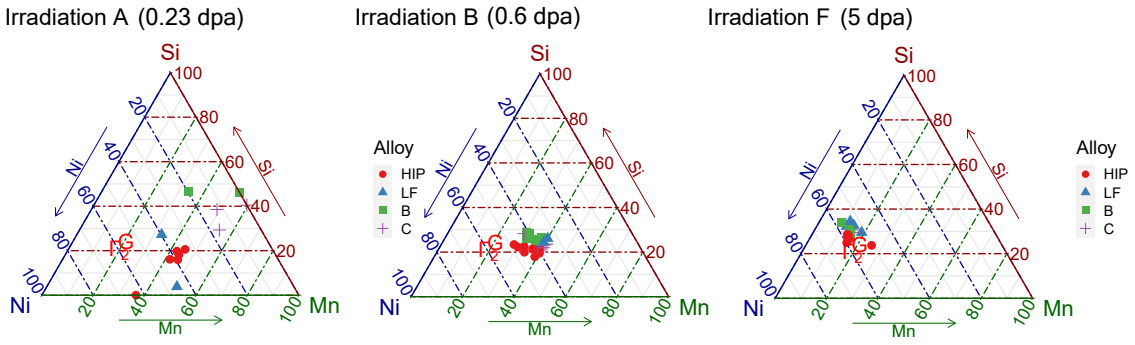

Figure 6.32: Mn, Ni and Si ternary plots illustrating average cluster composition for APT datasets from each self-ion irradiation. Colour/shape indicates the alloy origin of each dataset.

fluence increases. A correlation between smaller clusters and a larger proportion of Mn implies this species dominating early in cluster development. The role of Mn is discussed in more detail below in Section 6.5.3.

Si content remains roughly constant despite changing dose, with Ni atoms contributing most to cluster growth - indicated by the transition to higher Ni contents as dose (and cluster size) increased. The compositions lie around those predicted by thermodynamics, with clusters at higher dose more grouped than those at lower dose.

Cluster size distributions

As exposure increases, MNS clusters are free to grow through diffusion, eventually resulting in a ripening effect whereby some clusters grow at the expense of others. This differing in cluster sizes can be seen by comparing the cluster size distributions for each irradiation, as is done in Figure 6.33.

There continues to be a range of cluster sizes as dose increases, indicating that clusters

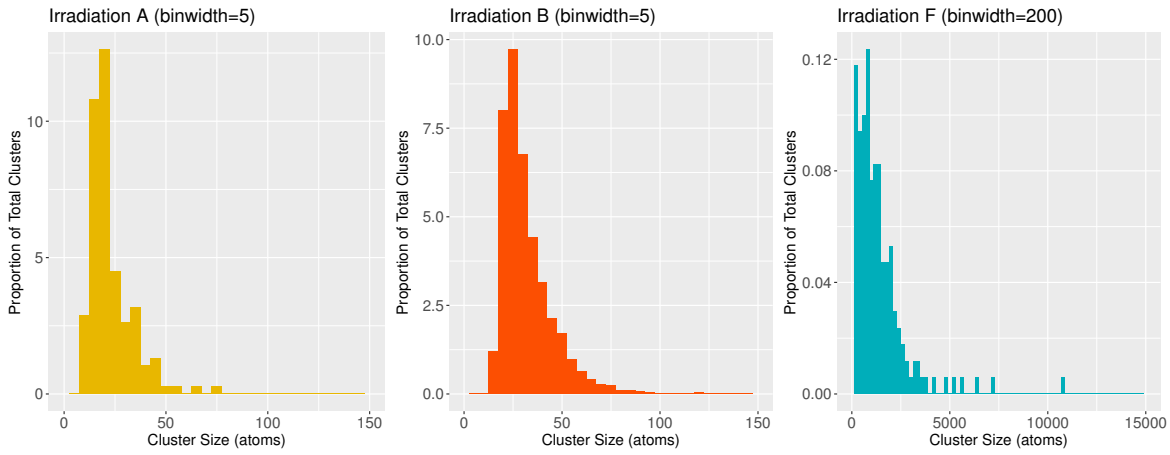

Figure 6.33: Cluster size distributions for the 0.23 dpa (Irradiation A), 0.6 dpa (Irradiation B) and 5 dpa (Irradiation F) SA508 steel samples, ignoring Fe atoms and edge clusters. The count values for each bin are scaled such that the total area is equal to 1, and the y-axis used is then equal to this density multiplied by the binwidth, such to give the number of clusters in each size-range as a proportion of the total number of clusters (%).

continue to nucleate, grow and fragment as an irradiation progresses, preventing the coalescence of solute into a few very large clusters and, rather, retaining some clusters which are smaller in size due to delayed nucleation.

One common hypothesis as to the prevalence of smaller clusters is that ion bombardment causes some of the larger clusters to fragment ('collisional mixing'), reintroducing solute into a then supersaturated matrix, which in turn induces further cluster nucleation [197, 198]. However, cluster evolution under these conditions would be expected to produce a binomial cluster distribution [199] - this only appears for Irradiation F, and even then to a very slight extent at around 4000 atoms (see Figure 6.33).

This work does not indicate a continuous increase in cluster N_d with dose, nor is proportionality between dose and defect density observed [200, 201]. The average N_d and V_f values for each irradiation are shown in Table 6.12. The drop in N_d in Irradiation F reflects the ripening of large clusters at the expense of smaller ones, as well as a saturation of the matrix damage available for cluster nucleation. The observation of this Oswald Ripening in the Irradiation F samples implies a surface energy effect is at play, in turn suggesting that by this point the cluster have developed into a distinct phase.

Table 6.12: Average cluster volume fractions and number densities for the APT samples for each of the different ion irradiation conditions.

Irradiation	Average Cluster Volume Fraction (%)(3sf)	Average Cluster Number Density (m^{-3}) (3sf)
A (0.23 dpa)	0.01 ± 0.01	$1.14 \pm 0.80 \times 10^{23}$
B (0.6 dpa)	0.46 ± 0.15	$5.57 \pm 1.96 \times 10^{24}$
F (5 dpa)	0.83± 0.31	$1.87 \pm 1.11 \times 10^{23}$

Although V_f did increase with dose, the increment between 0.6 dpa and 5 dpa was less than that been 0.23 dpa and 0.6 dpa. This could be a result of the increased flux (necessary to produce the higher damage) inhibiting cluster growth through cascade mixing effects

(disordering, inverse coarsening etc) [202], such that the clusters in Irradiation F samples could not grow proportionally to dose. Conversely, it is another symptom of the saturation effect, where there is a reduction in solute available for segregation [83]. It could also reflect the changing temperatures between irradiations, with the low irradiation temperature in condition B limiting thermal recovery and thus having a disproportionate increase in cluster N_d [81, 84] - although the exact impact of temperature is known to be complex.

Influence of detected cluster nucleation site (Irradiation F)

By utilising the high damage of Irradiation F, features of ion-irradiation beyond cluster size and N_d were more easily determined. In particular, distinction could be made between those clusters of apparent homogeneous nucleation and those attached to dislocations, due to the enhanced dislocation decoration at this dose (to reiterate, those clusters classified as homogeneous would likely have nucleated on matrix damage, but have been designated as such to distinguish from those on clear, solute-decorated features).

Clusters clearly nucleated on MNS dislocations had the largest median size (shown in Figure 6.23). Access to a rapid diffusion pathway likely fuels cluster growth at these features, potentially at the expense of smaller clusters, enabling larger sizes to be reached. However, dislocations did not give rise to the largest clusters seen, these were homogeneous. It is worth considering that, where clusters form on dislocations, despite the faster solute diffusion, there is more competition for resources, with multiple clusters often seen on the same dislocation network (likely a result of the favourable nucleation mechanics associated with linear defects). This may explain why homogeneous clusters can reach anomalous sizes - a cluster nucleated in a solute rich matrix, in the absence of clusters with dislocation-enhanced diffusion, could grow according to typical Oswald ripening mechanics with limited competition once a critical size was reached. Having multiple clusters supplied by fast-diffusing solute may reduce the impact of ripening behaviour, allowing many to

grow big, but not one to grow much bigger.

The larger spread in composition seen in homogeneously nucleated clusters mirrors the greater spread in cluster size also seen for these features. This reflects how cluster composition changes with growth, tending towards a steady-state composition as size increases.

Solute segregation to dislocations and interfaces

It is well established that the reduction in solute free energy at linear and planar defects promotes solute segregation - amplified by thermal and RIS effects [203]. Consequently, features of this type were seen across the three ion-irradiations conducted in this work.

Dislocations Early-stage solute segregation to dislocations was mostly characterised by P enrichment in Irradiation A. This was seen even in the alloys B and C, which had relatively lower P contents and did not exhibit P atmosphere formation. One possibility is that a higher dislocation density in forged steels, particularly in bainitic regions, could result in preferable P uptake on these linear defects, reducing the amount available for migration to point defects and the formation of P atmospheres. Considering alloys B and C have reduced P content compared to the large forging, this phenomenon would be amplified.

It is difficult to tell whether P found on dislocations was present prior to irradiation, as this segregation feature is seen in un-irradiated steels. At low dpa there were some dislocations visible with Mo and C attached (but not P) reflecting the presence of Mo and C dislocation segregation in as-received samples (shown Figure 6.9). This could be an indicator that those dislocations only containing phosphorus were formed during irradiation; it is these dislocations which are associated with post-irradiation ductility, as it has been shown that pre-existing mobile dislocations are rendered static by irradiation damage [204]. As dose increases, there are fewer instances of lone Mo and C decoration, instead Mn, Ni and Si atoms begin to dominate at linear defects.

The observation of MNS-decorated dislocations in APT specimens from Irradiation B and F, but not in those produced in Irradiation A or neutron-irradiation, implies this radiation-induced behaviour may be synonymous with higher damage levels. Shown in Irradiation B was the evidence of early stage solute clustering on a dislocation line (Figure 6.14), initially appearing part of a typical, decorated dislocation until closer inspection. This phenomenon developed at 5 dpa, with clear solute clustering along dislocations found in APT reconstructions. Evolution of segregated dislocations into cluster nucleation on dislocations was a key conclusion from recent work by Odette et al. [203], and results from this thesis support that analysis.

Interfaces As dose increased, there was also greater evidence of solute segregation to interfaces, though this does not account for the reduced sampling statistics of carbide interfaces and grain boundaries compared to dislocations.

The absence of Mo segregation at the 5 dpa carbide interfaces (shown in Figure 6.30) was unexpected, given the usual propensity for Mo to be enriched in this feature-type. This may imply a dominant, saturating effect of Ni and Si diffusion to carbide boundaries under Irradiation F conditions, coupled with Mo segregation to irradiation-induced Mn-rich clusters. However, given the Irradiation F carbides were of similar type and composition to the one analysed from Irradiation A, which appeared to show a more subtle interfacial peak (Figure 6.28), it could be that this Mo reduction is a consequence of a particular carbide type rather than changing irradiation conditions. More carbide types from all irradiations would have to be investigated to provide evidence of differing Mo behaviour under irradiation.

The development of Ni/Si clusters at carbide and grain boundaries under Irradiation F, demonstrated by Figure 6.30, is, given homogeneous enrichment was seen as lower dpa, likely an indication that the enhanced radiation-induced diffusion at 5 dpa is causing Ni previously located at interfaces to segregate to specific defects within the boundary.

Inhomogeneity in intra-boundary segregation has been seen in previous work by Jenkins et al. (in neutron-irradiated RPV steel), but additional evidence of both its occurrence and its potential impact on mechanical properties is yet to be presented [165]. Due to a lack of encountered grain boundaries in Irradiation F, detailed analysis is not possible in this case, but observations of this nature highlight the need for further work on this aspect of irradiated grain boundary characterisation.

Dislocation loops

Additionally, increasing dose also revealed decorated dislocation loops (Figure 6.27), which could not be identified in the lower damage samples. This type of damage is readily expected even at low dose [205] (anything greater than 0.05 dpa [206]) - given that sub-nm loops are a form of cascade-induced defect known to act as cluster nucleation sites [203] - but is only visible in APT where sufficient solute has been transported through RIS and RED. It is already reported that the number of dislocation loops is expected to increase with dose [207].

Results from the 5 dpa samples showed both circular and elliptical decorated loop morphologies, the latter tending to larger diameters. This is in-keeping with existing literature documenting interstitial (smaller and circular) and vacancy (larger and elliptical) <a> dislocation loops in zirconium [208–210].

6.5.3 Role of manganese in irradiation-induced solute clustering

Due to incorporation in carbides, the amount of Mn present in APT volumes varies considerably between datasets. Despite this, results suggest a prominent role of Mn in cluster formation during ion irradiation. This is most noticeable in Irradiation A, where Mn was shown to be the only species of Mn, Ni and Si, to be consistently displaying an inhomogeneous distribution prior to the clear onset of solute clustering (Figure 6.3). In

addition, the proportion of Mn in clusters was highest at low dpa, indicating its role in early cluster formation through dumbbell formation and the resultant enhanced diffusion of solute to defect sinks [67].

Following Irradiation F, the distinct regions enriched in Mn, with little to no Ni and Si, implies a diversity in favourable segregation beyond that seen at lower damage levels. Given these clusters are observed at higher doses, it may be that depletion of Ni and Si in the matrix reduces the supersaturation of these elements, limiting ongoing nucleation of MNS clusters. If Mn were the species responsible for stabilising young vacancy clusters – a result of attractive Mn–Mn, Mn–interstitial and Mn–vacancy interactions [211] – then the relative excess of Mn in the alloy compared to Ni and Si could produce stable Mn-defect clusters without the expected development into MNS features. Interestingly, it seems the formation of these features in Irradiation F coincides with a reduced Mn content in the MNS clusters, implying that at some point during irradiation it becomes favourable for Mn atoms in solution to segregate to the Mn-rich features (clusters and dislocations) rather than the MNS features. One hypothesis explaining this behaviour is the domination of thermodynamics as clusters grow, due to formation of a distinct phase (as evidenced by the coarsening behaviour, which is indicative of a surface energy effect caused by the presence of a phase boundary). This would cause MNS cluster composition to favour the proposed thermodynamically stable G and Γ_2 phases (or another, with a solute ratio better reflected by compositions seen in this work), which have reduced Mn compared to the cluster compositions seen at lower fluence.

Of note is the co-presence of C, Mo and Cr at Mn-rich clusters. Mn is known to have a weak attractive interaction with interstitial C atoms, resulting in correlated segregation [212]. Why this effect is only seen at the higher dpa could be a consequence of radiation induced diffusion, coupled with elevated temperature and the enhanced carbon contamination introduced by a longer ion irradiation. Mo and Cr are elements also found in carbides, which

may produce a coupled segregation behaviour of these carbide forming species. However, their presence could also be separate from any influence of Mn, instead a consequence of higher damage allowing migration of these species, where at lower dpa it was not previously possible. Segregation only at non-MNS Mn-enriched sites could be a result of this late onset diffusion, with the Mn features formed later in the irradiation and thus not yet saturated with Ni and Si atoms, allowing enhanced segregation of Mo and Cr.

6.5.4 Role of manufacturing route on irradiation response

On the whole, samples from each of the four manufacturing routes behaved analogously to self-ion irradiation. Average cluster compositions and N_d were similar, within error, although there were sometimes differences in the spread in the amount of solute clustering exhibited.

Perhaps the greatest variation occurred in the Irradiation A samples. From a materials processing viewpoint, it is likely that it is either those alloys that contain the most previously existing defects (being more susceptible to matrix damage under irradiation) or those that have the greatest saturation of mobile solute, which are likely to show clustering behaviour earliest. In Irradiation A, it was shown that the forged samples, LF and C, associated with a low/negligible fraction of ferrite compared to HIPed and B, were more likely to contain some solute clustering at the intermediate (0.12) and high (0.23) dpa. Based on TEM investigations in this work (Chapter 4, Section 4.3), the lower dislocation density of ferritic regions compared to bainitic ones is the most significant link between this difference in solute clustering onset observed across the four alloys and the corresponding microstructures. In Irradiation F, the sample types with the highest proportion of clusters visibly lying on dislocations were the HIPed and forged B alloys (65% and 63% respectively). Interestingly, these are the same materials with later onset solute clustering in Irradiation

A, implying an underlying link between higher ferrite content and the propensity of nucleation on dislocations.

However, it is also worth considering that, at the low cluster densities observed in Irradiation A, the amount of volume sampled becomes important, as clusters are so sparsely distributed that a small enough APT tip volume could not include any, despite their presence in non-sampled regions. Subsequently it cannot be decisively concluded that there is less solute clustering throughout the HIP and B alloys. Furthermore, this theory concerning the role of ferrite fails to hold true for higher doses, as any difference in the number of existing defects does not appear to translate into a difference in cluster N_d, nor any appreciable differences in cluster compositions. Thus, it could be that either irradiation-induced matrix damage outweighs existing defects to such an extent as dpa increases that any underlying influence of defected microstructure becomes obsolete, or there is no discernible role played by subtle microstructural differences on irradiation solute clustering in these samples.

P content

The results from Irradiation A implied a role of P content in early-stage RIS behaviour. Given P was then seen in the largest homogeneous clusters in the Irradiation F samples, it follows that temperature may be the determining factor, with P mobility increased at higher temperatures (as discussed above in Section 6.5.1). Looking at results where P segregation was seen, there is a link between the amount of phosphorus in samples and the nature of cluster development.

For Irradiation A (the 0.23 dpa subset), a plot indicating the cluster P content vs cluster size (Figure 6.34a) reveals a broader size distribution of MNS clusters found in the HIP and LF samples. Accordingly, the higher proportion of small cluster sizes in the B and C alloys could indicate a slower growth of MNS clusters where P concentration is lower. It is implied that P atmospheres correspond to enhanced growth of spatially complementary

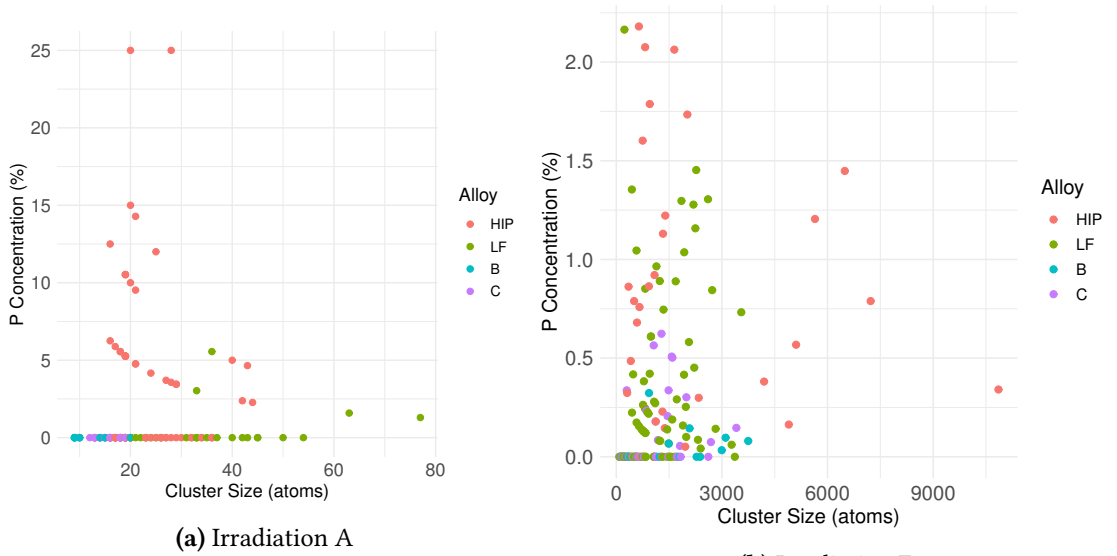

(a) Irradiation A

(b) Irradiation F

Figure 6.34: Plot of cluster size (atoms) vs P content for the clusters found in the 0.23 dpa (Irradiation A) and 5 dpa (Irradiation F) samples, coloured by alloy origin.

MNS clusters, either by indicating MD regions where cluster formation is favourable or by inducing favourable thermodynamics for cluster growth. This mirrors what was seen in the 5 dpa clusters, where alloys B and C had fewer P containing clusters, in addition to many of the larger clusters being more likely to contain P - potentially a result of the further growth of the P containing clusters in Irradiation A.

Having elevated P levels is also an important consideration with regards to grain boundary embrittlement – P was shown to be increasingly mobile under irradiation, with evidence of enhanced migration to grain boundaries (alongside other solute species). As with standard steel metallurgy, ignoring irradiating environments, controlling P content is beneficial for this reason. Although many factors are at play in determining grain boundary strength and alloy fracture mechanics, it is worth considering the heightened P content in the HIPed steel as potential cause for concern.

Influence of tempering: Forgings B and C

Ion irradiation allowed comparison of two forged alloys (B and C) which differed only in the degree of tempering they were subjected to. Based on preliminary results across the three irradiations conducted, there does not seem to be a quantifiable difference in the irradiation response of these steels at low dpa. In particular, if there were any notable difference, its subtly is beyond that measurable following relatively low dose irradiation.

In the higher dose Irradiation F samples, there was noticeably a larger variance in the extent of solute clustering (both V_f and N_d) for alloy B, which matches that seen in the HIPed ferrite samples. This suggests that ferrite grains introduce heterogeneity into solute clustering, potentially a result of the lower dislocation content of ferrite grains influencing the extent of cluster growth as dose increases.

It should be mentioned that, of the samples investigated, there, qualitatively, appeared to be a greater density of decorated dislocations in alloy C. The as-received TEM of this sample did reveal particularly high dislocation densities, which reflects its lower tempering duration [179], and those dislocations retained during the irradiation process would act as linear segregation sites. However, the higher frequency of decorated dislocations does not appear to affect the amount of solute available for cluster formation, as the two forgings generally showed very similar solute clustering behaviour.

6.6 Conclusions

Whilst ion irradiation has been shown, both in this study, and in existing literature, not to simulate the effect of neutron exposure, in this context it has been demonstrated that the use of charged-particles is pertinent when aiming to compare between alloys or investigate the general irradiation response of novel materials. The following chapter gives

a qualitative review of the observations seen in the HIPed and forged alloys subjected to both neutron and ion irradiation.

Based on the results presented in this chapter, the following conclusions have been formulated:

- Successive Fe^{4+} irradiations induced Mn-Ni-Si clustering in four SA508 Class 3 Grade 1 steels with differing manufacturing routes. Cluster V_f increased with dose, but cluster N_d was shown to increase until dropping at the highest dpa condition. Approximately 0.1 dpa, 300°C captures the very early stages of MNS cluster nucleation.
- Cluster size grew consistently with increasing irradiation damage. Where the nucleation site of clusters could be identified, those nucleating on MNS-decorated dislocations were larger, on average, but the greatest sizes were reached by a few clusters which had apparently 'homogeneously' nucleated (not attached to any defect visible in APT).
- At 5 dpa, clusters and dislocations rich in Mn were formed, in addition to the MNS-type clusters and dislocations typically seen. At these features, correlative segregation of C, Mo and Cr was observed, potentially linked to positive Mn-(C/Mo/Cr) interactions, but conclusive theories as to the exact nature of this phenomenon require further study. The growth of the Mn-rich clusters may be a product of favourable Mn diffusion to these features at the expense of existing MNS clusters, which appear to tend to the proposed thermodynamically favourable compositions as MNS cluster size increases.
- MNS cluster compositions shifted towards higher Ni:Mn ratios as fluence increased, with Si content remaining approximately constant.
- There is no conclusive evidence indicating manufacturing route (role of HIP process or varying tempering extents) influencing irradiation response. Notably, P-rich atmospheres were only observed after the higher temperature irradiations in the alloy

types (HIPed and LF) containing more P. Further work investigating defects with TEM may provide a better insight into the influence of starting dislocation density on the onset of solute clustering.

- Dislocation loops of interstitial and vacancy types, similar to those observed in zirconium-based alloys, were observed in SA508 steel after exposure to 5 dpa of self-ion irradiation damage.
- High dpa ion-irradiation can induce solute clustering within carbide and grain boundaries, resulting in inhomogeneous interface solute distribution.

Chapter 7

Discussion of Ion vs. Neutron Irradiation of SA508 Grade 3 Class 1 Steel

As discussed in the literature review presented in Chapter 2, there exists multiple, fundamental reasons why characterisation data obtained through irradiation of materials using charged particles and neutrons, respectively, cannot be directly compared. However, in the light of this work, and in-keeping with current discussions as to the validity of studies using ions [87, 98], it is important to investigate and attempt to understand the differing behaviour observed in materials subjected to both forms of irradiation.

Given that ion irradiation is not equivalent to using neutrons, in-depth comparison of numerical microstructural characterisation data, such as solute cluster number density and composition, is ill-advised. Therefore, this chapter will focus on a qualitative discussion of the type of damage induced by the two particle types, primarily as observed through APT. Where quantitative data is presented, it will be used as an indication of observed behaviour and should not be inferred as an absolute comparison. Comparisons of the ease of conducting

both forms of investigation will also be commented on, for the benefit of future experiments.

7.1 Cluster Development

Figure 7.1 presents an overview of the APT reconstructions of forged SA508 across the different neutron and ion irradiations completed in this work. Ion irradiation allowed higher damage levels to be produced, beyond that efficiently possible using fast reactors. When considering the resulting differences in clustering behaviour between the ion and neutron samples, the most appropriate comparisons can be made between the ANSTO samples and the low-dose self-ion conditions.

Based on visual appearance, it is the Irradiation B (0.6 dpa) samples which best match the aesthetics of the neutron-irradiated APT specimens. Cluster number density is of the same order of magnitude, and the clusters themselves have similar characteristics; small, ill-defined regions of Mn, Ni and Si enrichment. The average cluster sizes were also comparable across the shared alloy types, with the neutron clusters slightly larger, containing approximately 70 atoms (not including Fe) at 0.2 dpa, and the 0.6 dpa Fe^{4+} clusters containing around 61 atoms. By using the investigation of depth-dependent damage on the Irradiation B LF sample (Section 6.2.2), it can be seen that a slightly lower dpa (nearer 0.4) gives the best 'match', considering N_d, V_f and cluster size, with the 0.2 dpa neutron samples. In this regime, the cluster compositions are also similar (≈ 35at.% Mn, 40at.% Ni and 25at.% Si). Given Irradiation B used an irradiation temperature (T_{irr}) roughly equal to that of the OPAL reactor (≈ 150°C), in this case an increase in target damage (by approximately a factor of 2-3) was required to give similar visual damage profiles and cluster statistics using APT. This need for higher dpa in charged-particle irradiations to mirror MNS V_f in neutron studies has been previously postulated by Almirall et al. [103], and is likely a result of enhanced point-defect recombination at higher fluxes.

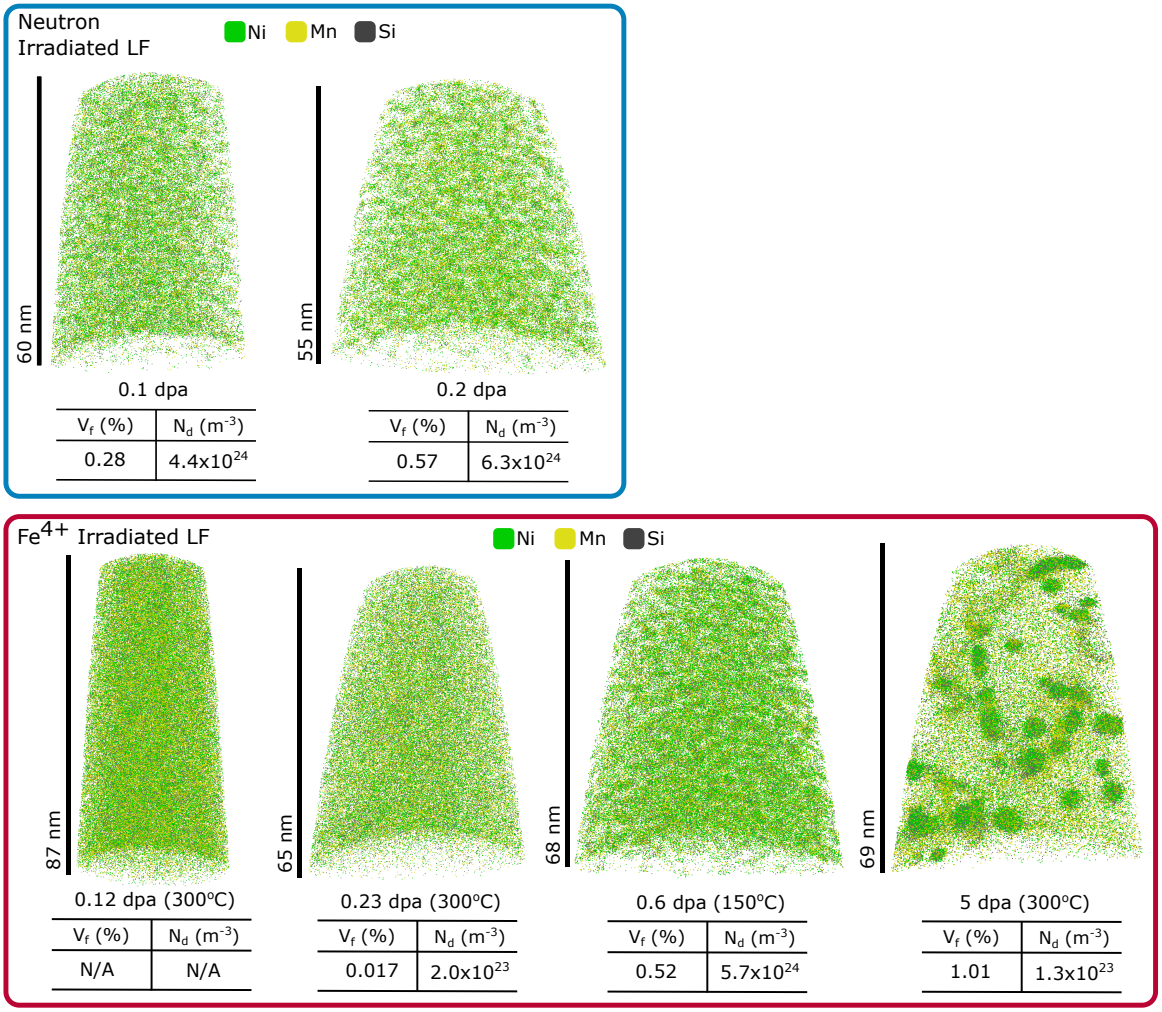

V_f (%)	N_d (m^{-3})
0.28	4.4×10^{24}

V_f (%)	N_d (m^{-3})
0.57	6.3×10^{24}

V_f (%)	N_d (m^{-3})
N/A	N/A

V_f (%)	N_d (m^{-3})
0.017	2.0×10^{23}

V_f (%)	N_d (m^{-3})
0.52	5.7×10^{24}

V_f (%)	N_d (m^{-3})
1.01	1.3×10^{23}

Figure 7.1: Atom maps from LF samples produced by the neutron and self-ion irradiations, with only Mn, Ni and Si atoms shown for clarity. The average cluster volume fraction and number density for each sample type, according to the irradiation it was subjected to or depth-based dpa (for self-ion samples), are shown to 2sf.

Cluster volume fraction is consistently lower for the ion-irradiated samples compared to the neutron-irradiated ones; this is a similar result to that recorded by Was et al., who observed a reduction in the size of G-phase precipitates in HT9 steel following Fe^{2+} ion irradiation compared to neutron, whilst number density remained approximately the same [85]. Predicting V_f based on the values obtained from different doses (based on depth) of the Irradiation B LF datasets would give a much lower V_f at 0.2 dpa than observed in the

ANSTO LF tips, assuming a linear relationship between dose and V_f (around 0.4% compared to 0.6%). A better match was seen in the 0.1 dpa Irradiation B samples compared to the three-month neutron-irradiated samples. Based on this, as a first approximation where T_{irr} is comparable, the best self-ion irradiation equivalence to the OPAL reactor damage is found at lower dpa. As dpa increases, self-ion damage appears to induce less cluster growth than seen under neutron irradiation.

Although Irradiation A delivered approximately the same target dpa values ($\approx$ 0.1 or 0.2, depth-depending) on the samples as the three-month and six-month ANSTO irradiations, equivalent damage was not observed. Irradiation A failed to induce significant cluster nucleation, with consistent clustering only seen at 0.23dpa, and even then to a much reduced extent compared to in the ANSTO samples. Existing literature has suggested a complex interplay between the use of temperature and dose in ion irradiations attempting to simulate neutron exposure [87, 101]. Irradiation A provided the opportunity to investigate the impact of an elevated ion irradiation temperature on replicating neutron irradiation damage, with increased temperature postulated to result in equivalent defect arrival times in the ion and neutron samples [99, 100, 213]. The results of this work show that an $\sim$ 145 K increase in T_{irr} does not translate to significant irradiation-induced segregation in RPV steels. Clearly this was an insufficient temperature shift to give analogous behaviour at a similar dpa.

The high dose-rate possible with ion irradiation allowed the observation of cluster development beyond the stages seen in the ANSTO samples. This is of use when modelling irradiation effects at doses higher than realistically possible from a test reactor, whilst also improving understanding of the trends in cluster development with dose. Despite nuanced differences in the exact extent of clustering in the self-ion and neutron specimens, the expectation would be that the nature of cluster growth mechanics and solute saturating behaviour would be analogous, although the rate of which development occurred would differ due to the underlying differences in physical processes.

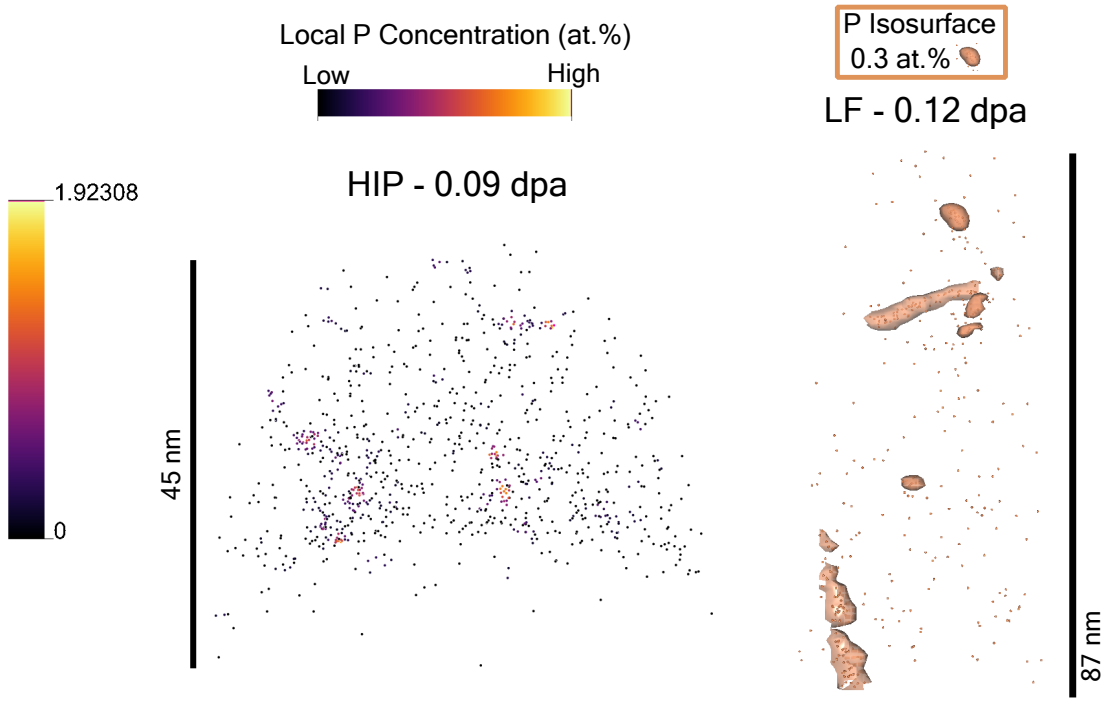

Figure 7.2: Atom maps containing local concentration values and isosurfaces to illustrate the presence of P atmospheres and dislocation segregation in self-ion Irradiation A samples.

7.2 Role of P

Results indicated a difference in the behaviour of phosphorus in the ion-irradiated samples compared to the neutron-irradiated materials. In the neutron-irradiated specimens, P segregation was only seen to carbide interfaces and grain boundaries. However, in self-ion Irradiation A, more complex P behaviour was observed.

Ion Irradiation A produced a relatively low amount of damage, with observations indicative of the early-stages of segregation behaviour. One particular feature was the onset of P segregation prior to the formation of solute clustering; this segregation was seen in the form of dislocation decoration and diffuse P atmospheres. A reminder of the appearance of these features is given in Figure 7.2. Although P was seen to be contained within clusters in the neutron-irradiated samples at a comparable dpa (the 3 month ANSTO samples),

there was no evidence of distinct P segregation, specifically the forming of atmospheres. Given distinct P segregation was also seen in Irradiation F, it is possible that the response is solely linked to irradiation temperature (as discussed in Section 6.5.1, Chapter 6). However, there is also the possibility that this phenomenon occurs more strongly in ion-irradiated samples, and would not be observed in neutron reactor specimens until higher damage levels, regardless of irradiation temperature. This may explain why P clustering behaviour has been reported in 0.6 dpa neutron-irradiated Fe-Cr samples (at 300°C) by Pariege et al., though at a reduced amount compared to that observed in equivalent dpa self-ion-irradiated samples of the same compositions [126].

This enhanced influence of P during ion irradiation was also suggested by Röder et al., who reported seeing an increased P effect on hardening in ion irradiation compared to neutron [97]. They attributed this difference in the the role of P to early stage stabilisation by P atoms during ion irradiation, similar to the possible P-vacancy atmospheres seen in this work.

7.3 Radiation-induced Solute Segregation

Alongside the formation of solute clusters, additional solute-segregation types were induced following ion irradiation which were not identified in the ANSTO specimens. Primarily, this difference in damage constituted the presence of decorated network-dislocations and dislocation loops. Furthermore, although enhanced segregation to interfaces was seen for both irradiation types, the degree of solute enrichment at these features was heightened following Fe^{4+} irradiation.

More complex solute-dislocation interactions were visible in self-ion APT maps. Dislocation loops could be observed in Irradiation F, where they were not present in the neutron-irradiated samples; this is in-keeping with the expectation that more dislocation

loops form at higher flux, due to an increased rate of the defect interactions which cause stable, extended defects [29, 214]. Beyond the impact of higher damage, there generally was less evidence of dislocation decoration in the ANSTO samples, even where the nature of clustering was comparable. This could be a result of either differing levels of RIS for each irradiation type, with enhanced RIS under ion irradiation, or of an increase in dislocation density (ρ) associated with ion irradiation [215]. A difference in dislocation densities produced by the two irradiating particles could also explain lower cluster number density in ion irradiation results compared to the value produced by extrapolating neutron irradiation data. It has been suggested that an increase in ρ corresponds to an increase in point-defect sinks (causing annihilation), suppressing MNS cluster nucleation [216], but there is insufficient evidence of any differing in ρ in this work to support this theory.

In addition to decoration of dislocations, clusters lying on decorated network-dislocations were more commonly observed in the ion-irradiated, compared to the neutron-irradiated, samples. This reflects the conclusion by Odette et al. who noted that high dpa-rate ion irradiations more frequently display a cluster-dislocation association [203].

Even where the extent of clustering was lower in the self-ion-irradiated samples, there was evidence of increased solute segregation to interfaces compared to where neutron irradiation was applied. This implies segregation to interfaces occurs earlier in Fe^{4+} irradiations with respect to cluster nucleation, but contradicts evidence of reduced RIS in ion-irradiation. It could be that the lower irradiation temperature of the OPAL reactor does more to inhibit interface enrichment than the reduced recombination of neutron irradiation enhances it. However, even in the low temperature neutron and ion irradiations, interface segregation was observed, despite suggestions that low solute diffusion mobility in this temperature regime would cause no detectable boundary segregation behaviour [34] (although this is for a lower fluence than was used in this work).

7.4 Application to Alloy Comparison Studies

In this project, the underlying theme is investigating the impact that processing route has on the radiation response of steel. As a method for comparing multiple samples, ion irradiation proved to be a superior technique, given the reduced time to obtain viable samples, the relative ease of implementation and the variety of conditions possible. Generally ion-irradiation was more efficient and still allowed comparison between the steels, even if the conditions were not equivalent to what would be experienced by components for commercial fission power generation. Through the UK National Ion Beam Centre, self-ion irradiations could be organised without significant waiting times, with large amounts of flexibility possible concerning the irradiation conditions chosen. Subsequent sample preparation was eased by the lack of residual radioactivity, although APT tip fabrication was complicated by the depth-dependent damages profiles associated with ion-irradiations.

The capability of the Fe^{4+} irradiations to generate high damage levels allowed a large portion of the possible damage spectrum for each material to be compared, inducing features which would have taken substantial neutron irradiation times in order to observe in APT. This was most prominently the case for solute segregation to dislocations, dislocation loops and interfaces.

7.5 Summary

As anticipated, there are significant differences in the irradiation behaviour of RPV steels under neutron and self-ion bombardment. Many of these differences are likely due to flux effects, combined with disparate particle interaction behaviour. Where temperature was raised in an attempt to better simulate low-dose neutron damage with ions, damage levels were significantly reduced, suggesting a different approach would be better suited. Of the

low-dose ion irradiations conducted, the results from Irradiation B (0.6dpa, 150°C) appeared most similar to that seen in the ANSTO samples. This suggests that a consistent irradiation temperature could be used in combination with increased dpa. However, this is a theory based only on one set of irradiations; a more extensive, systematic review of correlating neutron- and ion-induced damage would be required to make any concrete conclusions.

As with other ion irradiation studies [102, 107], this work has primarily illustrated the effectiveness of self-ion irradiation as a method for exploring the radiation response of novel materials at an amplified rate. Exploring methods of reproducing neutron studies using ions was not the focus of this research; ultimately, comparing the defects induced in comparative alloy types was the intended outcome, which ion irradiation enabled across multiple damage regimes. Notably, the similar damage features inflicted in Irradiation B to the ANSTO samples indicated that the microstructures analysed were not outside the realm of that possible after neutron irradiation, highlighting how alternative irradiation particles are still a useful tool to study the impact of commercial reactor environments.

Chapter 8

Conclusions

This thesis presented work detailing the irradiation response (both neutron and self-ion) of SA508 Grade 3 Class 1 steel produced via a variety of manufacturing routes. Overall, two neutron irradiations, successfully utilising the OPAL reactor at ANSTO, and three Fe^{4+} irradiations, using the ion accelerator at DCF, were employed.

The primary analytical focus of this research was the application of extensive APT characterisation to irradiated specimens, with the aim of charting the development of MNS clusters and the onset of solute segregation across multiple base-microstructures. In total, 218 APT tips were produced using FIB, of which 144 yielded datasets that were reconstructed and analysed in full. For the neutron irradiations, nanoindentation was also applied in order to quantify the impact of defected microstructure on mechanical properties.

Based on the data obtained in this work, the principal conclusions are outlined below.

Microstructure of HIPed SA508 steel → HIP manufacturing is a potential novel method for the fabrication of SMR components. Characterisation of a HIPed SA508 Grade 3 Class 1 specimen in the as-received condition revealed a larger fraction of polygonal ferrite than present in classically forged RPV steels. This characterisation prompted the decision for

subsequent irradiation in this research to focus on the role of microconstituent phases on the onset of solute segregation. Beyond the inclusion of polygonal ferrite, EDS and TEM analysis also revealed the Al, Si and O rich oxide inclusions (formed as a result of the HIP process) within the HIP steel microstructure, the most significant impact of which is a relative reduction in matrix Si content compared to forged SA508 of comparable composition.

MNS development in low-dose neutron-irradiated steel → Solute clusters enriched in Mn, Ni and Si were found in the ANSTO samples following three-month and six-month neutron irradiations. Nanoindentation revealed that, whilst hardness (and thus yield strength) increased with N_d, the expected linear relationship was not identifiable in this research. This suggests additional hardening defects within the irradiated microstructures, inducing embrittlement beyond the levels expected from MNS cluster formation alone.

Role of polygonal ferrite in HIPed SA508 irradiation response → Targeting ferritic grains during characterisation of the neutron-irradiated and higher-dose ion-irradiated samples provided little evidence of a significant difference in the irradiation response of the two microconstitiuent phases found in the HIPed microstructure. APT analysis across the two irradiation types showed little distinction between the response of bainite and polygonal ferrite in HIPed material, nor a distinction between the HIPed and forged post-irradiation microstructures. There was a slight difference in the neutron-induced hardening between the HIPed and LF ANSTO samples; after 0.1 dpa of neutron irradiation damage, nanoindentation showed that the LF sample (containing significantly less ferrite) was shown to harden less that the HIPed sample. If this is a true reflection of the behaviour of HIPed SA508 under irradiation, it is a potential cause for concern when considering the use of this HIPing over traditional forging for the manufacture of nuclear components.

P atmospheres in Fe^{4+} irradiations → In the 300°C, circa 0.1 dpa self-ion irradiation (A), at a dpa prior to the observation of MNS clustering, P atmospheres were found to have formed within the alloys of higher initial P content (HIP and LF). These atmospheres are comparable to those observed in previous studies of similarly ion-irradiated materials, however, were not present following either the neutron irradiations nor the lower temperature Fe^{4+} ion irradiations in this work. Subsequently, the formation of these clusters is likely linked to higher irradiation temperatures, resulting in enhanced P diffusion giving rise to P-vacancy complex formation prior to the development of MNS solute clusters. Should a similar phenomenon occur during neutron irradiation at elevated temperatures, observation of P atmospheres may be relevant to developing an enhanced understanding of the early stages of the evolution of hardening features in neutron-irradiated steels.

Mn-rich clusters in 5 dpa Fe^{4+} irradiation → Beyond the observation of typically observed Mn, Ni and Si enriched solute clusters, APT analysis indicated that the higher damage (5 dpa) self-ion irradiation samples contained some clusters (and decorated dislocations) primarily incorporated of Mn, with some Ni, Mo and C. Concurrently, those MNS clusters present in these APT volumes were found to have a reduced Mn content compared to in the Fe^{4+} Irradiation A and B samples. This dual-phase solute clustering has not, to the author's knowledge, been previously identified in irradiated low-Cu RPV steels. The implication is that higher dpa ion-irradiation leads to a depletion of Ni and Si from the alloy matrix (due to MNS cluster growth), leaving an excess of Mn (which is of higher starting composition). The excess Mn atoms produce stable solute-vacancy clusters, which grow through enhanced diffusion kinetics. At higher dpa, it becomes more favourable for Mn atoms in solution to contribute to the growth of the Mn-rich clusters than the MNS clusters, as the MNS clusters favour the proposed thermodynamically stable G and Γ_2 phases. Whether these features are of a distinct phase could be confirmed by

extracting crystallographic information (either using TEM or potentially XRD at this scale).

Comparison of neutron and ion irradiation → Ion irradiation was able to produce similar defects to that seen following the ANSTO irradiations, although this work focused on the defects visible using APT. Critically, the use of Fe^{4+} ions allowed this damage to be produced in a significantly shorter time-frame. Accordingly, the higher dpa condition (5 dpa) could not have reasonably been achieved using neutron bombardment, preventing examination of developed clustering and dislocation enrichment (as seen in the Irradiation F samples). Based on this work, there is a place for ion-irradiated materials as surrogates for those produced in commercial nuclear reactors. This is given the ability of heavy-ion irradiation to largely reproduce low-dose neutron-irradiated microstructures, whilst the damage observed in higher dose ion-irradiation appears an intuitive development of the microstructures seen in neutron-irradiated specimens. For a more comprehensive comparison as to the embrittlement induced by both particle types, and to enhance the ion-irradiation work generally, micro-mechanical testing of the ion-irradiated samples would have been desirable - this would give insight into whether comparable clustering behaviour corresponds to similar hardening levels.

Chapter 9

Future Work

Following on from the research completed as part of this thesis, there are areas of study which would benefit from additional investigation.

Early-stage P atmosphere formation under neutron irradiation at commercial reactor operation temperatures This work used neutron irradiation to produce small-scale Mn, Ni and Si solute clustering, however, this was at an irradiation temperature of 150°C (dictated by the operational conditions of the OPAL reactor). Low-dose Fe^{4+} irradiation at 300°C revealed the development of P atmospheres in SA508 steel samples (with sufficiently high P contents) prior to the onset of MNS clustering.

In order to investigate the timeline of cluster development in a fission environment, low-dose neutron irradiation at ≈ 300°C would be required. There is also the potential for a correlative study whereby TEM is used to investigate the defect concentration within an APT tip, which is then analysed in the atom probe in order to determine whether these P atmospheres are (as proposed) nucleating on matrix damage introduced by irradiation. It would also be informative to use nanoindentation to see if the presence of early-stage P segregation corresponds to hardening.

Effect of microstructure on number density of irradiation-induced defects Much of this research looked at the impact of polygonal ferrite grains in novel HIPed SA508 steel on irradiation response. The use of APT allowed the development of solute-vacancy clusters to be investigated, with little discernible difference between the ferritic and bainitic clustering behaviour identified, however any defects not clearly decorated by solute atoms could not be observed by employing APT alone. A more involved set of TEM investigations on the HIPed and forged materials would allow identification of matrix damage, such as dislocation loops, which act a precursors for MNS clustering. This would enable comparison in neutron irradiation response beyond the observation of clustering, and potentially shed light on the origins of the difference in relative hardening exhibited by the 0.1 dpa HIP and LF ANSTO samples in this project. Observation of dislocations and fine-scale microstructure would also be relevant for further work comparing the irradiation response of steels with different forging durations (as was studied here with alloys B and C).

Furthermore, TEM provides a wider field of view, and, when combined with STEM, could allow the amount of solute segregation and irradiation-defect production to be correlated with local environment, such as proximity to carbides and grain boundaries. This would counteract some of the limitations presented by the relatively small volumes analysed with APT, whilst also providing improved statistics when comparing the irradiation response of different grain types (important for conclusions on the viability of HIP-manufacturing for the production of nuclear components).

Irradiation-induced clustering at interfaces As part of the investigation of 5 dpa self-ion irradiated SA508, APT revealed solute clustering within planar interfaces (specifically grain boundaries and carbides). This observation was a result of random sampling in APT specimen production, and thus the frequency with which these features were encountered was low. Despite this, the intra-boundary clustering analysed was interesting, as it has

rarely been reported.

There is therefore scope for a study into the development of clustering on grain boundaries and carbide interfaces, utilising irradiated materials in combination with correlative TKD and APT to target the regions of interest. Given that grain boundaries and carbides are critical features in controlling steel mechanical properties, an understanding of the development of any potentially deleterious solute clustering is of potential interest to this field of study.

Improved data on the use of ion irradiation for the study of materials for use in nuclear components Although there is already a high volume of publications describing the benefits and limitations of studying the irradiation behaviour of materials used in nuclear fission components, there is limited comparative experimental data. It is clear that ion irradiation has a place in nuclear studies, given that the speed and reduced costs allows a more regular turnover of experiments across a large breadth of conditions and materials. The biggest limitation, however, continues to be a lack of comprehensive understanding of the validity of results obtained from ion irradiation studies, with respect to improving the understanding of microstructural and mechanical changes induced by a neutron-irradiation environment.

More work utilising the systematic altering of self-ion irradiation conditions (such as temperature, fluence and particle type) for a given alloy – combined with APT, TEM and mechanical testing – would improve comparisons between neutron and self-ion irradiation results. It would also allow ion irradiation studies to be better presented in the context of neutron irradiation, with the potential to improve correlative models.

Bibliography

[1] The Royal Society. *Nuclear cogeneration: civil nuclear energy in a low-carbon future*. Tech. rep. 2020.

[2] Huibin Ke et al. "Thermodynamic and kinetic modeling of Mn-Ni-Si precipitates in low-Cu reactor pressure vessel steels". In: *Acta Materialia* 138 (2017), pp. 10–26.

[3] G.R Odette and G E Lucas. "Embrittlement of Nuclear Reactor Pressure Vessels". In: *Journal of Nuclear Materials* 53 (2001), pp. 18–22.

[4] Mark Wenman. *Linking Microstructure to Neutron Irradiation Defects in Advanced Manufacture of Steels*. 2016.

[5] *Economics of Nuclear Power*. 2017.

[6] S J Zinkle and G S Was. "Materials challenges in nuclear energy". In: *Acta Materialia* 61.3 (2013), pp. 735–758.

[7] IAEA. *Integrity of Reactor Pressure Vessels in Nuclear Power Plants: Assessment of Irradiation Embrittlement Effects in Reactor Pressure Vessel Steels*. IAEA Nuclear Energy Series No. NP-T-3.11. 2009.

[8] K Suzuki. *Neutron irradiation embrittlement of ASME SA508, C1. 3 Steel*. 1982.

[9] C. R F Azevedo. *A review on neutron-irradiation-induced hardening of metallic components*. 2011.

[10] C. English and J. Hyde. "Radiation Damage of Reactor Pressure Vessel Steels". In: *Comprehensive Nuclear Materials*. Ed. by R M Konings. Elsevier Ltd, 2012. Chap. 4.05, pp. 151–180.

[11] G. R. Odette. "On the dominant mechanism of irradiation embrittlement of reactor pressure vessel steels". In: *Scripta Metallurgica* 17.10 (1983), pp. 1183–1188.

[12] J. Russell Hawthorne. "Composition influences and interactions in radiation sensitivity of reactor vessel steels". In: *Nuclear Engineering and Design* 89.1 (1985), pp. 223–232.

[13] Jeremy T Busby et al. *Materials degradation in light water reactors: life after 60*. Tech. rep. Oak Ridge National Laboratory, 2008.

[14] J. C. van Duysen and G. Meric de Bellefon. *60th Anniversary of electricity production from light water reactors: Historical review of the contribution of materials science to the safety of the pressure vessel*. 2017.

[15] Adam Vaughan. "Power from mini nuclear plants 'would cost more than from large ones'". In: *The Guardian* (12-07-2017).

[16] L.E. Steele. *Neutron Irradiation Embrittlement of Reactor Pressure Vessel Steels*. Tech. rep. IAEA, 1975.

[17] Wei Guo et al. "Microstructure and mechanical characteristics of a laser welded joint in SA508 nuclear pressure vessel steel". In: *Materials Science and Engineering: A* 625 (2015), pp. 65–80.

[18] M K Miller et al. "APT characterization of irradiated high nickel RPV steels". In: *Journal of Nuclear Materials* 361.2-3 SPEC. ISS. (2007), pp. 248–261.

[19] H. V. Atkinson and S. Davies. "Fundamental aspects of hot isostatic pressing: An overview". In: *Metallurgical and Materials Transactions A: Physical Metallurgy and Materials Science* 31.12 (2000), pp. 2981–3000.

[20] NNUMAN. *Impact Report 2016*. Tech. rep. 2016.

[21] H Pous-Romero et al. "The prediction of toughness and strength in high integrity forgings". In: *Proceedings of the 19th International Forgemasters Meeting* (2014), pp. 502–506.

[22] H. K.D.H. Bhadeshia. "Diffusional formation of ferrite in iron and its alloys". In: *Progress in Materials Science* 29 (1985), pp. 312–386.

[23] Lin Cheng, Kaiming Wu, and Xiangliang Wan. "Growth Behavior of Intragranular Ferrite Idiomorphs in an Fe-0.09%C-1.48%Mn-0.2Si Steels". In: *steel research international* 85.5 (2014), pp. 836–843.

[24] Y. T. Chi et al. "Investigation of idiomorphic ferrite and allotriomorphic ferrite using electron backscatter diffraction technique". In: *Materials Science and Technology (United Kingdom)* 33.5 (2017), pp. 537–545.

[25] T. Yokomizo et al. "Three-dimensional distribution, morphology, and nucleation site of intragranular ferrite formed in association with inclusions". In: *Materials Science and Engineering A* 344.1-2 (Mar. 2003), pp. 261–267.

[26] Stéphanie Jumel and Jean Claude Van-Duysen. "INCAS: An analytical model to describe displacement cascades". In: *Journal of Nuclear Materials* 328 (2004), pp. 151–164.

[27] W. J. Phythian and C. A. English. "Microstructural evolution in reactor pressure vessel steels". In: *Journal of Nuclear Materials* 205 (1993), pp. 162–177.

[28] J M Hyde et al. "A comparison of the structure of solute clusters formed during thermal ageing and irradiation". In: *Ultramicroscopy* 111.6 (2011), pp. 664–671.

[29] Christopher D Hardie et al. “Effects of irradiation temperature and dose rate on the mechanical properties of self-ion implanted Fe and Fe-Cr alloys”. In: *Journal of Nuclear Materials* 439 (2013), pp. 33–40.

[30] C. Abromeit. “Aspects of simulation of neutron damage by ion irradiation”. In: *Journal of Nuclear Materials* 216.C (1994), pp. 78–96.

[31] E A Little. “Neutron-irradiation hardening in irons and ferritic steels”. In: *International Metals Reviews* 21:1 (1976), pp. 25–60.

[32] Todd Allen et al. “Materials challenges for nuclear systems”. In: *Materials Today* 13.12 (2010), pp. 14–23.

[33] X.M Chen et al. “Combined Hardening and Non-hardening Embrittlement of an Interstitial Free Steel”. In: *Materials Letters* 67 (2012), pp. 107–109.

[34] E A Kuleshova et al. “Mechanisms of radiation embrittlement of VVER-1000 RPV steel at irradiation temperatures of (50–400)°C”. In: *Journal of Nuclear Materials* 490 (2017), pp. 247–259.

[35] Alan J. Ardell and Pascal Bellon. “Radiation-induced solute segregation in metallic alloys”. In: *Current Opinion in Solid State and Materials Science* 20.3 (2016), pp. 115–139.

[36] Todd R Allen et al. “Characterization of microstructure and property evolution in advanced cladding and duct: Materials exposed to high dose and elevated temperature”. In: *Journal of Materials Research* 30.09 (2015), pp. 1246–1274.

[37] J. E. Zelenty. “Understanding thermally induced embrittlement in low copper RPV steels utilising atom probe tomography”. In: *Materials Science and Technology* 31.8 (2015), pp. 981–988.

[38] B. Marini et al. “Effect of the bainitic and martensitic microstructures on the hardening and embrittlement under neutron irradiation of a reactor pressure vessel steel”. In: *Journal of Nuclear Materials* 465 (2015), pp. 20–27.

[39] Lin Shao et al. “Standardization of accelerator irradiation procedures for simulation of neutron induced damage in reactor structural materials”. In: *Nuclear Instruments and Methods in Physics Research, Section B: Beam Interactions with Materials and Atoms* 409 (2017), pp. 251–254.

[40] G.R. Odette and B.D. Wirth. “A computational microscopy study of nanostructural evolution in irradiated pressure vessel steels”. In: *Journal of Nuclear Materials* 251 (1997), pp. 157–171.

[41] G. R. Odette and G. E. Lucas. “Recent progress in understanding reactor pressure vessel steel embrittlement”. In: *Radiation Effects and Defects in Solids* 144.1-4 (June 1998), pp. 189–231.

[42] Philip M. Rice and Roger E. Stoller. “Correlation of nanoindentation and conventional mechanical property measurements”. In: *Materials Research Society Symposium-Proceedings* 649.1 (2001), Q7.11.1–Q7.11.6.

[43] C. Gasparrini et al. “Micromechanical testing of unirradiated and helium ion irradiated SA508 reactor pressure vessel steels: Nanoindentation vs in-situ microtensile testing”. In: *Materials Science and Engineering A* 796 (2020), p. 139942.

[44] C Heintze et al. “Ion irradiation combined with nanoindentation as a screening test procedure for irradiation hardening”. In: *Journal of Nuclear Materials* 472 (2016), pp. 196–205.

[45] Koji Fukuya. “Current understanding of radiation-induced degradation in light water reactor structural materials”. In: *Journal of Nuclear Science and Technology* 50.3 (2013), pp. 213–254.

[46] M. Lambrecht, L. Malerba, and A. Almazouzi. “Influence of different chemical elements on irradiation-induced hardening embrittlement of RPV steels”. In: *Journal of Nuclear Materials* 378.3 (2008), pp. 282–290.

[47] Ki Sig Kang. *Effects of nickel on irradiation embrittlement of light water reactor pressure vessel steels*. Tech. rep. IAEA, 2005.

[48] M. K. Miller and M. G. Burke. “An atom probe field ion microscopy study of neutron-irradiated pressure vessel steels”. In: *Journal of Nuclear Materials* 195.1-2 (1992), pp. 68–82.

[49] J. T. Buswell et al. “Irradiation-induced microstructural changes, and hardening mechanisms, in model PWR reactor pressure vessel steels”. In: *Journal of Nuclear Materials* 225 (1995), pp. 196–214.

[50] Jing Lei et al. “Study on the mechanical properties evolution of A508-3 steel under proton irradiation”. In: *Nuclear Instruments and Methods in Physics Research Section B: Beam Interactions with Materials and Atoms* 338 (2014), pp. 13–18.

[51] P Asoka-Kumar et al. “Composition and magnetic character of nanometre-size Cu precipitates in reactor pressure vessel steels: Implications for nuclear power plant lifetime extension”. In: *Philosophical Magazine Letters* 82.11 (2002), pp. 609–615.

[52] B. A. Gurovich et al. “Fine structure behaviour of VVER-1000 RPV materials under irradiation”. In: *Journal of Nuclear Materials* 389.3 (2009), pp. 490–496.

[53] M. Hernández-Mayoral and D. Gómez-Briceño. “Transmission electron microscopy study on neutron irradiated pure iron and RPV model alloys”. In: *Journal of Nuclear Materials* 399.2-3 (2010), pp. 146–153.

[54] P Auger et al. “APFIM investigation of clustering in neutron-irradiated FeCu alloys and pressure vessel steels”. In: *Journal of Nuclear Materials* 225 (1995), pp. 225–230.

[55] M. K. Miller and S. S. Brenner. “Fim/atom Probe Study of Irradiated Pressure Vessel Steels”. In: *Res Mechanica: International Journal of Structural Mechanics and Materials Science* 10.3 (1984), pp. 161–168.

[56] D Vaumousse, A Cerezo, and P J Warren. “A procedure for quantification of precipitate microstructures from three-dimensional atom probe data”. In: *Ultramicroscopy* 95.SUPPL. (2003), pp. 215–221.

[57] M K Miller and K F Russell. “Embrittlement of RPV steels: An atom probe tomography perspective”. In: *Journal of Nuclear Materials* 371.1-3 (2007), pp. 145–160.

[58] M. K. Miller, P. Pareige, and M. G. Burke. “Understanding pressure vessel steels: an atom probe perspective”. In: *Materials Characterization* 44 (Jan. 2000), pp. 235–254.

[59] G R Odette. “Radiation Induced Microstructural Evolution in Reactor Pressure Vessel Steels”. In: *MRS Proceedings* 373 (1995), p. 137.

[60] F. Bergner, A. Ulbricht, and H.-W. Viehrig. “Acceleration of irradiation hardening of low-copper reactor pressure vessel steel observed by means of SANS and tensile testing”. In: *Philosophical Magazine Letters* 89.12 (2009), pp. 795–805.

[61] F. Bergner et al. “Post-irradiation annealing behavior of neutron-irradiated FeCu, FeMnNi and FeMnNiCu model alloys investigated by means of small-angle neutron scattering”. In: *Journal of Nuclear Materials* 454 (2014), pp. 22–27.

[62] P. D. Styman et al. “Post-irradiation annealing of Ni-Mn-Si-enriched clusters in a neutron-irradiated RPV steel weld using Atom Probe Tomography”. In: *Journal of Nuclear Materials* 459 (2015), pp. 127–134.

[63] Peter B. Wells et al. “Evolution of manganese-nickel-silicon-dominated phases in highly irradiated reactor pressure vessel steels”. In: *Acta Materialia* 80 (2014), pp. 205–219.

[64] D. J. Sprouster et al. “Structural characterization of nanoscale intermetallic precipitates in highly neutron irradiated reactor pressure vessel steels”. In: *Scripta Materialia* 113 (Mar. 2016), pp. 18–22.

[65] P. B. Wells. “The Character, Stability and Consequences of Mn-Ni-Si Precipitates in Irradiated Reactor Pressure Vessel Steels”. Ph.D Thesis. UCSB, 2016.

[66] Kristina Lindgren et al. “On the Analysis of Clustering in an Irradiated Low Alloy Reactor Pressure Vessel Steel Weld”. In: *Microscopy and Microanalysis* 23.02 (2017), pp. 376–384.

[67] R. Ngayam-Happy et al. “Formation and evolution of MnNi clusters in neutron irradiated dilute Fe alloys modelled by a first principle-based AKMC method”. In: *Journal of Nuclear Materials* 426 (2012), pp. 198–207.

[68] R. Ngayam-Happy, C. S. Becquart, and C. Domain. “First principle-based AKMC modelling of the formation and medium-term evolution of point defect and solute-rich clusters in a neutron irradiated complex Fe-CuMnNiSiP alloy representative of reactor pressure vessel steels”. In: *Journal of Nuclear Materials* 440 (2013), pp. 143–152.

[69] G. Bonny et al. “On the thermal stability of late blooming phases in reactor pressure vessel steels: An atomistic study”. In: *Journal of Nuclear Materials* 442.1-3 (2013), pp. 282–291.

[70] N. Almirall et al. “On the elevated temperature thermal stability of nanoscale Mn-Ni-Si precipitates formed at lower temperature in highly irradiated reactor pressure vessel steels”. In: *Scientific Reports* 9.1 (2019), pp. 1–12.

[71] Jia Hong Ke et al. “Cluster dynamics modeling of Mn-Ni-Si precipitates in ferritic-martensitic steel under irradiation”. In: *Journal of Nuclear Materials* 498 (2018), pp. 83–88.

[72] Y. Matsukawa et al. “The two-step nucleation of G-phase in ferrite”. In: *Acta Materialia* 116 (Sept. 2016), pp. 104–113.

[73] N. Almirall et al. “Precipitation and hardening in irradiated low alloy steels with a wide range of Ni and Mn compositions”. In: *Acta Materialia* 179 (2019), pp. 119–128.

[74] Kristina Lindgren et al. “Evolution of precipitation in reactor pressure vessel steel welds under neutron irradiation”. In: *Journal of Nuclear Materials* 488 (2017), pp. 222–230.

[75] K. Fukuya et al. “Microstructural evolution in medium copper low alloy steels irradiated in a pressurized water reactor and a material test reactor”. In: *Journal of Nuclear Materials* 312.2-3 (2003), pp. 163–173.

[76] K. Dohi et al. “Effect of neutron flux on low temperature irradiation embrittlement of reactor pressure vessel steel”. In: *Journal of Nuclear Materials* 265.1-2 (1999), pp. 78–90.

[77] Kenji Dohi et al. “Effect Of Neutron Flux At High Fluence On Microstructural And Hardness Changes Of RPV Steels”. In: *Proceedings Of The ASME Pressure Vessels And Piping Conference 2010, Vol 9.* ASME, 2010, pp. 95–102.

[78] F Bergner et al. “Flux dependence of cluster formation in neutron-irradiated weld material”. In: *Journal of Physics Condensed Matter* 20.10 (2008).

[79] A. Wagner et al. “Effect of neutron flux on the characteristics of irradiation-induced nanofeatures and hardening in pressure vessel steels”. In: *Acta Materialia* 104 (2016), pp. 131–142.

[80] J. R. Hawthorne and A. L. Hiser. “Fluence-rate effects on irradiation embrittlement and composition and temperature effects on annealing/reirradiation sensitivity”. In: *Nuclear Engineering and Design* 108.1-2 (1988), pp. 221–232.

[81] Rodolfo Kempf, Horacio Troiani, and Ana Maria Fortis. “Effect of lead factors on the embrittlement of RPV SA-508 cl 3 steel”. In: *Journal of Nuclear Materials* 434.1-3 (2013), pp. 411–416.

[82] E. Meslin et al. “Characterization of neutron-irradiated ferritic model alloys and a RPV steel from combined APT, SANS, TEM and PAS analyses”. In: *Journal of Nuclear Materials* 406 (2010), pp. 73–83.

[83] L. Debarberis et al. “Effect of irradiation temperature in PWR RPV materials and its inclusion in semi-mechanistic model”. In: *Scripta Materialia* 53.6 (2005), pp. 769–773.

[84] R. J. McElroy et al. “Low temperature embrittlement of LWR RPV support structures”. In: *International Journal of Pressure Vessels and Piping* 54.1-2 (1993), pp. 171–211.

[85] G. S. Was et al. “Emulation of reactor irradiation damage using ion beams”. In: *Scripta Materialia* 88 (2014), pp. 33–36.

[86] Gary S Was. “Challenges to the use of ion irradiation for emulating reactor irradiation”. In: *Journal of Materials Research* 30.09 (2015), pp. 1158–1182.

[87] S. J. Zinkle and L. L. Snead. “Opportunities and limitations for ion beams in radiation effects studies: Bridging critical gaps between charged particle and neutron irradiations”. In: *Scripta Materialia* 143 (2018), pp. 154–160.

[88] C.A. English. “Low-dose neutron irradiation damage in FCC and BCC metals”. In: *Journal of Nuclear Materials* 108 (1982), pp. 104–123.

[89] Hyung Ha Jin et al. “Effect of irradiation temperature on microstructural changes in self-ion irradiated austenitic stainless steel”. In: *Journal of Nuclear Materials* 493 (2017), pp. 239–245.

[90] R. S. Nelson, D. J. Mazey, and J. A. Hudson. “The use of ion accelerators to simulate fast neutron-induced voidage in metals”. In: *Journal of Nuclear Materials* 37.1 (Oct. 1970), pp. 1–12.

[91] M. P. Short et al. “Modeling injected interstitial effects on void swelling in self-ion irradiation experiments”. In: *Journal of Nuclear Materials* 471 (2016), pp. 200–207.

[92] F. A. Garner. “Impact of the injected interstitial on the correlation of charged particle and neutron-induced radiation damage”. In: *Journal of Nuclear Materials* 117.C (1983), pp. 177–197.

[93] James F. Ziegler and Jochen P. Biersack. “The Stopping and Range of Ions in Matter”. In: *Treatise on Heavy-Ion Science*. Springer US, 1985, pp. 93–129.

[94] Rudolf Sizmann. “The effect of radiation upon diffusion in metals”. In: *Journal of Nuclear Materials* 69-70.C (Feb. 1978), pp. 386–412.

[95] A. Müller, V. Naundorf, and M. P. MacHt. “Point defect sinks in self-ion-irradiated nickel: A self-diffusion investigation”. In: *Journal of Applied Physics* 64.7 (1988), pp. 3445–3455.

[96] C Heintze, F Bergner, and M. Hernandez-Mayoral. “Ion-irradiation-induced damage in Fe-Cr alloys characterized by nanoindentation”. In: *Journal of Nuclear Materials*. Vol. 417. 2011, pp. 980–983.

[97] F. Röder et al. “Nanoindentation of ion-irradiated reactor pressure vessel steels – model-based interpretation and comparison with neutron irradiation”. In: *Philosophical Magazine* 6435 (2018), pp. 1–23.

[98] Brenden Heidrich et al. “Roadmap for the application of ion beam technologies to the challenges of nuclear energy technologies”. In: *Nuclear Instruments and Methods in Physics Research, Section B: Beam Interactions with Materials and Atoms* 441 (2019), pp. 41–45.

[99] N. H. Packan, K. Farrell, and J. O. Stiegler. “Correlation of neutron and heavy-ion damage. I. The Influence of Dose Rate and Injected Helium on Swelling in Pure Nickel”. In: *Journal of Nuclear Materials* 78.1 (1978), pp. 143–155.

[100] B. Radiguet, P. Pareige, and A. Barbu. “Irradiation induced clustering in low copper or copper free ferritic model alloys”. In: *Nuclear Instruments and Methods in Physics Research, Section B: Beam Interactions with Materials and Atoms* 267.8-9 (2009), pp. 1496–1499.

[101] R. M. Mayer. “Nucleation and growth of voids by radiation: VII. Correlation of Charged Particle and Neutron Irradiations”. In: *Journal of Nuclear Materials* 95.1-2 (1980), pp. 100–107.

[102] Michael J Fluss, Peter Hosemann, and Jaime Marian. “Charged-Particle Irradiation for Neutron Radiation Damage Studies”. In: *Characterization of Materials*. 2012.

[103] N. Almirall et al. “On the use of charged particles to characterize precipitation in irradiated reactor pressure vessel steels with a wide range of compositions”. In: *Journal of Nuclear Materials* 536 (2020), p. 152173.

[104] Ce Zheng et al. “Radiation induced segregation and precipitation behavior in self-ion irradiated Ferritic/Martensitic HT9 steel”. In: *Journal of Nuclear Materials* 491 (2017), pp. 162–176.

[105] Z. Jiao and G. S. Was. “Segregation behavior in proton- and heavy-ion-irradiated ferritic-martensitic alloys”. In: *Acta Materialia* 59.11 (2011), pp. 4467–4481.

[106] H. Watanabe et al. “Radiation induced hardening of ion irradiated RPV steels”. In: *Journal of Nuclear Materials*. Vol. 417. 1-3. North-Holland, Oct. 2011, pp. 932–935.

[107] D. J. Mazey. “Fundamental aspects of high-energy ion-beam simulation techniques and their relevance to fusion materials studies”. In: *Journal of Nuclear Materials* 174.2-3 (1990), pp. 196–209.

[108] L. K. Mansur. “Theory and experimental background on dimensional changes in irradiated alloys”. In: *Journal of Nuclear Materials* 216.C (1994), pp. 97–123.

[109] R.W. Nichols and D.R. Harries. “Brittle Fracture and Irradiation Effects in Ferritic Pressure Vessel Steels”. In: *ASTM STP-341* (1963), p. 162.

[110] G.M. Gordon and H.H. Klepfer. “Engineering Significance of Ferrite Grain Size on the Radiation Sensitivity of Pressure Vessel Steels”. In: *ASTM STP-426* (1967), p. 48.

[111] P. D. Edmondson et al. “Atom probe tomography characterization of neutron irradiated surveillance samples from the R. E. Ginna Reactor Pressure Vessel”. In: *Journal of Nuclear Materials* 470 (2016), pp. 147–154.

[112] L. E. Steele and U. Potapovs. “Radiation embrittlement of reactor vessel steels and suggestions for its control”. In: *Nuclear Engineering and Design* 8 (July 1968), pp. 58–70.

[113] Mary Grace Burke et al. *Microstructural aspects of irradiation damage in A508 Gr 4N forging steel: Composition and flux effects*. Tech. rep. 1447. 2004, pp. 194–207.

[114] M. Akamatsu et al. “Experimental evidence of several contributions to the radiation damage in ferritic alloys”. In: *Journal of Nuclear Materials* 225 (1995), pp. 192–195.

[115] F. A. Smidt and H. E. Watson. “Effect of residual elements on radiation strengthening in iron alloys, pressure vessel steels, and welds”. In: *Metallurgical Transactions* 3.8 (1972), pp. 2065–2073.

[116] R. G. Carter et al. “Microstructural characterization of irradiation-induced Cu-enriched clusters in reactor pressure vessel steels”. In: *Journal of Nuclear Materials* 298 (2001), pp. 211–224.

[117] M K Miller et al. “APT characterization of high nickel RPV steels”. In: *Journal of Nuclear Materials* 351 (2006), pp. 187–196.

[118] L.T. Belkacemi-Rebrab et al. “Striking effect of solute elements (Mn, Ni) on radiation-induced segregation/precipitation in iron-based model alloys”. In: *Journal of Nuclear Materials* 548 (2021), p. 152807.

[119] A. Kryukov et al. “Irradiation embrittlement of reactor pressure vessel steel at very high neutron fluence”. In: *Journal of Nuclear Materials* 422 (2012), pp. 173–177.

[120] MK Miller and MG Burke. “An APFIM Survey of Grain Boundary Segregation and Precipitation in Irradiated Pressure Vessel Steels”. In: *Effects of Radiation on Materials: Sixteenth International Symposium*. Ed. by A.S Kumar et al. Philadelphia: ASTM International, 1994, pp. 492–492–11.

[121] R J Stofanak et al. “Irradiation Damage Behavior of Low Alloy Steel Wrought and Weld Materials”. In: *10th International Symposium on Environmental Degradation of Materials in Nuclear Power Systems—Water Reactors*. Ed. by G. S. Was and L Nelson. NACE, 2002.

[122] Luca Messina et al. “Solute diffusion by self-interstitial defects and radiation-induced segregation in ferritic Fe–X (X=Cr, Cu, Mn, Ni, P, Si) dilute alloys”. In: *Acta Materialia* 191 (June 2020), pp. 166–185. eprint: 1910.11440.

[123] E. Vincent, C. S. Becquart, and C. Domain. “Ab initio calculations of self-interstitial interaction and migration with solute atoms in bcc Fe”. In: *Journal of Nuclear Materials* 359.3 (2006), pp. 227–237.

[124] Y. Nishiyama et al. “Effects of neutron-irradiation-induced intergranular phosphorus segregation and hardening on embrittlement in reactor pressure vessel steels”. In: *Acta Materialia* 56.16 (2008), pp. 4510–4521.

[125] L. Malerba et al. “Ab initio calculations and interatomic potentials for iron and iron alloys: Achievements within the Perfect Project”. In: *Journal of Nuclear Materials* 406.1 (2010), pp. 7–18.

[126] C. Pareige, V. Kuksenko, and P. Pareige. “Behaviour of P, Si, Ni impurities and Cr in self ion irradiated Fe-Cr alloys - Comparison to neutron irradiation”. In: *Journal of Nuclear Materials* 456 (2015), pp. 471–476.

[127] P Pareige et al. “Atom probe characterization of the microstructure of nuclear pressure vessel surveillance materials after neutron irradiation and after annealing treatments”. In: *Journal of Nuclear Materials* 249.2-3 (1997), pp. 165–174.

[128] M K Miller and P Pareige. “Atomic Level Characterization of Neutron Irradiated Pressure Vessel Steels”. In: *Materials Research Society Symposium Proceedings*. Vol. 650. Oak Ridge National Laboratory, 2001, R6.1.1–12.

[129] M. G. Burke and S. S. Brenner. “Microstructural Investigation of Irradiated Pressure Vessel Steel Weld Material”. In: *Journal de Physique Colloques* 47.C2 (1986), pp. 239–244.

[130] G. M. Worrall et al. “A study of the precipitation of copper particles in a ferrite matrix”. In: *Journal of Nuclear Materials* 148 (1987), pp. 107–114.

[131] P. D. Styman et al. “Precipitation in long term thermally aged high copper, high nickel model RPV steel welds”. In: *Progress in Nuclear Energy*. Vol. 57. Pergamon, 2012, pp. 86–92.

[132] M K Miller et al. “Atom probe tomography characterizations of high nickel, low copper surveillance RPV welds irradiated to high fluences”. In: *Journal of Nuclear Materials* 437.1-3 (2013), pp. 107–115.

[133] P. Pareige, J. C. Van Duysen, and P. Auger. “An APFIM study of the microstructure of a ferrite alloy after high fluence neutron irradiation”. In: *Applied Surface Science* 67 (1993), pp. 342–347.

[134] E. Meslin, B. Radiguet, and M. Loyer-Prost. “Radiation-induced precipitation in a ferritic model alloy: An experimental and theoretical study”. In: *Acta Materialia* 61 (Sept. 2013), pp. 6246–6254.

[135] Stephen C. Glade et al. “Positron annihilation spectroscopy and small angle neutron scattering characterization of nanostructural features in high-nickel model reactor pressure vessel steels”. In: *Journal of Nuclear Materials* 351.1-3 (2006), pp. 197–208.

[136] Jonathan M. Hyde and Colin A. English. "An Analysis of the Structure of Irradiation Induced Cu-Enriched Clusters in Low and High Nickel Welds". In: *Materials Research Society Symposium Proceedings*. Vol. 650. Cambridge University Press, 2000, R6.6.

[137] Leigh T. Stephenson et al. "New techniques for the analysis of fine-scaled clustering phenomena within Atom Probe Tomography (APT) data". In: *Microscopy and Microanalysis*. Vol. 13. 6. Cambridge University Press, 2007, pp. 448–463.

[138] J M Hyde et al. "A sensitivity analysis of the maximum separation method for the characterisation of solute clusters". In: *Ultramicroscopy* 111 (2011), pp. 440–447.

[139] J M Hyde et al. "Characterisation of the early stages of solute clustering in 1Ni-1.3Mn welds containing Cu". In: *Ultramicroscopy* 109.5 (2009), pp. 510–517.

[140] Shipeng Shu et al. "Multi-technique characterization of the precipitates in thermally aged and neutron irradiated Fe-Cu and Fe-Cu-Mn model alloys: Atom probe tomography reconstruction implications". In: *Acta Materialia* 146 (2017), pp. 237–252.

[141] Emmanuelle A. Marquis. "Atom probe tomography applied to the analysis of irradiated microstructures". In: *Journal of Materials Research* 30.09 (2015), pp. 1222–1230.

[142] P.D. Edmondson et al. "Corrigendum to "Atom probe tomography characterization of neutron irradiated surveillance samples from the R.E. Ginna Reactor Pressure Vessel"". In: *Journal of Nuclear Materials* 489 (2017), pp. 236–237.

[143] ASTM International. *ASTM A508 / A508M-18, Standard Specification for Quenched and Tempered Vacuum-Treated Carbon and Alloy Steel Forgings for Pressure Vessels*. West Conshohocken, PA, 2018.

[144] O.K. Chopra and A.S. Rao. "Degradation of LWR core internal materials due to neutron irradiation". In: *NUREG/CR-7027 ANL-10/11 Report, Environ. Sci. Div. Argonne Natl. Lab* January (2010).

[145] R. E. Stoller et al. "On the use of SRIM for computing radiation damage exposure". In: *Nuclear Instruments and Methods in Physics Research, Section B: Beam Interactions with Materials and Atoms* 310 (2013), pp. 75–80.

[146] D. J. Larson et al. "Atom probe tomography spatial reconstruction: Status and directions". In: *Current Opinion in Solid State and Materials Science* 17.5 (2013), pp. 236–247.

[147] Baptiste Gault et al. *Atom Probe Microscopy*. Springer, 2012.

[148] Baptiste Gault et al. "Atom probe tomography". In: *Nature Reviews Methods Primers* 1.1 (2021), pp. 1–30.

[149] A Cerezo et al. "Performance of an energy-compensated three-dimensional atom probe". In: *Review of Scientific Instruments* 69.1 (1998), pp. 49–58.

[150] Baptiste Gault et al. "Dynamic reconstruction for atom probe tomography". In: *Ultramicroscopy* 111.11 (2011), pp. 1619–1624.

[151] J. M. Hyde et al. “Atom probe tomography of reactor pressure vessel steels: An analysis of data integrity”. In: *Ultramicroscopy* 111 (2011), pp. 676–682.

[152] D. Haley, P. Choi, and D. Raabe. “Guided mass spectrum labelling in atom probe tomography”. In: *Ultramicroscopy* 159 (2015), pp. 338–345.

[153] D. Haley, P. Choi, and D. Raabe. “Guided mass spectrum labelling in atom probe tomography”. In: *Ultramicroscopy* 159 (2015), pp. 338–345.

[154] Andrew J. London. “Quantifying Uncertainty from Mass-Peak Overlaps in Atom Probe Microscopy”. In: *Microscopy and Microanalysis* 25.2 (2019), pp. 378–388.

[155] B. Gault et al. “Estimation of the Reconstruction Parameters for Atom Probe Tomography”. In: *Microscopy and Microanalysis* 14.12 (2008), pp. 296–305.

[156] A. Morley et al. “Determining the composition of small features in atom probe: bcc Cu-rich precipitates in an Fe-rich matrix”. In: *Ultramicroscopy* 109.5 (2009), pp. 535–540.

[157] F. Vurpillot, A. Bostel, and D. Blavette. “Trajectory overlaps and local magnification in three-dimensional atom probe”. In: *Applied Physics Letters* 76.21 (May 2000), pp. 3127–3129.

[158] Jonathan M. Hyde et al. “Analysis of Radiation Damage in Light Water Reactors: Comparison of Cluster Analysis Methods for the Analysis of Atom Probe Data”. In: *Microscopy and Microanalysis* 23.02 (2017), pp. 366–375.

[159] J. M. Hyde et al. “Uncertainties and assumptions associated with APT and SANS characterisation of irradiation damage in RPV steels”. In: *Journal of Nuclear Materials* 449.1-3 (2014), pp. 308–314.

[160] Olof C. Hellman et al. “Analysis of three-dimensional atom-probe data by the proximity histogram”. In: *Microscopy and Microanalysis* 6.5 (2000), pp. 437–444.

[161] Julie M. Cairney et al. “Mining information from atom probe data”. In: *Ultramicroscopy* 159 (2015), pp. 324–337.

[162] J. M. Hyde, A. Cerezo, and T. J. Williams. “Statistical analysis of atom probe data: Detecting the early stages of solute clustering and/or co-segregation”. In: *Ultramicroscopy* 109.5 (2009), pp. 502–509.

[163] Paul D. Styman et al. “Quantitative methods for the APT analysis of thermally aged RPV steels”. In: *Ultramicroscopy* 132 (Sept. 2013), pp. 258–264.

[164] L. T. Stephenson et al. “Estimating the physical cluster-size distribution within materials using atom-probe”. In: *Microscopy Research and Technique* 74.9 (2011), pp. 799–803.

[165] Benjamin M. Jenkins et al. “The Effect of Composition Variations on the Response of Steels Subjected to High Fluence Neutron Irradiation”. In: *Materialia* (2020), p. 100717.

[166] Yimeng Chen, Peter H. Chou, and Emmanuelle A. Marquis. “Quantitative atom probe tomography characterization of microstructures in a proton irradiated 304 stainless steel”. In: *Journal of Nuclear Materials* 451.1-3 (2014), pp. 130–136.

[167] Leigh T. Stephenson et al. “Point-by-point compositional analysis for atom probe tomography”. In: *MethodsX* 1.1 (2014), pp. 12–18.

[168] M K Miller, K F Russell, and G B Thompson. “Strategies for fabricating atom probe specimens with a dual beam FIB”. In: *Ultramicroscopy* 102.4 (2005), pp. 287–298.

[169] Xiaodong Li and Bharat Bhushan. “A review of nanoindentation continuous stiffness measurement technique and its applications”. In: *Materials Characterization* 48.1 (Feb. 2002), pp. 11–36.

[170] Xiaoyuan Lou and David Gandy. “Advanced Manufacturing for Nuclear Energy”. In: *Journal of Nuclear Materials* 71.8 (2019), pp. 2834–2836.

[171] David Legland, Ignacio Arganda-Carreras, and Philippe Andrey. “MorphoLibJ: Integrated library and plugins for mathematical morphology with ImageJ”. In: *Bioinformatics* 32.22 (2016), pp. 3532–3534.

[172] S. Morito et al. “Block boundary analyses to identify martensite and bainite”. In: *Materials Today: Proceedings* 2 (2015), S913–S916.

[173] P. Van Uffelen and M. Suzuki. “Oxide fuel performance modeling and simulations”. In: *Comprehensive Nuclear Materials*. Vol. 3. Elsevier, 2012, pp. 535–577.

[174] J. K. MacKenzie. “Second Paper on Statistics Associated with the Random Disorientation of Cubes”. In: *Biometrika* 45.1-2 (1958), pp. 229–240.

[175] M. K. Miller and M. G. Hetherington. “Local magnification effects in the atom probe”. In: *Surface Science* 246.1-3 (1991), pp. 442–449.

[176] Christian Oberdorfer, Sebastian Manuel Eich, and Guido Schmitz. “A full-scale simulation approach for atom probe tomography”. In: *Ultramicroscopy* 128 (2013), pp. 55–67.

[177] D. W. Saxey. “Correlated ion analysis and the interpretation of atom probe mass spectra”. In: *Ultramicroscopy* 111.6 (2011), pp. 473–479.

[178] R. K.W. Marceau, P. Choi, and D. Raabe. “Understanding the detection of carbon in austenitic high-Mn steel using atom probe tomography”. In: *Ultramicroscopy* 132 (2013), pp. 239–247.

[179] J. Pešička et al. “The evolution of dislocation density during heat treatment and creep of tempered martensite ferritic steels”. In: *Acta Materialia* 51.16 (Sept. 2003), pp. 4847–4862.

[180] MarÍa Í.J. Balart et al. “Evolution of Non-metallic Inclusions Through Processing in Ti-V Microalloyed 316L and Al-V Microalloyed 17-4PH Stainless Steels for Hipping Applications”. In: *Metallurgical and Materials Transactions A: Physical Metallurgy and Materials Science* 51.12 (2020), pp. 6439–6460.

[181] Michael K. Miller. “Atom probe tomography characterization of solute segregation to dislocations and interfaces”. In: *Microscopy Research and Technique* 69.5 (2006), pp. 7808–7813.

[182] J. Zelenty et al. “Secondary precipitation within the cementite phase of reactor pressure vessel steels”. In: *Scripta Materialia* 115 (2016), pp. 118–122.

[183] E. D. Eason et al. “A physically-based correlation of irradiation-induced transition temperature shifts for RPV steels”. In: *Journal of Nuclear Materials* 433.1-3 (2013), pp. 240–254.

[184] M. Lambrecht et al. “On the correlation between irradiation-induced microstructural features and the hardening of reactor pressure vessel steels”. In: *Journal of Nuclear Materials* 406.1 (2010), pp. 84–89.

[185] J. Böhmert, H. W. Viehrig, and A. Ulbricht. “Correlation between irradiation-induced changes of microstructural parameters and mechanical properties of RPV steels”. In: *Journal of Nuclear Materials* 334.1 (2004), pp. 71–78.

[186] G. R. Odette and D. Frey. “Development of mechanical property correlation methodology for fusion environments”. In: *Journal of Nuclear Materials* 85-86.PART 2 (1979), pp. 817–822.

[187] R. E. Stoller and S. J. Zinkle. “On the relationship between uniaxial yield strength and resolved shear stress in polycrystalline materials”. In: *Journal of Nuclear Materials* 283-287.PART I (2000), pp. 349–352.

[188] Arne Wagner et al. “Influence of the copper impurity level on the irradiation response of reactor pressure vessel steels investigated by SANS”. In: *Nuclear Instruments and Methods in Physics Research, Section B: Beam Interactions with Materials and Atoms* 280 (2012), pp. 98–102.

[189] A. J. E. Foreman and M. J. Makin. “Dislocation movement through random arrays of obstacles”. In: *Canadian Journal of Physics* 45.2 (1967), pp. 511–517.

[190] L.P. Makin and Brian Ralph. “On the ageing of an aluminium-lithium-zirconium alloy”. In: *Journal of Materials Science* 19.12 (1984), pp. 3835–3843.

[191] M. Yi. *A Complete Guide to Grouped Bar Charts*. 2019.

[192] Luca Messina et al. “Exact ab initio transport coefficients in bcc Fe-X (X=Cr, Cu, Mn, Ni, P, Si) dilute alloys”. In: *Physical Review B - Condensed Matter and Materials Physics* 90.10 (2014), p. 104203.

[193] C. Domain and C. S. Becquart. “Diffusion of phosphorus in α-Fe: An ab initio study”. In: *Physical Review B - Condensed Matter and Materials Physics* 71.21 (2005), p. 214109.

[194] E. Meslin et al. “Theoretical study of atomic transport via interstitials in dilute Fe-P alloys”. In: *Physical Review B - Condensed Matter and Materials Physics* 75.9 (2007), p. 094303.

[195] H. Abe and E. Kuramoto. “Interaction of solutes with irradiation-induced defects of electron-irradiated dilute iron alloys”. In: *Journal of Nuclear Materials* 271-272 (1999), pp. 209–213.

[196] B. Gómez-Ferrer, C. Heintze, and C. Pareige. “On the role of Ni, Si and P on the nanostructural evolution of FeCr alloys under irradiation”. In: *Journal of Nuclear Materials* 517 (2019), pp. 35–44.

[197] H. J. Frost and K. C. Russell. “Particle stability with recoil resolution”. In: *Acta Metallurgica* 30.5 (1982), pp. 953–960.

[198] K. H. Heinig et al. “Interfaces under ion irradiation: Growth and taming of nanostructures”. In: *Applied Physics A: Materials Science and Processing* 77.1 (2003), pp. 17–25.

[199] Alan Xu et al. “Ion-irradiation-induced clustering in W-Re and W-Re-Os alloys: A comparative study using atom probe tomography and nanoindentation measurements”. In: *Acta Materialia* 87 (2015), pp. 121–127.

[200] T J Koppenaal and R J Arsenault. “Neutron-irradiation-strengthening in fee single crystals”. In: *Metallurgical Reviews* 16.1 (1971), pp. 175–196.

[201] S.J Zinkle and Y Matsukawa. “Observation and analysis of defect cluster production and interactions with dislocations”. In: *Journal of Nuclear Materials* 329-333 (2004), pp. 88–96.

[202] Jia Hong Ke et al. “Flux effects in precipitation under irradiation – Simulation of Fe-Cr alloys”. In: *Acta Materialia* 164 (2019), pp. 586–601.

[203] G.R. Odette et al. “Precipitation in reactor pressure vessel steels under ion and neutron irradiation: On the role of segregated network dislocations”. In: *Acta Materialia* 212 (2021), p. 116922.

[204] M. Briceño et al. “Effect of ion irradiation-produced defects on the mobility of dislocations in 304 stainless steel”. In: *Journal of Nuclear Materials* 409.1 (2011), pp. 18–26.

[205] D. Terentyev et al. “Hardening due to dislocation loop damage in RPV model alloys: Role of Mn segregation”. In: *Journal of Nuclear Materials* 457 (2015), pp. 173–181.

[206] H. Watanabe et al. “Hardening and microstructural evolution of A533b steels irradiated with Fe ions and electrons”. In: *Journal of Nuclear Materials* 471 (2016), pp. 243–250.

[207] E. A. Kuleshova et al. “Precipitation kinetics of radiation-induced Ni-Mn-Si phases in VVER-1000 reactor pressure vessel steels under low and high flux irradiation”. In: *Journal of Nuclear Materials* 553 (2021), p. 153091.

[208] A. Jostsons, P. M. Kelly, and R. G. Blake. “The nature of dislocation loops in neutron irradiated zirconium”. In: *Journal of Nuclear Materials* 66.3 (1977), pp. 236–256.

[209] M. Griffiths. “A review of microstructure evolution in zirconium alloys during irradiation”. In: *Journal of Nuclear Materials* 159.C (1988), pp. 190–218.

[210] Cong Dai et al. “Stability of vacancy and interstitial dislocation loops in α-zirconium: atomistic calculations and continuum modelling”. In: *Journal of Nuclear Materials* 554 (2021), p. 153059.

[211] A. Bakaev et al. “Interaction of minor alloying elements of high-Cr ferritic steels with lattice defects: An ab initio study”. In: *Journal of Nuclear Materials* 444.1-3 (2014), pp. 237–246.

[212] D Terentyev et al. “Mechanisms of radiation strengthening in Fe-Cr alloys as revealed by atomistic studies”. In: *Journal of Nuclear Materials* 442 (2013), pp. 470–485.

[213] L. K. Mansur. “Correlation of neutron and heavy-ion damage. Ii. The Predicted Temperature Shift If Swelling with Changes in Radiation Dose Rate”. In: *Journal of Nuclear Materials* 78.1 (1978), pp. 156–160.

[214] T. Muroga, H. Watanabe, and N. Yoshida. “Correlation of fast neutron, fusion neutron and electron irradiations based on the dislocation loop density”. In: *Journal of Nuclear Materials* 174.2-3 (1990), pp. 282–288.

[215] Ceri A. Williams et al. “Effects of heavy-ion irradiation on solute segregation to dislocations in oxide-dispersion-strengthened Eurofer 97 steel”. In: *Journal of Nuclear Materials* 412.1 (2011), pp. 100–105.

[216] Hailong Liu et al. “The effect of dislocations on MnNi-rich clusters in self-ion irradiated FeMnNi alloy”. In: *Journal of Nuclear Materials* 519 (2019), pp. 64–73.

Appendix A

ANSTO TEM

Initial Transmission Electron Microscopy (TEM) work on this material was conducted by Dr Claudia Gasparrini, at that time representing Imperial College, focusing on STEM-EDX (scanning transmission electron microscopy energy dispersive spectroscopy) and HRTEM (high-resolution TEM). The STEM-EDX characterisation of bainite and ferrite samples indicated the presence of particles, mainly consisting of aluminium oxide and manganese-silicon-nitride. The intermetallic phase appeared to have often nucleated adjacent to molybdenum carbide particles in both the unirradiated and irradiated samples. The oxide particles are seemingly of the same nature as that observed using SEM-EDS in the as-received samples (discussed in Chapter 4). Nitrides are also likely induced by the HIP process, given that the nitrogen content of the HIPed steel is significantly higher compared to the forged samples.

Characterisation conducted by TEM in bright field mode (BF) on the three-month irradiated HIPed sample did not show any visible irradiation-induced damage features; black dots visible on the surface were later identified as surface oxide (Fe_3O_4) by centred dark field (CDF) imaging and selected area diffraction patterns (SADPs). Analysis of the unirradiated and neutron irradiated HIPed bainite grains by HRTEM imaging indicated

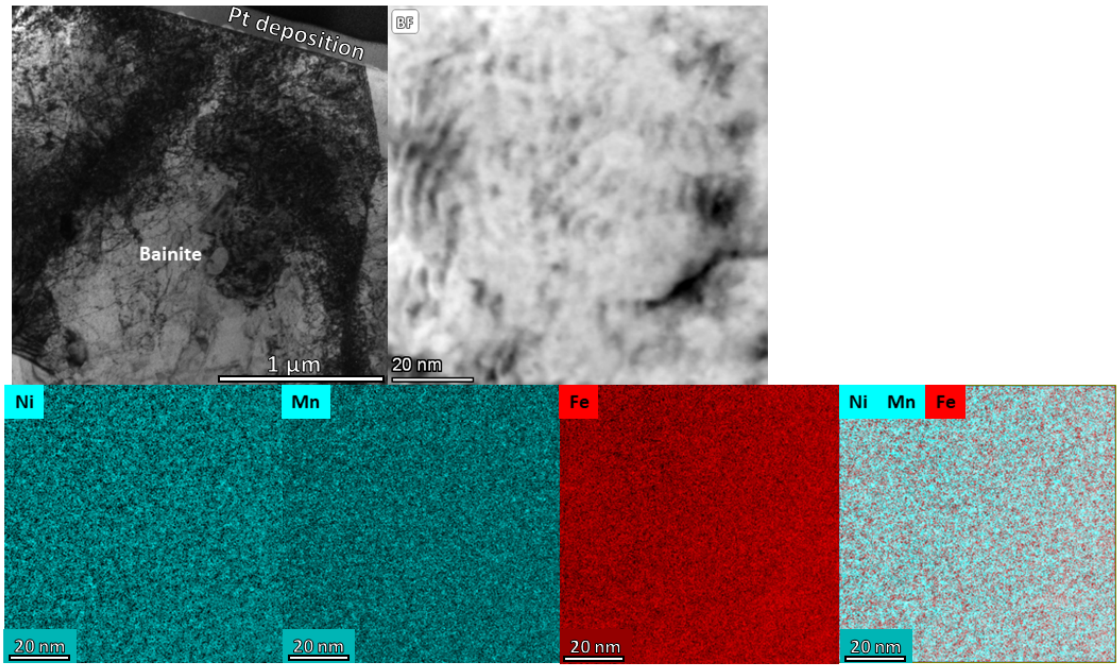

Figure A.1: STEM-EDX analysis of a bainite grain extracted from neutron irradiated sample: BF TEM images (top) and STEM-EDX maps of the region shown at high magnification of Ni, Mn, Fe and all three elements together.

only a d-spacing associated with ferrite and magnetite (Fe_3O_4). Specifically, 2.017 Å and 2.02 Å d-spacings were calculated - which are related to the ferrite phase (a=b=c= 2.8664 Å where the (1 1 0) is 2.027 Å) - whilst d-spacings of 2.502 Å, 2.409 Å and 1.713 Å were related to magnetite phase (a=b=c=8.3960 Å where the (3 1 1) is 2.5320 Å, the (2 2 2) is 2.4243 Å and (4 2 2) is 1.7146 Å).

STEM-EDX analysis was performed using a higher sensitivity Super-X EDX detector, allowing visualisation of an inhomogeneous distribution of solute in the neutron irradiated sample. The use of four single silicon drift detectors enabled the acquisition of more counts in a short amount of time, minimising the impact of any sample drift; this is particularly crucial in this analysis, since the expected clusters are of nanometre scale. Specifically, the distributions of Ni and Mn overlapped when these elements were plotted together (see Figure A.1). The uneven distribution of the solute shown in Figure A.1 for Mn, Ni and Fe is,

however, subtle and no indisputable evidence of cluster formation can be derived.

Unfortunately, Dr Gasparrini leaving the project prevented any further TEM characterisation of the ANSTO irradiated material.

Appendix B

Application of Maximum Separation Method to Fe^{4+} Irradiation Features

In some instances, additional study into the impact of Maximum Separation Method (MSM) parameter choice was conducted for the self-ion irradiated samples. Parameter-tuning beyond that detailed in Chapter 3, Section 3.6 is described below.

B.1 Investigation into MSM Parameters for P atmospheres

Given how diffuse these features are, a much higher d_{max} than conventionally employed in RPV solute clustering must be selected. Iteration through MSM parameters showed a large amount of variation between samples in terms of which d_{max} and NN_{order} values best captured what could be seen visually.

The distribution of P through each dataset differed significantly, thus, where in some cases a d_{max} of 1.5 nm was appropriate, in other cases it captured P atoms which clearly

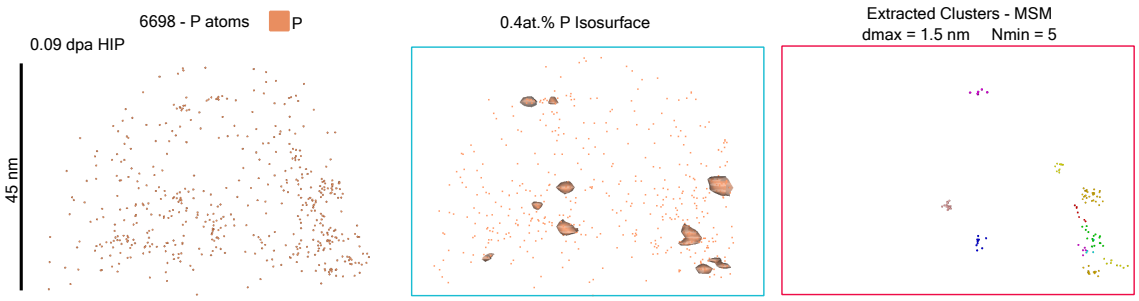

Figure B.1: Comparing the use of isosurfaces and MSM to extract P atmospheres from the same APT atom map (0.09 dpa HIP).

lay outside of the P enriched regions. Of note is that, whilst increasing order does not dramatically change the number of clusters identified, it does result in more Fe atoms being incorporated in clusters. Fe in clusters is generally treated as an artefact in RPV steel analysis, however that is a result of the higher density associated with MNS clustering. It is therefore difficult to definitively say whether Fe incorporated in these clusters is an artefact.

For a low irradiation damage HIPed steel dataset, the P atmosphere isolation possible using isoconcentration surfaces and cluster analysis (MSM) is shown in Figure B.1. Creating interfaces for 0.4at.% P produced 10 identified atmospheres, whereas MSM yielded 11. This is a likely result of MSM filtering out regions where too few P atoms ($N < N_{min}$) are present.

B.2 MSM Order Parameter Changing for Irradiation A Mn-Ni-Si Clusters

As the clusters were more spatially defined in self-ion Irradiation A, compared to the those found in the analyses of neutron irradiated materials, attempts to better define them using the core-linkage algorithm (incorporating a nearest-neighbour 'order' parameter to MSM) were made.

Figure B.2 compares the clusters shown in a slice to those extracted from that region

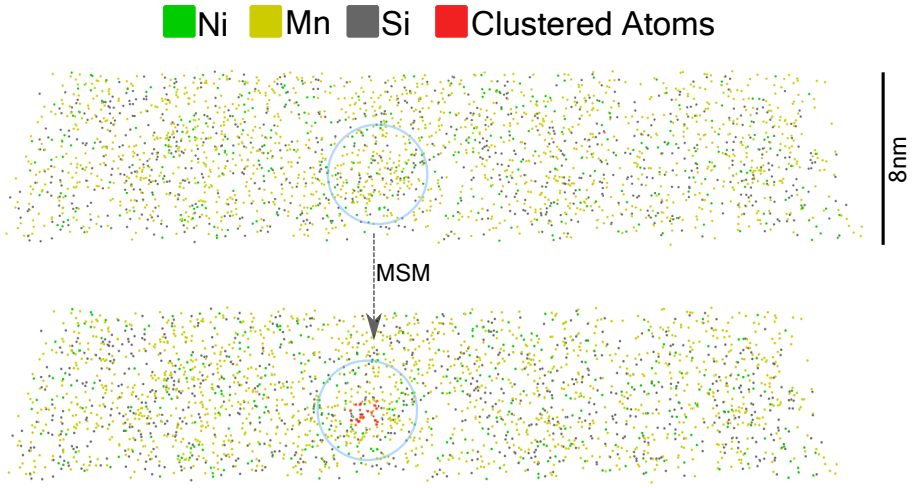

Figure B.2: Reduced view of a 8 nm thick slice of atom map from Forging B showing the identification of a cluster using MSM, where d_{max} = 0.5 nm and N_{min} = 13. The atoms determined to be part of a cluster are shown in red (within the blue circle)

using the parameters described in the caption.

Ultimately, tuning the MSM nearest-neighbour order value did not yield improved cluster identification, and thus an order of NN = 1 was deemed most suitable in this case.